Reversible allylic substitution based responsive polymer materials

Klemm, B.

DOI
10.4233/uuid:f1ececbd-070f-415f-b4e5-3ea56bdc1731

Publication date
2024

Document Version
Final published version

Citation (APA)
Klemm, B. (2024). *Reversible allylic substitution based responsive polymer materials*. [Dissertation (TU Delft), Delft University of Technology]. https://doi.org/10.4233/uuid:f1ececbd-070f-415f-b4e5-3ea56bdc1731

Reversible allylic substitution based responsive polymer materials

Benjamin
Klemm

Reversible allylic substitution based responsive polymer materials

Dissertation

for the purpose of obtaining the degree of doctor
at Delft University of Technology
by the authority of the Rector Magnificus, prof.dr.ir. T.H.J.J. van der Hagen
chair of the Board of Doctorates
to be defended publicly on
Friday 12 of April 2024 at 10:00 o'clock.

by

Benjamin KLEMM

Master of Science in Chemical Engineering, Delft University of Technology, Netherlands

Master of Science in Water Technology, University of Groningen, Wageningen University and University of Twente, Netherlands

born in Karl-Marx-Stadt, now Chemnitz, Germany

This dissertation has been approved by the promoters.

Composition of the doctoral committee:

Rector Magnificus	chairperson
Dr. R. Eelkema	Delft University of Technology, promoter
Prof. dr. J.H. van Esch	Delft University of Technology, promoter

Independent members:

Prof. Dr. S. Picken	Delft University of Technology
Prof. Dr. A. Urakawa	Delft University of Technology
Prof. Dr. M. Kamperman	University of Groningen
Prof. Dr. C.A. Nijhuis	University of Twente
Dr. P.E. Boukany	Delft University of Technology
Dr. habil. E. Mendes	Delft University of Technology, reserve member

The work described in this thesis was carried out in the Advanced Soft Matter (ASM) group at Delft University of Technology, Faculty of Applied Science. The research has been funded by a consolidator grant (726381) from the European Research Council (ERC).

Cover by: Benjamin Klemm

Printed by: Ipskamp Drukkers, Enschede

ISBN: 978-94-6384-566-3

This dissertation is
dedicated to my family

TABLE OF CONTENTS

1. GENERAL INTRODUCTION

2. ORGANOCATALYSIS IN AQUEOUS MEDIA

3. TEMPORALLY PROGRAMMED POLYMER-SOLVENT INTERACTIONS USING A CHEMICAL REACTION NETWORK

4. NAKED EYE THIOL-ANALYTE DETECTION VIA SELF-PROPAGATING, AMPLIFIED CHEMICAL REACTION CYCLE

5. NUCLEOPHILE-TRIGGERED PRODRUG RELEASE FROM POLYMER HYDROGELS

ABOUT THE AUTHOR AND LIST OF PUBLICATIONS

1

GENERAL INTRODUCTION

A property of living systems is the ability to respond to stimuli from their surrounding environment, which include temperature, light, changes in pH , peptides and hormones.[1,2] The underlying mechanisms are based on arrays of complex (bio)chemical reactions and enzymatic conversions, which allow specialized functions such as signal transduction and intracellular transport.[3–5]

A prominent example of nature's signal transduction cascade is the 'fight or flight' response triggered by the release of adrenaline in anticipation of danger. Here, released neurotransmitter molecules bind to specific extracellular plasma membrane receptors in liver cells, causing morphological changes in their protein structure.[6] This in turn leads to an amplification of the input signal, commonly referred to as 'second' messenger molecules. With the exponential increase of messengers in response to the adrenaline recognition, information is transferred inside the cell.[7] As a result, glycogen stored in the liver is converted by glycogen phosphorylase enzyme into glucose[8], which then is used as energy input for macroscopic responses, ranging from sweating, dilated pupils to increased heart contraction.[6]

In contrast, artificial or synthetic materials capable of performing such primary processes by adapting and interacting with their environment, are entirely absent. An interesting approach to translate such rudimentary cellular processes into synthetic materials is the use of organocatalysis. Organocatalytic transformations provide a simpler strategy than compared to biocatalysis by using small molecule catalysts. Using organocatalysts enables not only control over chemical reactions, but also provides cheap, reusable precursors which are often more reliable than enzymes and less cytotoxic than metal catalysts.[9]

Artificial catalysts that are activated by external signals have been used to control material properties in supramolecular systems.[10,11]

By taking inspiration from nature, we sought to exploit organocatalysis in the design of new strategies for signal-responsive materials, where signal transduction between systems is achieved though signal recognition, signal translation and ultimately converted into macroscopic material response (Figure 1). In this thesis, we will describe the implementation of this new concept for the development of signal-triggered and autonomous material (de)formation/(de)swelling, signal-amplified material degradation and signal-controlled cargo release.

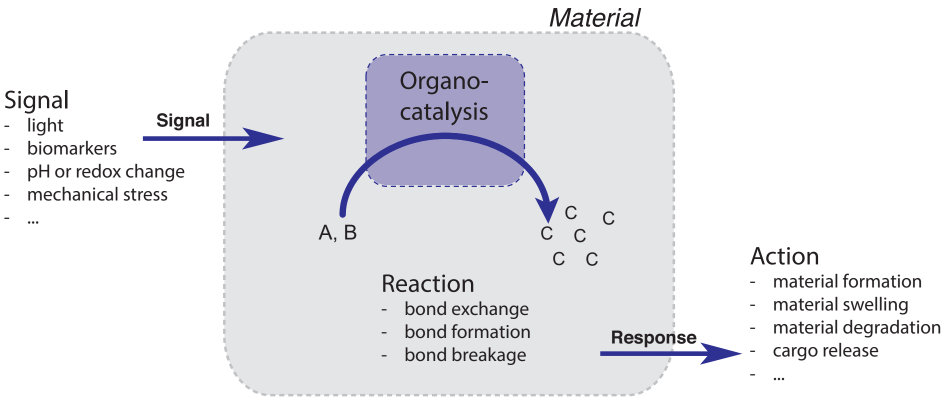

Figure 1: Schematics of the general concept inspired by nature using organocatalysis embedded in signal-responsive materials, where signal transduction between systems is achieved though signal-recognition, signal translation and ultimately converted into macroscopic material response e.g. material (de)formation, (de)swelling, degradation or signal-controlled cargo release.

1.1 SIGNAL TRANSDUCTION IN SYNTHETIC MATERIALS

Inspired by living systems and their primary processes, many research groups have been focused on mimicking signal transduction in synthetic analogues to develop ‘smart’ signal-responsive materials, which are capable of sensing their environment and respond in a preprogrammed or autonomous fashion.[12] Materials with autonomous response mechanism can find many applications ranging from regenerative medicine, optoelectronics to nanomachines.[13–15] Generally, to obtain signal-responsive materials, signal-sensitive moieties are incorporated into polymeric materials, which are then activated or triggered by stimuli input. The activation event can result in changes in conformation, solubility or polarity amongst others which ultimately leads to a macroscopic change in the material, e.g. (de)swelling or (dis)assembly.[16,17] Classical responsive chemical systems operate near or at thermodynamic equilibrium, which enables switching between two equilibrium states (from state A to B) upon signal activation only. Thus, changes from state A to B remain typically stable until counter-activation by signal-input, which reverts the system back to state A.[16] In contrast, however, to obtain autonomously operating synthetic materials, the activation of non-interacting building blocks is frequently coupled to out-of-equilibrium chemical reaction networks (CRNs).[18] For the design of CRNs, an increasing number of chemical reactions has been reported in the last decade, including methylation, imine formation, carboxylic acid activation, esterification and thiol-disulfide exchange, amongst others.[19]

Importantly, such CRNs consist of two or more competing reactions, but at least need an (i) activation and a (ii) depletion reaction. While the activation reaction sustains the active material due to the availability of chemical fuel, the depletion reaction causes the material to disassemble back to its precursor in the absence of fuel.[20] This enables autonomous collective material response, where an out-of-equilibrium state is sustained until the system depletes all of its fuel reserves. The transient cycling between activated and non-activated states via input of chemical energy has been reported for many systems, including molecular motors[21], supramolecular (dis)assembly[3,22–24], polymer crosslinking[25], polymer aggregation[26] and system self-replication[27–29].

1.2 SIGNAL AMPLIFICATION CASCADES IN SYNTHETIC MATERIALS

An intrinsic part of the signalling cascade in living cells is their ability to detect and subsequently amplify an external signal input using enzyme catalysis.[30] Mimicking signal amplification in synthetic analogues, which are independent of enzymatic transformations, is extremely challenging and rare. Only a few examples have been shown in literature using small molecule reagents[31,32], self-immolative polymers[33–35], or polymeric materials[36,37], which employ signals ranging from hydrogen peroxide[38], thiols[39,40] to fluoride[41–45], amongst others[46–48]. Commonly, these systems suffer from challenging synthetic procedures and often experience issues with background interference.[36,49,50]

By realizing artificial materials able of translating and amplifying ultralow concentrations of signal into a global macroscopic change can find many applications ranging from advanced forensics[30] to socio-environmental diagnostics[30,37,51,52]. It is therefore useful to find new strategies to develop signal transduction in synthetic materials by utilizing signal-amplified reaction cascades.

1.3 SIGNAL RESPONSIVE CARGO RELEASE IN SYNTHETIC MATERIALS

One of the most important aspects in drug delivery is the target specific release of drugs and to prevent unspecific drug release.[53] Indeed, many drug candidates are cytotoxic, meaning those drugs cause harm to healthy cells via accumulation, leading to side effects.[54] Although a large number of different drug carriers has been established over the years (e.g. micelles, gels, polymersomes or nanoparticles), many carriers are not stimuli-responsive.[55] Incorporation of stimuli-responsiveness enables drug carriers to interact with their surroundings though target specific recognition of stimuli.

In an ideal scenario, the drug carriers would reach their target site without drug leakage, where the availability of a signal would trigger the release of the drug. Many different triggers have been envisioned, mainly focusing around the localized environment of a tumor site. In particular, these environments express specific small molecules or enzymes, acidic pH, elevated temperatures or changed redox conditions.[56] Hence, platforms capable to respond to these signals would be highly advantageous through precision drug release and to minimize side effects.

A promising strategy to develop signal-responsive carriers is to link signal-responsive prodrugs to a carrier material. Prodrugs or caged drugs are chemically modified therapeutics that are inactive until their activation via stimulus-induced removal of the cage group.[57] A variety of stimuli have been used for controlled drug activation, such as glutathione (GSH)[58,59], reactive oxygen species (ROS)[60,61] or enzymes[62–64]. However, material development approaches are mostly based on either non-covalent linkage (e.g. encapsulation[65,66], self-assembly[66–68]) or is achieved through complex synthesis procedures, which are often limited to polymer conjugates[69,70] or dendrimer systems[62].

1.4 RESEARCH AIM

The aim of the work described in this thesis is to develop signal-responsive materials that are capable to respond to signals from their environment. We investigated the design and implementation of nucleophilic substitution reactions using electron deficient Morita-Baylis-Hillman (MBH) adducts with tertiary amines or phosphines to directly or indirectly alter material properties by generating meta-stable, positively charged intermediates. The corresponding intermediate salts can be reversed to its neutral precursor upon addition of nucleophile-signals, essentially releasing its conjugate cargo. Eventually, by utilizing the principle of selectively switching between ‘charge’ states and/or controlled release of substituents and their incorporation into material scaffolds, we were able to preprogram specific material responses aiming for applications, such as controlled drug delivery, autonomous material actuators or signal-detection platforms.

1.5 THESIS OUTLINE

In **Chapter 1**, we provide an overview of the current state-of-the-art research in signal-responsive, interactive materials using CRNs to control material properties, molecular self-amplification strategies and signal-controlled drug release. After this introductory chapter, the **2nd Chapter** covers a literature review on organocatalysis in aqueous media with focus on nucleophilic and base catalysis. Noteworthy, the nucleophilic substitution reaction described in this sub-chapter was the fundamental inspiration for the design and development of the CRN presented in **chapter 3**. In **Chapter 3**, we describe the design of a CRN based on reversible formation of positive charges on a tertiary amine substrate, which are removed using nucleophilic signals. Controlling the deactivation kinetics, we were able to demonstrate pre-programmable material’s behavior in nanoscale supramolecular block-copolymer micelles and macroscale polymeric hydrogels. In **Chapter 4**, we introduce allylic phosphonium salts as platform for detecting thiol analytes through a self-propagating amplification cycle that triggers macroscopic degradation of disulfide-crosslinked hydrogels. Finally, in **Chapter 5**, we describe the concept and development of prodrug-linkers based on tertiary amine drugs and MBH-adducts, their incorporation into hydrogel scaffolds and the controlled release of drug conjugates upon biomarker nucleophile triggers in the presence of cancer cells for drug delivery. Lastly, this thesis ends with a **summary** of all chapters and conclusive statements.

1.6 REFERENCES

1 C. Kiel, E. Yus and L. Serrano, *Cell*, 2010, **140**, 33–47.
2 D. L. Nelson, M. M. Cox, K. Beginnen, B.-S. (M.) and F. Glauner, *Lehninger biochemie*, Springer, 2001.
3 J. Boekhoven, W. E. Hendriksen, G. J. M. Koper, R. Eelkema and J. H. van Esch, *Science.*, 2015, **349**, 1075–1079.
4 E. Karsenti, *Nat. Rev. Mol. cell Biol.*, 2008, **9**, 255–262.
5 M. M. Cox and D. L. Nelson, *Lehninger principles of biochemistry*, Macmillan, 2008.
6 B. D. Gomperts, P. E. R. Tatham and I. M. Kramer, *Signal transduction*, Gulf Professional Publishing, 2002.
7 K. Lounsbury, in *Pharmacology*, Elsevier, 2009, pp. 103–112.
8 T. Traut, *Allosteric regulatory enzymes*, Springer, 2008.
9 M. P. van Der Helm, B. Klemm and R. Eelkema, *Nat. Rev. Chem.*, 2019, **3**, 491–508.
10 F. Trausel, C. Maity, J. M. Poolman, D. S. J. Kouwenberg, F. Versluis, J. H. Van Esch and R. Eelkema, *Nat. Commun.*, 2017, **8**, 879.
11 J. Boekhoven, J. M. Poolman, C. Maity, F. Li, L. Van Der Mee, C. B. Minkenberg, E. Mendes, J. H. Van Esch and R. Eelkema, *Nat. Chem.*, 2013, **5**, 433–437.
12 K. Liu, M. Tebyetekerwa, D. Ji and S. Ramakrishna, *Matter*, 2020, **3**, 590–593.
13 J. Boekhoven and S. I. Stupp, *Adv. Mater.*, 2014, **26**, 1642–1659.
14 A. R. Hirst, B. Escuder, J. F. Miravet and D. K. Smith, *Angew. Chem. Int. Ed.*, 2008, **47**, 8002–8018.
15 B. A. Grzybowski, K. Fitzner, J. Paczesny and S. Granick, *Chem. Soc. Rev.*, 2017, **46**, 5647–5678.
16 A. Walther, *Adv. Mater.*, 2020, **32**, 1905111.
17 T. Masuda, A. Terasaki, A. M. Akimoto, K. Nagase, T. Okano and R. Yoshida, *RSC Adv.*, 2015, **5**, 5781–5787.
18 S. A. P. van Rossum, M. Tena-Solsona, J. H. van Esch, R. Eelkema and J. Boekhoven, *Chem. Soc. Rev.*, 2017, **46**, 5519–5535.
19 B. Rieß, R. K. Grötsch and J. Boekhoven, *Chem*, 2020, **6**, 552–578.
20 J. Boekhoven, A. M. Brizard, K. N. K. Kowlgi, G. J. M. Koper, R. Eelkema and J. H. van Esch, *Angew. Chem. Int. Ed.*, 2010, **122**, 4935–4938.
21 K. Mo, Y. Zhang, Z. Dong, Y. Yang, X. Ma, B. L. Feringa and D. Zhao, *Nature*, 2022, **609**, 293–298.
22 S. Panja, C. Patterson and D. J. Adams, *Macromol. Rapid Commun.*, 2019, **40**, 1900251.
23 J. P. Wojciechowski, A. D. Martin and P. Thordarson, *J. Am. Chem. Soc.*, 2018, **140**, 2869–2874.
24 T. Heuser, E. Weyandt and A. Walther, *Angew. Chem. Int. Ed.*, 2015, **54**, 13258–13262.
25 B. Zhang, I. M. Jayalath, J. Ke, J. L. Sparks, C. S. Hartley and D. Konkolewicz, *Chem. Commun.*, 2019, **55**, 2086–2089.
26 M. P. van Der Helm, C. Wang, B. Fan, M. Macchione, E. Mendes and R. Eelkema, *Angew. Chem. Int. Ed.*, 2020, **132**, 20785–20792.
27 S. M. Morrow, I. Colomer and S. P. Fletcher, *Nat. Commun.*, 2019, **10**, 1–9.
28 P. Adamski, M. Eleveld, A. Sood, Á. Kun, A. Szilágyi, T. Czárán, E. Szathmáry and S. Otto, *Nat. Rev. Chem.*, 2020, **4**, 386–403.
29 I. Colomer, S. M. Morrow and S. P. Fletcher, *Nat. Commun.*, 2018, **9**, 2239.
30 P. Scrimin and L. J. Prins, *Chem. Soc. Rev.*, 2011, **40**, 4488–4505.
31 H. Mohapatra, H. Kim and S. T. Phillips, *J. Am. Chem. Soc.*, 2015, **137**, 12498–12501.
32 H. Kim, M. S. Baker and S. T. Phillips, *Chem. Sci.*, 2015, **6**, 3388–3392.
33 W. Seo and S. T. Phillips, *J. Am. Chem. Soc.*, 2010, **132**, 9234–9235.
34 A. M. DiLauro, G. G. Lewis and S. T. Phillips, *Angew. Chem. Int. Ed.*, 2015, **127**, 6298–

6303.
35 G. I. Peterson, M. B. Larsen and A. J. Boydston, *Macromolecules*, 2012, **45**, 7317–7328.
36 T. Wu, X. Feng and X. Sun, *Polym. Chem.*, 2022, **13**, 922–928.
37 D.-H. Lee, S. A. Valenzuela, M. N. Dominguez, M. Otsuka, D. J. Milliron and E. V Anslyn, *Cell Reports Phys. Sci.*, 2021, **2**, 100552.
38 E. Sella, A. Lubelski, J. Klafter and D. Shabat, *J. Am. Chem. Soc.*, 2010, **132**, 3945–3952.
39 E. Sella, R. Weinstain, R. Erez, N. Z. Burns, P. S. Baran and D. Shabat, *Chem. Commun.*, 2010, **46**, 6575–6577.
40 S. N. Semenov, L. J. Kraft, A. Ainla, M. Zhao, M. Baghbanzadeh, V. E. Campbell, K. Kang, J. M. Fox and G. M. Whitesides, *Nature*, 2016, **537**, 656–660.
41 Y.-H. Chen, W.-C. Chien, D.-C. Lee and K.-T. Tan, *Anal. Chem.*, 2019, **91**, 12461–12467.
42 M. S. Baker and S. T. Phillips, *J. Am. Chem. Soc.*, 2011, **133**, 5170–5173.
43 R. Perry-Feigenbaum, E. Sella and D. Shabat, *Chem. Eur. J.*, 2011, **17**, 12123–12128.
44 J.-A. Gu, V. Mani and S.-T. Huang, *Analyst*, 2015, **140**, 346–352.
45 X. Sun, S. D. Dahlhauser and E. V Anslyn, *J. Am. Chem. Soc.*, 2017, **139**, 4635–4638.
46 K. Arimitsu, M. Miyamoto and K. Ichimura, *Angew. Chem. Int. Ed.*, 2000, **112**, 3567–3570.
47 D.-G. Cho and J. L. Sessler, *Chem. Soc. Rev.*, 2009, **38**, 1647–1662.
48 H. Mohapatra, K. M. Schmid and S. T. Phillips, *Chem. Commun.*, 2012, **48**, 3018–3020.
49 X. Sun, D. Shabat, S. T. Phillips and E. V Anslyn, *J. Phys. Org. Chem.*, 2018, **31**, e3827.
50 S. Goggins and C. G. Frost, *Analyst*, 2016, **141**, 3157–3218.
51 V. Delplace and J. Nicolas, *Nat. Chem.*, 2015, **7**, 771–784.
52 X. Sun, A. A. Boulgakov, L. N. Smith, P. Metola, E. M. Marcotte and E. V Anslyn, *ACS Cent. Sci.*, 2018, **4**, 854–861.
53 L. Li, W.-W. Yang and D.-G. Xu, *J. Drug Target.*, 2019, **27**, 423–433.
54 S. Ganta, H. Devalapally, A. Shahiwala and M. Amiji, *J. Control. release*, 2008, **126**, 187–204.
55 C. Liu, Y. Fang, X. Zhang, Y. R. Neupane, Z. Jiang, G. Pastorin and S. Soh, *Mater. Chem. Front.*, 2021, **5**, 4317–4326.
56 R. Jia, L. Teng, L. Gao, T. Su, L. Fu, Z. Qiu and Y. Bi, *Int. J. Nanomedicine*, 2021, 1525–1551.
57 V. Abet, F. Filace, J. Recio, J. Alvarez-Builla and C. Burgos, *Eur. J. Med. Chem.*, 2017, **127**, 810–827.
58 J. Li, M. Yuan, T. Qiu, M. Lu, S. Zhan, Y. Bai, M. Yang, X. Liu and X. Zhang, *J. Biomater. Sci. Polym. Ed.*, 2023, **34**, 650–673.
59 J. Zhuang, B. Zhao, X. Meng, J. D. Schiffman, S. L. Perry, R. W. Vachet and S. Thayumanavan, *Chem. Sci.*, 2020, **11**, 2103–2111.
60 I. Piergentili, P. R. Bouwmans, L. Reinalda, R. W. Lewis, B. Klemm, H. Liu, R. M. de Kruijff, A. G. Denkova and R. Eelkema, *Polym. Chem.*, 2022, **13**, 2383–2390.
61 Z. Zhao, X. Liu, M. Hou, R. Zhou, F. Wu, J. Yan, W. Li, Y. Zheng, Q. Zhong and Y. Chen, *Adv. Mater.*, 2022, **34**, 2110560.
62 A. Gopin, S. Ebner, B. Attali and D. Shabat, *Bioconjug. Chem.*, 2006, **17**, 1432–1440.
63 H. Jin, J. Lu and X. Wu, *Bioorg. Med. Chem.*, 2012, **20**, 3465–3469.
64 G. Fumagalli, L. Polito, E. Colombo, F. Foschi, M. S. Christodoulou, F. Galeotti, D. Perdicchia, I. Bassanini, S. Riva and P. Seneci, *ACS Med. Chem. Lett.*, 2019, **10**, 611–614.
65 Q. Chen, X. Huang, G. Zhang, J. Li, Y. Liu and X. Yan, *RSC Adv.*, 2023, **13**, 1684–1700.
66 X. Xu, Y. Jiang and C. Lu, *Anal. Chem.*, 2022, **94**, 10221–10226.
67 D. Wang, C. Du, S. Wang, L. Li, T. Liu, J. Song, Z. He, Y. Zhai, B. Sun and J. Sun, *ACS Appl. Mater. Interfaces*, 2022, **14**, 51200–51211.
68 P. Zhong, H. Meng, J. Qiu, J. Zhang, H. Sun, R. Cheng and Z. Zhong, *J. Control. Release*, 2017, **259**, 176–186.
69 T. Eom, W. Yoo, Y.-D. Lee, J. H. Park, Y. Choe, J. Bang, S. Kim and A. Khan, *J. Mater.*

Chem. B, 2017, **5**, 4574–4578.

70 J. Anderski, L. Mahlert, J. Sun, W. Birnbaum, D. Mulac, S. Schreiber, F. Herrmann, D. Kuckling and K. Langer, *Int. J. Pharm.*, 2019, **557**, 182–191.

2

ORGANOCATALYSIS IN AQUEOUS MEDIA

Even though enzymes are the cornerstones of living systems, it has so far proven difficult to deploy artificial catalysts in a biological setting. Organocatalysts are arguably well-suited artificial catalysts for this purpose because, compared with enzymes and inorganic catalysts, they are simpler, often less toxic and widely accessible. This review describes how organocatalysts that operate in aqueous media might enable us to selectively access new chemical transformations and provide new possibilities for chemical biology and biomedicine. Organocatalysts can be categorized according to the mechanisms by which they activate substrates, drawing comparisons with enzymes. We describe the characteristics of a catalyst that are necessary for biological compatibility and in vivo applicability, and use these to evaluate a selection of organocatalytic reactions. The attributes of the catalyst (such as functional groups and pK_a values) and the reaction (such as the microenvironment surrounding intermediates) are key considerations when developing efficient organocatalysis in aqueous media. Although we only know of a limited set of organocatalytic reactions with biological potential, on the basis of recent developments we expect a bright future for organocatalysis in biology, to the benefit of chemical biology and biomedicine.

This chapter is based on:
M.P. van der Helm*, B. Klemm* and R. Eelkema, Nat. Rev. Chem., 2019, **3**, 491-508. *These authors contributed equally.

2.1 INTRODUCTION

Enzymes are crucial components of living systems. Along with enzyme catalysis, synthetic transition metal catalysis has seen widespread use under biologically relevant conditions.[1–8] By contrast, applications of synthetic organocatalysis in biological systems are only emerging, despite organocatalysis being a powerful tool to selectively access new transformations in chemical biology. For example, by constructing protein conjugates we can gain a better understanding of cellular biochemistry and eventually come closer to the creation of de novo life. Organocatalysts are well suited to this and other tasks because, compared with enzymes or inorganic catalysts, they are simpler to design and modify, more accessible and often less toxic. Organocatalysts can even be considered minimalistic biocatalysts because they can often closely approximate the amino acid residues and cofactors that make up an enzyme. Function can follow form, such that organocatalytic mechanisms can closely mimic enzymatic ones. Despite this, although enzymatic reactions commonly proceed in aqueous environments, performing organocatalytic reactions in these solutions remains a considerable challenge.[9–12] H_2O is a solvent with a high surface tension, polarity and hydrogen-bonding ability — properties that can detract from organic reactions. Indeed, the major drawbacks for using H_2O as a solvent are the insolubility of most organic compounds, poor hydrolytic stability of chemical compounds and catalytic intermediates, and destabilization of transition states by disruption of hydrogen bonds.[10,13,14] However, landmark studies have shown that these challenges can be overcome (Figure 1).

The landmark organocatalysis studies have been reviewed[10–12,15–19] and we instead focus on aqueous organocatalytic reactions, categorizing each type and providing background and examples, including relevant comparisons with enzymatic reactions. We will then evaluate the reactions for their biocompatibility and in vivo applicability, according to our criteria for implementing promising candidates in biological environments. The scope of this review encompasses reactions in which all reactants, co-solvents, reagents and products are homogeneously dissolved in H_2O or aqueous buffer as the major solvent. Attention must also be paid to catalyst loadings, which in the case of organocatalysts are variable and usually higher than those used for enzymes and transition metal catalysts.

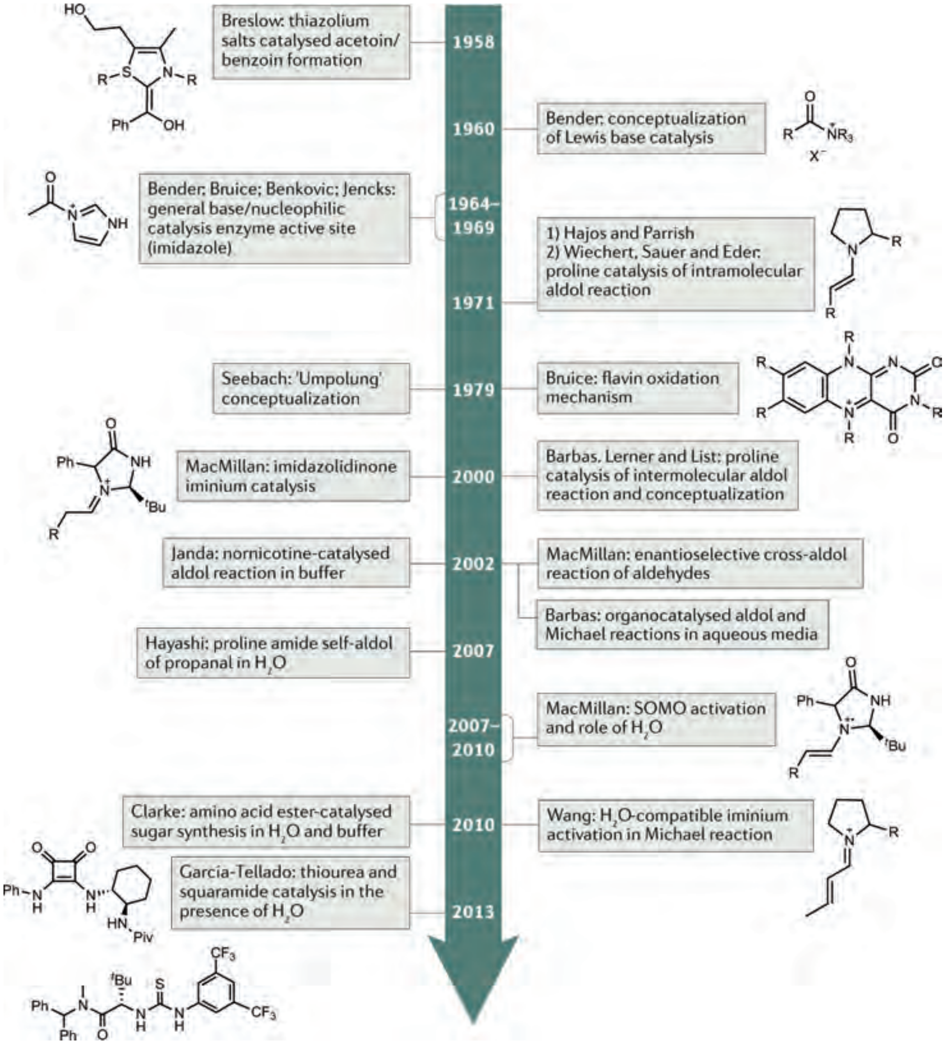

Figure 1. Organocatalysis has developed rapidly in little over half a century. Landmark discoveries are either conceptual contributions or examples of organocatalysis in (buffered) H_2O (or H_2O/organic solvent mixtures). SOMO, singly-occupied molecular orbital.

Altogether, organocatalysts that operate efficiently in aqueous and even biological environments would find applications ranging from smart materials such as soft robotics or self-healing materials to more biomedically relevant applications like controlled drug delivery or on-demand drug synthesis in tumour cells. The examples of organocatalysts discussed in this chapter are displayed in the Supplementary Information Table S1. The diversity of organocatalyst structures is reflected in the different mechanisms (Table 1) by which they activate substrates. However, this chapter will focus only on nucleophilic, general / or specific base catalysis.

2.2 ORGANOCATALYTIC ACTIVATION

Seminal studies by Barbas, List and MacMillan saw organocatalysis popularized as a third strategy in asymmetric catalysis, next to transition metal and enzymatic catalysis.[20–22] However, examples of organocatalysis extend beyond asymmetric catalysis and we describe here any bond-breaking and bond-forming transformation.

In covalent activation, the catalyst forms a covalent bond to the substrate to afford an activated intermediate. In terms of aqueous reactions, catalysts that activate a carbonyl substrate to form an enamine and iminium, typically as part of an overall asymmetric aldol reaction, have received the most attention.[23,24] More generally, the modes of covalent activation (Table 1) are nucleophilic catalysis, as well as general and specific acid or base catalysis.

Table 1: Categories of covalent organocatalysis in aqueous media.

Category	Covalent activation reaction mechanism	Example reactions
[Enamine – HOMO activation]		
Enamine Catalysis	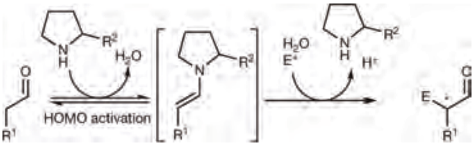	Aldol reaction Michael reaction
[Iminium – LUMO activation]		
Iminium Catalysis	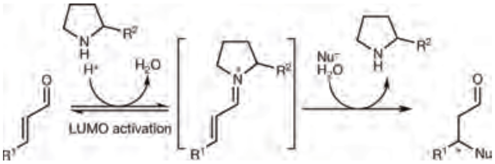	Michael reaction
[Radical cation – SOMO activation]		
SOMO Catalysis	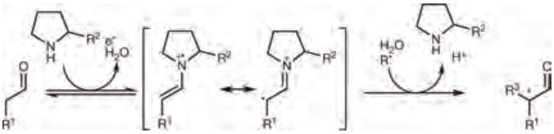	No examples in H_2O
[Breslow – intermediate]		

N-heterocyclic carbene Catalysis	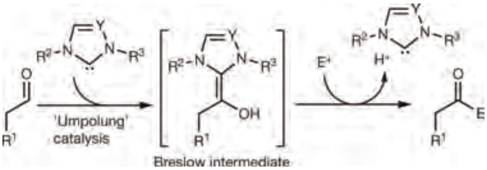	Enal coupling Benzoin condensation
	[Lewis base – complex]	
Nucleophilic Catalysis	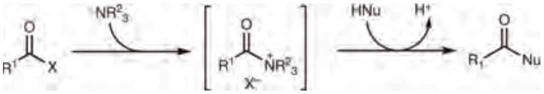	Ester hydrolysis Morita-Baylis-Hillman reaction Acetylation Substitution Hydrazone/oxime formation Native chemical ligation
	[Tetrahedral intermediate]	
General Base Catalysis	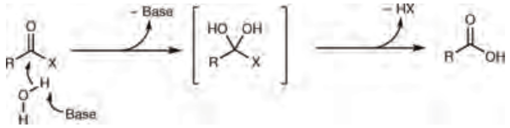	Knoevenagel condensation Multicomponent synthesis of azapyrrolizidines
Specific Base Catalysis	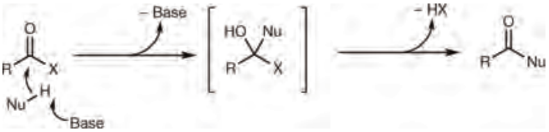	

*The examples are sorted according to their mechanisms, each of which is represented by archetypical reactions and catalysts, where applicable. SOMO, singly-occupied molecular orbital.

In non-covalent activation, the catalyst accelerates the reaction by non-covalently binding a substrate through one or more modes. Along with singly-occupied molecular orbital activation, these pathways will not be discussed here because they are rarely observed in H_2O because this solvent competes strongly with substrates for catalyst binding. Supramolecular catalysis in H_2O has been reviewed[25] and will not be discussed here either.

2.3 NUCLEOPHILIC AND GENERAL/SPECIFIC BASE CATALYSIS

An organic base can generally act as a Brønsted or Lewis base. In catalysis, the former leads to either general or specific base catalysis, and the latter is important in nucleophilic catalysis[26]. General and specific acid–base catalysis is a much older concept than nucleophilic catalysis, which was described by

Bender in 1960.[26] The interest in using small organic molecules as catalysts was furthered by an emerging fascination for enzyme structures and mechanistic elucidation. For example, the discovery of a role for the imidazolyl group of a His residue at the active site of α-chymotrypsin (Figure 2a) inspired and aided the understanding of how imidazole performs nucleophilic catalysis in hydrolysis (Supplementary Table S1, reaction 1a) and acyl transfer reactions.[27–36]

α-Chymotrypsin is an example of a serine protease — enzymes that hydrolyse peptides or esters at an active site featuring a His residue near an Asp in a conserved arrangement that enhances the basicity of the His. Thus, the His can deprotonate a proximal Ser residue such that it can attack the substrate at the carbonyl group. Ser receives an acyl group from the substrate[37–39] (Figure 2b) to afford an esterified intermediate, which can be hydrolysed to give the acid derivative of the substrate and regenerate serine protease. Once more, His plays a key role by effecting H_2O deprotonation to facilitate the hydrolysis[40] (Figure 2b).

Imidazoyl groups are highly polar and amphoteric, and the imidazole–imidazolium conjugate pair can perform general acid–base catalysis. As we now describe, such imidazoyl groups can also perform nucleophilic catalysis. Contemporary with Bender's publication, Jencks formulated three criteria for nucleophilic catalysis: the catalyst must have a higher reactivity towards the substrate than the acceptor molecule; the reactive intermediate should be more susceptible towards attack by the acceptor than the substrate; and the equilibrium constant for forming the reactive intermediate must be smaller than that for the product[41]. If these criteria are satisfied, the catalytic reaction is faster than the uncatalysed background reaction and the catalyst does not remain bound to the reaction products[41]. One reaction that sometimes fulfils these criteria is imidazole-catalysed hydrolysis of an ester RCO_2R', which could conceivably proceed through a nucleophilic pathway in which the formation of an N-acetyl imidazole intermediate is rate-limiting[28,42] (Figure 2c). The other possibility is the occurrence of a general base mechanism, in which imidazole and H_2O are a source of the nucleophile ^{-}OH. The most favourable pathway depends on the relative suitability of imidazole and $^{-}OR'$ as leaving groups[42]. Esters with poorer (more basic) leaving groups are subject to general base catalysis, whereas esters with better (less basic) leaving groups such as substituted phenolates undergo nucleophilic catalysis[27,29] (Figure 2c, top). The nucleophilic pathway is pH-dependent and is favoured under basic conditions in which imidazole ($pK_a \approx 6.9$) is more likely to exist as a neutral species[43].

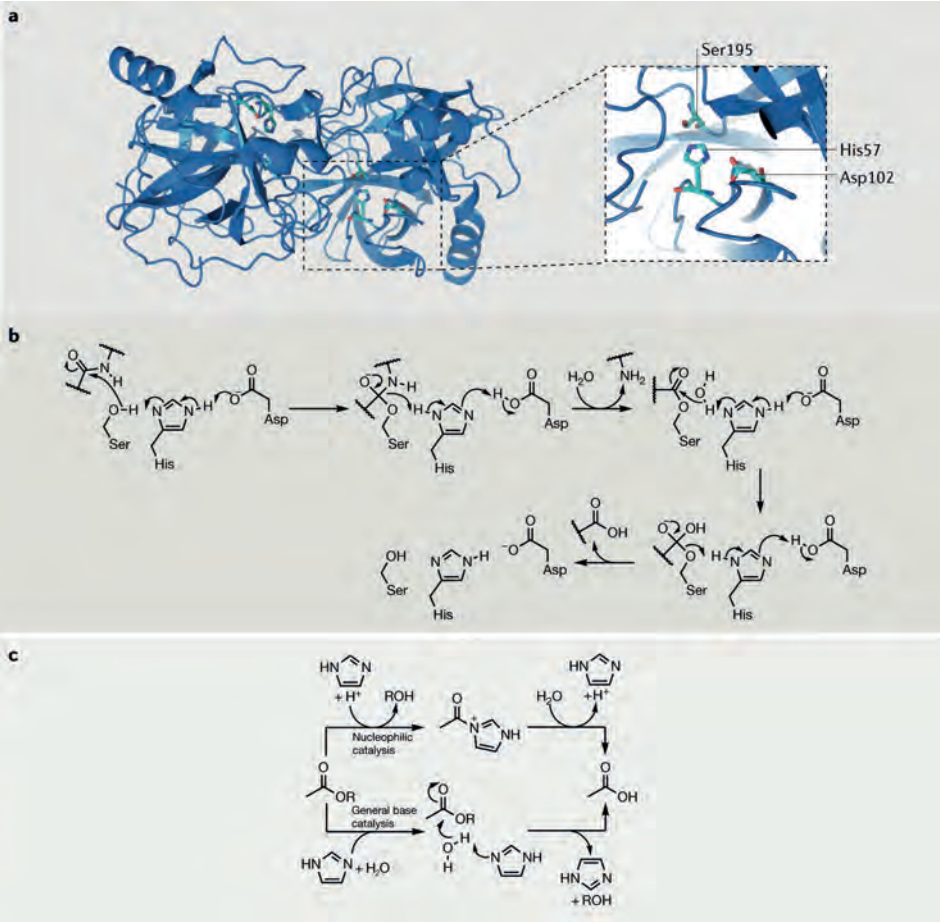

Figure 2. a) The X-ray structure of α-chymotrypsin (from Bos Taurus, Protein Databank identifier: 4CHA)[44] features an active site with Ser195, His57 and Asp102 as a catalytic triad. Structure visualized using the PyMOL Molecular Graphics System[45]. **b)** The general mechanism of serine proteases involves the collective H^+ transfer chain enabling deprotonation of the Ser195 side chain followed by attack on the substrate peptide, which then undergoes hydrolysis. **c)** Ester hydrolysis is catalysed by imidazole, either through a nucleophilic (top) or general base (bottom) mechanism, depending on the basicity of the −OR group[28,42].

Aside from well-established applications in the hydrolysis of activated esters, the catalysts imidazole (**1**) and/or histidine are active in other reactions, including the aldol reaction (through an enamine intermediate, see above), hydrolysis of N-acetylserinamide, RNA cleavage and thioester hydrolysis[43]. The catalysts can not only take the form of a small molecule or protein[40,46–48] but also be imidazole-functionalized nanoparticles[49] or polymers[50,51]. The dipeptide Ser–His was purported as a minimalistic enzyme for the hydrolysis of phosphate ester bonds of DNA, peptide bonds in proteins[52] and 4-nitrophenyl acetate. However, it was later found that only activated esters such as the latter substrate fall in the scope of the dipeptide (imidazole itself has a similar scope)[53]. Thus, the search for de novo catalysts for the formation or hydrolysis of amides in H_2O remains a challenging research area[54]. One approach towards this involves direct selection to screen for catalytically active phages through self-assembly of the product[55]. Some of the phages active for ester and amide hydrolysis did not feature Ser–His sequences, and some did not contain His at all. This interesting result indicates that such phages must operate through a mechanism distinct from that described above. Indeed, further experiments gave no evidence for Michaelis–Menten kinetics, leading to the suggestion that the catalytic mechanism resembles that of small-molecule organocatalysis[55]. The selection approach using active phages is an interesting step towards identifying efficient new organocatalysts, although their activity does not yet compare with proteases and esterases developed through natural evolution[54]. To date, the hydrolysis of amide bonds under mild conditions, although a facile reaction when using hydrolytic enzymes, remains difficult for organic small-molecule catalysts. Furthermore, the conceptual and mechanistic relevance of using the hydrolysis of activated esters to mimic that of amides is questionable[53,56].

Imidazole is not only a H_2O-soluble catalyst for bond-breaking reactions, but also for bond-formation reactions such as the Morita–Baylis–Hillman (MBH) reaction, in which it serves as a nucleophilic catalyst. Indeed, MBH reactions of aldehydes and cyclic enones, when conducted in the presence of imidazole, afford higher yields in shorter reaction times and have a wider substrate scope that includes typically unreactive and sterically bulky aldehydes[57]. In the case of the MBH reaction of cyclic enones and isatin (Supplementary Table S1, reaction 2), the bicyclic imidazolyl alcohol **3** is an even better catalyst than imidazole[58–60]. Experimental and computational evidence suggest that this high activity is a result of **3** mediating effective intramolecular H^+ transfer[60]. We note that this reaction of cyclic enones and isatin, although conducted in H_2O, requires a surfactant to establish a hydrophobic environment in which the organic reactants combine.

Pyridine (**4**) and its derivatives are the catalysts of choice for acetylations, in which they act as nucleophilic catalysts that form reactive N-acetylpyridinium intermediates. Pyridine itself has a modest Brønsted basicity ($pK_a \approx 5.2$), such that in neutral aqueous solutions it exists predominantly as its free base (in contrast to alkylamine catalysts, which are more basic)[61]. Consequently, pyridine is an effective catalyst for the hydrolysis of Ac_2O (Supplementary Table S1, reaction 3). Evidence for a nucleophilic catalytic mechanism reaction comes in the relative inactivity of comparably basic but more hindered 2-methyl-substituted pyridines[62]. However, when the hydrolysis of Ac_2O is conducted in H_2O, the direct reaction with the solvent dominates the pyridine-mediated pathways.

Pyridine has been exploited as a catalyst for the hydrolysis of ArOAc substrates but the rate accelerations are not comparable with pyridine-catalysed acylations using anhydrides or imidazole-catalysed hydrolyses of activated esters[61,63]. Additionally, pyridine also has been observed to catalyse maleimide polymerization in H_2O through a non-radical pathway[64]. However, this mechanism is unclear and pyridine may rather serve as a nucleophilic initiator, as is the case for other amines in polar solvents[64,65].

4-(Dimethylamino)pyridine (DMAP, **5**; $pK_a \approx 9.2$) is more reactive and basic than pyridine, such that in neutral aqueous solution it exists in its protonated catalytically inactive form. This protonation can be curbed by incorporating 4-(alkylmethylamino)pyridine groups into surface-crosslinked micelles (**2**), in which hydrophobic microenvironments facilitate efficient catalysis of (phosphate) ester hydrolysis even when the bulk solution is acidic (Supplementary Table S1, reaction 1b)[66]. Other recent catalytic applications of DMAP and its derivatives include affinity protein-labelling[67], activation and acetyl transfer from acetyl-coenzyme A to Lys (using peptide-appended DMAP analogue featuring a thiol)[68] and the related histone-selective acylation using nucleosome-binding catalysts and acyl donors (a reaction typically performed by histone acetyltransferases)[69]. Outside biology, DMAP-functionalized polyacrylonitrile fibres catalyse the aqueous-phase Gewald reaction, in which a ketone/aldehyde (or its equivalent) condenses with an α-cyanoester and S_8 to give a 3-substituted 2-aminothiophene[70].

1,4-Diazabicyclo[2.2.2]octane (DABCO, **6**; $pK_{a1} \approx 3.0$, $pK_{a2} \approx 8.8$) is a versatile tertiary amine organocatalyst that is more basic than imidazole and pyridine but less basic than DMAP. DABCO-catalysed MBH reactions of PhCHO with acrylonitrile or cyclic enones proceed rapidly in H_2O because this hydrogen-bonding solvent stabilizes the reactive enolate intermediate and/or activates PhCHO to nucleophilic attack (Supplementary Table S1, reaction 5)[71,72]. This hydrogen-bonding effect is apparently a more important contributor to rate enhancement than are polarity and hydrophobic effects, because both salting-in and salting-out experiments lead to rate enhancement[71]. The related catalyst 3-quinuclidinol (**7**) is even more active than DABCO or DMAP in the MBH reaction[71].

DABCO has been used in Knoevenagel condensations in H_2O for the formation of α,β-unsaturated carbonyl compounds[73,74]. In such reactions, DABCO likely acts either as a general base that deprotonates the active methylene compound or as a specific base (Supplementary Table S1, reaction 9) that deprotonates H_2O (these studies included no information on solution pH to distinguish these two mechanisms) to give OH^-, which is known to catalyse such reactions[75]. More generally, a typical problem faced by those wishing to conduct these condensations in H_2O is the limited solubility of many organic starting materials. The products are usually insoluble in H_2O, such that phase separation drives the reaction to completion.

Knoevenagel condensations of highly reactive methylene compounds in H_2O are often fast even in the absence of a catalyst because the hydrophobic effect[76] causes the organic reactants to partially phase-separate into small droplets[77]. Thus, the rates of reactions with negative activation volumes are greatly increased. Aside from this general effect, hydrogen-bond donation from H_2O can also provide a rate enhancement[78], as has been observed in the MBH reaction catalysed by **7**[71]. The role of DABCO as a nucleophilic catalyst has also been confirmed in the allylic substitution of vinyl phosphonates with N-centred and S-centred nucleophiles (Supplementary Table S1, reaction 4)[79].

The reader will undoubtedly realize the prevalence of nitrogen bases in our discussion so far. It is consequently no surprise that piperidine (**11**) is also catalytically active in the Knoevenagel reaction in H_2O, for example, in a multicomponent reaction affording azapyrrolizidines in high regioselectivity, chemoselectivity and diastereoselectivity (Supplementary Table S1, reaction 10)[80,81]. It is not clear whether piperidine (**11**) catalyses the reaction by base catalysis or by giving rise to an iminium intermediate. As with some examples above, the products in this reaction are insoluble, making this a heterogeneous reaction system.

Primary amines such as aniline **8** are common nucleophilic organocatalysts for reactions in H_2O[82]. For example, aniline catalyses hydrazone and oxime formation through a transamination mechanism (Figure 3a; Supplementary Table S1, reaction 6). These reactions are often applied to bioconjugations such as functionalization of polymers[83] and biomolecules for *in vitro* and *in vivo* studies[82,84].

The nucleophilic catalytic mechanism of aniline was elucidated by Cordes and Jencks back in 1962[41] (Figure 3a). Aniline condenses with the aldehyde or ketone to give the first reactive tetrahedral intermediate (a carbinolamine), from which H_2O is eliminated to give the Schiff base (imine). The imine is subsequently attacked by the hydrazine or alkoxyamine (or semicarbazide[41]) to afford the second tetrahedral intermediate (a geminal diamine) that extrudes aniline and the hydrazone or oxime product (or semicarbazone[41])[84]. Despite being a carbonyl condensation reaction, the equilibrium favours hydrazone formation in H_2O, and hence fulfils Jencks' criteria for nucleophilic catalysis[41]. The reaction is accelerated by acid catalysis[85] but is slow at neutral pH, such that applications in most biological systems are challenging. High (super-stoichiometric) concentrations of aniline are required to realize significant rate enhancements[86], motivating the development of second-generation and third-generation aniline catalysts for bioconjugation in biological settings[84]. Increasing catalytic efficiency requires closely studying the pK_a and substituent effects of the catalyst[84,87–89], and more basic catalysts typically promote protonation of the Schiff base and accelerate the reaction[84,90].

Aside from engineering the catalyst, the choice of reactants is also crucial and ortho substituents on aryl aldehydes can greatly enhance rates (for example, by intramolecular general acid catalysis with phosphate groups[91])[84,92]. Organocatalysed ligations of peptides by means of hydrazone/oxime formation at pH 7.0 can experience up to 40-fold rate enhancements in the presence of super-stoichiometric aniline[90,93]. However, the biocompatibility of aniline is questionable at high concentrations, motivating efforts to search for alternatives such as p-aminophenylalanine[94].

Aside from purely synthetic aniline derivatives, bioconjugates have also been investigated. For example, an aniline-terminated DNA strand, when hybridized to a complementary hydrazide-terminated DNA strand, catalyses the condensation of the hydrazide group with 4-nitrobenzaldehyde under physiological conditions[95]. The related amine–acid organocatalyst **9** similarly promotes rapid hydrazone crosslink exchange (Supplementary Table S1, reaction 7) in hyaluronan hydrogels in the presence of human umbilical vein endothelial cells at physiological pH and temperature[96]. A recent study has shown how the aldehyde product of the protein aldol ligation can be further functionalized in a tandem organocatalyst-mediated β-hydroxyoxime ligation catalysed by 4-methoxyaniline at neutral pH[97]. The rate of this organocatalysed oxime formation exhibits an unexpected pH dependence, with the yield of conjugation product being higher at pH 7.5 than at pH 4.5. A possible explanation may be the hydrogen bonding between the β-OH moiety and the protonated aldehyde or Schiff base intermediate[97]. Lastly, it has been demonstrated that p-aminophenylalanine can be incorporated into artificial enzymes[98], each with a hydrophobic binding pocket that affords rate enhancements outperforming aniline by a factor of >550 for a model hydrazone formation reaction[98].

Organocatalysed click reactions are not only limited to hydrazone and oxime formation, as demonstrated by the use of thiol catalysts in native chemical ligation (NCL). NCL is an effective method for the chemoselective formation of a covalently linked ligation product from two unprotected peptides under aqueous conditions[99,100]. Specifically, a thioester-terminated peptide undergoes transthioesterification with a thiol catalyst, to afford an activated thioester than can undergo a further transthioesterification with another peptide with an N-terminal Cys. After intramolecular acyl transfer from the S atom to the terminal N, one then has a polypeptide with a native amide bond at the ligation site (Supplementary Table S1, reaction 8)[99]. Mixed catalyst systems (BnSH/PhSH) or 2-mercaptoethanesulfonate sodium salt (MESNA) are typical catalysts but they are slow even for sterically unhindered peptides, which can therefore instead participate in side reactions[99,101,102]. Alkylthiols and arylthiols with different pK_a values[99] have been tested and it appears that whereas arylthiols with higher pK_a values are more effective, the opposite trend is observed for alkylthiols such as MESNA and BnSH. At present, (4-mercaptophenyl)acetic acid (MPAA, **11**) is the best catalyst and also has improved H_2O solubility and no offensive odour[99]. Since the disclosure of its activity, MPAA has been extensively used in NCL reactions, although the quest for better-performing catalysts has not ended.

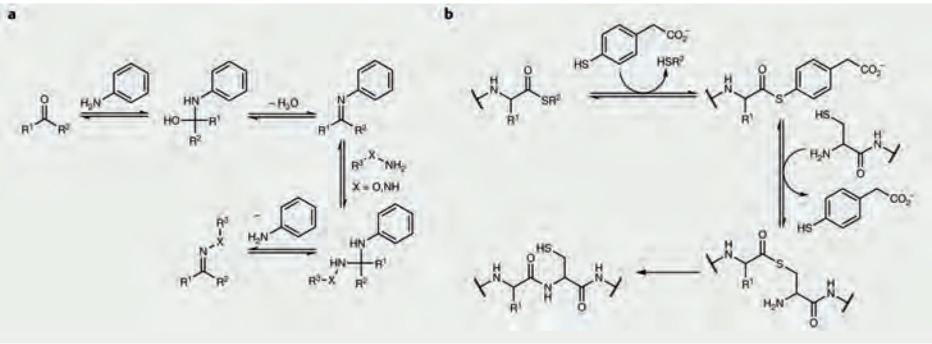

Figure 3. Transamination and transthioesterification in organocatalysis. **a)** Aniline-catalysed hydrazone and oxime formation involves transamination through a N-phenylimine intermediate[41]. **b)** Arylthiol-catalysed native chemical ligation proceeds by the catalytic thiol displacing another thiol to give a reactive thioester that is attacked by a Cys thiol[99]. The ligation is completed once the acyl transfers from the S to the N atom of the Cys.

For example, mercaptobenzylsulfonates have been investigated, and although they are not faster than MPAA, their greater polarity leads to greater H_2O solubility and aids the purification process[103]. Akin to aniline catalysis, the thiol-catalysed NCL appears to be an example of nucleophilic catalysis, with a reactive thioester intermediate forming from the starting thioester and thiol catalyst[99,102,104] (Figure 3b). The rate-determining step for arylthiol catalysts is the first transthioesterification, analogous to aniline-catalysed hydrazone/oxime formation having to proceed through the limiting Schiff base formation. However, the opposite holds true for alkylthiols, which have greater basicity such that the second transthioesterification becomes rate determining[99,102]. The full mechanistic details of these catalysed NCL reactions have not been elucidated[99] and other studies have focused on catalysts for ligations that use an N,S-acyl shift reaction. Thus, H_2O-soluble alkyldiselenol catalysts for transthioesterification and ligation have been developed and are superior to MPAA-based systems. They are particularly efficient at pH 4.0, which, although not relevant to in vivo or in vitro experiments, does enable complex peptide syntheses[105].

2.4 CONCLUSION AND OUTLOOK

The examples of aqueous organocatalysis described in this review highlight the importance of Jencks' criteria, in particular the pK_a and energy of the catalyst–substrate intermediate complex relative to those of the reactants and products[41]. Additionally, organocatalysis in aqueous media is very sensitive to the nature of the catalyst (e.g. functional groups and pk_a values). Thus, the field can benefit from improvements in catalyst design, which might involve simply adding or varying substituents on the catalyst (as is the case for aniline derivatives[84,87–89]) or engineering the catalyst to establish a favourable active-site microenvironment such that it can operate under unusual conditions (for example, DMAP in surface-crosslinked micelles[95] or designer enzymes with unnatural catalytic residues[98]). The latter examples take inspiration from enzymes, in which a hydrophobic pocket often serves as an optimal chemical environment, as we have seen in the biocatalytic examples described here. Organocatalyst engineering is arguably still a young field and there is tremendous potential for organocatalysis to be exploited in biological environments. To this end, we stated our criteria for organocatalysis to succeed in biological settings and evaluated known conversions for their biocompatibility and potential for *in vivo* applications. Altogether, we expect a bright future for rationally designed organocatalytic processes and encourage their application in biology.

2.5 REFERENCES

1 A. Küchler, M. Yoshimoto, S. Luginbühl, F. Mavelli and P. Walde, *Nat. Nanotechnol.*, 2016, **11**, 409–420.
2 S. Schoffelen and J. C. M. van Hest, *Soft Matter*, 2012, **8**, 1736–1746.
3 F. Wen, Y. Dong, L. Feng, S. Wang, S. Zhang and X. Zhang, *Anal. Chem.*, 2011, **83**, 1193–1196.
4 A. E. Speers and B. F. Cravatt, *Chem. Biol.*, 2004, **11**, 535–546.
5 Y. Bai, J. Chen and S. C. Zimmerman, *Chem. Soc. Rev.*, 2018, **47**, 1811–1821.
6 J. Li, J. Yu, J. Zhao, J. Wang, S. Zheng, S. Lin, L. Chen, M. Yang, S. Jia and X. Zhang, *Nat. Chem.*, 2014, **6**, 352–361.
7 J. P. C. Coverdale, I. Romero-Canelón, C. Sanchez-Cano, G. J. Clarkson, A. Habtemariam, M. Wills and P. J. Sadler, *Nat. Chem.*, 2018, **10**, 347–354.
8 M. Tomás-Gamasa, M. Martínez-Calvo, J. R. Couceiro and J. L. Mascareñas, *Nat. Commun.*, 2016, **7**, 12538.
9 D. G. Blackmond, A. Armstrong, V. Coombe and A. Wells, *Angew. Chem. Int. Ed.*, 2007, **46**, 3798–3800.
10 M. Raj and V. K. Singh, *Chem. Commun.*, 2009, 6687–6703.
11 M. Gruttadauria, F. Giacalone and R. Noto, *Adv. Synth. Catal.*, 2009, **351**, 33–57.
12 P. I. Dalko, *Comprehensive Enantioselective Organocatalysis: Catalysts, Reactions, and Applications, 3 Volume Set*, John Wiley & Sons, 2013.
13 F. Cruz-Acosta, P. de Armas and F. García-Tellado, *Chem. Eur. J.*, 2013, **19**, 16550–16554.
14 J. Clayden, N. Greeves and S. Warren, *Organic chemistry*, Oxford University Press, USA, 2012.
15 I. D. V Ingram, S. B. Lawrenson and M. North, in *Encyclopedia of Sustainable Technologies*, Elsevier, 2017, pp. 629–643.
16 C. Jimeno, *Org. Biomol. Chem.*, 2016, **14**, 6147–6164.
17 S. Toma, R. Sebesta and M. Meciarova, *Curr. Org. Chem.*, 2011, **15**, 2257–2281.
18 U. M. Lindström, *Chem. Rev.*, 2002, **102**, 2751–2772.
19 S. Bhowmick, A. Mondal, A. Ghosh and K. C. Bhowmick, *Tetrahedron: Asymmetry*, 2015, **26**, 1215–1244.
20 W. Notz and B. List, *J. Am. Chem. Soc.*, 2000, **122**, 7386–7387.
21 B. List, R. A. Lerner and C. F. Barbas, *J. Am. Chem. Soc.*, 2000, **122**, 2395–2396.
22 K. A. Ahrendt, C. J. Borths and D. W. C. MacMillan, *J. Am. Chem. Soc.*, 2000, **122**, 4243–4244.
23 J. Mlynarski and J. Paradowska, *Chem. Soc. Rev.*, 2008, **37**, 1502–1511.
24 J. Mlynarski and S. Baś, *Chem. Soc. Rev.*, 2014, **43**, 577–587.
25 M. De Rosa, P. La Manna, C. Talotta, A. Soriente, C. Gaeta and P. Neri, *Front. Chem.*, 2018, **6**, 84.
26 M. L. Bender, *Chem. Rev.*, 1960, **60**, 53–113.
27 T. C. Bruice and G. L. Schmir, *J. Am. Chem. Soc.*, 1957, **79**, 1663–1667.
28 W. P. Jencks and J. Carriuolo, *J. Biol. Chem.*, 1959, **234**, 1280–1285.
29 J. F. Kirsch and W. P. Jencks, *J. Am. Chem. Soc.*, 1964, **86**, 837–846.
30 J. Gerstein and W. P. Jencks, *J. Am. Chem. Soc.*, 1964, **86**, 4655–4663.
31 W. P. Jencks and J. Carriuolo, *J. Biol. Chem.*, 1959, **234**, 1272–1279.
32 W. P. Jencks and J. Carriuolo, *J. Am. Chem. Soc.*, 1961, **83**, 1743–1750.
33 W. P. Jencks, D. G. Oakenfull and K. Salvesen, *J. Am. Chem. Soc.*, 1971, **93**, 188–194.
34 J. F. Kirsch and W. P. Jencks, *J. Am. Chem. Soc.*, 1964, **86**, 833–837.
35 W. P. Jencks, *Catalysis in chemistry and enzymology*, Courier Corporation, 1987.
36 V. Gold and D. Bethell, *Advances in physical organic chemistry*, Academic Press, 1976.

37 T. A. Steitz and R. G. Shulman, *Annu. Rev. Biophys. Bioeng.*, 1982, **11**, 419–444.

38 K. Faber and S. Riva, *Synthesis.*, 1992, **1992**, 895–910.

39 P. Carter and J. A. Wells, *Nature*, 1988, **332**, 564–568.

40 K. L. Duncan and R. V Ulijn, *Biocatalysis*, 2015, **1**, 67–81.

41 E. H. Cordes and W. P. Jencks, *J. Am. Chem. Soc.*, 1962, **84**, 826–831.

42 F. Schneider, *Angew. Chem. Int. Ed. English*, 1978, **17**, 583–592.

43 P. Nieri, S. Carpi, S. Fogli, B. Polini, M. C. Breschi and A. Podestà, *Sci. Rep.*, 2017, **7**, 45760.

44 H. Tsukada and D. M. Blow, *J. Mol. Biol.*, 1985, **184**, 703–711.

45 L. Schrödinger, *PyMOL Mol. Graph. Syst. Version 1.8.*, 2015.

46 L. Schoonen, K. S. van Esterik, C. Zhang, R. V Ulijn, R. J. M. Nolte and J. C. M. van Hest, *Sci. Rep.*, 2017, **7**, 14772.

47 M. D. Nothling, A. Ganesan, K. Condic-Jurkic, E. Pressly, A. Davalos, M. R. Gotrik, Z. Xiao, E. Khoshdel, C. J. Hawker and M. L. O'Mara, *Chem*, 2017, **2**, 732–745.

48 S. Bezer, M. Matsumoto, M. W. Lodewyk, S. J. Lee, D. J. Tantillo, M. R. Gagné and M. L. Waters, *Org. Biomol. Chem.*, 2014, **12**, 1488–1494.

49 G. Chadha and Y. Zhao, *Org. Biomol. Chem.*, 2013, **11**, 6849–6855.

50 C. G. Overberger and K. W. Dixon, *J. Polym. Sci. Polym. Chem. Ed.*, 1977, **15**, 1863–1868.

51 E. H. Wanderlind, D. G. Liz, A. P. Gerola, R. F. Affeldt, V. Nascimento, L. C. Bretanha, R. Montecinos, L. Garcia-Rio, H. D. Fiedler and F. Nome, *ACS Catal.*, 2018, **8**, 3343–3347.

52 Y. Li, Y. Zhao, S. Hatfield, R. Wan, Q. Zhu, X. Li, M. McMills, Y. Ma, J. Li and K. L. Brown, *Bioorg. Med. Chem.*, 2000, **8**, 2675–2680.

53 M. J. MacDonald, L. D. Lavis, D. Hilvert and S. H. Gellman, *Org. Lett.*, 2016, **18**, 3518–3521.

54 Y. Maeda, O. V Makhlynets, H. Matsui and I. V Korendovych, *Annu. Rev. Biomed. Eng.*, 2016, **18**, 311–328.

55 Y. Maeda, N. Javid, K. Duncan, L. Birchall, K. F. Gibson, D. Cannon, Y. Kanetsuki, C. Knapp, T. Tuttle and R. V Ulijn, *J. Am. Chem. Soc.*, 2014, **136**, 15893–15896.

56 F. M. Menger and M. J. Ladika, *J. Am. Chem. Soc.*, 1987, **109**, 3145–3146.

57 S. Luo, P. G. Wang and J.-P. Cheng, *J. Org. Chem.*, 2004, **69**, 555–558.

58 J. C. Gomes, M. T. Rodrigues Jr, A. Moyano and F. Coelho, *European J. Org. Chem.*, 2012, **2012**, 6861–6866.

59 J. C. Gomes, J. Sirvent, A. Moyano, M. T. Rodrigues Jr and F. Coelho, *Org. Lett.*, 2013, **15**, 5838–5841.

60 L. Raich, H. Santos, J. C. Gomes, M. T. Rodrigues Jr, R. Galaverna, M. N. Eberlin, F. Coelho, C. Rovira and A. Moyano, *ACS Catal.*, 2018, **8**, 1703–1714.

61 A. R. Fersht and W. P. Jencks, *J. Am. Chem. Soc.*, 1970, **92**, 5432–5442.

62 A. R. Butler and I. H. Robertson, *J. Chem. Soc. Perkin Trans. 2*, 1975, 660–663.

63 M. L. Bender and B. W. Turnquest, *J. Am. Chem. Soc.*, 1957, **79**, 1656–1662.

64 D. Decker, *Macromol. Chem. Phys.*, 1973, **168**, 51–58.

65 M. Azechi, N. Toyota, K. Yamabuki, K. Onimura and T. Oishi, *Polym. Bull.*, 2011, **67**, 631–640.

66 G. Chadha and Y. Zhao, *Chem. Commun.*, 2014, **50**, 2718–2720.

67 T. Tamura and I. Hamachi, *Labeling proteins by affinity-guided DMAP chemistry*, Springer, 2015.

68 Y. Amamoto, Y. Aoi, N. Nagashima, H. Suto, D. Yoshidome, Y. Arimura, A. Osakabe, D. Kato, H. Kurumizaka and S. A. Kawashima, *J. Am. Chem. Soc.*, 2017, **139**, 7568–7576.

69 T. Ishiguro, Y. Amamoto, K. Tanabe, J. Liu, H. Kajino, A. Fujimura, Y. Aoi, A. Osakabe, N. Horikoshi and H. Kurumizaka, *Chem*, 2017, **2**, 840–859.

70 P. Li, J. Du, Y. Xie, M. Tao and W.-Q. Zhang, *ACS Sustain. Chem. Eng.*, 2016, **4**, 1139–1147.

71 V. K. Aggarwal, D. K. Dean, A. Mereu and R. Williams, *J. Org. Chem.*, 2002, **67**, 510–514.

72 J. Augé, N. Lubin and A. Lubineau, *Tetrahedron Lett.*, 1994, **35**, 7947–7948.

73 Y. Yu and Z. Wang, *J. Chinese Chem. Soc.*, 2013, **60**, 288–292.

74 M. S. Abaee and S. Cheraghi, *Turkish J. Chem.*, 2014, **38**, 650–660.

75 E. V Dalessandro, H. P. Collin, M. S. Valle and J. R. Pliego, *RSC Adv.*, 2016, **6**, 57803–57810.

76 F. Bigi and C. Quarantelli, *Curr. Org. Synth.*, 2012, **9**, 31–39.

77 S. Otto and J. B. F. N. Engberts, *Org. Biomol. Chem.*, 2003, **1**, 2809–2820.

78 J. J. Gajewski, *Acc. Chem. Res.*, 1997, **30**, 219–225.

79 A. Seingeot, Y. Charmasson, M. Attolini and M. Maffei, *Heteroat. Chem.*, 2017, **28**, e21352.

80 B. Rajarathinam, K. Kumaravel and G. Vasuki, *ACS Comb. Sci.*, 2017, **19**, 455–463.

81 B. Rajarathinam and G. Vasuki, *Org. Lett.*, 2012, **14**, 5204–5206.

82 J. Lv, Q. Zhang, M. Cai, Y. Han and S. Luo, *Chem. Asian J.*, 2018, **13**, 740–753.

83 F. Trausel, C. Maity, J. M. Poolman, D. S. J. Kouwenberg, F. Versluis, J. H. Van Esch and R. Eelkema, *Nat. Commun.*, 2017, **8**, 879.

84 D. K. Kölmel and E. T. Kool, *Chem. Rev.*, 2017, **117**, 10358–10376.

85 W. P. Jencks, *J. Am. Chem. Soc.*, 1959, **81**, 475–481.

86 C. Godoy-Alcántar, A. K. Yatsimirsky and J. Lehn, *J. Phys. Org. Chem.*, 2005, **18**, 979–985.

87 P. Crisalli and E. T. Kool, *J. Org. Chem.*, 2013, **78**, 1184–1189.

88 P. Crisalli and E. T. Kool, *Org. Lett.*, 2013, **15**, 1646–1649.

89 D. Larsen, M. Pittelkow, S. Karmakar and E. T. Kool, *Org. Lett.*, 2015, **17**, 274–277.

90 A. Dirksen, T. M. Hackeng and P. E. Dawson, *Angew. Chem. Int. Ed.*, 2006, **118**, 7743–7746.

91 O. Dilek, A. M. Sorrentino and S. Bane, *Synlett*, 2016, **27**, 1335–1338.

92 F. Trausel, B. Fan, S. A. P. van Rossum, J. H. van Esch and R. Eelkema, *Adv. Synth. Catal.*, 2018, **360**, 2571–2576.

93 A. Dirksen, S. Dirksen, T. M. Hackeng and P. E. Dawson, *J. Am. Chem. Soc.*, 2006, **128**, 15602–15603.

94 A. R. Blanden, K. Mukherjee, O. Dilek, M. Loew and S. L. Bane, *Bioconjug. Chem.*, 2011, **22**, 1954–1961.

95 D. W. Domaille and J. N. Cha, *Chem. Commun.*, 2014, **50**, 3831–3833.

96 J. Lou, F. Liu, C. D. Lindsay, O. Chaudhuri, S. C. Heilshorn and Y. Xia, *Adv. Mater.*, 2018, **30**, 1705215.

97 R. J. Spears, R. L. Brabham, D. Budhadev, T. Keenan, S. McKenna, J. Walton, J. A. Brannigan, A. M. Brzozowski, A. J. Wilkinson and M. Plevin, *Chem. Sci.*, 2018, **9**, 5585–5593.

98 I. Drienovská, C. Mayer, C. Dulson and G. Roelfes, *Nat. Chem.*, 2018, **10**, 946–952.

99 E. C. B. Johnson and S. B. H. Kent, *J. Am. Chem. Soc.*, 2006, **128**, 6640–6646.

100 P. E. Dawson, T. W. Muir, I. Clark-Lewis and S. B. H. Kent, *Science.*, 1994, **266**, 776–779.

101 T. W. Muir, *Annu. Rev. Biochem.*, 2003, **72**, 249–289.

102 P. E. Dawson, M. J. Churchill, M. R. Ghadiri and S. B. H. Kent, *J. Am. Chem. Soc.*, 1997, **119**, 4325–4329.

103 B. Cowper, T. M. Sze, B. Premdjee, A. F. Bongat White, A. Hacking and D. Macmillan, *Chem. Commun.*, 2015, **51**, 3208–3210.

104 K. Mandal, B. L. Pentelute, D. Bang, Z. P. Gates, V. Y. Torbeev and S. B. H. Kent, *Angew. Chem. Int. Ed.*, 2012, **51**, 1481–1486.

105 M. Cargoët, V. Diemer, B. Snella, R. Desmet, A. Blanpain, H. Drobecq, V. Agouridas and O. Melnyk, *J. Org. Chem.*, 2018, **83**, 12584–12594.

2.6 SUPPLEMENTARY INFORMATION

Table S1: Overview of organocatalyzed reactions: activation mode, catalyst (loading), reaction conditions (pH, temperature T, time and additives, remarks and literature references.

Activation	#	Reaction variant	Catalyst* loading	Reaction conditions T (°C), time, additives and remarks	Ref.
Nucleophilic base catalysis	**1a**	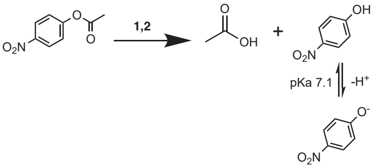 Ester hydrolysis (and phosphate ester)	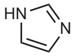 **1** Imidazole (super-stoichiometric)	pH: > 7 (basic favorable) T: RT Time: fast (min) Additives: organic solvent for ester Remarks: use of imidazole buffer	1-3
	1b		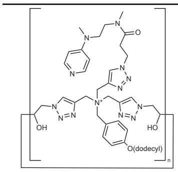 **2** DMAP-SCM (50 mol%)	pH: 4 - 8 T: 35 Time: fast (min) Additives: organic solvent for ester Remarks: use of HEPES buffer	4
	2	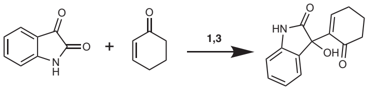 Morita-Baylis-Hillman (MBH) reaction	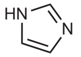 **1** 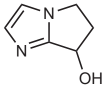 **3** Imidazole or bicyclic imidazolyl alcohol (10 mol%)	pH: n.d. T: RT Time: 4 h Additives: Sodium dodecyl Sulphate (SDS) Remarks: none	5-7
	3	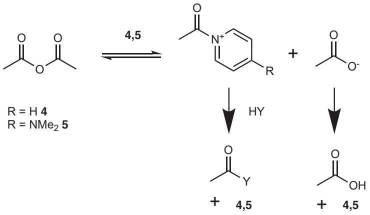 Acetylation/ hydrolysis with acetic anhydride	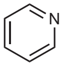 **4** 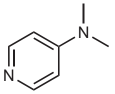 **5** Pyridine or DMAP (super-stoichiometric)	pH: 5.5 T: 25 Time: fast (min) Additives: organic solvent for acetic anhydride Remarks: use of pyridine buffer	8,9
	4	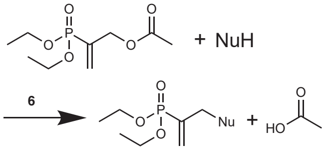	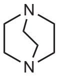 **6** DABCO (20 mol%)	pH: n.d. T: RT Time: overnight Remarks: sulphur and nitrogen-based	10

General/Specific base catalysis

	Synthesis of functionalized vinyl phosphonates		aliphatic and aromatic nucleophiles	
5	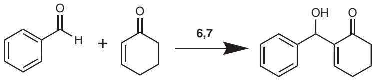 Morita-Baylis-Hillman (MBH) reaction (also acrylate instead of enone)	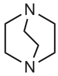 **6** 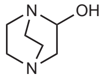 **7** DABCO or 3-hydroxy-quinuclidine (stoichiometric)	pH: n.d. T: RT Time: 4 h Remarks: Purification by flash chromatography	11
6	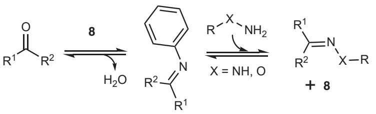 Hydrazone/oxime formation with aniline	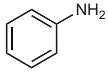 **8** Aniline (super-stoichiometric)	pH: 2.5 – 7.4 (acidic favorable) T: RT Time: min to h (depending on catalyst and reactants Additives: some cases DMF as co-solvent for reactants	12 - 18
7	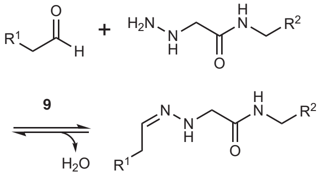 Hydrazone formation with benzimidazole derivative	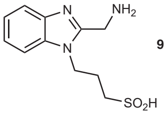 **9** 2-(aminomethyl)-benzimidazole derivative (super-stoichiometric)	pH: 7.4 T: 37 Time: min to h (depends on concentrations) Remarks: use of PBS buffer	19
8	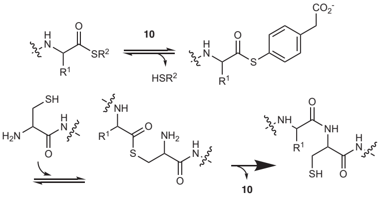 Native chemical ligation (NCL)	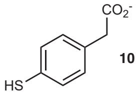 **10** 4-mercaptophenyl acetic acid (MPAA) (super-stoichiometric)	pH: 7.0 T: 25 Time: few hours (depends on cat. and reactants) Additives: TCEP Remarks: HPLC purification	20, 21
9	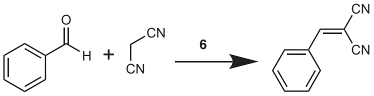 Knoevenagel condensation	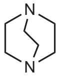 **6** DABCO (10 mol%)	pH: n.d. T: RT Time: 2 min Remarks: recycling of catalyst (six times) by recovery from the filtrate water	22

Iminium and /or base catalysis	**10**	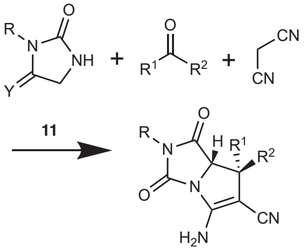 Multi-component reaction	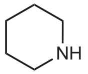 **11** Piperidine (10 mol%)	pH: n.d. T: RT-80 Time: 0.5- 8 h	23

Abbreviations & Notes: T, Temperature; RT, room temperature; n.d., not determined; Nu, nucleophile; SCM, surface crosslinked-micelle; DMF, N,N-dimethylformamide; TCEP, tris(2-carboxyethyl)-phosphine; Ar, aryl,; PBS, phosphate-buffered saline. Catalysts are numbered regardless of their ionization state or different R groups.

2.6.2 Supplementary references

1 J. F. Kirsch and W. P. Jencks, J. Am. Chem. Soc., 1964, **86**, 837–846.
2 T. C. Bruice and G. L. Schmir, J. Am. Chem. Soc., 1957, **79**, 1663–1667.
3 W. P. Jencks and J. Carriuolo, J. Biol. Chem., 1959, **234,** 1280–1285.
4 G. Chadha and Y. Zhao, Chem. Commun., 2014, **50**, 2718–2720.
5 J. C. Gomes, M. T. Rodrigues Jr, A. Moyano and F. Coelho, European J. Org. Chem., 2012, **2012**, 6861–6866.
6 J. C. Gomes, J. Sirvent, A. Moyano, M. T. Rodrigues Jr and F. Coelho, Org. Lett., 2013, **15**, 5838–5841.
7 L. Raich, H. Santos, J. C. Gomes, M. T. Rodrigues Jr, R. Galaverna, M. N. Eberlin, F. Coelho, C. Rovira and A. Moyano, ACS Catal., 2018, **8**, 1703–1714.
8 A. R. Fersht and W. P. Jencks, J. Am. Chem. Soc., 1970, **92**, 5432–5442.
9 A. R. Butler and I. H. Robertson, J. Chem. Soc. Perkin Trans. **2**, 1975, 660–663.
10 A. Seingeot, Y. Charmasson, M. Attolini and M. Maffei, Heteroat. Chem., 2017, **28**, e21352.
11 V. K. Aggarwal, D. K. Dean, A. Mereu and R. Williams, J. Org. Chem., 2002, **67**, 510–514.
12 E. H. Cordes and W. P. Jencks, J. Am. Chem. Soc., 1962, **84**, 826–831.
13 F. Trausel, C. Maity, J. M. Poolman, D. S. J. Kouwenberg, F. Versluis, J. H. Van Esch and R. Eelkema, Nat. Commun., 2017, **8**, 879.
14 D. K. Kölmel and E. T. Kool, Chem. Rev., 2017, **117**, 10358–10376.
15 P. Crisalli and E. T. Kool, J. Org. Chem., 2013, **78**, 1184–1189.
16 P. Crisalli and E. T. Kool, Org. Lett., 2013, **15**, 1646–1649.
17 D. Larsen, M. Pittelkow, S. Karmakar and E. T. Kool, Org. Lett., 2015, **17**, 274–277.
18 F. Trausel, B. Fan, S. A. P. van Rossum, J. H. van Esch and R. Eelkema, Adv. Synth. Catal., 2018, **360**, 2571–2576.
19 J. Lou, F. Liu, C. D. Lindsay, O. Chaudhuri, S. C. Heilshorn and Y. Xia, Adv. Mater., 2018, **30**, 1705215.
20 E. C. B. Johnson and S. B. H. Kent, J. Am. Chem. Soc., 2006, **128**, 6640–6646.
21 B. Cowper, T. M. Sze, B. Premdjee, A. F. Bongat White, A. Hacking and D. Macmillan, Chem. Commun., 2015, **51**, 3208–3210.
22 Y. Yu and Z. Wang, J. Chinese Chem. Soc., 2013, **60**, 288–292.
23 B. Rajarathinam, K. Kumaravel and G. Vasuki, ACS Comb. Sci., 2017, **19**, 455–463.

3

TEMPORALLY PROGRAMMED POLYMER-SOLVENT INTERACTIONS USING A CHEMICAL REACTION NETWORK

Out of equilibrium operation of chemical reaction networks (CRNs) enables artificial materials to autonomously respond to their environment by activation and deactivation of intermolecular interactions. Generally, their activation can be driven by various chemical conversions, yet their deactivation to non-interacting building blocks remains largely limited to hydrolysis and internal pH change. To achieve control over deactivation, we present a new, modular CRN that enables reversible formation of positive charges on a tertiary amine substrate, which are removed using nucleophilic signals that control the deactivation kinetics. The modular nature of the CRN enables incorporation in diverse polymer materials, leading to a temporally programmed transition from collapsed and hydrophobic to solvated, hydrophilic polymer chains by controlling polymer-solvent interactions. Depending on the layout of the CRN, we can create stimuli-responsive or autonomously responding materials. This concept will not only offer new opportunities in molecular cargo delivery but also pave the way for next-generation interactive materials.

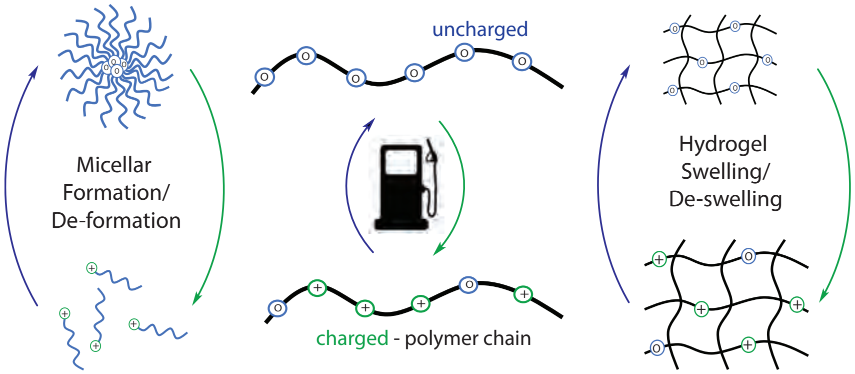

This chapter is published as:

B. Klemm, R. W. Lewis, I. Piergentili and R. Eelkema, Nat. Commun., 2022, **13**, 6242.

3.1 INTRODUCTION

Interactive materials, which are able to adapt and to interact with their surroundings by responding to events taking place in their environment[1], will find many applications ranging from regenerative medicine, optoelectronics to nanomachines.[2–4] Response to environmental cues through controlled material growth and decay is a unique property, which enables nature to perform complex functions, for example signal transduction, cell-division and intracellular transport.[5,6] Here, the conversion of chemical fuels such as adenosine triphosphate (ATP) are used to temporally control out-of-equilibrium assembly into supramolecular structures.[7]

Synthetic analogues of these active materials can be designed by coupling the activation of non-interacting building blocks to fuel-driven chemical reaction networks (CRNs).[8] Crucially, the availability of chemical fuel sustains the active material, while depletion of the fuel causes the material to disassemble back to its precursor.[9] Besides strategies that involve activation of the surroundings, such as a transient pH change[10–13], a widely applied strategy is the direct activation of building blocks by a chemical fuel.[9] In such systems, the chemical fuel reacts with an inactive building block, converting it to an activated intermediate (activation). A second reaction subsequently converts the intermediate to its inactive precursor state by spontaneously forming a waste product (deactivation).[14] A wide variety of material activation processes have been described in literature, which are typically powered by various chemical fuels (e.g. carbodiimide fuels[15], methylation agents[5], redox-reagents[16,17] or thioesters[18]) or physical stimuli, such as light or ultrasound to name a few.[19–21] In contrast, the deactivation mechanism (excluding enzymatic reactions) for chemically fuelled non-equilibrium CRNs at present relies frequently on hydrolysis[9,15,22–25] or internal pH change[10–13]. Notable exceptions[26,27] concern deactivation reactions that use either redox chemistry[17,28–30], alkene cross-metathesis[31], chemical clocks[32] or spontaneous chemical degradation[18].

This work describes the development and application of a new type of CRN, based on nucleophilic substitution by using allylic electrophiles as chemical fuel. This class of CRNs is characterized by a wide range of reactivities and substrate structures[33,34], rendering it highly versatile and potentially widely applicable. In particular, the wide range of nucleophilic reactivities and their prevalence in nature opens the door to precise nucleophilic control over the deactivation step, enabling highly tuneable and responsive CRNs. So far, studies of transient materials have focused on applying existing CRNs to different material classes, frequently composed of low molecular weight amphiphiles[20,32,35,36], gelator assemblies[10,11,29], nanoparticles[22] or (block)-copolymers[13,16,17,23,24,37–41]. In particular for polymer materials, established (de)activation strategies are generally used (e.g. pH change, carbodiimide/hydrolysis, redox-reagents or light). In contrast, new CRNs are commonly developed for a specific material class or connected to the design of the molecular building blocks. In consideration of current methods for the development of materials with autonomous behaviour and pre-programmed response, we lack a general framework.[42] Thus, the development of scalable CRNs and their applicability to a variety of different materials for the design of interactive structures is an extremely attractive challenge.

In this work, we introduce a general strategy towards developing interactive synthetic materials by using a CRN that can be applied to polymers of varying structure and composition, and is scalable from small molecule models (molecular level) to nanoscale supramolecular materials (block copolymer micelles) to macroscale macromolecular crosslinked superstructures (polymer hydrogels). These materials undergo a temporally programmed transition from collapsed, hydrophobic polymer chains to solvated, hydrophilic polymer domains by controlling polymer-solvent interactions. We can achieve stimuli-responsive or autonomous material changes by controlling these interactions using our CRN strategy to reversibly form positive charges along a polymer backbone in aqueous buffer, at physiological pH.

3.2 RESULTS AND DISCUSSION

The CRN central to this work is based on the allylic substitution of electron deficient Morita-Baylis-Hillman allyl acetates with tertiary nitrogen nucleophiles. In this reaction, a metastable, positively charged quaternary nitrogen adduct is formed[43,44]. While previous studies have rationalized the formation of this adduct[45,46] or isolated their bromine and chlorine counterion – salts from non-aqueous solutions, we discovered that the formation of the acetate counterion – adduct (activated intermediate) is stable in buffered aqueous solution at neutral pH and room temperature. Subsequent addition of competing S or N-terminal nucleophiles initiates a second allylic substitution on the activated intermediate, which reverses the quaternary nitrogen to the neutral amine, forming the allylic reaction product (waste) and thus completing the reaction cycle (Figure 1a). Both the substitution of the tertiary amine on the allyl acetate as well as the subsequent substitution of the nucleophile on the quaternary amine intermediate likely proceed via conjugate additions followed by elimination of the allylic leaving group from the enolate, mechanisms that are related to E1cB type eliminations and the Morita-Baylis-Hillman reaction.

In the newly developed CRN, the allyl substrate diethyl(α-acetoxymethyl) vinylphosphonate (DVP)[47] acts as a fuel, enabling a reversible switch between charge states of the nitrogen centre. We are able to manipulate the CRN and the subsequent material response by delicate design of the allylation reaction (activation) and its successive substitution reaction in the presence of nucleophiles (deactivation). Highly nucleophilic thiols in water[48,49], such as 2-mercaptoethanol (SH-**3**, Figure 1b), react first with the activated intermediate before attacking the fuel itself. This allows for signal-controlled cycling between 'charged' and 'uncharged' species, referred to as signal-induced cycling (Figure 1a-right). We studied two common tertiary amines (Figure 1b) in a small molecule CRN: DABCO (t-Am-**1**) and pyridine (t-Am-**2**) and evaluated their behaviour in the CRN. Furthermore, we investigated the potential of chemically fuelled, out-of-equilibrium systems, where competition of (de)activation reactions leads to autonomous cycling (Figure 1a-right). Here, we sought for weak nucleophiles, which were not reactive with the fuel. Amino acids such as threonine (NH_2-**4**, Figure 1b) are prime candidates, due to their weak nucleophilicity (nucleophilicity index (*N)* = 12.69 in water[50]). The primary amine pK_a of threonine is 9.1 meaning that at neutral pH, it is mostly present as the protonated amine species (> 97%).[51] Under optimised conditions, this allows for an initial accumulation of the charged activated intermediate, which is later reversed by the delayed substitution from excess NH_2-**4** to form the uncharged waste products (DVP-N + DVP-2-N, Figure 1b).

To bridge this concept towards synthetic materials, we synthesised block and statistical copolymers of N,N-dimethylacrylamide and 4-vinylpyridine (P1 and P2, Figure 1c-left) by a two-step reversible addition fragmentation chain-transfer (RAFT) process.[52] The pK_a of poly(4-vinylpyridine) is 5.0 ± 0.3[53] meaning that at neutral pH the free base species is dominant, making it an excellent candidate for reversible charge formation in neutral pH buffered aqueous systems.

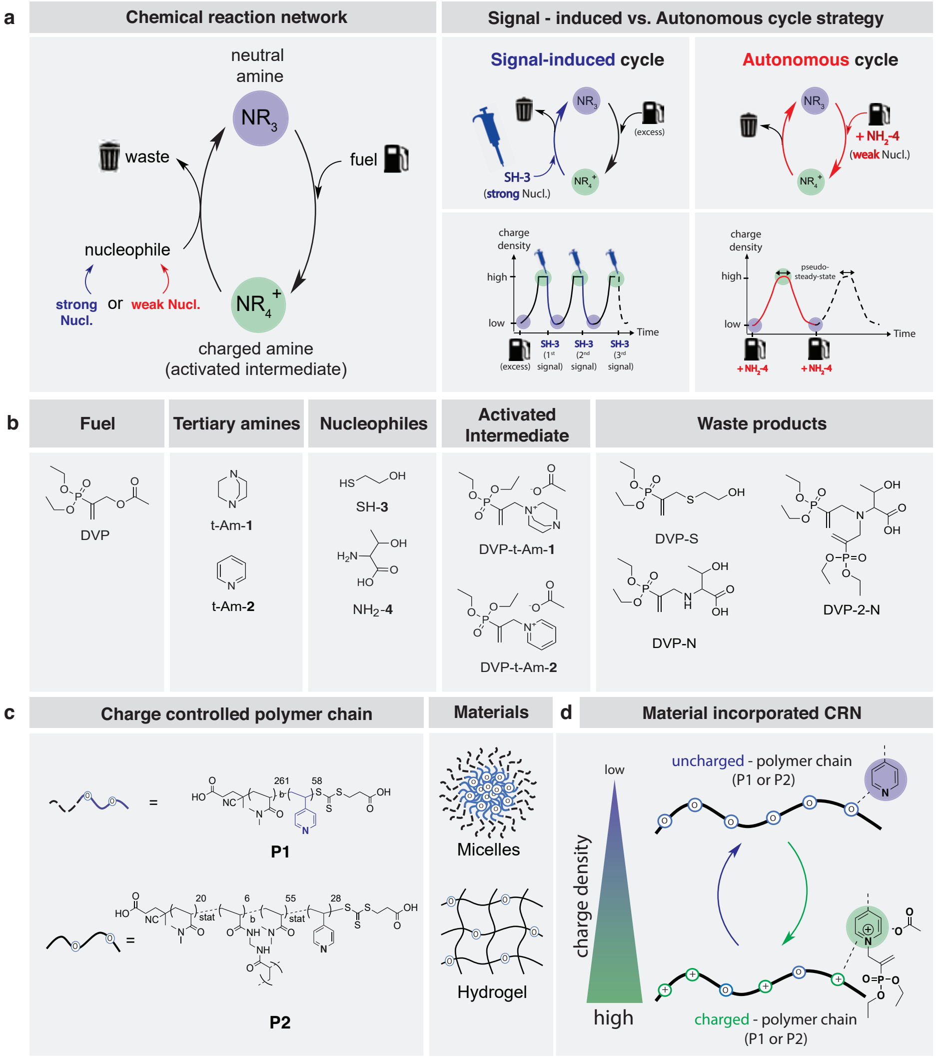

Figure 1: Schematics of the chemical reaction network (CRN), its conditions and components. **(a)** Generic CRN and CRN strategy used to achieve stimuli-responsive or autonomous material changes. **(b)** Chemical structure of fuel, nucleophiles and tertiary amines (used in the small molecule model CRN), as well as their activated intermediates and waste products. **(c)** RAFT synthesised polyamine copolymers (P1, P2) used for the preparation of polymeric materials: (1) micellar dispersions and (2) bulk polymer hydrogels. **(d)** Temporally programmed charge (de)formation on polyamine-functionalized polymer chains using our CRN strategy and charge density distribution. Specifically, fuelled tertiary amines generate charged quaternary nitrogens (activated intermediate), which in turn creates hydrophilic domains along the polymer backbone. A secondary nucleophilic substitution results in the regeneration of the uncharged polyamine by substitution of the intermediate (deactivation) towards the waste product.

With those polymers in hand, we prepared two types of materials: (1) supramolecular micellar dispersions and (2) macromolecular polymer hydrogels (Figure 1c-right). Fuelling these materials with DVP, we anticipated polymer dissolution in micellar dispersions by induced hydrophilization and polymeric network expansion within hydrogels by osmotic pressure forced water intake. The subsequent decay of the intermediate species will convert the positive charge along the polymer, and in turn lead to micellar re-formation and hydrogel contraction due to the loss of charges and osmotic pressure[54] (Figure 1d).

3.2.1 SIGNAL-INDUCED AND AUTONOMOUS SMALL-MOLECULE MODEL CRN

In the small molecule CRN (Figure 2a), amine substrates t-Am-**1** or t-Am-**2** react with DVP to generate an intermediary allylammonium ion (DVP-t-Am-**1** or DVP-t-Am-**2**). After fuel activation, reaction with a thiol (SH-**3**) forms a waste product (DVP-S) and regenerates the amine substrate, thus completing one cycle. Using sub-stoichiometric amounts of amine (0.2 eq.) with excess fuel (1.0 eq.) we first converted t-Am-**1** and t-Am-**2** to the activated intermediates (0.2 eq.), which upon SH-**3** addition (0.2 eq.) reversed back to the neutral amine. The remaining unreacted fuel (~0.8 eq.) then spontaneously regenerates the activated intermediate, which allows for continuous cycling upon consecutive thiol additions. Using ^{1}H NMR spectroscopy, we confirmed four consecutive reaction cycles by controlled deionization of the activated intermediate with 4x SH-**3** additions (0.2 eq.) at stable pH conditions (Figure 2b/c). We conducted a reaction rate study to further understand the reactivity of DVP towards the tertiary amines and nucleophiles with their order being t-Am-**1** > SH-**3** > t-Am-**2** >> NH2-**4** (Figure S2). As t-Am-**1** (N = 18.80 in CH_3CN[55]) is more nucleophilic than t-Am-**2** (N = 12.90 in CH_2Cl_2[55]), we can attribute these kinetic variations to the difference in nucleophilicity of the employed tertiary amine.[56] Hence, it was not surprising that complete conversion of DVP to DVP-t-Am-**1** is on average ~9.0 ± 0.8 fold faster than that of DVP-t-Am-**2** (Figure 2b/c).

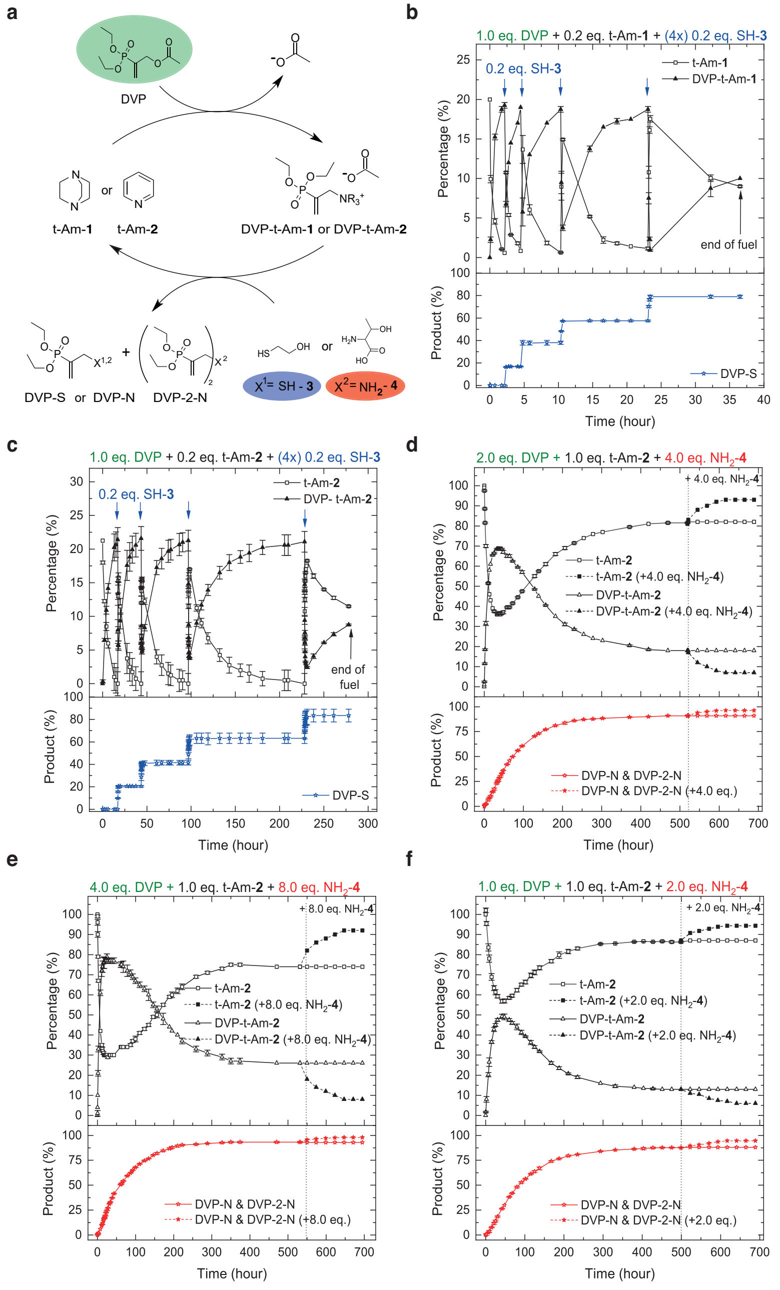

Figure 2: Small molecule CRN model for signal-induced and fuel-driven autonomous cycle. **(a)** CRN of fuel with t-Am-**1** (DABCO) or t-Am-**2** (pyridine) and SH-**3** in signal-induced mode or fuel with t-Am-**2** and excess NH_2-**4** in fuel-driven autonomous mode. Conversion of the reactants was monitored by ^1H NMR over time in D_2O/phosphate buffer 1:9 (pH = 7.4, 0.1 M (signal-induced cycle) or 0.5 M (autonomous cycle)) at room temperature. **(b)** Signal induced cycle (SI, Figure S6)

with t-Am-**1**: DVP (42 mM, 1.0 eq.), t-Am-**1** (0.2 eq.) and four times addition of SH-**3** (0.2 eq.). **(c)** Signal induced cycle (SI, Figure S7) with t-Am-**2**: DVP (42 mM, 1.0 eq.), t-Am-2 (0.2 eq.) and four times addition of SH-**3** (0.2 eq.). Autonomous cycle (SI, Figure S8 – S10) with fuel/nucleophile variations at constant t-Am-**2** (8.5 mM, 1.0 eq.) concentration **(d)**: DVP (2.0 eq.) and NH_2-**4** (4.0 eq.), **(e)** DVP (4.0 eq.) and NH_2-**4** (8.0 eq.), **(f)** DVP (1.0 eq.) and NH_2-**4** (2.0 eq.). **(d – f)** At observed equilibrium an additional 4.0, 8.0 and 2.0 equivalents of NH_2-**4** were added to one of the duplicate reaction mixtures respectively. The error bars represent the standard deviation of duplicate measurements. For **(d,e)** the product percentages were normalized to 100. Activated intermediates were isolated by exchanging their counterion from acetate to chloride (for full characterisation see SI).

Similarly, for the progression of the deactivation reaction, DVP-S formed on average ~30 ± 3.4 times faster using t-Am-**1** than when using t-Am-**2** (Figure 2b/c). The blank reaction of DVP with thiol (no tertiary amine) using a ratio of 1:1, takes ~110 hours to reach completion (SI, Figure S3 & S5). Addition of thiol to a mixture of activated intermediate in excess DVP predominantly leads to reaction with the activated intermediate (Figure 2b,c). This observation confirms that the reactivity of thiol with the activated intermediate (DVP-t-Am-1 or DVP-t-Am-2) is kinetically highly favoured over the background reaction with DVP. Although reaction kinetics are amine dependent, in both cases the formation of waste product follows quantitatively after each SH-**3** addition event (Figure 2b/c), which confirms the absence of unwanted SH-**3** side reactivity such as disulfide formation. Next, we studied systems using the weaker NH_2-**4** nucleophile in an effort to achieve transient non-equilibrium ionic species formation (Figure 2a). First, we explored the reaction rates (SI, Figure S2) and the background reaction (no t-Am-**2**) with a DVP:NH_2-**4** ratio of 1:4, which reached full conversion after 46 days (SI, Figure S4 & S5). Introducing t-Am-**2** to the system (t-Am-**2**:DVP:NH_2-**4** = 1:2:4), we observed the formation of approximately 69% DVP-t-Am-**2** within the first ~32 h by ^{1}H NMR. This was followed by a reaction plateau of ~13 h (pseudo-steady state of the activated intermediate, DVP-t-Am-**2**) and subsequently the recovery of 81% t-Am-**2** in response to the deactivation reaction (decay of DVP-t-Am-**2,** Figure 2d). When the network appeared to reach equilibrium (~521 h), an additional 4.0 eq. of NH_2-**4** were supplied to the system, which lead to an additional recovery of 12% t-Am-**2** (93% total t-Am-**2** recovery) before equilibrium was re-established.

In an effort to tune the amplitude of the activation reaction, we varied the concentration of DVP fuel. Supply of more fuel (4.0 eq.) accelerated the activation reaction with maximum values of 80% DVP-t-Am-**2**, as shown in Figure 2e. On the contrary however, the deactivation reaction remained incomplete even with an additional boost of NH_2-**4**, levelling off at 92% t-Am-**2** recovery. The extra fuel extended the pseudo-steady-state of the activated intermediate (reaction plateau) to 22 h. Evidently, the amount of fuel provides control over the formation of activated intermediate and its reaction plateau. Logically, less fuel (1.0 eq.) slowed down the activation reaction (50% DVP-t-Am-**2** peak formation) and shortened its pseudo-steady-state to ~6 h, while the deactivation reaction remained at a maximum recovery of 94% t-Am-**2**, even after addition of extra NH_2-**4** (Figure 2f).

3.2.2 SIGNAL-INDUCED MICELLE DISASSEMBLY WITH PROGRAMMED CARGO RELEASE AND RE-UPTAKE

To program the behaviour of a synthetic material, we combined our CRN with micelle forming block-copolymer P1, which is based on dimethylacrylamide (DMA) as the water-soluble block and 4-vinylpyridine (4VP) as the hydrophobic block (Figure 3a). Upon solubilization of 2.2 mg/mL P1 in aqueous-buffer we observed the formation of amphiphilic micelles using dynamic light scattering (DLS) (SI, Figure S13, t = 0 h) and transmission electron microscopy (TEM). TEM revealed uniform, narrowly dispersed micelles (Figure 3d) with an average diameter (D_{TEM} based on a sample population of n = 1202 in 3.6 μm^2) of 18 ± 4.4 nm, as determined by statistical image analysis (Figure 3c-top). This value agrees with the Z-averaged hydrodynamic diameter (D_{DLS}) obtained from DLS (D_{DLS} = 52 nm, Figure 3b-bottom). The discrepancy between D_{TEM} and D_{DLS} can be explained by the fact that TEM excludes the length of the hydrophilic DMA chain as a result of dry sample measurements.[57] Having established the formation of micellar dispersions, we first conducted signal-induced micellar (dis)assembly experiments with excess fuel (3.2 eq. DVP), P1 (1.0 eq. 4VP) and consecutive (4x) signal additions (1.0 eq. SH-**3**) (Figure 3a).

Upon fuelling the micellar solution, the DLS light scatter intensity (scatter count, Figure 3b-middle) dropped rapidly with a 12 ± 0.7 fold reduction (from 8.1 to 0.6 Mcps) in the first 10 h reaching its minimum at t = 105 h (0.3 Mcps). Simultaneously, ^{1}H NMR measurements showed a 28% (t = 10 h) to 74% (t = 105 h) conversion towards the charged activated intermediate (Figure 3b-top). This observation indicates that partial ionization of the micellar core by DVP (28%) is sufficient to cause a significant switch in the hydrophilicity of the core, leading to micelle disassembly. Hereafter, the disassembled state equilibrium was slowly reached (up to 105 hours), due to the decreasing presence of neutral polyamine units. At the same time, amine quaternization on the polymer becomes increasingly dominated by charge repulsion effects[58], which explains the incomplete conversion of DVP (74 ± 4.5%).

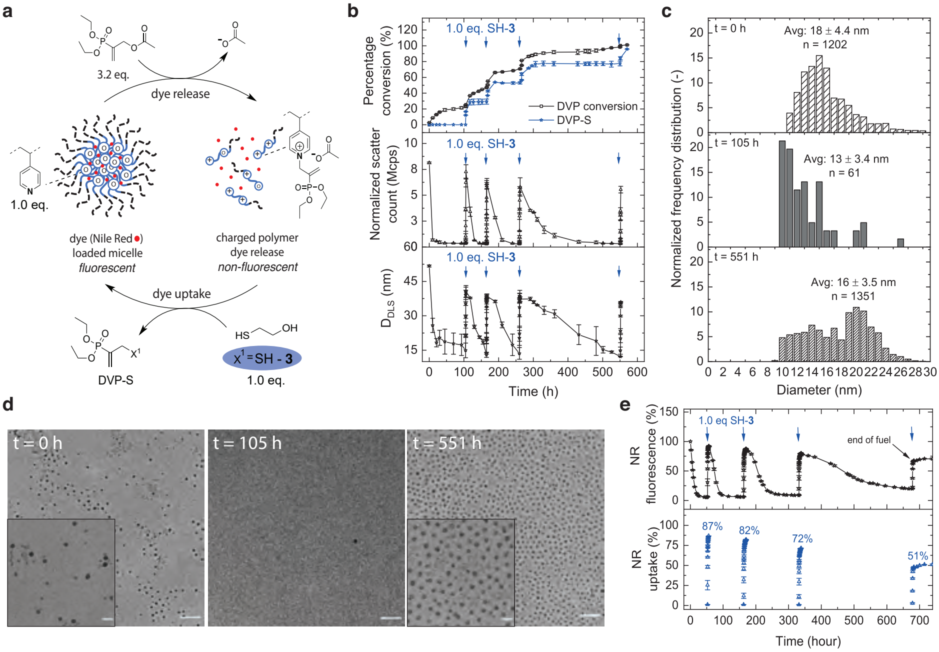

Figure 3: Signal-induced micellar (dis)assembly reaction network in the absence and presence of Nile Red (NR). **(a)** Micellar dispersions (2.2 mg/mL P1) were fuelled with DVP (13 mM, 3.2 eq.) and sequential additions of SH-**3** (1.0 eq.) as signal (blue arrow) in 1.0 mL phosphate buffer (0.1 M, pH = 7.4 and 10% D_2O) (SI, Figure S11). Micellar dispersion in **(e)** contained 15.5 ± 0.1 µg NR/mg of polymer (encapsulation efficiency of 39%), while micellar dispersions in **(b)**, **(c)** and **(d)** were without NR. **(b)** Stack graph: (top) DVP conversion and DVP-S formation observed by ^{1}H NMR. (middle) Corresponding DLS measured normalized scatter count (Mcps). (bottom) Corresponding DLS measured Z-averaged diameter (D_{DLS} in nm). **(c)** Normalized frequency distribution based on TEM image analysis for micellar (dis)assembly reaction network. At t = 0 h: initial micelle assembly. At t = 105 h: disassembled micellar state upon fuel exposure (DVP was added shortly after t = 0 h). At t = 551 h: signal induced micelle (re)assembled state after four sequential cycles and complete consumption of fuel. **(d)** TEM images of signal-induced micellar (dis)assembly reaction network (Scale bar: 200 nm, insert: 50 nm). (left) At t = 0 h: with no fuel/ signal. (middle) At t = 105 h: deformed micelles upon fuel exposure. (right) At t = 551 h: signal induced micelle (re)assembly after four sequential cycles. **(e)** Micellar (dis)assembly with corresponding dye uptake profile followed by NR fluorescence at an excitation wavelength of 540 nm and an emission wavelength of 645 nm. The error bars represent the standard deviation of duplicate measurements. Additional DLS and fluorescence data are presented in Figures S13 & S15.

Micellar solubilization was further confirmed by the measured decrease of the D_{DLS} from 52 ± 0.4 to 15 ± 3.2 nm during the first 105 hours (Figure 3b-bottom), which is consistent with TEM image analysis (D_{TEM} = 13 ± 3.4 nm at t = 105 h, Figure 3c-middle). In addition, the number of residual micellar structures (Figure 3d) decreased substantially (n = 61 for an identical image area compared to n = 1202 at the start).

To complete the cycle, we initiated the deactivation reaction after 105 hours by addition of signal SH-**3** (1.0 eq.). We observed a prompt response in ^{1}H NMR and DLS measurements by rapid formation of waste product DVP-S (93 ± 8.5% in 1 h), along with an increase in scatter count (7.2 ± 0.7 Mcps) and Z-averaged diameter (D_{DLS} = 41 ± 2.5 nm) to near starting values (Figure 3b). Importantly, the re-assembled state (at t ~106 h) is not at equilibrium, as unreacted excess fuel (~2.2 eq.) spontaneously regenerates the quaternized polyamine units.

Subsequently, the cycle starts again, until achieving maximum species ionization leading to micelle disassembly. After confirming three additional consecutive cycles, TEM image analysis (Figure 3c-bottom) showed the re-occurrence of micellar structures (Figure 3d) with an average diameter of 16 ± 3.5 nm at large population size (n = 1365 in 3.6 µm^2). Fundamentally, switching between hydrophobic/hydrophilic states by manipulation of the underlying molecular CRN was observed for other micellular systems[13,38,39,59–61] and recently elucidated by mechanistical modelling studies[40]. However, we also observed that the recovered micellar diameter decreased slightly with each cycle, as seen in TEM (from 18 to 16 nm) and DLS (from 51 to 36 nm). Such changes may be caused by the increasing accumulation of waste product with each cycle, which is known to limit cycle efficiency.[23,62]

After time-programming micellar (dis)assembly states using SH-signals, we investigated if similar behaviour could be achieved with loaded micelles and whether it is possible to release and re-uptake molecular cargo. To achieve this, micelles were loaded with Nile Red (NR) dye[63] as model cargo. NR is a solvatochromic dye which exhibits strong fluorescence in hydrophobic environments, while in water its fluorescence is quenched[64]. We exposed NR-loaded micelles to fuel (3.2 eq. DVP vs. vinyl pyridine) and monitored their fluorescence. During the first 10 hours after fuelling, the fluorescence decreased by 77 ± 0.3%, ultimately reaching a steady 95 ± 0.1% reduction in fluorescence after 52 h (Figure 3e). Upon SH-**3** (1.0 eq.) signal addition, the fluorescence increases promptly, reaching a value close to its original intensity, which corresponds to 87 ± 0.2% NR re-uptake within 4 h (t = 56 h). The transient increase in fluorescence is attributed to the re-established hydrophobic core unit and hence re-assembled micellar structures.

We conducted three additional signal-addition cycling between micelle (dis-) assembly states, which corroborate earlier findings without NR in DLS and ^1H NMR under identical conditions. Interestingly, we observed an increasingly less efficient cargo re-uptake after each cycle (from 1st cycle: 87% to 4th cycle: 51%). We experimentally determined that this behaviour is related to the increasing waste accumulation inside the micelle upon signalling (SI, Figure S16), as seen in micellar fuelling experiments without NR.

3.2.3 AUTONOMOUS MICELLE (DIS)ASSEMBLY WITH PROGRAMMED CARGO RELEASE – UPTAKE

Having established controllable signal-responsive micellar (dis)assembly, we further investigated autonomous cycling by concurrent competition between activation and deactivation reactions in the CRN with an excess of NH_2-**4**. Autonomous fuelling experiments were performed at optimized conditions with 2.2 mg/mL P1 (which corresponds to a 4VP concentration of 4.0 mM), 2.0 eq. DVP and 8.0 eq. NH_2-**4** in aqueous-buffer (Figure 4a). The micelle disassembly process reaches its apex at t = ~48 h, corresponding to 59 ± 2.0% formation of charged pyridine units (activated intermediate) after 1.1 eq. DVP conversion (55.5 ± 0.9%) and 0.52 eq. of waste product formation (26 ± 0.2% DVP-N and DVP-2-N) (Figure 4b-top). We found that the transition to the disassembled state occurred upon formation of ~60% of activated intermediate (t = 48 h), as demonstrated by a simultaneous drop in DLS measured scatter count from 11.9 to 0.5 Mcps and D_{DLS} from 53 to 23 nm (Figure 4b-middle/bottom). Notably, we observe a larger number of remaining micellar structures (t = 48 h) in contrast to the signal-induced micellar (dis)assembly, in parallel with a D_{TEM} change from 19 ± 4.5 nm (n = 1065) before fuelling (t = 0 h) to 15 ± 4.2 nm (n = 91) after 48 h (Figure 4c/d).

Nevertheless, from 48 to 504 hours the deactivation reaction kinetically outperforms the activation reaction due to continued depletion of fuel reserves (from 55.5 to ~100%). This ultimately leads to further accumulation of waste product (from 26 to 95%) until equilibrium is reached after approximately 504 hours (Figure 4b-top).

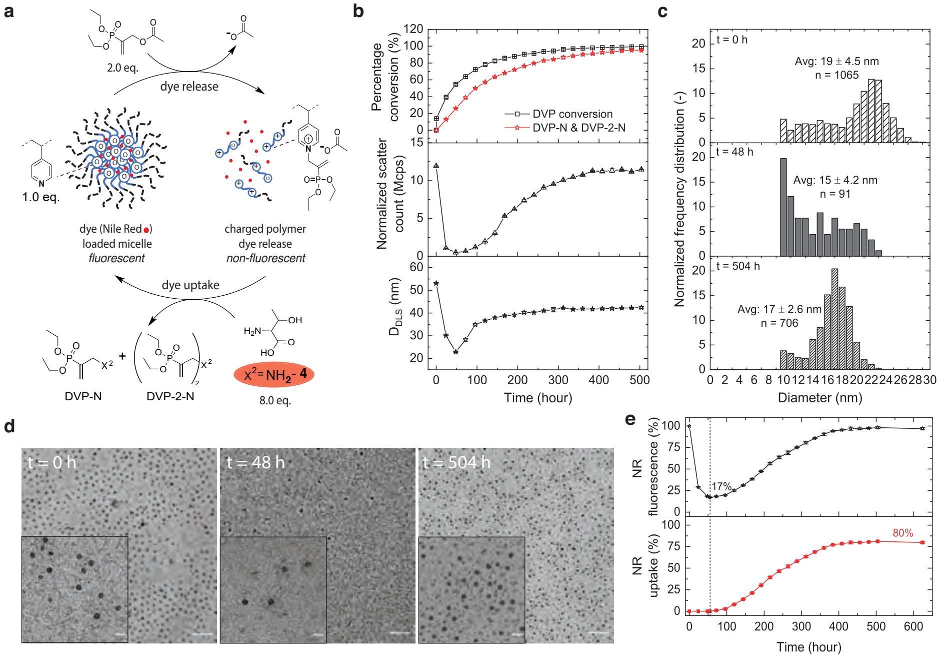

Figure 4: Fuel-driven out-of-equilibrium micellar (dis)assembly reaction network in the absence and presence of Nile Red (NR). **(a)** Micellar dispersions (2.2 mg/mL P1) were fuelled with DVP (8.0 mM, 2.0 eq.) and NH$_2$-**4** (8.0 eq.) in 1.0 mL phosphate buffer (0.5 M, pH = 7.4 and 10% D$_2$O) (SI, Figure S12). Micellar dispersion in **(e)** contained 15.5 ± 0.1 μg NR/mg of polymer (encapsulation efficiency of 39%), while micellar dispersions in **(b)**, **(c)** and **(d)** were without NR. **(b)** Stack graph (top) DVP conversion and DVP-N & DVP-2-N formation observed by ^{1}H NMR. (middle) Corresponding DLS measured normalized scatter count (Mcps). (bottom) Corresponding DLS measured Z-averaged diameter (D_{DLS} in nm). **(c)** Normalized frequency distribution based on TEM image analysis for micellar (dis)assembly reaction network. At t = 0 h: initial micelle assembly. At t = 48 h: disassembled micellar state upon fuel exposure (DVP was added shortly after t = 0 h). At t = 504 h: micellar (re)assembled state. **(d)** TEM images of fuel-driven out-of-equilibrium micellar (dis)assembly reaction network (Scale bar: 200 nm, insert: 50 nm). (left) At t = 0 h: with no fuel/nucleophile. (middle) At t = 48 h: micellar disassembled state upon fuel/nucleophile exposure. (right) At t = 504 h: micellar (re)assembled state. **(e)** Micellar (dis)assembly with corresponding dye uptake profile followed by NR fluorescence at an excitation wavelength of 540 nm and an emission wavelength of 645 nm. The error bars represent the standard deviation of duplicate measurements. For (**b**–top) DVP conversion and product percentages were normalized to 100. Additional DLS and fluorescence data are presented in Figures S14 & S15.

During that period, DLS measured scatter count increases from 0.5 to 11.4 Mcps, while D_{DLS} recovered to 42 nm (Figure 4b-middle/bottom). In good agreement with DLS, TEM image analysis also revealed an increase in micellar diameter (D_{TEM} = 17 ± 2.6 nm) and qualitatively a much larger number of micellar structures could be observed (n = 706) (Figure 4c/d). As the CRN depletes its fuel reserve, the rate of deactivation becomes higher than the activation rate and thus reverts the charged polyamine units to their uncharged precursor. This leads to increasing hydrophobicity on the polymer backbone, which ultimately results in reassembled micellar structures at equilibrium state. Lastly, we addressed autonomous cargo release and re-uptake by conducting NR probed micellar fuelling experiments at conditions identical to the no-cargo micellar experiments (Figure 4e). Using the fuel-driven out-of-equilibrium CRN strategy, 83 ± 0.3% of cargo was released in 55 hours. Hereafter, fluorescence intensity steadily increased back to nearly the original level, corresponding to 80 ± 1.0% cargo re-uptake over the next ~19 days. This way, we achieved autonomous (dis)assembly of micellar-macromolecular structures with time-programmed cargo release and re-uptake.

3.2.4 TEMPORALLY PROGRAMMED HYDROGEL SWELLING

To further demonstrate our CRN strategy, we aimed to achieve reversible expansion–contraction of a polymeric hydrogel network by temporally controlling its water in – and outflux (Figure 5a). We co-polymerized DMA and 4VP to generate a water-soluble statistical copolymer (P2 precursor). We then crosslinked this copolymer with bis(acrylamide) to form cube shaped polymer hydrogels (P2) with polyamine concentrations of 97 mg/mL. The resulting gels had a water content of 90 wt% and dimensions of approximately 1.4 x 1.2 x 0.5 cm (L/W/H). We hypothesized that network expansion can be induced by charge generation upon fuel addition. The increasing concentration of charges in the polymer network will lead to an increase in osmotic pressure in the material which makes the hydrogel swell (expansion) until it is balanced by elastic network forces.[54,65]

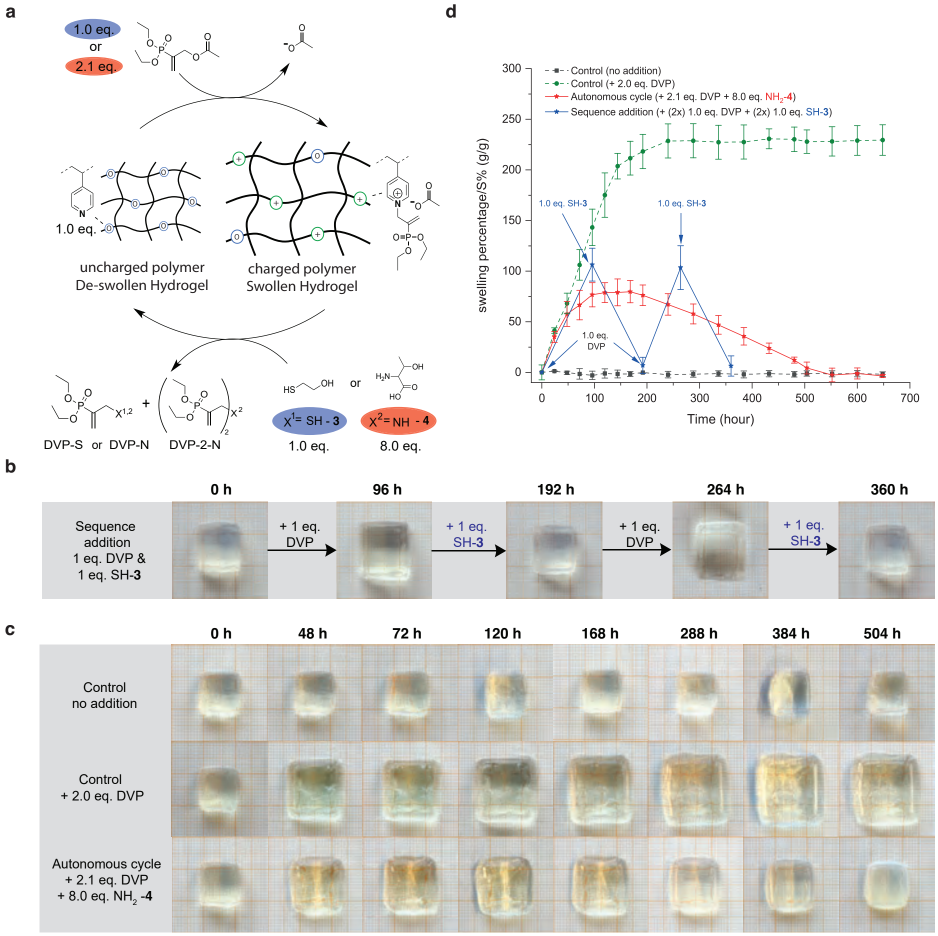

Figure 5: Temporally programmed hydrogel swelling and de-swelling. **(a)** Hydrogel (de)swelling using signal-responsive or autonomous CRN strategy. The transition from un-swollen to swollen state was monitored visually by time-lapse photographs on millimetre paper and via hydrogel weight measurements (run in triplet) over time in phosphate buffer (pH = 7.4, 0.1 M) at room temperature. **(b)** Time-lapse photographs of signal-responsive hydrogels without solution. **(c)** Time-lapse photographs of fuel-driven out-of-equilibrium cycle hydrogels without solution in comparison to control hydrogels. **(d)** Swelling percentage (S%) for temporally programmed signal-responsive (blue) and autonomous (red) hydrogel (de)swelling over time. Control hydrogel measurements without reactants (grey) and with 2.0 eq. DVP (green). The error bar represents the standard deviation. Additional hydrogel time-lapse photographs are shown in Figure S17 – S19.

In addition, potential repulsive forces between the ionized activated intermediates on the polymer might add to the swelling forces and thus to the expansion of the hydrogel.[66]

To test this hypothesis, we observed fuelled/non-fuelled hydrogels via photographs over time and evaluated their swelling percentage (S%, SI - Eq.S4), where the difference in weight between equilibrium swollen hydrogels (at t = 0) and the fuel activated swollen hydrogels (t) is compared. First, polyamine-containing hydrogels were activated with DVP (43.2 mM, 1.0 eq. vs. vinyl pyridine).

Successful material expansion (Figure 5b) was observed with a maximum of 106 ± 16% increase in S% 96 h after fuelling (Figure 5d-blue), while control hydrogels remained at equilibrium weight (Figure 5d-grey). This drastic increase in volume was further confirmed visually by comparing fuelled hydrogels to their non-fuelled counterparts (Figure 5b). Next, we investigated the reversibility of the system by addition of SH-**3** (1.0 eq.). The nucleophilic triggering of the system resulted in hydrogel contraction to near starting values 96 h after signal introduction (S% = 7 ± 8%). To demonstrate the repeatability of the system, signal-responsive (de)swelling was repeated by re-fuelling (S% = 104 ± 22%) and subsequent SH-**3** signalling (S% = 6 ± 10%) to temporally program the materials swelling behaviour (Figure 5b/d-blue). Turning our attention to kinetics, we were surprised that swelling proceeds at a similar time-scale as de-swelling (t ~96 h). We suggest here, that the large hydrogel size limits SH-**3** diffusion into the material. Another potential factor, which affects the diffusive influx of SH-**3**, is the convective counterforce of water out-flux with decreasing ionization.

Next, we explored transient hydrogel swelling by exposing equilibrium-swollen gels to DVP (13.2 mM, 2.1 eq. vs. vinyl pyridine) and excess NH_2-**4** (8.0 eq.) (Figure 5a). We observed temporary swelling of the polymeric hydrogel network with clear swelling maxima around t = 168 h (S% = 80 ± 11%), followed by de-swelling which approached starting values (S% = 4 ± 6%) after 504 hours (Figure 5c/d-red). This transient swelling study on synthetic hydrogel materials in aqueous media has shown a robust material response and thus the versatility of using the programmed solvent-material interaction strategy for autonomous cycling.

3.3 CONCLUSION

In this work, we have introduced a new CRN which operates through successive nucleophilic substitutions on electron deficient allyl acetates (fuel). By first combining a tertiary nitrogen species with the fuel, a cationic quaternary nitrogen intermediate can be formed. This intermediate is stable in pH 7.4 aqueous solutions until undergoing a second nucleophilic substitution with nucleophiles such as a thiol or primary amine. This process regenerates the starting neutral tertiary amine species, along with the formation of a waste product. Unlike most chemically fuelled non-enzymatic CRNs, the deactivation reaction can be controlled at constant pH by judicious choice of nucleophile. With strong nucleophiles such as 2-mercaptoethanol we were able to achieve signal-induced cycling between charge states with excess fuel (DVP) and sequential additions of nucleophile. By switching to weaker nucleophiles such as threonine, both fuel and nucleophile can be introduced simultaneously to yield fuel-driven out-of-equilibrium or autonomous cycling. By incorporating the tertiary nitrogen species into polymeric scaffolds, cycling between neutral and cationic amine species yields transitions between collapsed, hydrophobic polymer chains and solvated, hydrophilic polymer chains. In micellar dispersions, this allowed for the programmed release and re-uptake over time of a solvatochromic dye, acting as a model cargo. In bulk polymer hydrogels we used the CRN to control water influx, allowing us to control hydrogel swelling behaviour by fuel and nucleophile additions. Both material classes could operate under signal-induced and autonomous cycling conditions, leading to different types of behaviour. The principle of temporally programming the behaviour of synthetic materials, shown in this work, is applicable not only to constructing out-of-equilibrium synthetic structures but also as advanced strategy for controlled molecular cargo delivery. By using the underlying CRN, its scalability and applicability to different material classes combined with its possibilities of tuning the kinetic profile based on choice of nucleophile or choice of fuel[67], a variety of new designs for interactive structures can be envisioned. We therefore anticipate that this concept will contribute to the development of next generation soft materials, where signal or time-programmed control over charge density allows for interactive and adaptive material properties, such as stiffening, adhesion or motion.

3.4 REFERENCES

1 A. Walther, *Adv. Mater.*, 2020, **32**, 1905111.

2 J. Boekhoven and S. I. Stupp, *Adv. Mater.*, 2014, **26**, 1642–1659.

3 A. R. Hirst, B. Escuder, J. F. Miravet and D. K. Smith, *Angew. Chem. Int. Ed.*, 2008, **47**, 8002–8018.

4 B. A. Grzybowski, K. Fitzner, J. Paczesny and S. Granick, *Chem. Soc. Rev.*, 2017, **46**, 5647–5678.

5 J. Boekhoven, W. E. Hendriksen, G. J. M. Koper, R. Eelkema and J. H. van Esch, *Science.*, 2015, **349**, 1075–1079.

6 E. Karsenti, *Nat. Rev. Mol. cell Biol.*, 2008, **9**, 255–262.

7 Z. Leng, F. Peng and X. Hao, *Chempluschem*, 2020, **85**, 1190–1199.

8 S. A. P. van Rossum, M. Tena-Solsona, J. H. van Esch, R. Eelkema and J. Boekhoven, *Chem. Soc. Rev.*, 2017, **46**, 5519–5535.

9 J. Boekhoven, A. M. Brizard, K. N. K. Kowlgi, G. J. M. Koper, R. Eelkema and J. H. van Esch, *Angew. Chem. Int. Ed.*, 2010, **122**, 4935–4938.

10 T. Heuser, E. Weyandt and A. Walther, *Angew. Chem. Int. Ed.*, 2015, **54**, 13258–13262.

11 S. Panja, C. Patterson and D. J. Adams, *Macromol. Rapid Commun.*, 2019, **40**, 1900251.

12 L. Heinen and A. Walther, *Chem. Sci.*, 2017, **8**, 4100–4107.

13 E. Poros-Tarcali and J. Perez-Mercader, *Soft Matter*, 2021, **17**, 4011–4018.

14 G. Wang and S. Liu, *ChemSystemsChem*, 2020, **2**, e1900046.

15 M. Tena-Solsona, B. Rieß, R. K. Grötsch, F. C. Löhrer, C. Wanzke, B. Käsdorf, A. R. Bausch, P. Müller-Buschbaum, O. Lieleg and J. Boekhoven, *Nat. Commun.*, 2017, **8**, 1–8.

16 S. Nakamaru, S. Maeda, Y. Hara and S. Hashimoto, *J. Phys. Chem. B*, 2009, **113**, 4609–4613.

17 T. Masuda, A. Terasaki, A. M. Akimoto, K. Nagase, T. Okano and R. Yoshida, *RSC Adv.*, 2015, **5**, 5781–5787.

18 A. K. Dambenieks, P. H. Q. Vu and T. M. Fyles, *Chem. Sci.*, 2014, **5**, 3396–3403.

19 D. W. R. Balkenende, C. A. Monnier, G. L. Fiore and C. Weder, *Nat. Commun.*, 2016, **7**, 1–9.

20 C. G. Pappas, T. Mutasa, P. W. J. M. Frederix, S. Fleming, S. Bai, S. Debnath, S. M. Kelly, A. Gachagan and R. V Ulijn, *Mater. Horizons*, 2015, **2**, 198–202.

21 T. Ikegami, Y. Kageyama, K. Obara and S. Takeda, *Angew. Chem. Int. Ed.*, 2016, **128**, 8379–8383.

22 R. K. Grötsch, C. Wanzke, M. Speckbacher, A. Angı, B. Rieger and J. Boekhoven, *J. Am. Chem. Soc.*, 2019, **141**, 9872–9878.

23 J. Heckel, S. Loescher, R. T. Mathers and A. Walther, *Angew. Chem. Int. Ed.*, 2021, **60**, 7117–7125.

24 B. Zhang, I. M. Jayalath, J. Ke, J. L. Sparks, C. S. Hartley and D. Konkolewicz, *Chem. Commun.*, 2019, **55**, 2086–2089.

25 L. S. Kariyawasam, M. M. Hossain and C. S. Hartley, *Angew. Chem. Int. Ed.*, 2021, **60**, 12648–12658.

26 S. M. Morrow, I. Colomer and S. P. Fletcher, *Nat. Commun.*, 2019, **10**, 1–9.

27 N. Singh, A. Lopez-Acosta, G. J. M. Formon and T. M. Hermans, *J. Am. Chem. Soc.*, 2022, **144**, 410–415.

28 J. Leira-Iglesias, A. Tassoni, T. Adachi, M. Stich and T. M. Hermans, *Nat. Nanotechnol.*, 2018, **13**, 1021–1027.

29 J. P. Wojciechowski, A. D. Martin and P. Thordarson, *J. Am. Chem. Soc.*, 2018, **140**, 2869–2874.

30 B. Fan, Y. Men, S. A. P. van Rossum, G. Li and R. Eelkema, *ChemSystemsChem*, 2020, **2**,

e1900028.

31 I. Colomer, S. M. Morrow and S. P. Fletcher, *Nat. Commun.*, 2018, **9**, 2239.

32 G. Wang, B. Tang, Y. Liu, Q. Gao, Z. Wang and X. Zhang, *Chem. Sci.*, 2016, **7**, 1151–1155.

33 R. N. Reddi, E. Resnick, A. Rogel, B. V. Rao, R. Gabizon, K. Goldenberg, N. Gurwicz, D. Zaidman, A. Plotnikov, H. Barr, Z. Shulman and N. London, *J. Am. Chem. Soc.*, 2021, **143**, 4979–4992.

34 J. Zhuang, B. Zhao, X. Meng, J. D. Schiffman, S. L. Perry, R. W. Vachet and S. Thayumanavan, *Chem. Sci.*, 2020, **11**, 2103–2111.

35 K. Jalani, S. Dhiman, A. Jain and S. J. George, *Chem. Sci.*, 2017, **8**, 6030–6036.

36 S. Bal, K. Das, S. Ahmed and D. Das, *Angew. Chem. Int. Ed.*, 2019, **131**, 250–253.

37 G. Cheng and J. Perez-Mercader, *Chem*, 2020, **6**, 1160–1171.

38 T. Yoshizawa, M. Onoda, T. Ueki, R. Tamate, A. M. Akimoto and R. Yoshida, *Angew. Chem. Int. Ed.*, 2020, **59**, 3871–3875.

39 M. A. Würbser, P. S. Schwarz, J. Heckel, A. M. Bergmann, A. Walther and J. Boekhoven, *ChemSystemsChem*, 2021, **3**, e2100015.

40 J. Heckel, F. Batti, R. T. Mathers and A. Walther, *Soft Matter*, 2021, **17**, 5401–5409.

41 X. Lang, U. Thumu, L. Yuan, C. Zheng, H. Zhang, L. He, H. Zhao and C. Zhao, *Chem. Commun.*, 2021, **57**, 5786–5789.

42 S. G. J. Postma, I. N. Vialshin, C. Y. Gerritsen, M. Bao and W. T. S. Huck, *Angew. Chem. Int. Ed.*, 2017, **129**, 1820–1824.

43 M. Baidya, G. Y. Remennikov, P. Mayer and H. Mayr, *Chem. Eur. J.*, 2010, **16**, 1365–1371.

44 J. N. Kim, H. J. Lee, K. Y. Lee and J. H. Gong, *Synlett*, 2002, **2002**, 173–175.

45 A. Calcatelli, A. Cherubini-Celli, E. Carletti and X. Companyó, *Synthesis.*, 2020, **52**, 2922–2939.

46 G.-Y. Chen, F. Zhong and Y. Lu, *Org. Lett.*, 2011, **13**, 6070–6073.

47 A. Seingeot, Y. Charmasson, M. Attolini and M. Maffei, *Heteroat. Chem.*, 2017, **28**, e21352.

48 P. R. Wells, *Chem. Rev.*, 1963, **63**, 171–219.

49 X.-L. Liu, L.-Y. Niu, Y.-Z. Chen, Y. Yang and Q.-Z. Yang, *Sensors Actuators B Chem.*, 2017, **252**, 470–476.

50 F. Brotzel and H. Mayr, *Org. Biomol. Chem.*, 2007, **5**, 3814–3820.

51 Y. Henchoz, J. Schappler, L. Geiser, J. Prat, P.-A. Carrupt and J.-L. Veuthey, *Anal. Bioanal. Chem.*, 2007, **389**, 1869–1878.

52 G. Moad, E. Rizzardo and S. H. Thang, *Aust. J. Chem.*, 2012, **65**, 985–1076.

53 M. Satoh, E. Yoda, T. Hayashi and J. Komiyama, *Macromolecules*, 1989, **22**, 1808–1812.

54 S. K. De, N. R. Aluru, B. Johnson, W. C. Crone, D. J. Beebe and J. Moore, *J. Microelectromechanical Syst.*, 2002, **11**, 544–555.

55 M. Baidya and H. Mayr, *Chem. Commun.*, 2008, 1792–1794.

56 Y. Shi, G. Humphrey, P. E. Maligres, R. A. Reamer and J. M. Williams, *Adv. Synth. Catal.*, 2006, **348**, 309–312.

57 Q. Yan and Y. Zhao, *J. Am. Chem. Soc.*, 2013, **135**, 16300–16303.

58 M. Lemmers, E. Spruijt, L. Beun, R. Fokkink, F. Leermakers, G. Portale, M. A. C. Stuart and J. van der Gucht, *Soft Matter*, 2012, **8**, 104–117.

59 T. Heuser, A.-K. Steppert, C. Molano Lopez, B. Zhu and A. Walther, *Nano Lett.*, 2015, **15**, 2213–2219.

60 X. Hao, W. Sang, J. Hu and Q. Yan, *ACS Macro Lett.*, 2017, **6**, 1151–1155.

61 P. S. Schwarz, L. Tebcharani, J. E. Heger, P. Müller-Buschbaum and J. Boekhoven, *Chem. Sci.*, 2021, **12**, 9969–9976.

62 C. G. Pappas, I. R. Sasselli and R. V. Ulijn, *Angew. Chem. Int. Ed.*, 2015, **54**, 8119–8123.

63 M. K. Gupta, T. A. Meyer, C. E. Nelson and C. L. Duvall, *J. Control. release*, 2012, **162**, 591–598.

64 P. Greenspan and S. D. Fowler, *J. Lipid Res.*, 1985, **26**, 781–789.
65 P. J. Flory, *Principles of polymer chemistry*, Cornell University Press, 1953.
66 F. Lai and H. Li, *Soft Matter*, 2010, **6**, 311–320.
67 R. W. Lewis, B. Klemm, M. Macchione and R. Eelkema, *Chem. Sci.*, 2022, **13**, 4533–4544.

3.5 SUPPLEMENTARY INFORMATION

3.5.1 Instrumentation, materials and characterisation

All reagents and solvents were used without further purification unless otherwise stated. Tetraethylmethylene diphosphonate (TMP, 97%), para-formaldehyde (p-FA, 95%) 2-mercaptoethanol (SH-**3**, >99%), N,N-dimethylacrylamide (DMA, 99%) , 4-vinylpyridine (4VP, 95%), 4-((((2-carboxyethyl)thio)carbonothioyl)thio)-4-cyanopentanoic acid (CETCPA, 95%, ABCR), 3-(trimethylsilyl)-1-propanesulfonic acid sodium salt (DSS, 97%), *N,N'*-methylenebis(acrylamide) (BisAM, 97%), acetic anhydride (AA, >99%), dimethylaminopyridine (DMAP, >99%), triethylamine (Et_3N, 98%), L-Threonine (NH_2-**4,** >98%), 1,4-diazabicyclo[2.2.2]octane - DABCO (t-Am-**1,** >99%), pyridine (t-Am-**2,** >99%), tetramethylethylenediamine (TEMED, 99%) and ammonium persulfate (APS, 98%) were purchased from Sigma Aldrich or TCI Europe. For the preparation of aqueous-buffers, solid salts were used: sodium phosphate monobasic and sodium phosphate dibasic which were purchased from Sigma Aldrich. Unless stated otherwise, all stock solutions were prepared in D_2O/phosphate buffer mixtures 1:9 (0.1 M, pH = 7.4) for the signal-induced cycle and D_2O/phosphate buffer mixtures 1:9 (0.5 M, pH = 7.4) for the autonomous cycle experiments to avoid significant pH changes. All buffers were pH adjusted using sodium hydroxide (1 M) and hydrochloric acid (1 M). DMA and 4VP were passed through basic alumina prior to use to remove inhibitor. ESI-MS was performed using LTQ XL spectrometer equipped with Shimadzu HPLC setup operating at 0.2 mL/min flow rate with water/MeCN mobile phase containing 0.1 vol% formic acid and Discovery C18 column. Dynamic Light Scattering (DLS) measurements were performed on a Malvern Instruments Zetasizer Nano ZS, employing a 633 nm laser at a back-scattering angle of 173°. Measurements were performed in BRAND 1.5 mL PMMA semi-micro disposable cuvette (10 mm path length). TEM measurements were performed on a Jeol JEM1400 Transmission Electron Microscope with an operating voltage of 120kV. Fluorescence spectra were recorded with a fluorescence spectrometer Spex Fluorolog-3 equipped with a standard 90° setup, operated at a constant Voltage of 25 V. Photographs of the hydrogels were taken on a Canon EOS 600D single reflex camera with a Canon Macro Lens EF 100 mm 1:2.8 USM. The LED reactor was constructed from a 5-meter strip of 300 RGB 5050 SMD LEDs procured from ryslux (ebay) with λ_{max} of the blue lights measured to be 441 nm (Ocean Optics USB 4000 fibre coupled spectrometer). These LEDs were connected around a glass beaker of diameter 10 cm.

3.5.2 NMR spectroscopy

NMR spectra were recorded on an Agilent-400 MR DD2 NMR instrument at 25°C (399.7 MHz for ^{1}H, 100.5 MHz for ^{13}C and 161.9 MHz for ^{31}P) using residual solvent signals as internal reference. To suppress the water peak, PRESAT configuration (suppress one highest peak) was used. NMR spectra were processed by MNova NMR software (Mestrelab Research). Polymerization conversion (ρ) was calculated by monitoring reduction in the ^{1}H NMR integrals of the monomer unsaturated protons (∫M: 5.6 – 6.7 ppm for DMA, 5.5 – 6.7 ppm for 4VP) and aromatic protons in case of 4VP (7.5 ppm) relative to the internal standard DSS (~0 ppm). In the case of a copolymerization with both DMA and 4VP the conversion of both monomers was calculated (Eq. 1).

$$\rho = \frac{\int M\ (t0) - \int M\ (t)}{\int M\ (t0)}$$ **Eq. 1**

For a polymerization containing z monomers, $M_{n,conv}$ was calculated according to Equation 2. Here $[Mx]_0$ is the initial concentration of monomer *x*, $[CTA]_0$ is the initial chain transfer agent (CTA) concentration and M_{Mx} and M_{CTA} are the monomer *x* and CTA molecular weights, respectively.

$$M_{n,conv} = \sum_{x=1}^{Z} \rho * \frac{[M]_0}{[CTA]_0} * M_{Mx} + M_{CTA}$$ **Eq. 2**

3.5.3 Micelle dispersion and DLS measurements

The signal-induced cycle was performed with P1 (2.24 mg, 4.0 µmol, 1.0 eq. 4VP), DVP (3.2 eq.) in buffer and addition (4x) of the signal SH-**3** (1.0 eq.). Stock solutions of P1 and DVP were mixed in a 4.0 mL vial (total reaction volume 1.0 mL), stirred vigorously for 10 seconds and immediately transferred to PMMA disposable cuvettes and measured at specific time points. The signal SH-**3** (0.28 µL, 4.0 µmol) in buffer was added to the cuvette, 4 times at specific time points. In contrast, for the autonomous cycle P1 (4.0 µmol, 1.0 eq. 4VP), DVP (2.0 eq.) and NH_2-**4** (8.0 eq.) in buffer were mixed together in a 4.0 mL vial (total reaction volume 1.0 mL), stirred vigorously for 10 seconds and immediately transferred to PMMA disposable cuvettes and measured for t = 0 h and then every 24 hours.

3.5.4 TEM measurements

The morphologies of the micelles and their size were observed via Transmission Electron Microscopy (TEM). For both, the signal-induced and autonomous cycle, aliquots were taken at specific time points from the DLS measurement samples and drop casted onto a Formvar/Carbon 400 mesh Cu grid. The grids were exposed (30 s) to 3.0 µL uranyl acetate stain solution (2 wt% in H_2O), then washed (3x) with milli-Q water and dried on filter paper before loading it on the TEM single tilt holder. TEM pictures were processed and analysed using ImageJ to obtain the particle size distribution.

3.5.5 GPC measurements

The average molecular weight and dispersity (Đ) of the synthesized polymers was measured through a Shimadzu GPC with DMF LiBr (25 mM) as eluent. The system was equipped with a Shimadzu CTO-20AC Column oven, a Shimadzu RID-10A refractive index detector, a Shimadzu SPD-20A UV-Vis detector, PL gel guard column (MIXED, 5 µm), 50 mm x 7.5 mm, and 1× Agilent PLGel (MIXED, 5 µm), 300 mm × 7.5 mm, providing an effective molar mass range of 200 to 2×10^6 g/mol. DMF LiBr (25 mM) was used as an eluent with a flow rate of 1.0 mL/min at 50°C. The GPC columns were calibrated with low dispersity PMMA standards (Sigma Aldrich) ranging from 800 to 2.2×10^6 g/mol, and molar masses are reported as PMMA equivalents. A 3rd-order polynomial was used to fit the log M_p vs. time calibration curve for both systems, which was near linear across the molar mass ranges.

3.5.6 Fluorescence measurements

A Nile Red solution in THF (20.0 µL, 2.0 mg/mL) was added to a micellar dispersion P1 (2.0 mL, 12.0 µmol, 1.0 eq. 4VP) in buffer and incubated in the dark in an open vial to evaporate overnight the organic solvent (the mixture was measured in the NMR confirming that all THF had been evaporated before further usage). This solution was then mixed with DVP (3.2 eq.) in buffer to a total reaction volume of 3.0 mL and transferred to quartz cuvettes (path length of 1 cm) and immediately measured (t = 0 h). The signal SH-**3** (0.84 µL, 12.0 µmol, 1.0 eq.) was added in the cuvette at specific time points, which was repeated three times, hereafter (at specific time points). In case of the autonomous cycle, a Nile Red treated micellar dispersion (2.0 mL, 12.0 µmol, 1.0 eq. 4VP) was mixed with DVP (2.0 eq.) and NH_2-**4** (8.0 eq.) in buffer and transferred in quartz cuvettes (total reaction volume 3.0 mL) and immediately measured (t = 0 h). Hereafter, the reaction mixture was measured every 24 hours. Each solution was measured in the Fluorometer at an excitation wavelength of 540 nm and an emission wavelength of 645 nm. To determine the loading of the micelles, a micellar dispersion (2.0 mL, 12.0 µmol) was prepared with Nile Red (20 µL, 2.0 mg/mL in THF) addition and overnight solvent evaporation in the dark. The samples were centrifuged at 5000 rpm for 10 min and ~900 µL buffer was removed carefully without disturbing the pellet and replaced with fresh phosphate buffer, this step was repeated three times. After another centrifugation step and removal of the buffer, 900 µL of DMF was added and the vial was shaken to dissolve the loaded micelles. The fluorescence of the solution was measured at an excitation wavelength of 540 ± 20 nm and emission wavelength 620 ± 30 nm and compared to the calibration curve of known concentrations of Nile Red in 90% DMF in buffer (Figure S1), to determine the Nile Red loading per mg of polymer P1.

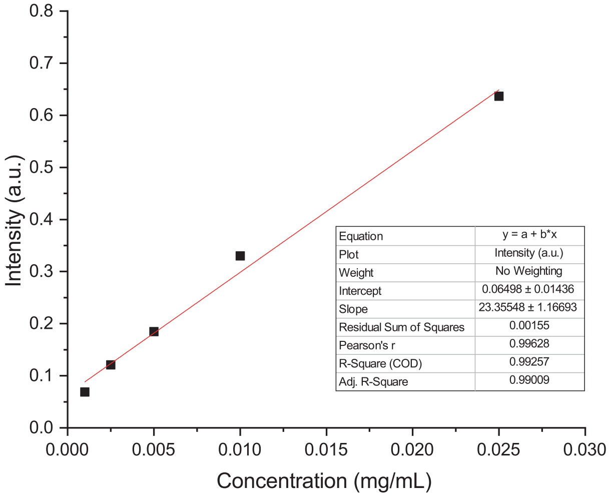

Equation	y = a + b*x
Plot	Intensity (a.u.)
Weight	No Weighting
Intercept	0.06498 ± 0.01436
Slope	23.35548 ± 1.16693
Residual Sum of Squares	0.00155
Pearson's r	0.99628
R-Square (COD)	0.99257
Adj. R-Square	0.99009

Figure S1: Calibration curve - Nile Red concentration (mg/mL) vs. fluorescence intensity (-).

3.5.7 Hydrogel preparation

p($4VP_{28}$-stat-DMA_{55}) (292.0 mg, 33.3 µmol) was mixed together with BisAM (31.0 mg, 200 µmol) and DMA (99.0 mg, 1000 µmol) in 2.5 mL deionized water and degassed for 10 min under Argon. Separately, stock solutions of TEMED and APS were prepared in 0.5 mL deionized water and degassed for 10 min under Argon. TEMED (266.6 mM) and APS (133.3 mM) were added to the degassed p($4VP_{28}$-stat-DMA_{55}), BisAM, DMA mixture and shaken for 1 min before adding the solution into a cast (0.7 mL per cast) and leaving it for curing overnight. The crude hydrogels were removed from their casts and washed twice with 10 mL phosphate buffer (0.1 M, pH = 7.4) and then left for 96 hours (the supernatant was exchanged with buffer every day) until equilibrium swelling had been achieved, before further usage.

3.5.8 Kinetic experiments

3.5.8.1 Reaction rate constants comparison: reaction of DVP with t-AM-1 & 2 and nucleophiles

Briefly, DVP (10.0 mg, 42 µmol, 1.0 eq.) and DSS as internal standard (1.0 eq.) were dissolved in 0.1 mL D_2O/0.4 mL phosphate buffer (0.1 M, pH = 7.4). Then, either t-Am-**1**, t-Am-**2**, SH-**3** or NH_2-**4** (0.2 eq.) dissolved in 0.5 mL phosphate buffer (0.1 M, pH = 7.4) were added to the reaction mixture. The reactions were immediately followed by ^1H NMR.

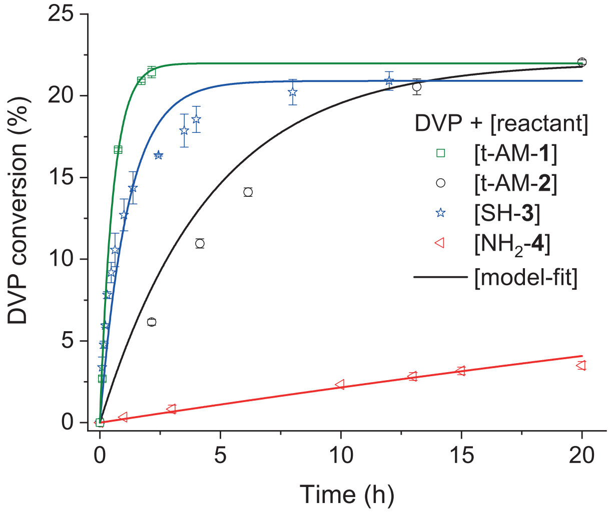

Figure S2: Conversion plot over time for the reaction of DVP (1.0 eq.) with t-AM-**1** (0.2 eq.), t-AM-**2** (0.2 eq.), SH-3 (0.2 eq.) or NH_2-**4** (0.2 eq.). All measurements were done in duplicate. Solid lines represent the k-value-model fit to the experimental data.

3.5.8.2 Fitting pseudo-first order reaction kinetics

To compare the reaction between DVP with t-AM-**1**/t-AM-**2** and DVP with SH-**3**/NH_2-**4**, reactions were performed at pseudo-first order conditions by using one of the reactants in excess (DVP). The concentrations used were 0.04 M (1.0 eq.) of DVP with 0.008 M (0.2 eq.) of either tertiary amines or S,N -terminal nucleophiles. The pseudo- first order reaction rate constants were calculated by fitting the conversion of DVP over time with Eq.3:

$$ln\left(\frac{[B]_t}{[B]_0}\right) = -k[A]_0t \qquad \textbf{Eq.3}$$

, where $[B]_0$ is the initial concentration of DVP in excess at t = 0, 0.04 M; $[B]_t$ is the concentration of DVP at every specific time point obtained by ^{1}H NMR, with DSS as internal standard; k is the pseudo-first order reaction rate constant and $[A]_0$ is the concentration of reactant (SH-**3**, NH_2-**4**, t-AM-**1** or t-AM-**2** = 0.008 M).

Table S1: Summary of the reaction rates for DVP with t-AM-1, t-AM-2, SH-3 or NH_2-4.

A

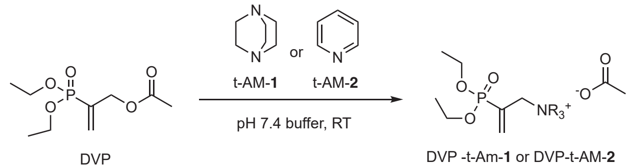

B

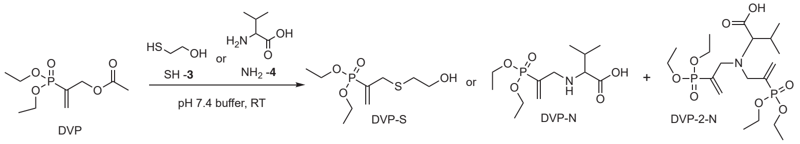

Scheme	Reaction	k (M^{-1}*h^{-1})	R^2
A	DVP + t-AM-1	43.5 ± 3.21	0.996
	DVP + t-AM-2	5.14 ± 0.62	0.992
B	DVP + SH-3	20.3 ± 4.74	0.982
	DVP + NH_2-4	0.27 ± 0.02	0.995

* Conditions: (A) 0.04 mM of DVP, 0.008 mM t-AM-1 or t-AM-2 in 0.1 M phosphate buffer (pH 7.4), 25 °C, (B) 0.04 mM of DVP, 0.008 mM of nucleophile (SH-3 or NH_2-4) in 0.1 M phosphate buffer (pH 7.4), 25 °C.

3.5.8.3 Reaction of DVP with SH-3 and DVP with NH_2-4 (Blank reactions)

DVP (10.0 mg, 42 µmol, 1.0 eq.) and DSS as internal standard (1.0 eq.) were dissolved in 0.1 mL D_2O/0.4 mL phosphate buffer (0.1 M, pH = 7.4). Then, SH-**3** (1.0 eq.) dissolved in 0.5 mL phosphate buffer (0.1 M, pH = 7.4) was added to the reaction mixture. The reaction was immediately followed by NMR until completion at t = 110 hours.

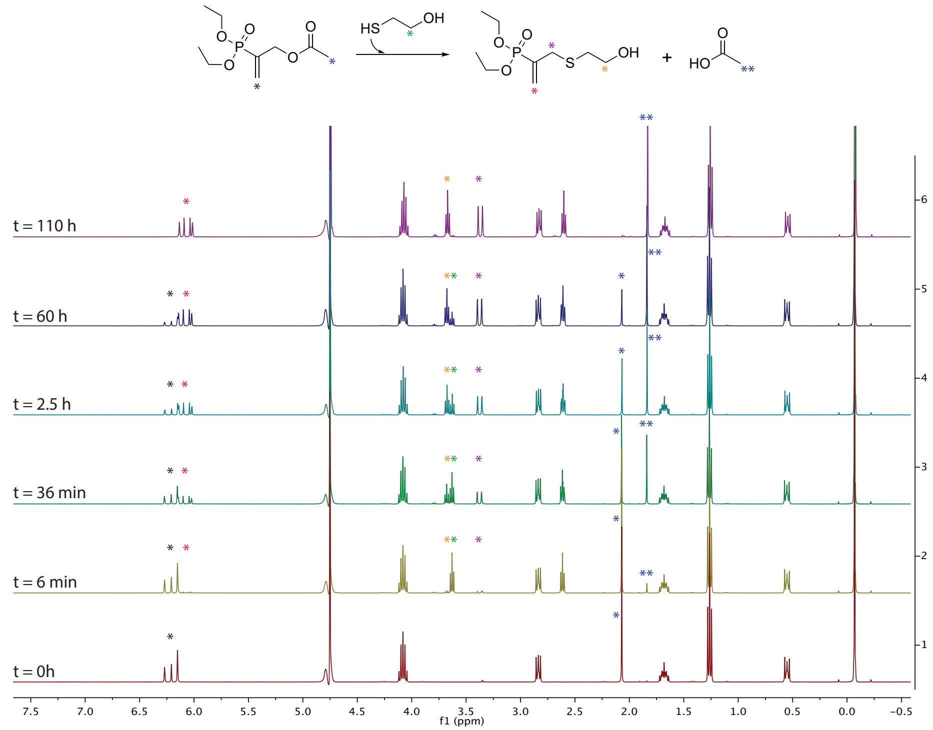

Figure S3: Reaction spectra of DVP with SH-**3** followed by ^{1}H NMR at different time points. The reaction was carried out in D_2O/phosphate buffer mixture 1:9 (0.1 M, pH = 7.4). The spectra were aligned with D_2O peak. The peak attributed to ~ 0.0 ppm corresponds to DSS internal standard.

DVP (4.0 mg, 17 µmol, 1.0 eq.) and DSS as internal standard (1.0 eq.) were dissolved in 0.1 mL D_2O/0.4 mL phosphate buffer (0.5 M, pH = 7.4). Then, NH_2-**4** (4.0 eq.) dissolved in 0.5 mL phosphate buffer (0.5 M, pH = 7.4) was added to the reaction mixture. The reaction was immediately followed by NMR until completion at t = 1104 hours.

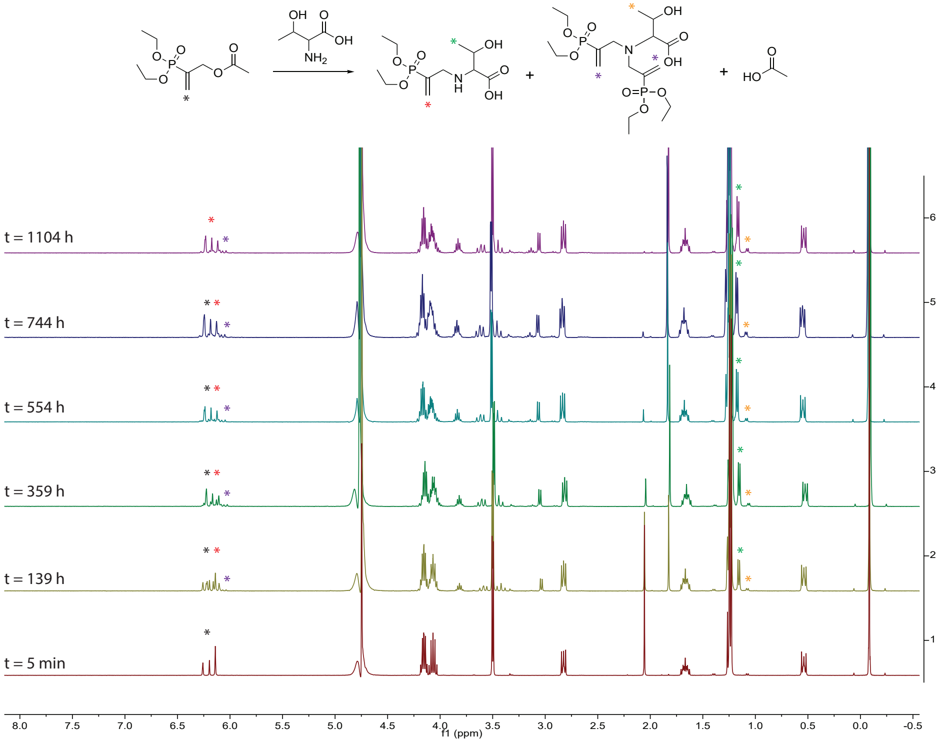

Figure S4: Reaction spectra of DVP with NH_2-**4** followed by ^1H NMR at different time points. The reaction was carried out in D_2O/phosphate buffer mixture 1:9 (0.5 M, pH = 7.4). The spectra were aligned with D_2O peak. The peak at ~ 0.0 ppm corresponds to DSS internal standard.

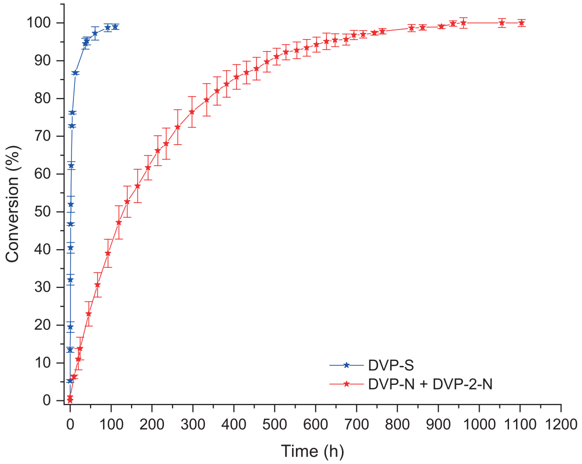

Figure S5: Conversion plot over time for the reaction of DVP (1.0 eq.) with SH-**3** (1.0 eq.) and DVP (1.0 eq.) with NH_2-**4** (4.0 eq.) in duplicate, respectively.

3.5.8.4 Thiol-addition conditions for signal-induced cycle – molecular study

DVP (10.0 mg, 42 µmol, 1.0 eq.) and DSS as internal standard (1.0 eq.) were dissolved in 0.1 mL D_2O/0.4 mL phosphate buffer (0.1 M, pH = 7.4). Then, t-Am-**1** or t-Am-**2** (0.2 eq.) dissolved in 0.5 mL phosphate buffer (0.1 M, pH = 7.4) were added to the reaction mixture to a total concentration of 8.5 mM of t-Am-**1** or t-Am-**2**. The reaction was immediately followed by ^{1}H NMR. Upon complete formation of intermediate (DVP–t-Am-**1** or DVP–t-Am-**2**), SH-**3** (0.2 eq.) in buffer was added to the solution and followed by ^{1}H NMR. Hereafter, sequential addition of thiol-signal was repeated three times until all DVP had been consumed.

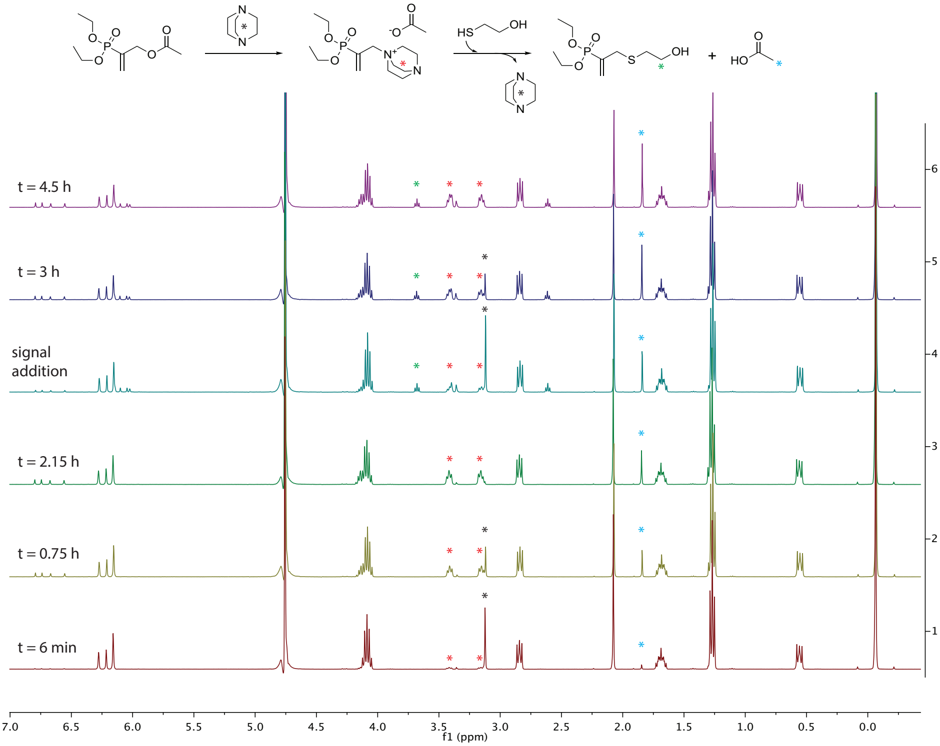

Figure S6: Reaction (signal-induced cycle) of DVP, t-Am-**1** with signal addition of SH-**3** followed by ^{1}H NMR at different time points. At t = 0 h: DVP and t-Am-**1** are added and followed by ^{1}H NMR upon complete formation of DVP–t-Am-**1** (t = 2.15 hours), then SH-**3** in equimolar amounts is added (signal addition) and the reaction is continuously followed by ^{1}H NMR until one full cycle was achieved (t = 4.5 hours). The reaction was carried out in D_2O/phosphate buffer mixture 1:9 (0.1 M, pH = 7.4). The spectra were aligned with D_2O peak. The peak at ~ 0.0 ppm corresponds to DSS internal standard.

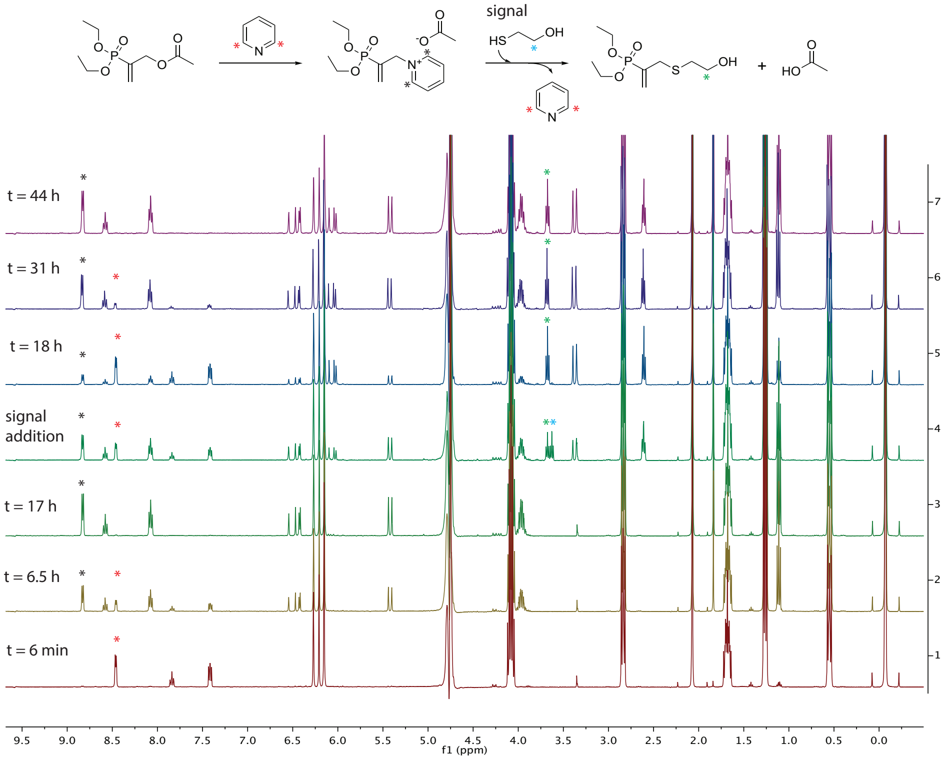

Figure S7: Reaction (signal-induced cycle) of DVP, t-Am-**2** with signal addition of SH-**3** followed by ^{1}H NMR at different time points. At t = 0 h: DVP and t-Am-**2** are added and followed by ^{1}H NMR upon complete formation of DVP-t-Am-2 (t = 17 hours), then SH-**3** in equimolar amounts is added (signal addition) and the reaction is continuously followed by ^{1}H NMR until one full cycle was achieved (t = 44 hours). The reaction was carried out in D_2O/phosphate buffer mixture 1:9 (0.1 M, pH = 7.4). The spectra were aligned with D_2O peak. The peak at ~ 0.0 ppm corresponds to DSS internal standard.

3.5.8.5 Amine-addition conditions for autonomous cycle – molecular study

The autonomous cycle reaction was subject to three conditions in which the DVP concentration was varied from 1.0 eq. to 4.0 eq. and NH_2-**4** from 2.0 eq. to 16.0 eq. at constant t-Am-**2** concentration (1.0 eq.), as follows in Table S2. Briefly, DVP, DSS as internal standard, t-Am-**2** and NH_2-**4** were dissolved in 0.1 mL D_2O/0.9 mL phosphate buffer 1:9 (0.5 M, pH = 7.4) and immediately followed by ^{1}H NMR.

Table S2: Autonomous cycle reactant data.

DVP (mg, mM)	DSS (mM)	t-Am-2 (mM)	NH_2-4 (mM)	DVP:t-Am-2:NH_2-4 (eq.:eq.:eq.)	Added NH_2-4 at Equilibrium (eq.)
2.0, 8.5	8.5	8.5	17.0	1.0:1.0:2.0	2.0
4.0, 17.0	17.0		34.0	2.0:1.0:4.0	4.0
8.0, 33.8	33.8		68.0	4.0:1.0:8.0	8.0

Upon observed reaction equilibrium, additional NH_2-**4** (2.0 eq., 4.0 eq. and 8.0 eq.) was added to the corresponding reaction mixture to drive the reaction to completion.

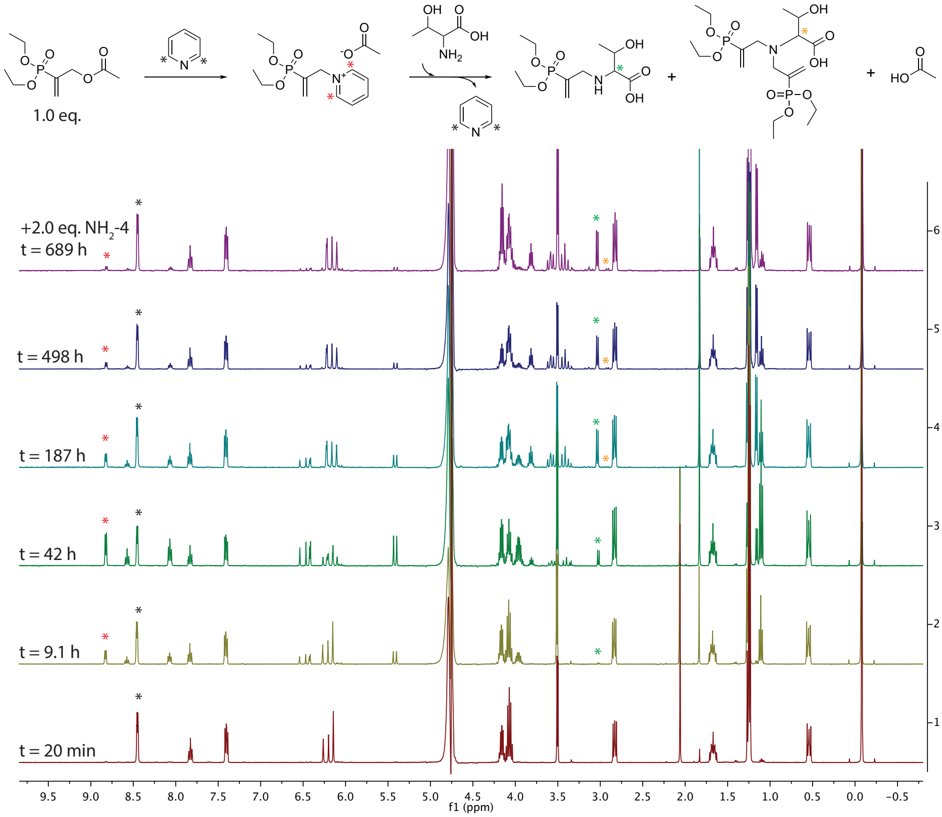

Figure S8: Reaction of DVP (1.0 eq.), t-Am-**2** (1.0 eq.) with NH_2-**4** (2.0 eq.) followed by ^{1}H NMR at different time points. The reaction was carried out in D_2O/phosphate buffer mixture 1:9 (0.5 M, pH = 7.4). The spectra were aligned with D_2O peak. The peak at ~ 0.0 ppm corresponds to DSS internal standard.

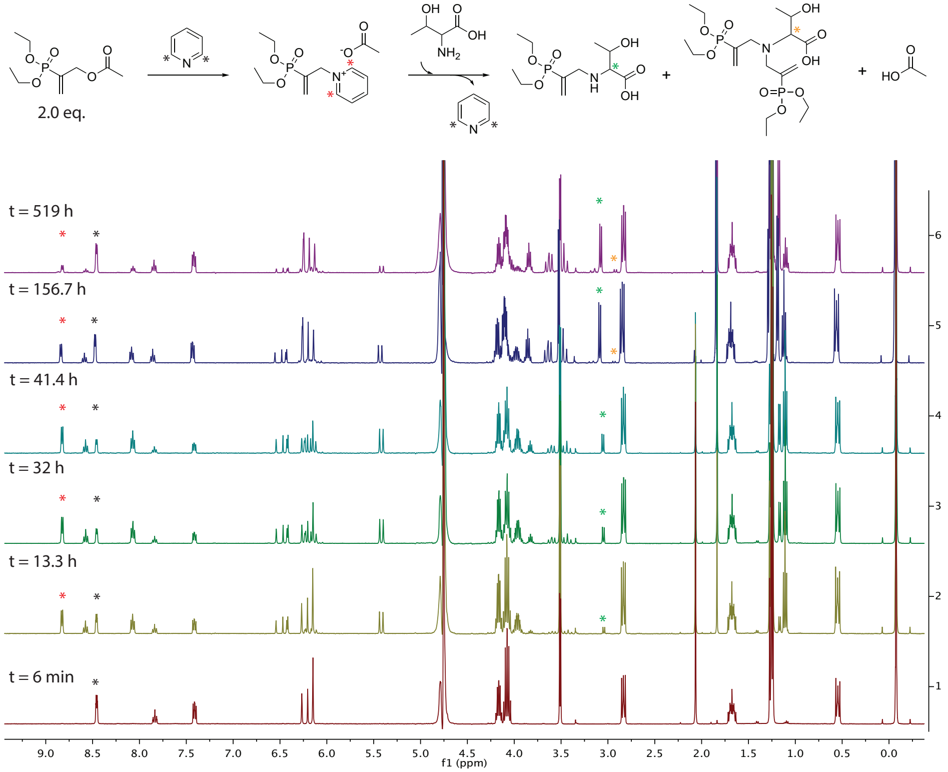

Figure S9: Reaction of DVP (2.0 eq.), t-Am-**2** (1.0 eq.) with NH_2-**4** (4.0 eq.) followed by ^1H NMR at different time points. The reaction was carried out in D_2O/phosphate buffer mixture 1:9 (0.5 M, pH = 7.4). The spectra were aligned with D_2O peak. The peak at ~ 0.0 ppm corresponds to DSS internal standard.

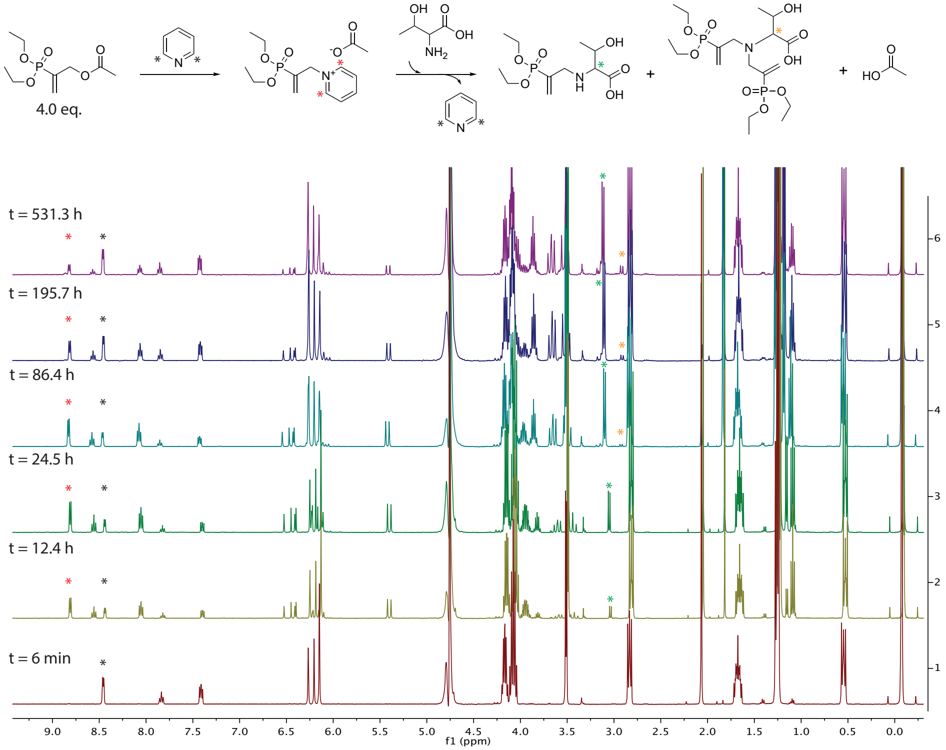

Figure S10: Reaction of DVP (4.0 eq.), t-Am-**2** (1.0 eq.) with NH_2-**4** (8.0 eq.) followed by ^1H NMR at different time points. The reaction was carried out in D_2O/phosphate buffer mixture 1:9 (0.5 M, pH = 7.4). The spectra were aligned with D_2O peak. The peak at ~ 0.0 ppm corresponds to DSS internal standard.

3.5.9 Micelle assembly - disassembly experiments

The signal-induced/autonomous cycle experiments for micelle assembly and disassembly were performed with reactant concentrations as described in 3.5.3 Micellar dispersions and DLS measurements. After addition of the reactants, the reaction mixture was vigorously stirred for 10 seconds and immediately followed by ^1H NMR.

3.5.9.1 Thiol-addition for signal-induced cycle – micelle study

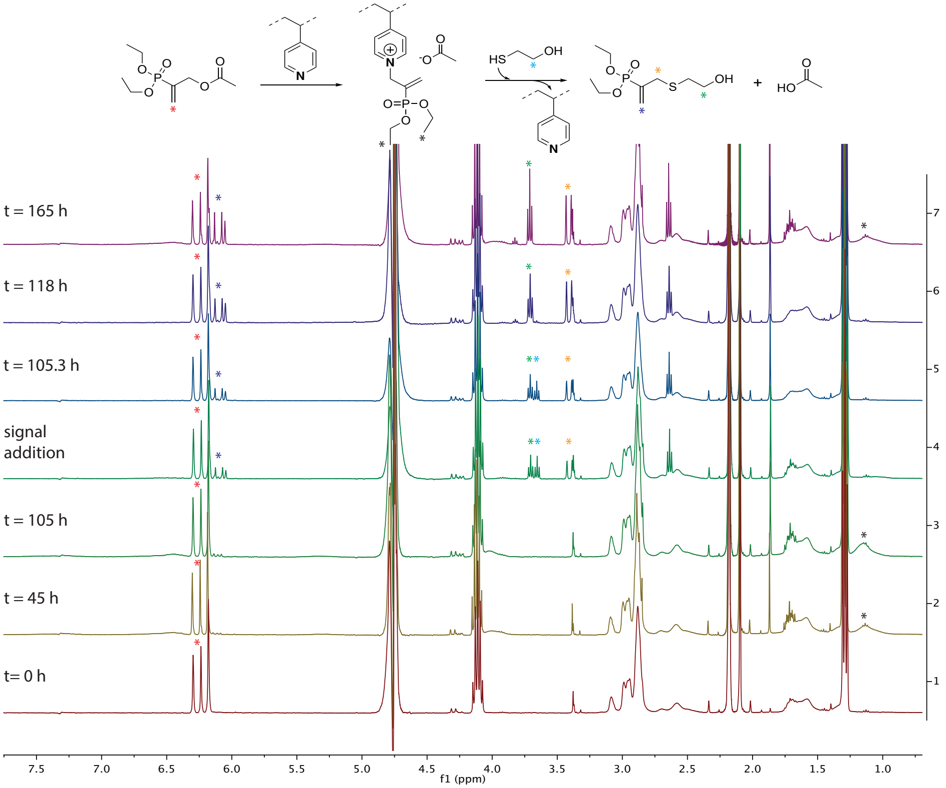

Figure S11: Reaction of DVP (3.2 eq.), P1 (1.0 eq. 4VP) with signal addition of SH-**3** followed by ^{1}H NMR at different time points. At t = 0: DVP and P1 are added and followed by ^{1}H NMR upon complete formation of DVP - polymer intermediate (t = 105 hours), then SH-**3** in equimolar amounts is added (signal addition) and the reaction is continuously followed by ^{1}H NMR until one full cycle is achieved (t = 165 hours). The reaction was carried out in D_2O/phosphate buffer mixture 1:9 (0.1 M, pH = 7.4). The spectra were aligned with the D_2O peak.

3.5.9.2 Amine-addition for autonomous cycle – micelle study

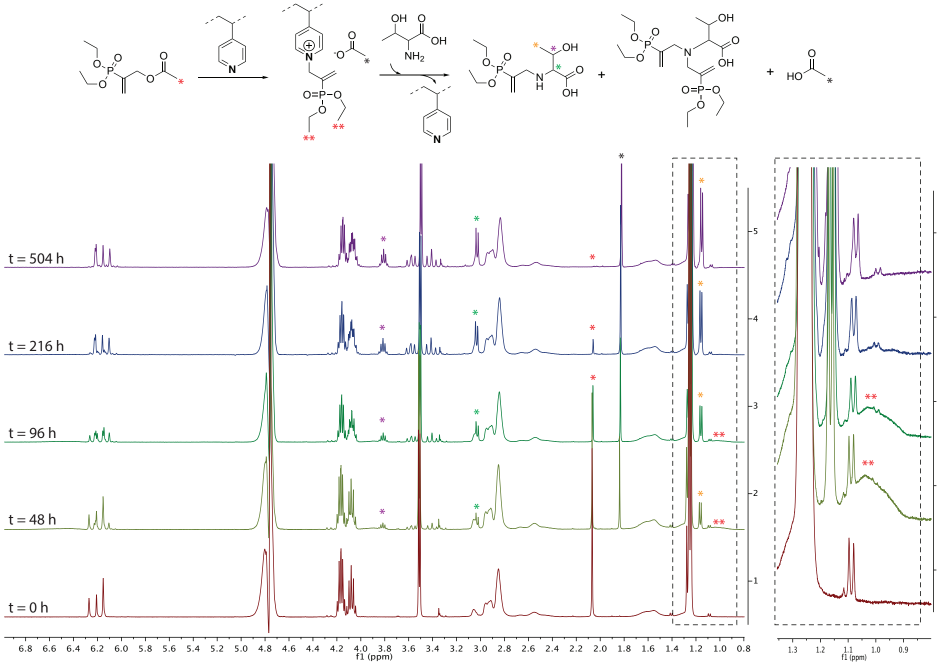

Figure S12: Reaction of DVP (2.0 eq.), P1 (1.0 eq. 4VP) with NH_2-**4** (8.0 eq.) followed by ^1H NMR at different time points. At t = 0: DVP, NH_2-4 and P1 are added and followed by ^1H NMR. One full cycle is achieved within 504 hours. The reaction was carried out in D_2O/phosphate buffer mixture 1:9 (0.5 M, pH = 7.4). The spectra were aligned with the D_2O peak.

3.5.10 DLS intensity and number% average for micelle assembly – disassembly

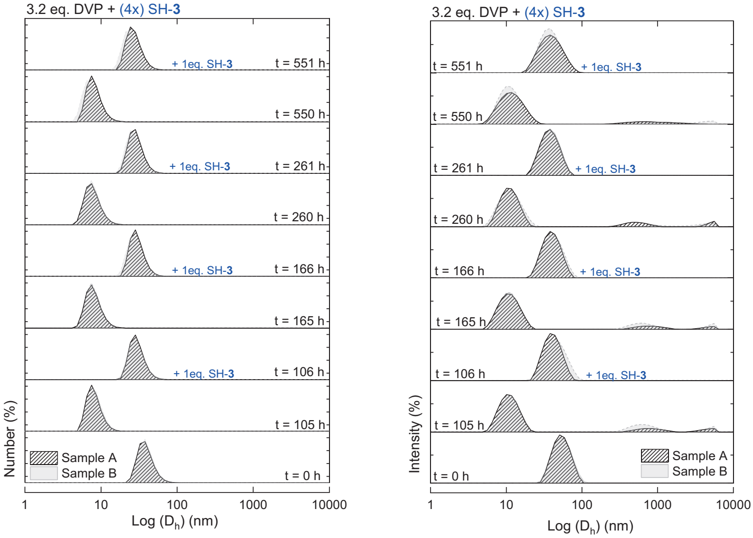

Figure S13: DLS data for signal-induced cycle (right) intensity plot over time with micellar size (nm) change upon signal addition (blue: 1.0 eq. SH-**3**), (left) number% average change over time upon signal addition. Measurements are shown in duplicate (Sample A&B).

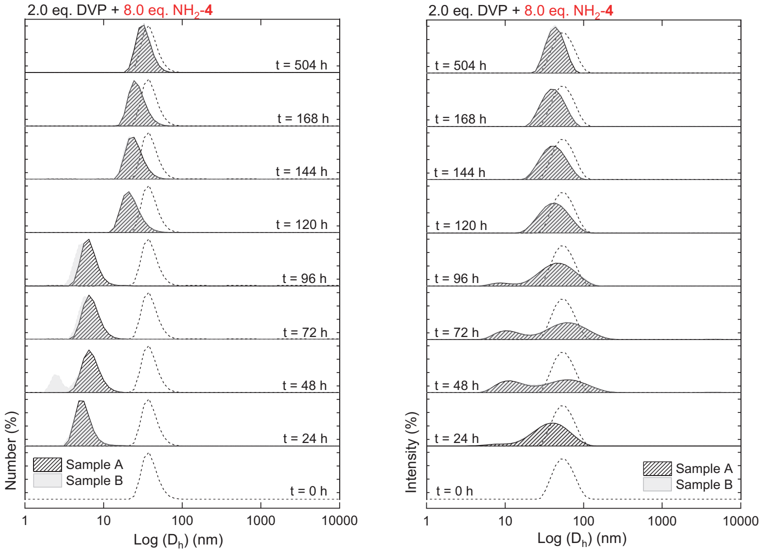

Figure S14: DLS data for autonomous cycle (right) intensity plot over time with micellar size (nm) change, (left) number% average change over time. Measurements are shown in duplicate (Sample A&B). The dotted line in the time measurements represents the t = 0 measurement and is shown for comparison.

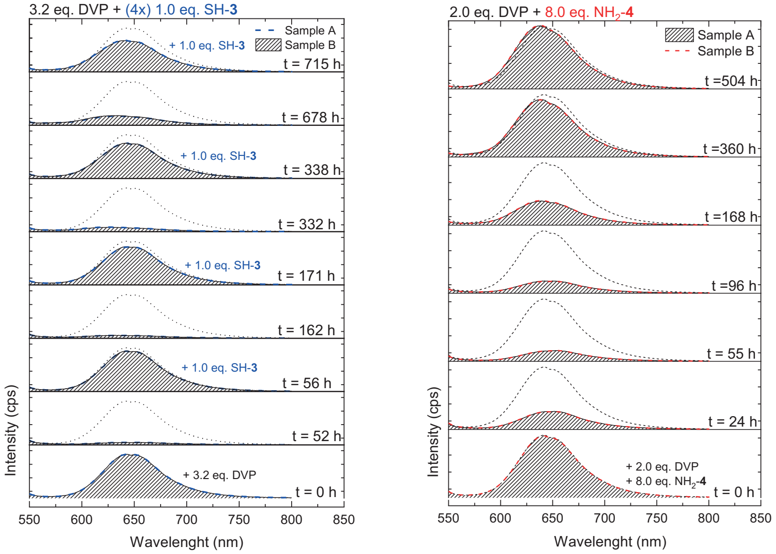

Figure S15: Fluorescence spectroscopy intensity plot for autonomous cycle (right) and signal-induced cycle (left) over time. Measurements are shown in duplicate (Sample A&B). The dotted line in the time measurements represents the t = 0 measurement and is shown for comparison.

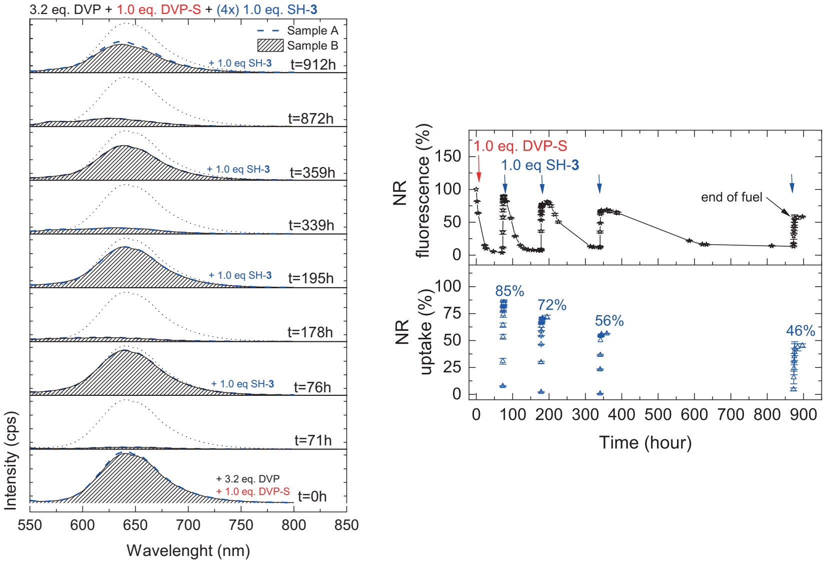

Figure S16: Fluorescence spectroscopy intensity plot for signal-induced cycle with 1.0 eq. of waste (DVP-S) added (right) and micellar (dis)assembly with corresponding dye uptake profile followed by NR fluorescence (left) at an excitation wavelength of 540 nm and an emission wavelength of 645 nm. Measurements are shown in duplicate (Sample A&B). The dotted line in the time measurements represents the t = 0 measurement and is shown for comparison.

3.5.11 Hydrogel swelling - de-swelling experiments

Hydrogels were swollen in buffer (0.1M, pH = 7.4) for 96 hours until equilibrium weight had been achieved. The equilibrium swelling percentage (equilibrium S%) was found by dividing the equilibrium swollen polymer W_s, by the weight of the oven dried polymer W_d, according to Eq.4.

$$equilibrium\ S\% = \frac{W_S - W_d}{W_d} * 100 \qquad \textbf{Eq.4}$$

The avg. equilibrium swelling percentage (equilibrium S%) was 1975 ± 165%, for all hydrogels used in this work. Water uptake and water loss, was calculated based on the weight difference between the equilibrium swollen hydrogels ($W_{equil.}$) and the time-observed hydrogels (W_t) and multiplied by 100. The S% (t) is the S% at each time point (t) minus the S% at t = 0, which was measured after equilibrium swelling had been achieved and corresponds to the weight measurement ($W_{t=0}$) before reactant addition. The weight average at $W_{equil.}$ is 0.84 g of water content for all observed hydrogels, while from $W_{equil.}$ to $W_{t=0}$ a std. deviation of ± 0.03 g of water was measured. Each hydrogel is normalized in reference to its equilibrium swollen state (defined as t=0) (Eq.5).

$$S\%\ (t) = \left(\frac{W_t - W_{equil.}}{W_{equil.}} * 100\right)_t - \left(\frac{W_{t=0} - W_{equil.}}{W_{equil.}} * 100\right)_{t=0} \qquad \textbf{Eq.5}$$

Hydrogels without added reactants (blank hydrogels) were submerged in 10 mL buffer. Their weight and photograph were taken at specific time points as stated for the hydrogels with added reactants. The non-fuelled hydrogels remained around starting values (Avg. S% = -6 ± 1.4%) for the entire observation time. The control with 2.0 eq. DVP, reached equilibrium after 240 h (Avg. S% = 187 ± 2.5%, from 240 h to 648 h).

3.5.11.1 Signal-induced hydrogel swelling and de-swelling

Equilibrium swollen hydrogels were placed in petri-dishes, weighed on a balance and photographed on top of millimetre paper (t = 0). Then, a stock solution of DVP (203.9 mg, 0.863 mmol) was prepared in 13.5 mL buffer (0.1 M, pH = 7.4). To each hydrogel (n=3) 4.2 mL of DVP stock solution (0.22 mmol, 1.0 eq.) was added (total reaction volume per hydrogel 5.2 mL). Time lapse photographs were taken every 24 hours until no further swelling was observed (t = 96 hours). Next, the remaining solution was removed using a pipette and stored. Hydrogels were dried, if necessary with paper tissue, before the weights of the swollen hydrogels were taken (W_t). After re-introduction of the stored solution, SH-**3** (1.0 eq.) prepared in buffer was added to the DVP-swollen hydrogels and again followed by taking every 24-hour photographs until no further de-swelling was observed (t = 192 hours). Hydrogels were then weighed without solution and photographed. The addition of DVP (1.0 eq.) for hydrogel swelling and the addition of SH-**3** (1.0 eq.) for de-swelling was repeated hereafter on the same hydrogels by using fresh stock solutions.

3.5.11.2 Autonomous hydrogel swelling and de-swelling

The conditions used in this experiment deviate from the previous procedure, since we optimized the reaction buffer and sterilized the hydrogels with sodium azide (0.02 wt%) against microbial growth before fuelling. Indeed, the availability of phosphates from buffer and a nitrogen source from amino acids provided favourable conditions for biological growth. Since the fuel reacts with sodium azide[1], we supplied extra fuel (additional 0.1 eq.) to the system, keeping in mind that sufficient DVP will be available (2.0 eq.) for the transient cycle (2.1 eq. DVP). Phosphate buffer at 0.1 M was chosen because of the good solvation properties of the material compared to 0.5 M, in which the polymers collapsed. Due to the decrease in buffer strength, however, we diluted the system to sustain consistent pH conditions. Equilibrium swollen hydrogels were placed in petri-dishes, weighted on a balance and photographed on top of millimetre paper (t = 0). Hereafter, a stock solution of NaN_3 (9.0 mg, 0.138 mmol) was prepared in 3.0 mL buffer (0.1 M, pH = 7.4, 1:9). To each hydrogel (n = 3), 1.0 mL of stock solution was added and the hydrogels were left for additional 24 hours. Next, stock solutions of DVP (326.7 mg, 1.38 mmol) in 30 mL buffer and NH_2-**4** (627.7 mg, 5.27 mmol) in 30 mL buffer were prepared. Three vials were then mixed with stock solutions (ratio NH_2-**4**:DVP:buffer = 10 mL:10 mL:13 mL) and shaken for 1 min before being added to the three hydrogels (total reaction volume per hydrogel = 35 mL). Time lapse photographs were taken every 24 hours for two hydrogels without solution and two hydrogels with solution. Hydrogel weights (W_t) were taken from two hydrogels every 24 hours. Note, that one hydrogel was left ‘undisturbed’ in the reaction mixture, meaning that the reaction solution was not removed for weighing purposes. This hydrogel was only photographed and compared to the ‘disturbed’ variants, for which the reaction mixture was removed for weighing and hereafter re-supplied.

3.5.12 Time-lapse observation for hydrogel experiments

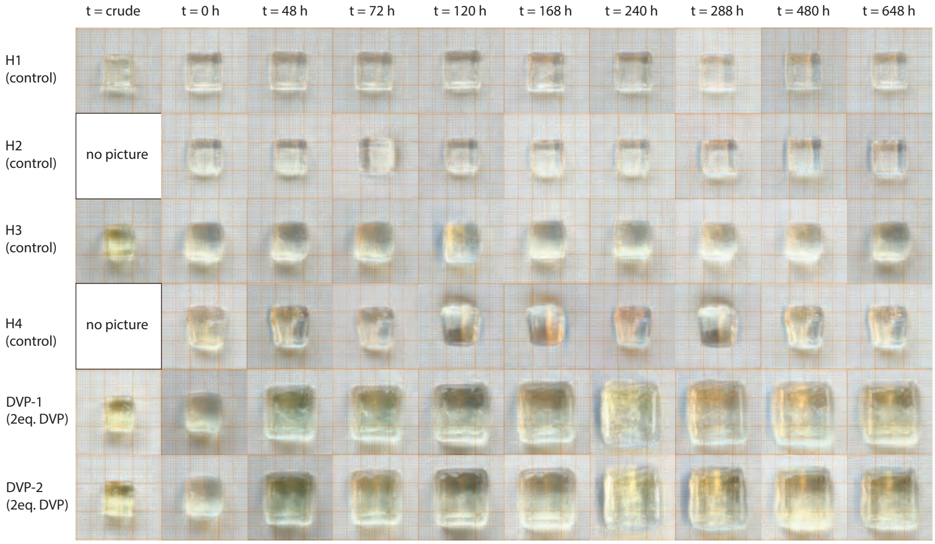

Figure S17: Photographs of hydrogels (H1 – H4, DVP 1-2) – crude hydrogels (out of the cast) and equilibrium swollen hydrogel state after t = 96 hours (t = 0). H1-H4 hydrogels were kept blank (no added reactants) and observed via photographs at different time points. DVP-1&2 (duplicate experiment) hydrogels were treated with DVP (2.0 eq.) at t = 0 and observed over time.

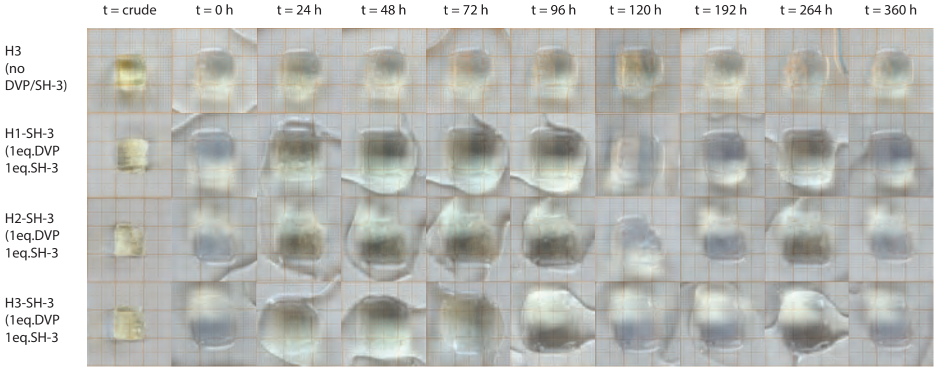

Figure S18: Photographs of hydrogels (H3, H1-SH-3 – H3-SH-3) - crude hydrogels (out of the cast) and equilibrium swollen hydrogel state after t = 96 hours in solution (t = 0). H3 hydrogel was kept blank (no added reactants) and observed via photographs at different time points. H1-SH-3 – H3-SH-3 (triplet experiment) hydrogels were treated with DVP (1.0 eq.) at t = 0 and observed over time in solution. At t = 96 hours, SH-3 (1.0 eq.) was added to the hydrogels. After de-swelling at t = 192 hours additional DVP (1.0 eq.) was added to the hydrogels. Then, after re-swelling at t = 264 hours, SH-3 (1.0 eq.) was added to de-swell the hydrogels with full de-swelling at t = 360 hours.

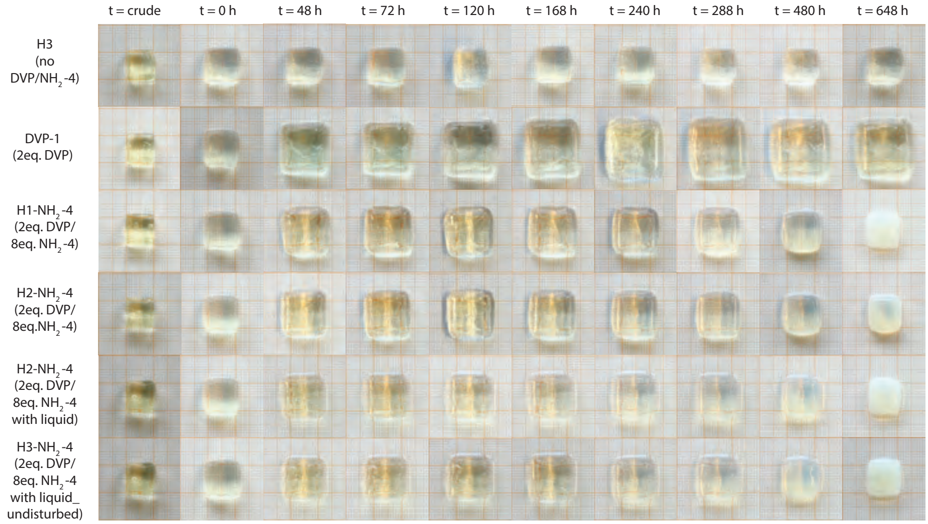

Figure S19: Photographs of hydrogels (H3, DVP-1 and H1 to H3-NH$_2$-4) - crude hydrogels (out of the cast) and equilibrium swollen hydrogel state after t = 96 hours (t = 0). H1 to H3-NH$_2$-4 hydrogels (triplet experiments) were treated with DVP (2.0 eq.) and NH$_2$-4 (8.0 eq.) at t = 0 and observed via photographs (no solution) at different time points. H3-NH$_2$-4 = photographs are with solution (undisturbed sample).

3.5.13 Synthesis procedures

3.5.13.1 Synthesis of p(4VP$_{58}$-b-DMA$_{261}$) – polymer for micelles (P1)

P1 was synthesised by a two-step RAFT polymerisation procedure (Scheme S1).

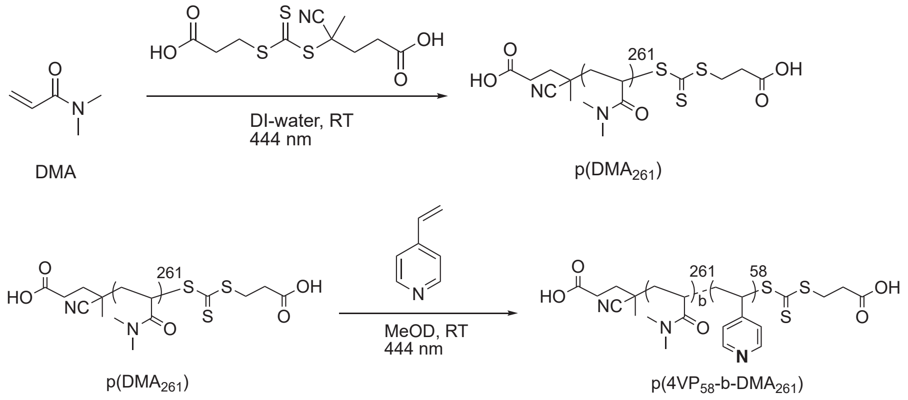

Scheme S1: Synthetic pathway for the preparation of P1 - p(4VP$_{58}$-b-DMA$_{261}$).

First, the water-soluble block (pDMA$_{261}$) was synthesised as follows. CETCPA (82.2 mg, 0.27 mmol), DMA (7.93 g, 80 mmol), DSS (21.3 mg, 0.10 mmol) and DI water (11.7 mL) were combined in a glass tube sealed with rubber septum.

The reaction mixture was deoxygenated by bubbling with argon for 30 minutes and placed into a LED reactor (444 nm). The reaction was quenched after 2 hours (87% conversion by ^{1}H NMR spectroscopy, $M_{n,conv}$ = 26.2 kDa) by removing the glass tube from the light source and opening to air. The polymer was then purified by dialysis using Spectra/por cellulose ester tubing (MWCO 500 – 1000 Da), followed by freeze drying to obtain a light-yellow powder.

p($4VP_{58}$-b) was then obtained by chain-extending $pDMA_{261}$ as follows. $pDMA_{261}$ (655 mg, 0.025 mmol), 4VP (210 mg, 2.0 mmol), DSS (2.0 mg, 0.01 mmol) and MeOD (1.0 mL) were combined and deoxygenated by bubbling with argon for 15 minutes. The solution was then injected into a degassed NMR tube sealed with a rubber septum and placed into the LED reactor (444 nm). The reaction was quenched after 17.5 h irradiation (72% conversion of 4VP by ^{1}H NMR spectroscopy) by removing the glass tube from the light source and opening to air. The polymer was then diluted with ethanol and twice precipitated into diethyl ether (125 mL).

Table S3. Polyamine block-copolymer synthesis and characterization data.

Polymer	**CTA**	**$[CTA]_0$: $[DMA]_0$: $[4VP]_0$**	**Reaction time (h)**	**NMR conv. (%)**	**Structure (code)**	**$M_{n,conv.}$ (kDa)**
$pDMA_{261}$	CETCPA	1:300:0	2.0	87 (DMA)	$pDMA_{261}$	26.2
P1	$pDMA_{261}$	1:0:80	18.0	72 (4VP)	p($4VP_{58}$-b-DMA_{261})	32.3

Table S4. Polyamine block-copolymer GPC data.

Polymer	**$M_{n,conv}$ (kDa)**	**$M_{n,GPC}$ (kDa)**	**$Đ$**
$pDMA_{261}$	26.2	28.5	1.14
P1	32.3	29.7	1.23

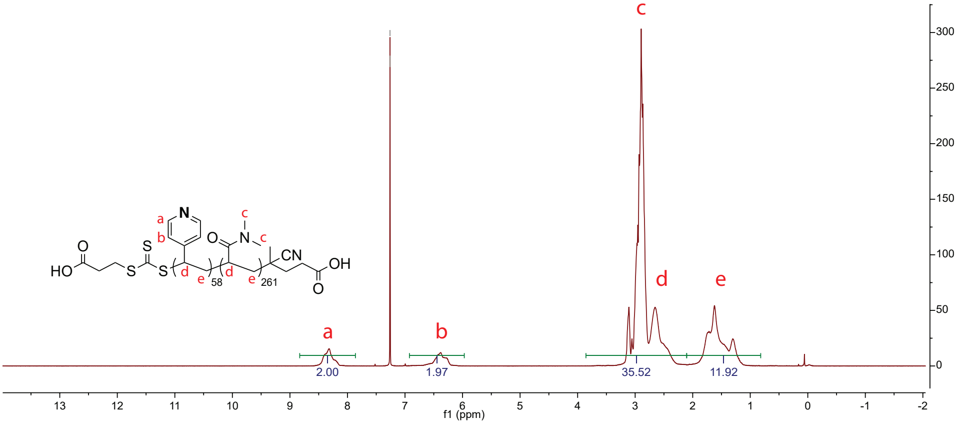

Figure S20: ^{1}H NMR ($CDCl_3$) of P1 demonstrating good (±10%) agreement between polymer structure determined by ^{1}H NMR conversion and ratio of p(4VP) aromatic signals to polymer backbone. $\int c+d_{th} = [6 \cdot (261) + 1 \cdot (58 + 261)] / 58 = 32.5$; $\int e_{th} = (2) \cdot (261 + 58) / 58 = 11.0$.

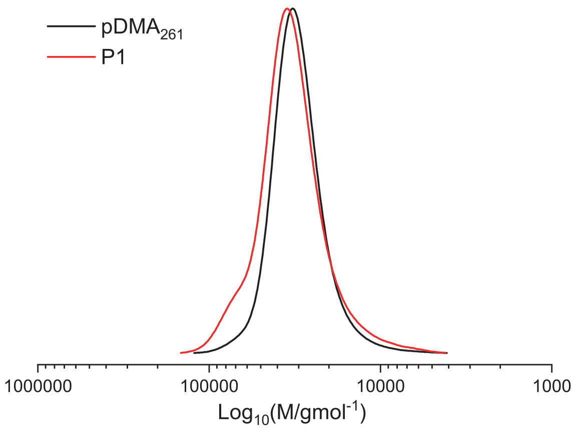

Figure S21: GPC traces of $pDMA_{261}$ and chain extended polyamine copolymer P1.

3.5.13.2 Synthesis of p($4VP_{28}$-stat-DMA_{55}) – P2 precursor used for hydrogel preparation

p($4VP_{28}$-stat) was synthesised by copolymerising 4VP and DMA, according to Scheme S2.

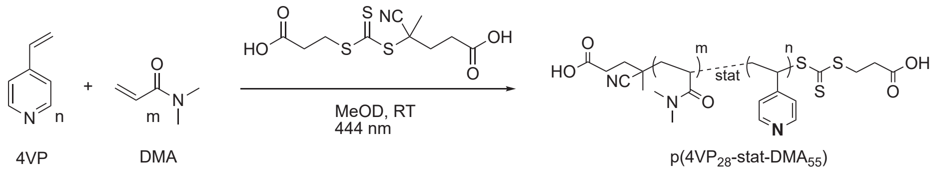

Scheme S2: Synthetic pathway for the preparation of p($4VP_{28}$-stat).

CETCPA (82 mg, 0.27 mmol), 4VP (820 mg, 7.80 mmol), DMA (2.40 g, 24.2 mmol) and DMSO (4.5 mL) were combined, chilled in an ice bath, and deoxygenated by bubbling with argon for 30 minutes. The solution was then irradiated in the LED reactor (444 nm) for 45 h, reaching 96% conversion of 4VP and 61% conversion of DMA by ^{1}H NMR spectroscopy. The polymer was isolated by twice precipitation into diethyl ether followed by drying in a vacuum oven.

Table S5. Polyamine copolymer synthesis and characterization data.

Polymer	CTA	$[CTA]_0$:$[DMA]_0$:$[4VP]_0$	Reaction time (h)	NMR conv. (%)	Structure	$M_{n,conv.}$ (kDa)
p($4VP_{28}$-stat)	CETCPA	1:90:30	45.0	61 (DMA) 96 (4VP)	p($4VP_{28}$-stat-DMA_{55})	8.8

Table S6. Polyamine block-copolymer GPC data.

Polymer	$M_{n,conv}$ (kDa)	$M_{n,GPC}$ (kDa)	Đ
p($4VP_{28}$-stat)	8.8	6.3	1.31

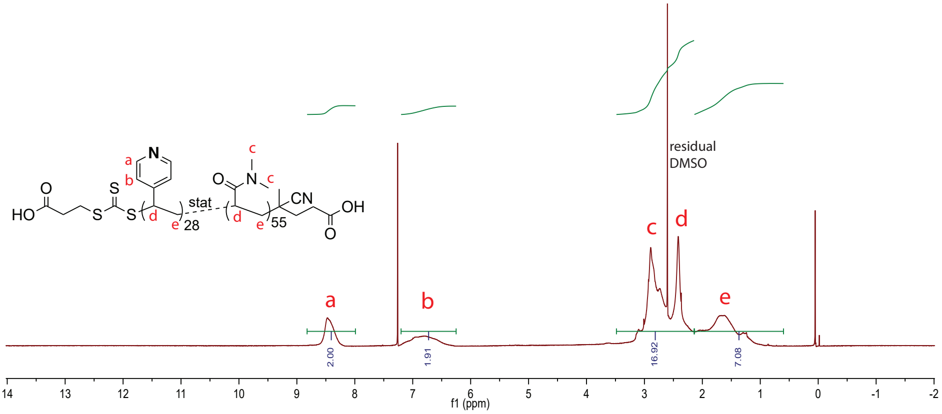

Figure S22: ^{1}H NMR ($CDCl_3$) of p($4VP_{28}$-stat) demonstrating good (±10%) agreement between polymer structure determined by ^{1}H NMR conversion and ratio of p(4VP) aromatic signals to polymer backbone. $\int c{+}d_{th} = [6 \cdot (55) + 1 \cdot (28 + 55)] / 28 = 14.75$; $\int e_{th} = [2 \cdot (55 + 28) / 28 = 5.9$.

3.5.13.3 Synthesis of diethyl(α-acetoxymethyl) vinylphosphonate (DVP)

DVP is a known compound and was synthesized following reported procedures[2,3]. Briefly, a mixture of tetraethyl methylene diphosphonate (TMP, 20.0 g, 69.4 mmol) in aqueous para-formaldehyde (30%, 50 mL) was heated under reflux. A solution of potassium carbonate (9.2 g, 138.8 mmol in 30 mL of H_2O) was slowly added over a period of 3 hours via a syringe pump. After cooling to room temperature, the reaction mixture was extracted with chloroform (5x 50 mL), washed with brine (2x 50 mL) and dried with Na_2SO_4. Then, the reaction mixture was concentrated under reduced pressure and the residue was subjected to vacuum distillation to afford diethyl (3-hydroxy-2-propenyl)phosphonate (HYP, 10.1 g, 75%) bp: 95 – 105 °C (0.001 torr) as a colourless oil.

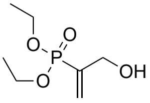

^{1}H NMR (400 MHz, $CDCl_3$) δ: 6.09 (d, *J* = 2.7 Hz, 1H), 6.01 (d, *J* = 20.0 Hz, 1H), 4.30 (d, *J* = 10.7 Hz, 2H), 4.20 – 4.00 (m, 4H), 2.30 (s, 1H), 1.33 (t, *J* = 7.0 Hz, 6H). **^{13}C NMR** (100.5 MHz, $CDCl_3$) δ: 140.0, 138.3, 128.9 (d, J = 7.2 Hz), 62.6 (d, J = 16.0 Hz), 62.3, 16.4 (d, J = 6.4 Hz). **^{31}P NMR** (161.9 MHz, $CDCl_3$) δ: 17.6 ppm. **MS** (ESI+) m/z: 195.06 (M+H) (expected m/z: 195.07).

To a cooled (0°C) solution of this phosphonate (6.0 g, 30.1 mmol), DMAP (0.227 g, 1.85 mmol) and Et_3N (6.46 mL, 46.35 mmol, 1.5 eq.) in dichloromethane (10 mL) was added dropwise a solution of acetic anhydride (3.21 mL, 34.0 mmol) in dichloromethane (100 mL) and the mixture was stirred at room temperature for 3 h. The reaction mixture was then washed with 15% Na_2CO_3 (2x 100 mL) until pH 9, with 5% HCl (pH 2) and brine before it was dried with Na_2SO_4. Then, the reaction mixture was concentrated under reduced pressure and the residue was purified by flash chromatography (ethyl acetate/methanol, 95:5) to furnish diethyl(α-acetoxymethyl) vinylphosphonate as a colourless oil (DVP, 6.1 g, 84%).

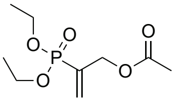

^{1}H NMR (400 MHz, $CDCl_3$) δ: 6.19 (dt, J = 22.4, 1.4 Hz, 1H), 6.01 (dt, J = 45.8, 1.6 Hz, 1H), 4.72 (dt, J = 8.9, 1.5 Hz, 2H), 4.23 – 3.93 (m, 4H), 2.09 (d, J = 1.3 Hz, 3H), 1.32 (t, J = 7.1, 1.3 Hz, 6H). **^{13}C NMR** (100.5 MHz, $CDCl_3$) δ: 170.3, 135.6, 133.8, 131.1 (d, J = 7.0 Hz), 63.1, 62.9, 62.3 (d, J = 5.7 Hz), 20.9, 16.4 (d, J = 6.3 Hz). **^{31}P NMR** (161.9 MHz, $CDCl_3$) δ: 15.9 ppm. **MS** (ESI+) m/z: 237.07 (M+H) (expected m/z: 237.08).

3.5.13.4 Synthesis of 1-(2-(diethoxyphosphoryl)allyl)-1,4diazabicyclo [2.2.2]octanium chloride (DVP-t-Am-**1**)

To a solution of DVP (20 mg, 85 µmol, 1.1 eq.) in 1.0 mL D_2O was added (1,4-diazabicyclo[2.2.2]octane) (t-Am-**1**, 1.0 eq.) and shaken for 10 min. The reaction progress was monitored by NMR. After the completion of the reaction, the mixture was extracted with chloroform. Hereafter, a few drops of 1 M HCl were added and then the mixture was extracted with chloroform (3x, 1 mL) again. The water layer was freeze dried to afford 1-(2-(diethoxyphosphoryl)allyl)-1,4-

diazabicyclo[2.2.2]octanium chloride (DVP-t-Am-**1**) as colourless, hydroscopic oil (17 mg, 62%).

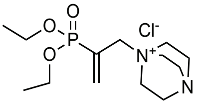

^{1}**H NMR** (400 MHz, DMSO-d_6) δ: 6.65 (d, J = 20.4 Hz, 1H), 6.57 (d, J = 3.0 Hz, 1H), 4.17 (d, J = 16.0 Hz, 2H), 4.12 – 4.01 (m, 4H), 3.39 (t, J = 7.4 Hz, 6H), 3.05 (t, J = 7.4 Hz, 6H), 1.28 (t, J = 7.0 Hz, 6H). ^{13}**C NMR** (100.5 MHz, DMSO-d_6) δ: 145.4 (d, J = 6.8 Hz), 62.9 (d, J = 13.7 Hz), 62.5 (d, J = 6.2 Hz), 52.1, 44.7, 16.1 (d, J = 6.0 Hz). ^{31}**P NMR** (161.9 MHz, DMSO-d_6) δ: 15.3 ppm. **MS** (ESI+) m/z: 289.18 (M-Cl) (expected m/z: 289.17).

3.5.13.5 Synthesis of 1-(2-(diethoxyphosphoryl)allyl)pyridinium chloride (DVP-t-Am-**2**)

To a solution of DVP (20 mg, 85 µmol, 1.1 eq.) in 1.0 mL D_2O was added pyridine (t-Am-**2**, 1.0 eq.) and shaken for 10 min. The reaction progress was monitored by NMR. After the completion of the reaction, the product was isolated by extraction with chloroform. Hereafter, few drops of 1 M HCl were added and then the mixture was extracted with chloroform (3x, 1 mL) again. The water layer was freeze dried to afford 1-(2-(diethoxyphosphoryl)allyl)pyridinium chloride (DVP-t-Am-**2**) as colourless, hydroscopic oil (16 mg, 65%).

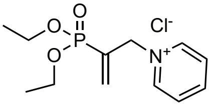

^{1}**H NMR** (400 MHz, DMSO-d_6) δ: 9.15 (d, J = 5.2 Hz, 2H), 8.69 (t, J = 7.8 Hz, 1H), 8.35 – 8.09 (m, 2H), 6.45 (d, J = 44.0 Hz, 1H), 6.30 (d, J = 20.9 Hz, 1H), 5.59 (d, J = 13.8 Hz, 2H), 3.99 – 3.84 (m, 4H), 1.12 (t, J = 7.1 Hz, 6H). ^{13}**C NMR** (100.5 MHz, DMSO-d_6) δ: 146.5, 145.4, 137.5 (d, J = 7.6 Hz), 133.9, 132.1, 128.0, 62.1 (d, J = 5.8 Hz), 61.2 (d, J = 12.4 Hz), 15.9 (d, J = 6.1 Hz).^{31}**P NMR** (161.9 MHz, DMSO-d_6) δ: 14.4 ppm. **MS** (ESI+) m/z: 256.10 (M-Cl) (expected m/z: 256.11).

3.5.13.6 Synthesis of 3-(2-hydroxyethylsulfanyl)prop-1-en-2 ylphosphonate (DVP-S)

To a solution of DVP (20 mg, 85 µmol, 1.0 eq.) in D_2O/phosphate buffer 1:9 (0.1 M, pH = 7.4) mixture was added t-Am-**1** (17 µmol, 0.2 eq.) and SH-**3** (93 µmol, 1.1 eq.) and the mixture was stirred at RT overnight. After lyophilization, the crude was purified by flash chromatography (ethyl acetate/methanol, 95:5) to furnish diethyl 3-(2-hydroxyethylsulfanyl)prop-1-en-2-ylphosphonate (DVP-S) as a colourless oil (16 mg, Yield: 74%).

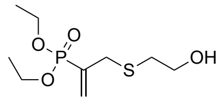

^{1}H NMR (400 MHz, $CDCl_3$) δ: 6.06 (d, *J* = 1.2 Hz, 1H), 6.03 (d, *J* = 67.6 Hz, 0H), 4.26 – 3.98 (m, 4H), 3.74 (t, *J* = 6.5 Hz, 2H), 3.40 (d, *J* = 13.3 Hz, 2H), 2.86 (s, 1H), 2.69 (t, *J* = 5.8 Hz, 2H), 1.33 (t, *J* = 7.1 Hz, 6H). **^{13}C NMR** (100.5 MHz, $CDCl_3$) δ: 137.1, 135.3, 131.3 (d, *J* = 8.8 Hz), 62.4 (d, *J* = 5.7 Hz), 60.6, 35.2, 33.2 (d, *J* = 13.7 Hz), 16.5 (d, *J* = 6.3 Hz). **^{31}P NMR** (161.9 MHz, $CDCl_3$) δ: 17.6 ppm. **MS** (ESI+) m/z: 255.08 (M+H) (expected m/z: 254.07).

3.5.13.7 Synthesis of 2-((2-(diethoxyphosphoryl)allyl)amino)-3-hydroxybutanoic acid (DVP-N)

To a solution of DVP (20 mg, 85 µmol, 1.0 eq.) in D_2O/phosphate buffer 1:9 (0.1 M, pH = 7.4) mixture was added t-Am-**1** (17 µmol, 0.2 eq.) and NH_2-**4** (85 µmol, 1.0 eq.) and the mixture was stirred at RT for 4 days. After lyophilization, the crude was solubilized in EtOAc and filtered. 2-((2-(diethoxyphosphoryl)allyl)amino)-3-hydroxybutanoic acid (DVP-N) was obtained by recrystallization in EtOAc as a white solid (15 mg, Yield: 60%).

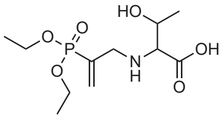

^{1}H NMR (400 MHz, methanol-d_4) δ: 6.39 (d, J = 5.4 Hz, 1H), 6.31 (d, J = 18.6 Hz, 1H), 4.31 – 4.06 (m, 4H), 4.04 – 3.97 (m, 1H), 3.97 – 3.76 (m, 2H), 3.30 (s, 1H), 1.39 (t, J = 3.7 Hz, 6H), 1.37 (t, J = 1.7 Hz, 3H). **^{13}C NMR** (100.5 MHz, methanol-d_4) δ: 171.6, 137.3 (d, J = 7.5 Hz), 132.3 (d, J = 180.8 Hz), 69.8, 67.4, 64.6 (dd, J = 6.2, 3.2 Hz), 21.4, 16.6 (d, J = 5.9 Hz). **^{31}P NMR** (161.9 MHz, MeOD) δ: 16.1. **MS** (ESI+) m/z: 296.14 (M+H) (expected m/z: 296.27).

3.5.14 NMR spectra

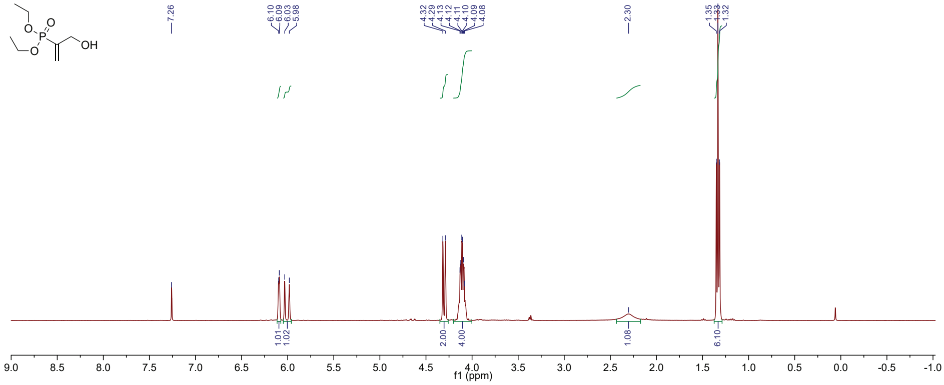

Figure S23: ^{1}H NMR, HYP in $CDCl_3$.

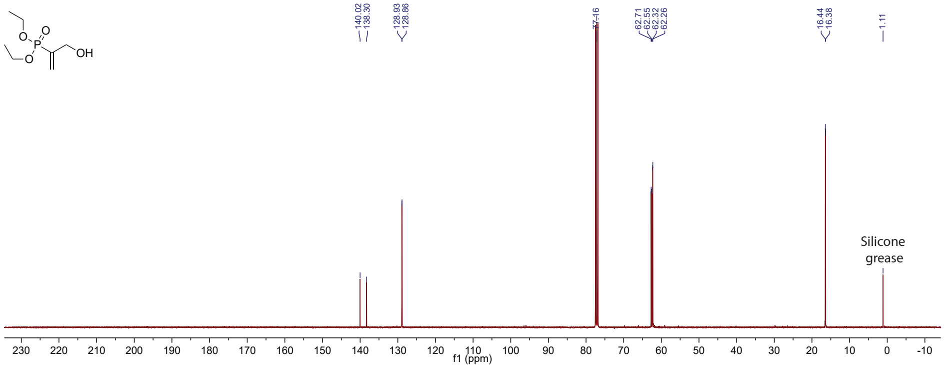

Figure S24: ^{13}C NMR, HYP in $CDCl_3$.

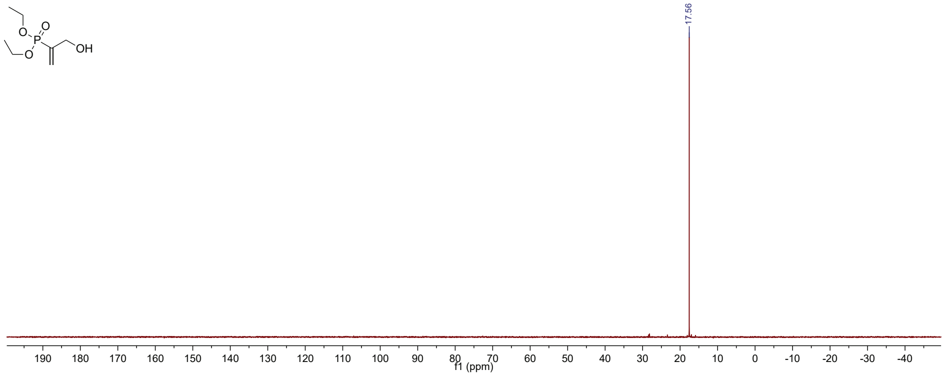

Figure S25: ^{31}P NMR, HYP in $CDCl_3$.

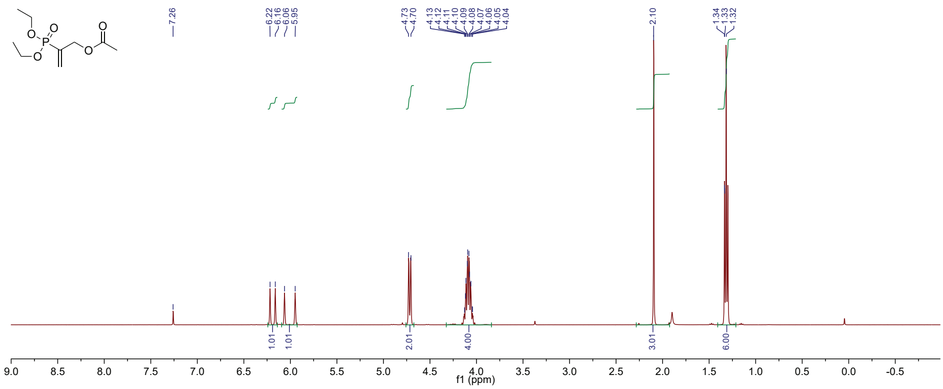

Figure S26: ^{1}H NMR, DVP in $CDCl_3$.

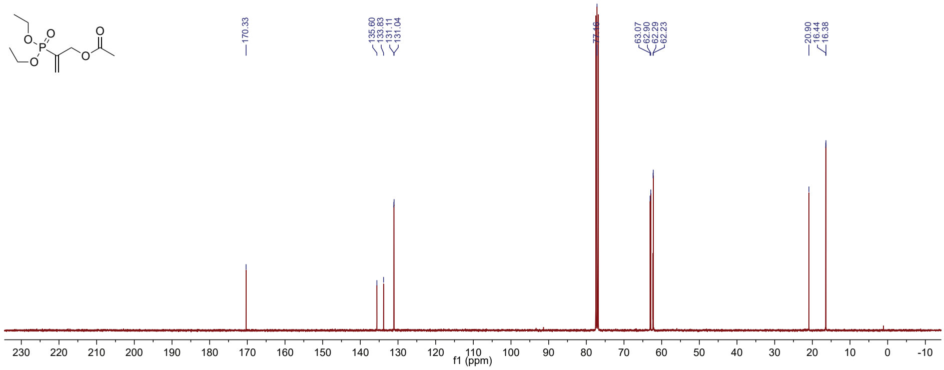

Figure S27: ^{13}C NMR, DVP in $CDCl_3$.

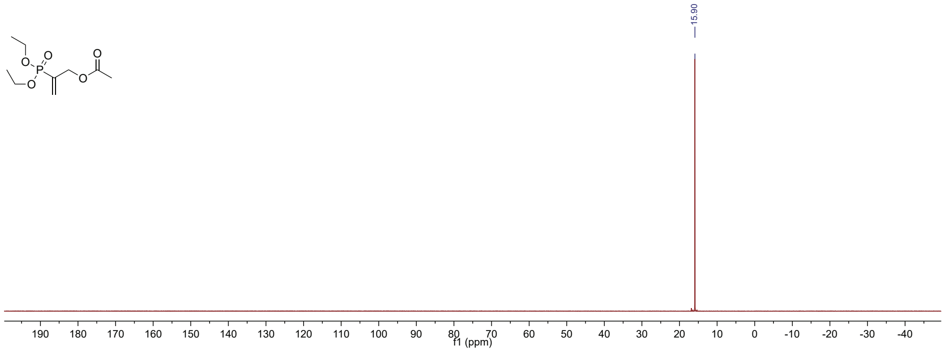

Figure S28: ^{31}P NMR, DVP in $CDCl_3$.

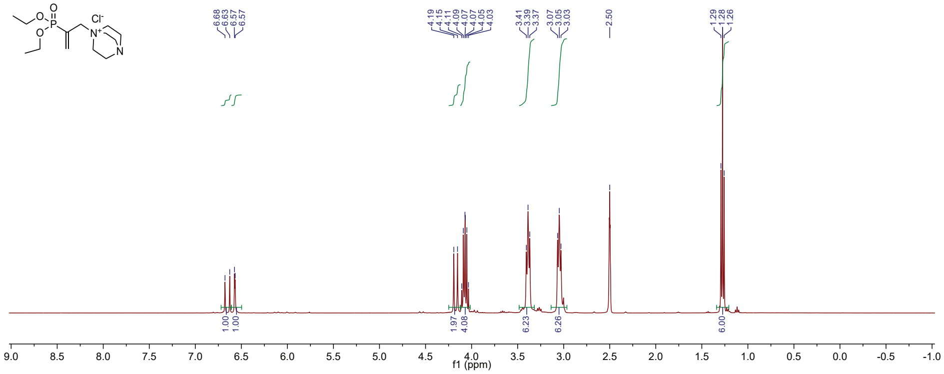

Figure S29: ^{1}H NMR, DVP-t-Am-1 in DMSO-d$_6$.

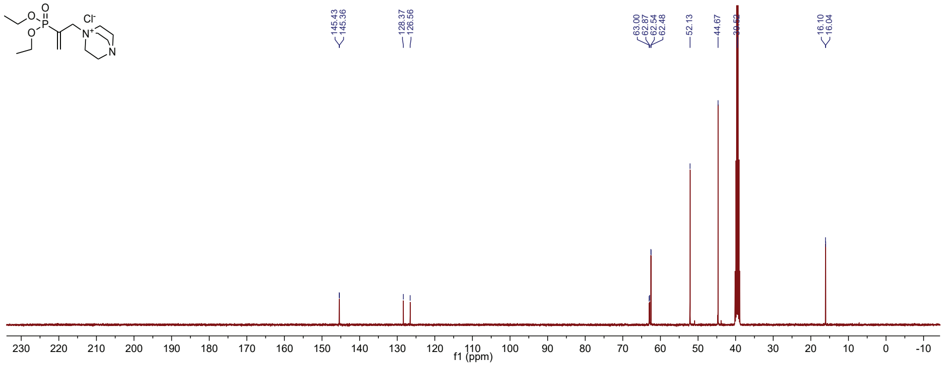

Figure S30: ^{13}C NMR, DVP-t-Am-1 in DMSO-d$_6$.

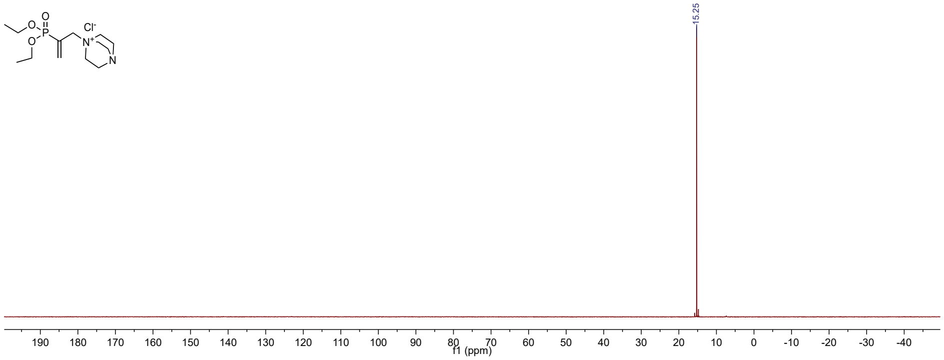

Figure S31: ^{31}P NMR, DVP-t-Am-1 in DMSO-d$_6$.

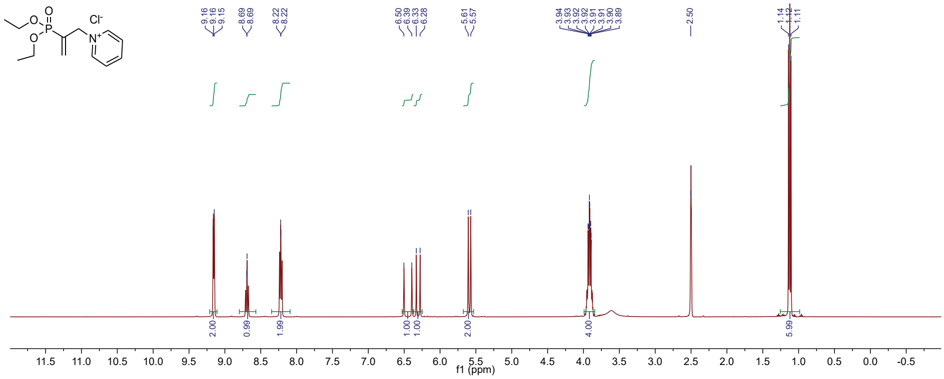

Figure S32: ^{1}H NMR, DVP-t-Am-2 in DMSO-d$_6$.

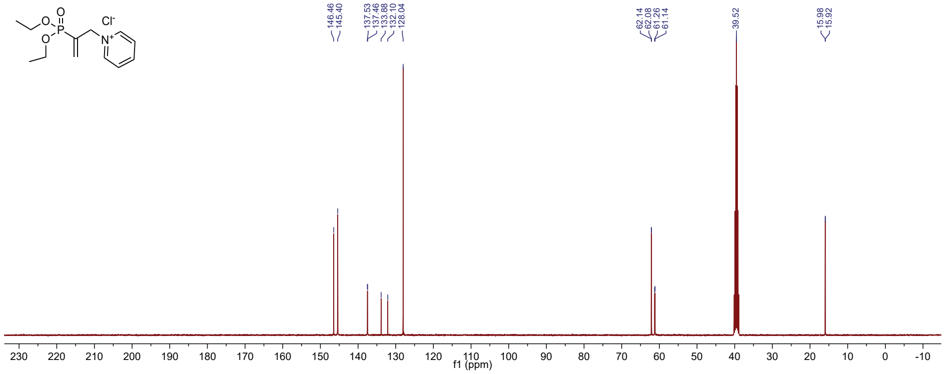

Figure S33: ^{13}C NMR, DVP-t-Am-2 in DMSO-d$_6$.

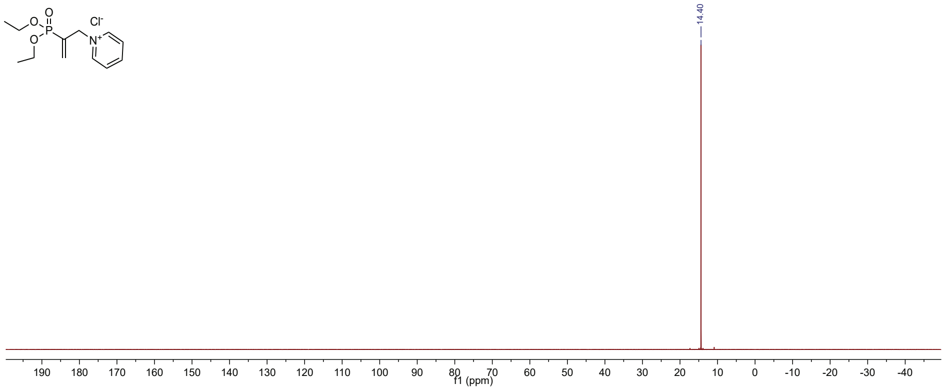

Figure S34: ^{31}P NMR, DVP-t-Am-2 in DMSO-d$_6$.

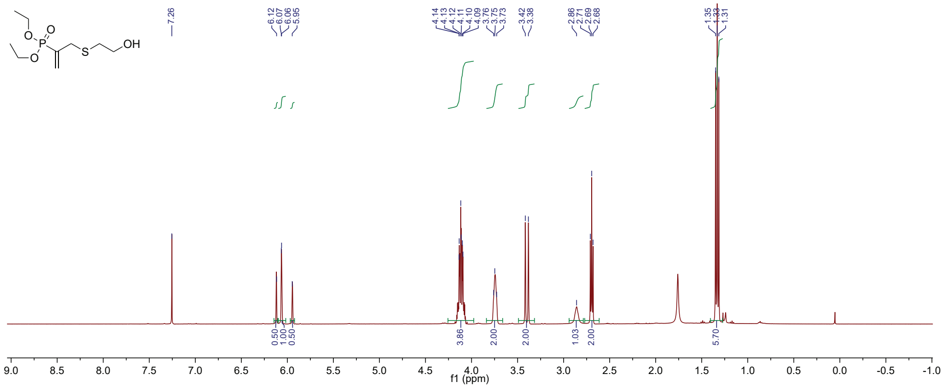

Figure S35: ^{1}H NMR, DVP-S in $CDCl_3$.

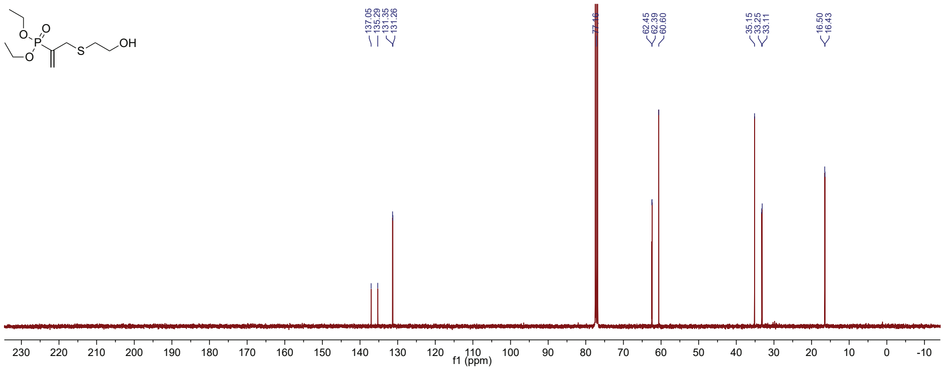

Figure S36: ^{13}C NMR, DVP-S in $CDCl_3$.

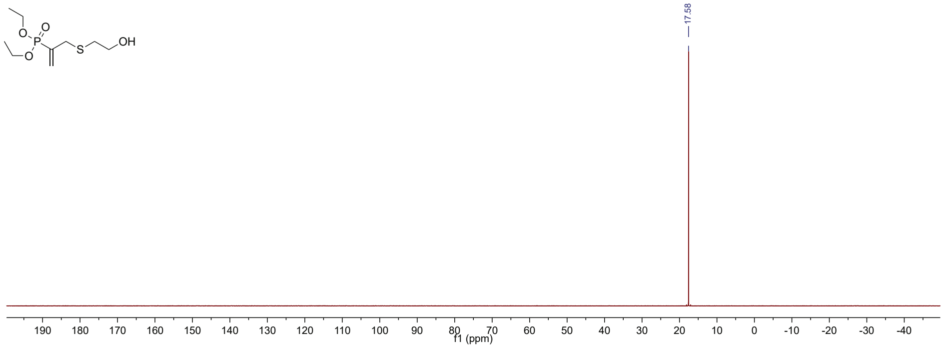

Figure S37: ^{31}P NMR, DVP-S in $CDCl_3$.

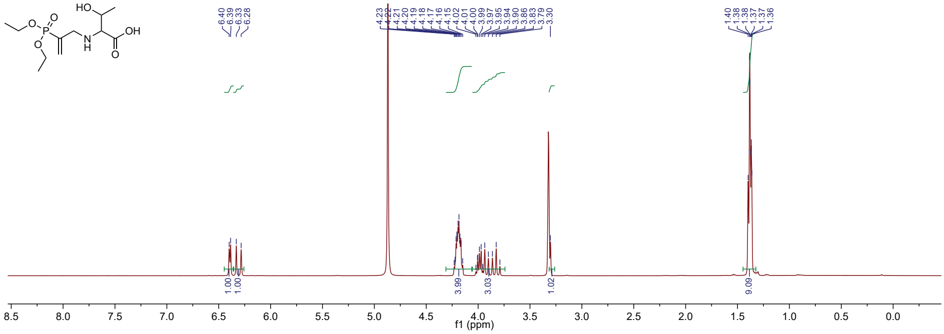

Figure S38: ^{1}H NMR, DVP-N in methanol-d$_4$.

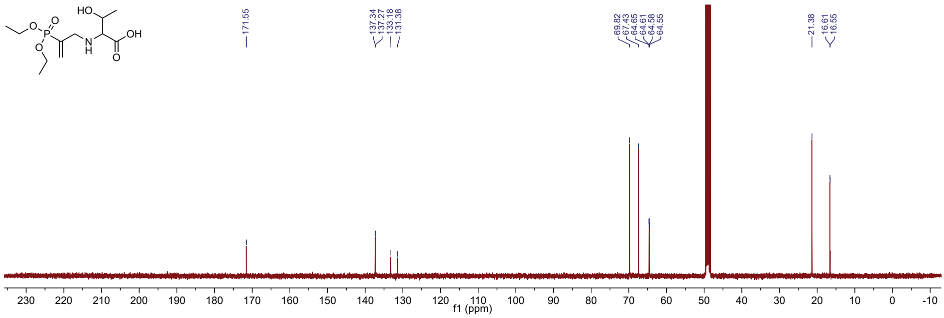

Figure S39: ^{13}C NMR, DVP-N in methanol-d$_4$.

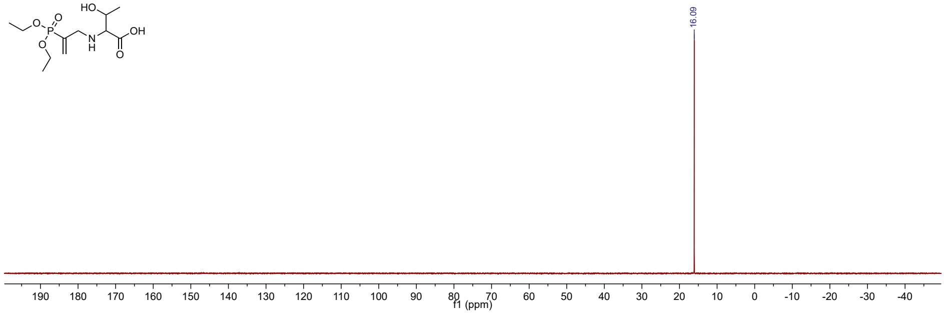

Figure S40: ^{31}P NMR, DVP-N in methanol-d$_4$.

3.5.15 2D NMR spectra

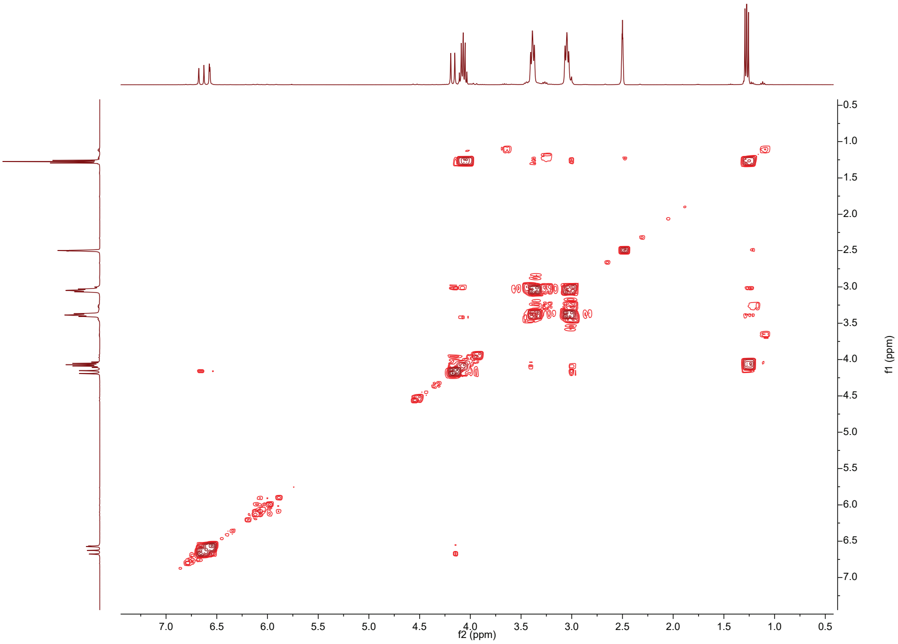

Figure S41: gCOSY NMR, DVP-t-Am-1 in DMSO-d_6.

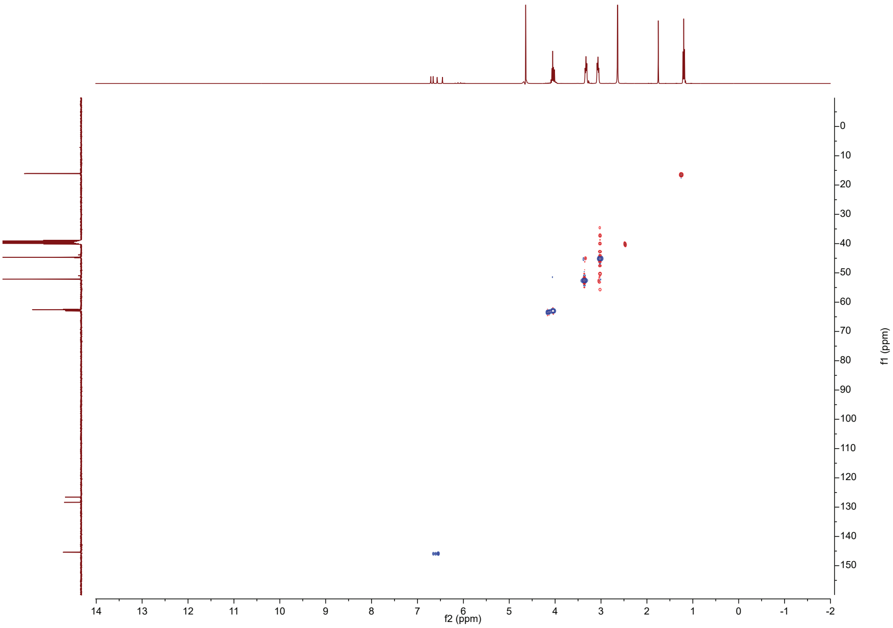

Figure S42: gHSQC NMR, DVP-t-Am-1 in DMSO-d_6.

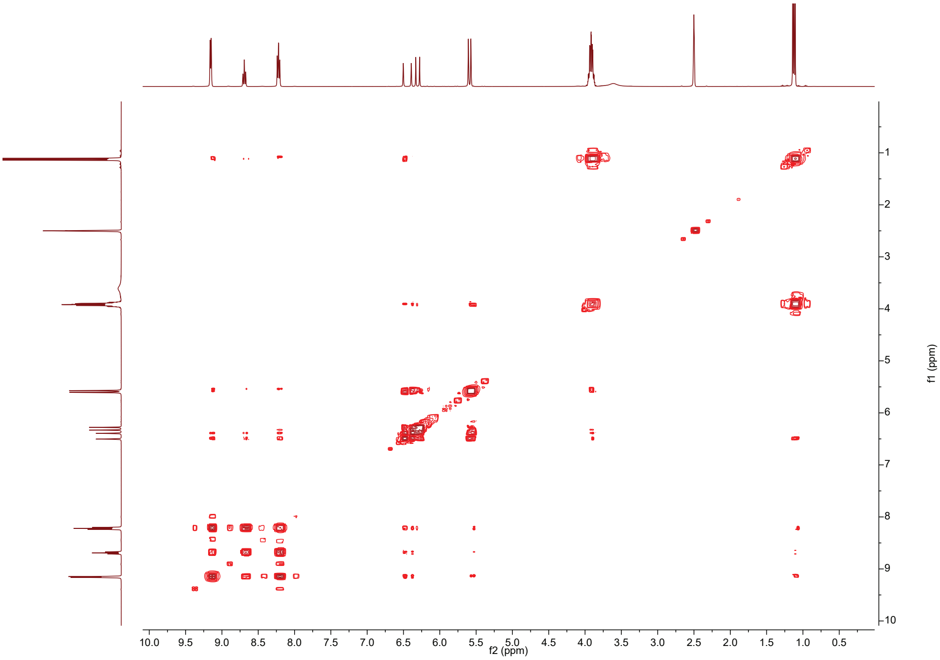

Figure S43: gCOSY, DVP-t-Am-2 in DMSO-d_6.

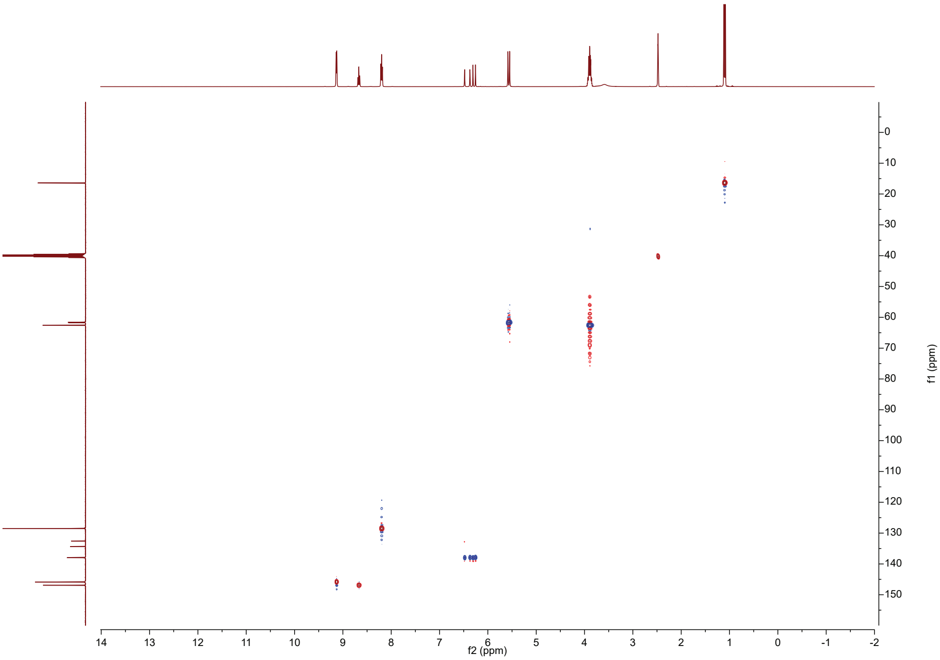

Figure S44: gHSQC, DVP-t-Am-2 in DMSO-d_6.

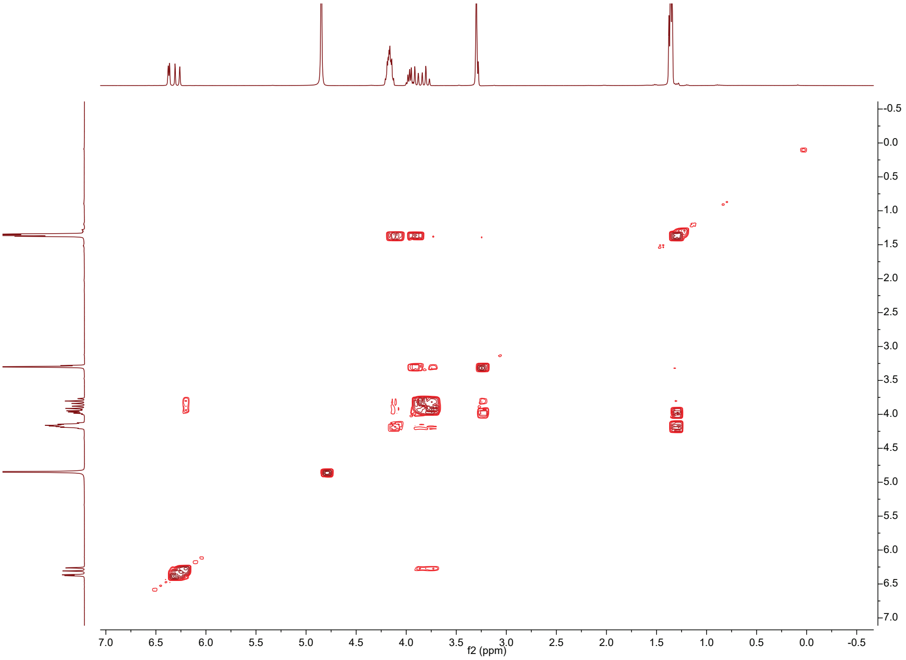

Figure S45: gCOSY, DVP-N in methanol-d$_4$.

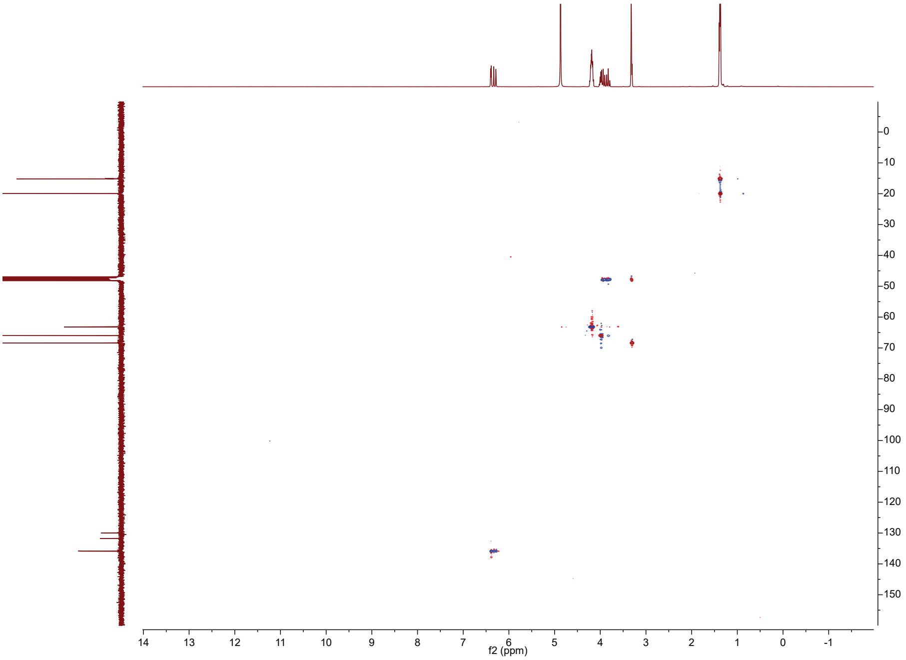

Figure S46: gHSQC, DVP-N in methanol-d$_4$.

3.5.16 LC-MS data

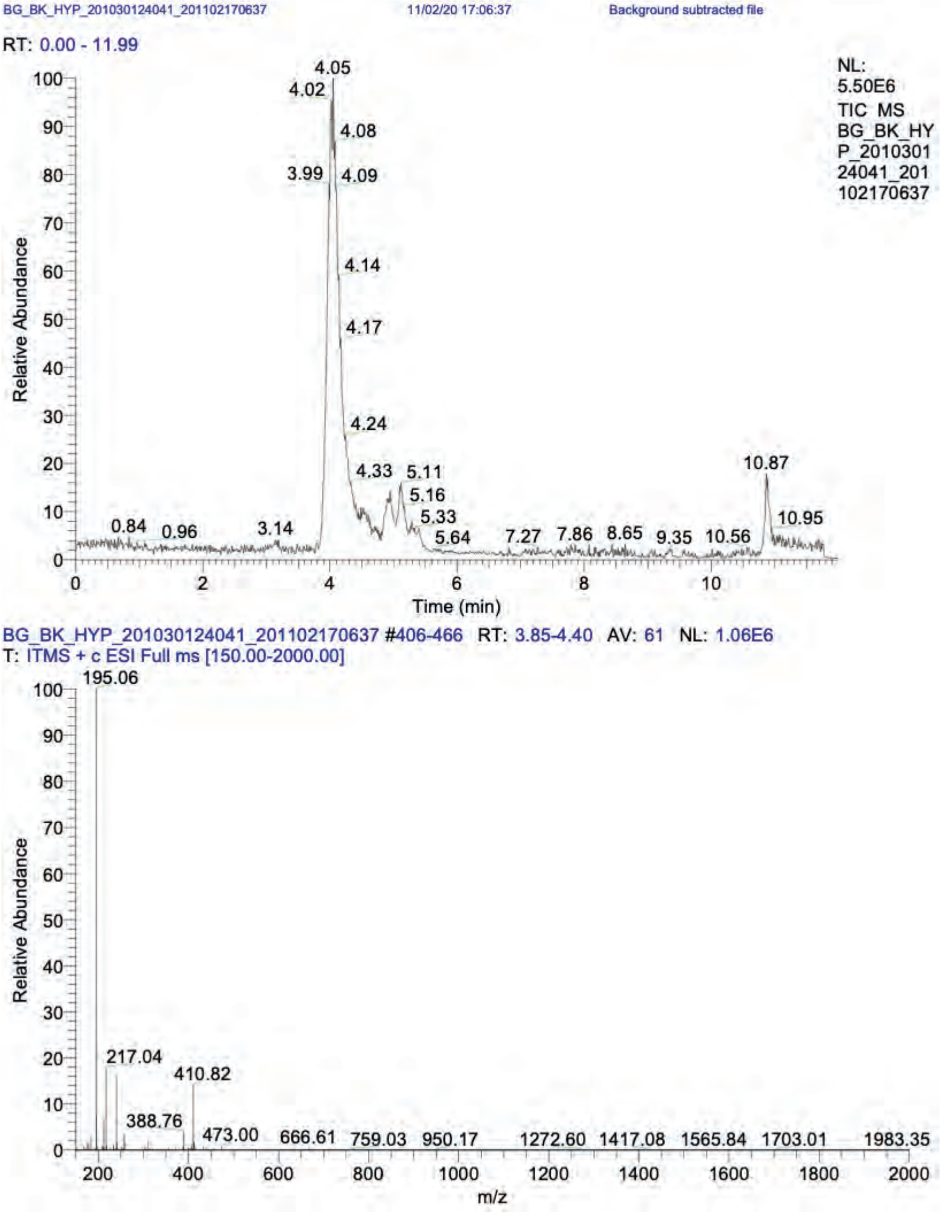

Figure S47: LCMS-data for compound HYP.

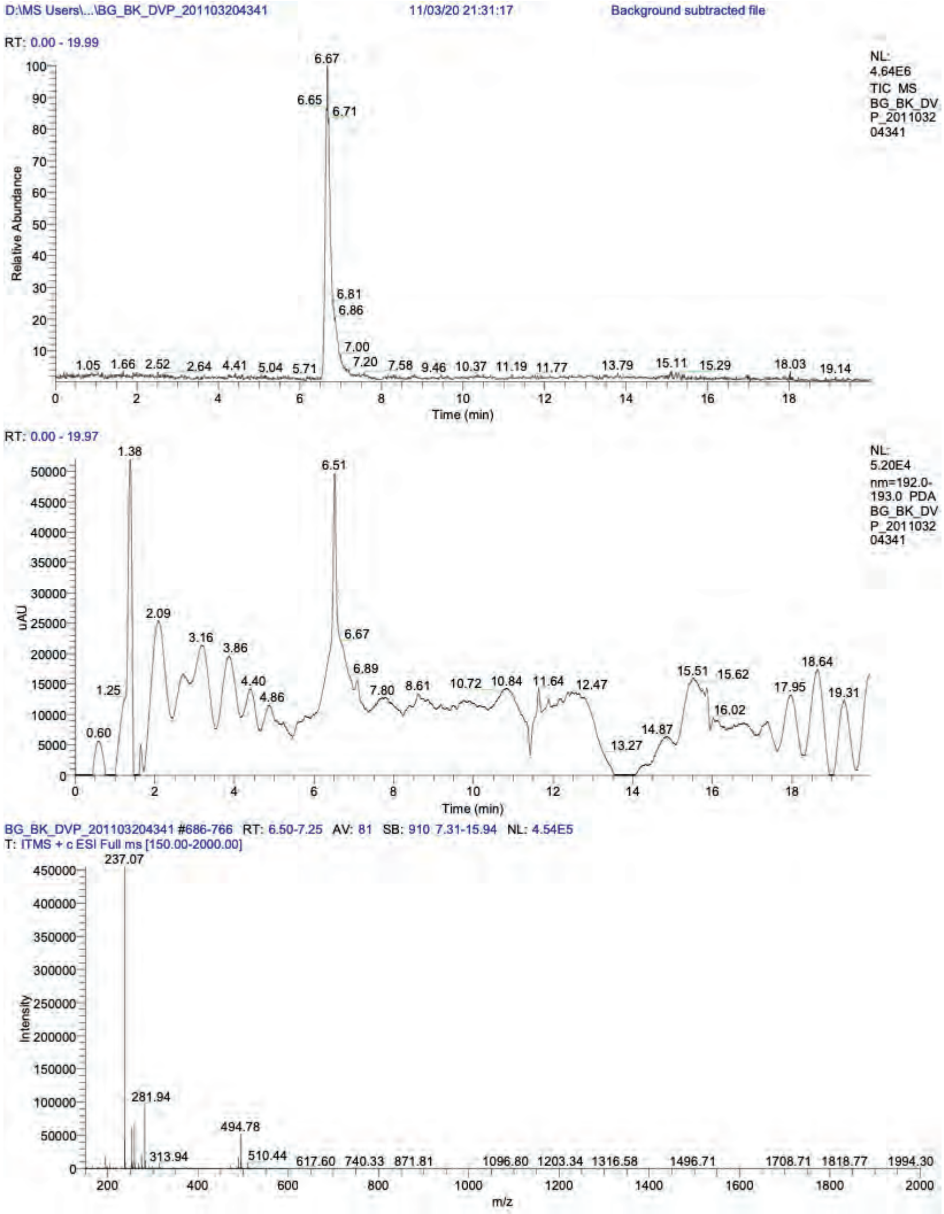

Figure S48: LCMS-data for compound DVP.

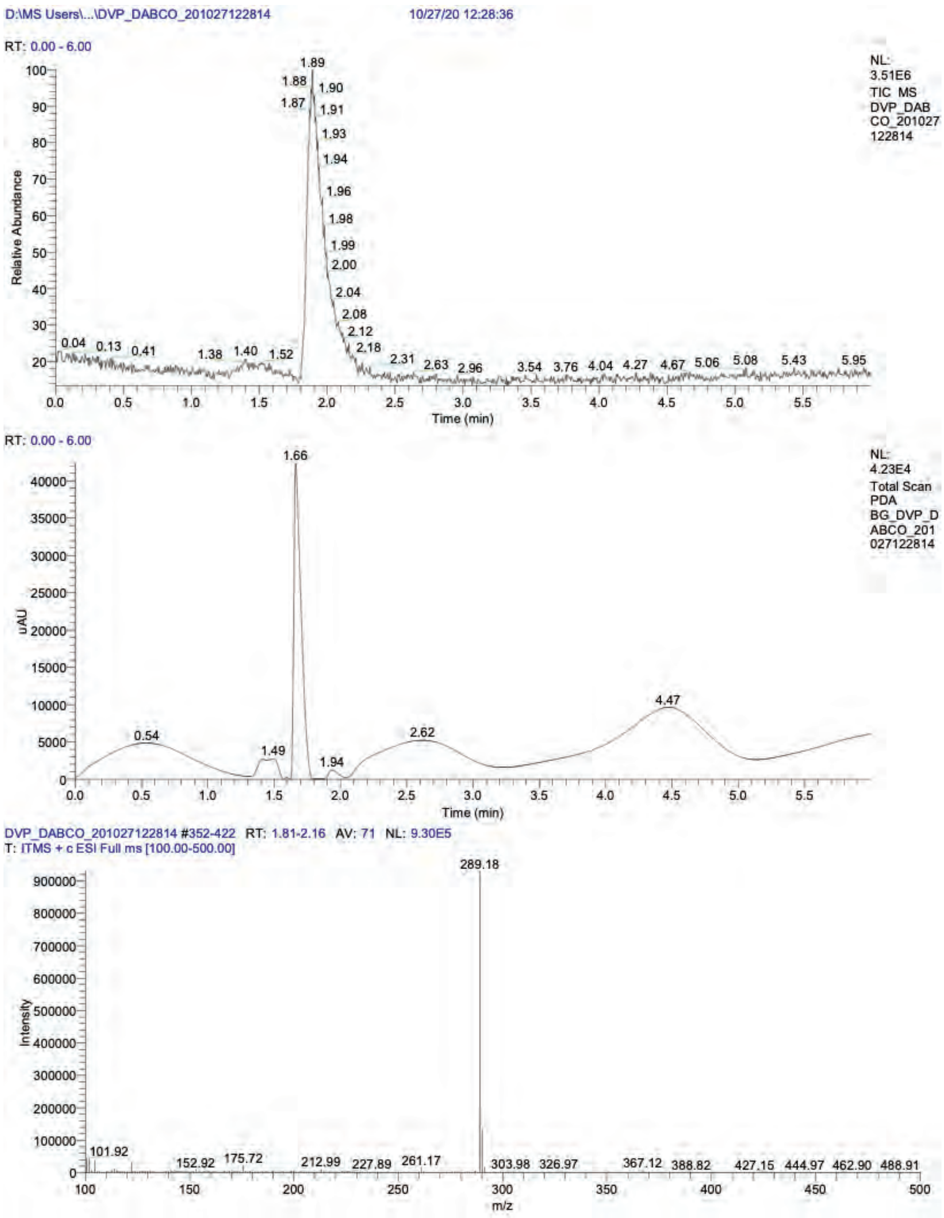

Figure S49: LCMS-data for compound DVP-t-Am-1.

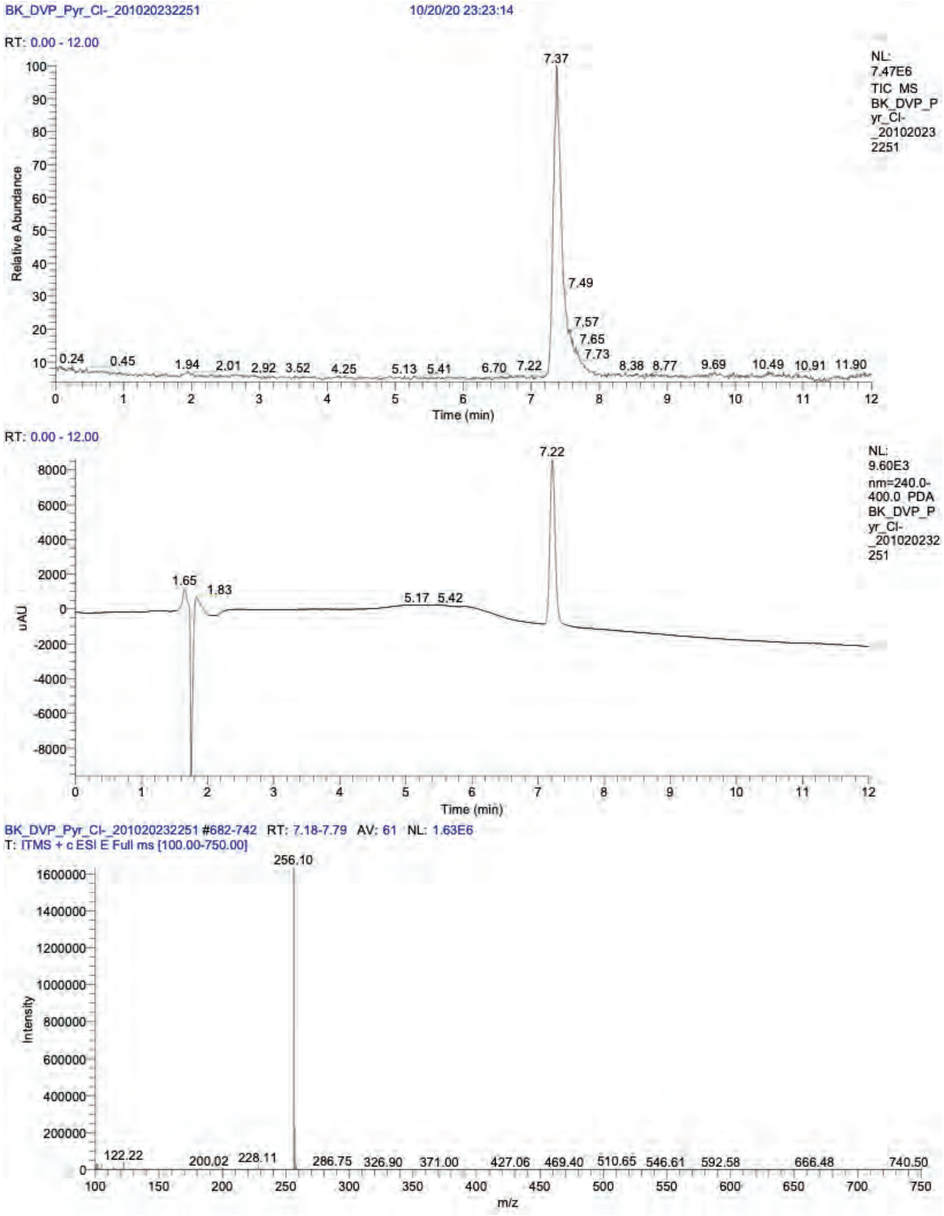

Figure S50: LCMS-data for compound DVP-t-Am-2.

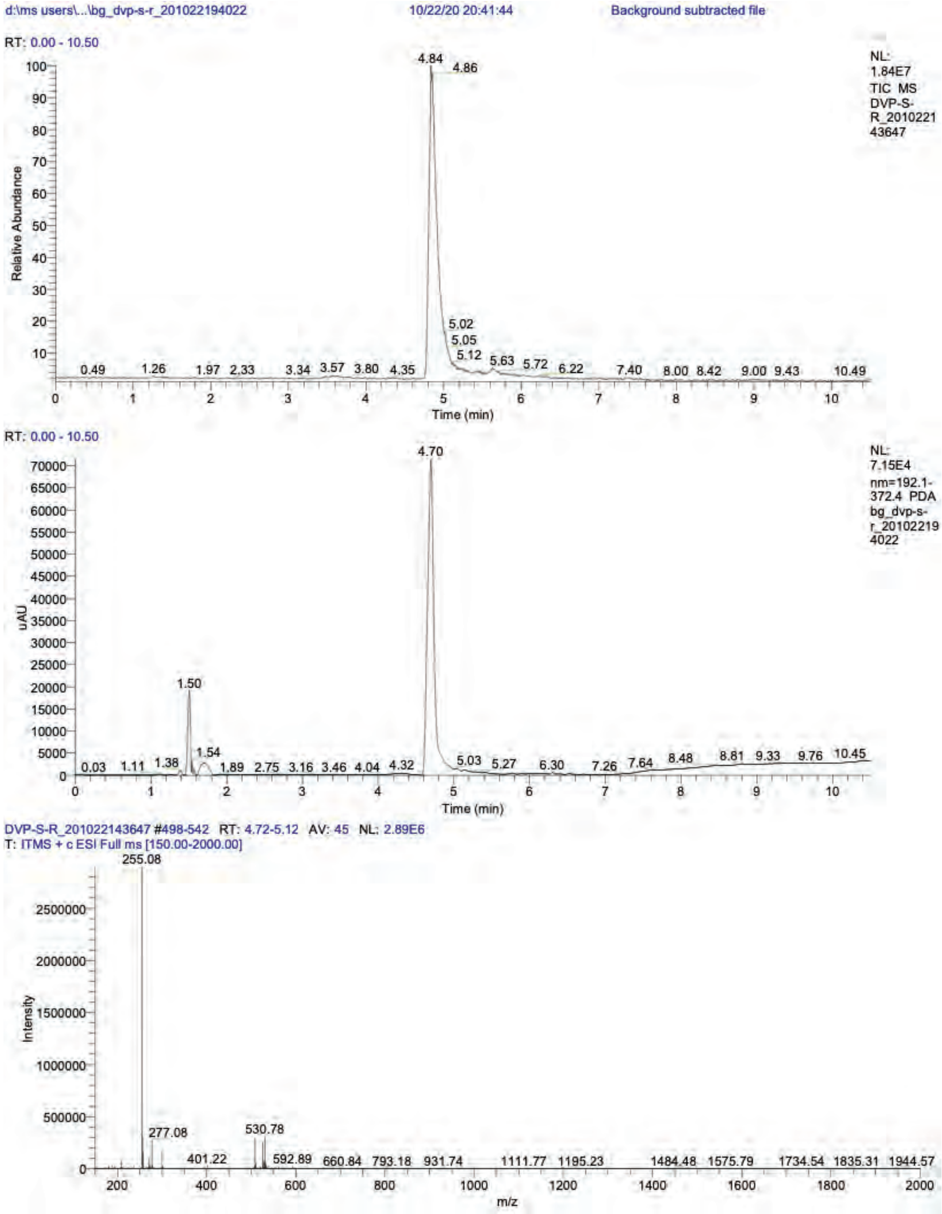

Figure S51: LCMS-data for compound DVP-S.

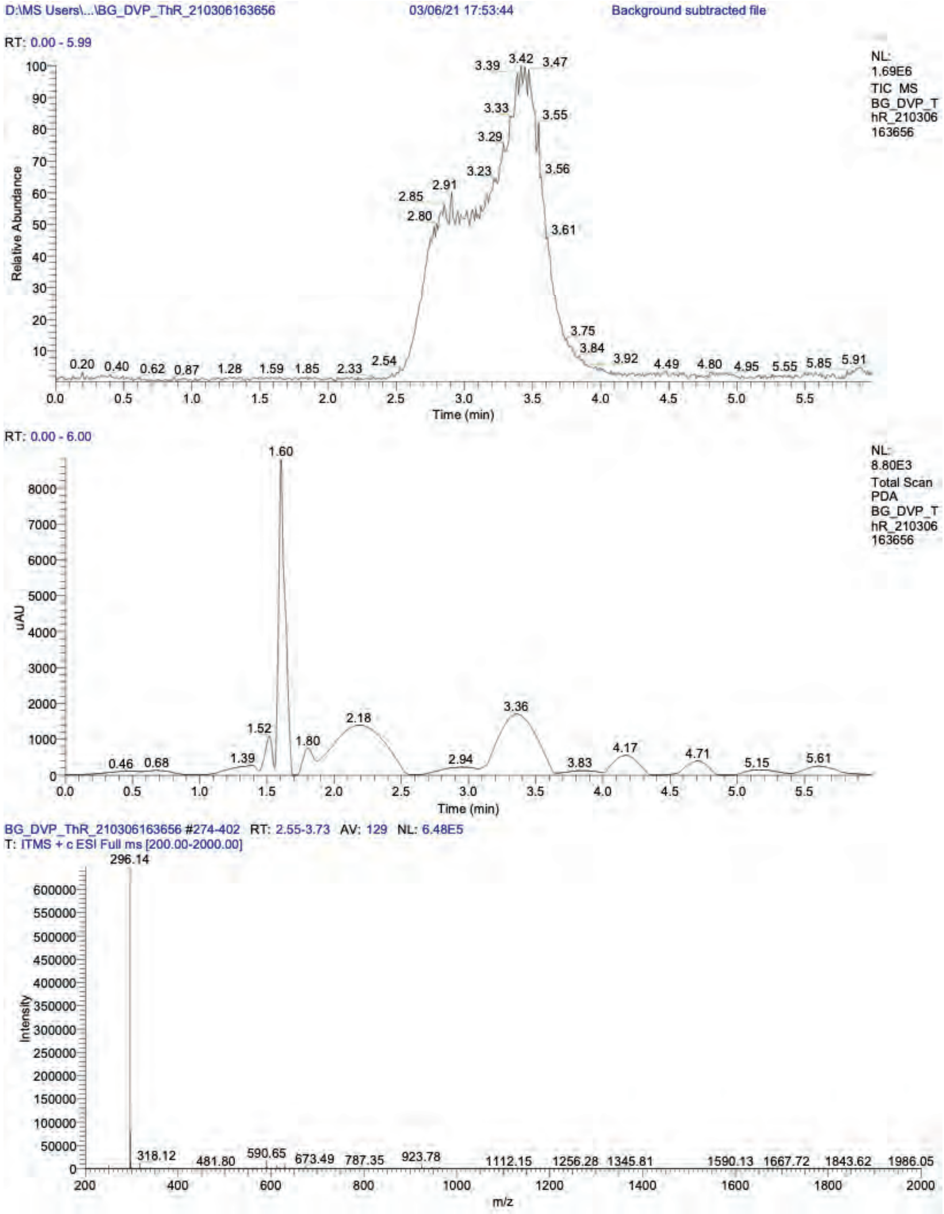

Figure S52: LCMS-data for compound DVP-N.

3.5.18 Supplementary references

1 A. Seingeot, Y. Charmasson, M. Attolini and M. Maffei, Heteroat. Chem., 2017, **28**, e21352.
2 M. Rambaud, A. del Vecchio and J. Villieras, Synth. Commun., 1984, **14**, 833–841.
3 C. Garzon, M. Attolini and M. Maffei, Tetrahedron Lett., 2010, **51**, 3772–3774.

4

NAKED-EYE-THIOL ANALYTE DETECTION VIA SELF-PROPARGATING, AMPLIFIED REACTION CYCLE

We present an approach for detecting thiol analytes through a self-propagating amplification cycle that triggers macroscopic degradation of a hydrogel scaffold. The amplification system consists of an allylic phosphonium salt that upon reaction with the thiol analyte releases a phosphine, which reduces a disulfide to form two thiols, closing the cycle and ultimately resulting in exponential amplification of the thiol input. When integrated in a disulfide-crosslinked hydrogel, the amplification process leads to physical degradation of the hydrogel in response to thiol analytes. We developed a numerical model to predict the behavior of the amplification cycle in response to varying concentrations of thiol triggers and validated it with experimental data. Using this system, we were able to detect multiple thiol analytes, including a small molecule probe, glutathione, DNA, and a protein, at concentrations ranging from 132 to 0.132 μM. In addition, we discovered that the self-propagating amplification cycle could be initiated by force-generated molecular scission, enabling damage-triggered hydrogel destruction.

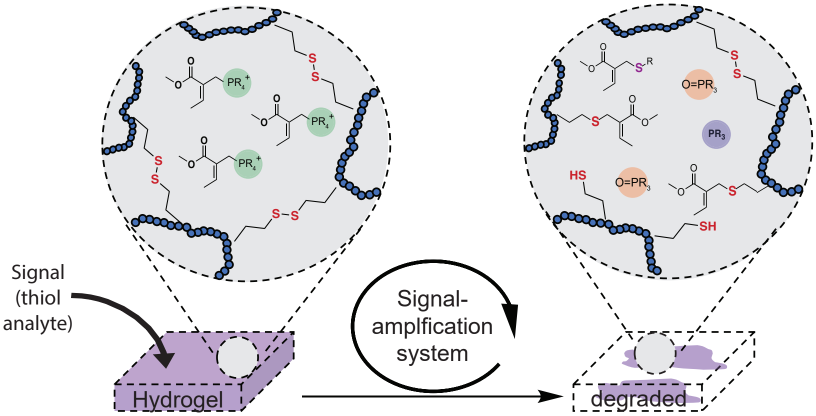

This chapter is published as:

B. Klemm, A. Roshanasan, I. Piergentili, J. van Esch and R. Eelkema, J. Am. Chem. Soc., 2023, **145**, 21222–21230.

4.1 INTRODUCTION

Living systems are commonly able to quantitatively detect and process (bio)chemical signals.[1–3] In contrast, synthetic analogues capable of detecting and amplifying an external signal input using only chemical reactions, and not requiring enzymatic transformations, is exceedingly rare and only a few systems[2,4–9] exist. Signal-responsive materials capable of translating and amplifying a signal[10] into a global macroscopic change will find many applications ranging from biomedical sensors[11,12], advanced forensics[13] to socio-environmental diagnostics[13–16] (assays to detect e.g. food pollutants, explosives or disease markers). Traditionally, chemo-sensors allow for sensitive detection by amplification of a reporter signal via a signal detection event, which is frequently coupled with photoluminescence or colorimetry to obtain an optical read-out.[3] A variety of chemical signals have been used as active triggers to initiate the self-propagating amplification reaction on reagents, including hydrogen peroxide[7], thiols[6,17] and fluoride[5,18–21], amongst others[4,8,22]. So far, studies on signal-amplified responsive synthetic materials using small molecule reagents[23,24] or self-immolative polymers[25–27] have been limited due to their challenging synthetic procedures to access reagents or polymers, and issues with background interference.[3,10,28] An alternative approach to achieve bio-inspired amplified response in synthetic soft materials is the β-mercaptoethanol (BME) or dithiothreitol (DTT)-mediated amplification cascade based on Meldrum's acid conjugated polymeric materials[15,28]. This strategy, first described by Anslyn and coworkers[9], detects thiol signals indirectly via thiol-exchange mediated release of BME and its subsequent reaction with a Meldrum's acid-based reagent. Once initiated, the reaction converts one equivalent of BME or DTT to decouple two equivalents of thiol. Using this approach, the authors were able to amplify initial thiol input and convert it to macroscopic material degradation and optical detection.[15] Inspired by these concepts, we sought to develop a new strategy for creating soft polymeric materials that are able to recognize, amplify and translate (bio)chemically relevant signals into global macroscopic material changes, regardless the quantities or molecular size of the applied signal. To realize this, we developed a new molecular approach for signal amplification in aqueous buffer by using allylic substitution of electron deficient allyl acetates with trivalent phosphines as signal amplifiers. More commonly, electron deficient allyl acetates are used together with tertiary nitrogen nucleophiles[29–31] to form positively charged

Morita-Baylis-Hillman acetate adducts. In contrast, the developed amplifier, is based on an inactive phosphorous moiety and an electrophilic double bond, which enables nucleophile-triggered substitution, converting the amplifier back into a neutral phosphine species. To our best knowledge, the controlled release of trivalent phosphines from allylic phosphonium salts[32–35] has not been shown so far.

This strategy enabled (i) control over disulfide redox chemistry by using the signal responsive allylic phosphonium ion, capable of direct thiol-analyte recognition and corresponding release of a phosphine species; (ii) coupling of this chemistry to a macroscopic response of a crosslinked hydrogel. Upon signal detection, the gels undergo physical degradation through chemical cascade reactions within the gel matrix. We were able to detect multiple analytes across a wide concentration range, and realized mechanical cascade initiation by cutting the gels, demonstrating damage-triggered material response.

4.2 RESULTS AND DISCUSSION

The signal-triggered amplification system (SAS) consists of two reactions in aqueous buffer (Figure 1). First, we activate a phosphine (PR_3) compound by allylic substitution on a quaternary allylphosphonium ion (PR_4^+) with thiol nucleophiles (SH-signal), which forms an allylic reaction product (Nuc. Product). In the second reaction, the liberated trivalent phosphine reduces a disulfide bond resulting in the formation of two thiol equivalents and the production of phosphine oxide ($O{=}PR_3$) (Figure 1a). The two new thiol molecules can perform another allylic substitution reaction on remaining allylphosphonium salt (P-salt), leading to liberation of more phosphine and subsequent disulfide reduction, propagating the cycle. As this iterative process continues, the quantity of thiol molecules is amplified, until all neutral phosphine is consumed. In this new molecular approach for signal amplification, we employ allylic phosphonium salt **1**. We were able to liberate trisodium tris(3-sulfophenyl)phosphine (TPPTS) from **1** upon addition of highly nucleophilic thiols[36,37] such as N-acetyl-cysteamine **4** (Figure 1b). To ultimately achieve thiol amplification, we further evaluated disulfide reduction by liberated TPPTS using N,N'-diacetylcystamine **3**. Using optimized conditions, sub-stoichiometric amounts of **4** are able to initiate the system, resulting in the formation of by-product **2** and the release of TPPTS. The liberated TPPTS then reduces **3**, forming two equivalents of **4** and one equivalent of phosphine oxide (OTPPTS). The equivalents of thiol formed in *n* cycles will theoretically be equal to 2^n. Two thiols initiate the release of two additional equivalents of TPPTS and consequently the process is self-propagating leading to an amplification of **4** (Figure 1b).

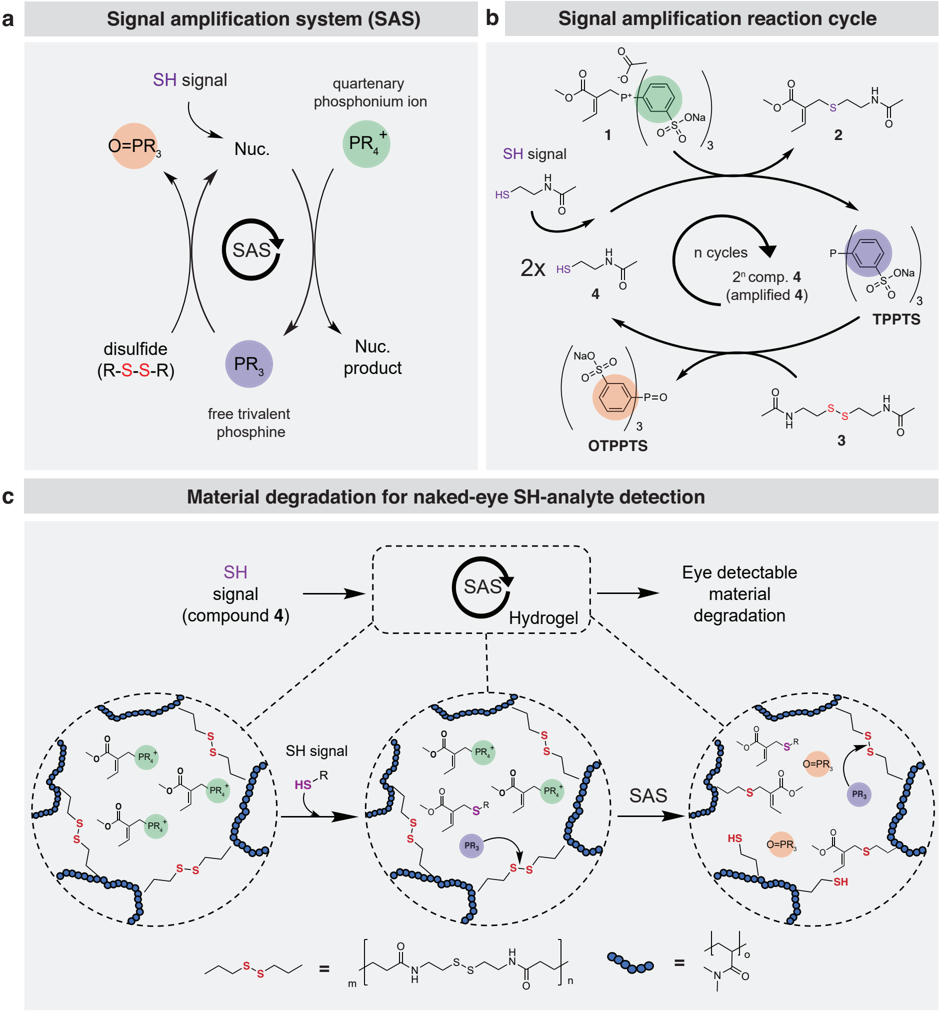

Figure 1: Schematics of the signal amplification system (SAS), its conditions, components and material degradation mechanism. **(a)** Generic SAS, consisting of nucleophilic substitution and disulfide reduction reaction. **(b)** Chemical structure of allylic phosphonium salt **1**, substitution product **2**, free phosphine (TPPTS), disulfide **3**, thiol **4** and oxidised phosphine (OTPPTS). Specifically, TPPTS is liberated from **1** upon SH-signal (compound **4**), which initiates disulfide reduction. The reduction reaction produces additional thiols which themselves continue to liberate more TPPTS. This cascade results in an amplification of the starting thiol signal. **(c)** BAC crosslinked DMA hydrogels used for naked eye SH analyte detection. Upon signal addition, liberated TPPTS inside the hydrogel matrix reduces disulfide crosslinks, which themselves liberate

more TPPTS. This results into a signal-triggered self-propagating amplification and ultimately into the degradation of the hydrogel material.

Having established the amplification system, we then sought to apply this chemistry to a synthetic material. For this, we fabricated hydrogel structures using *N,N*-dimethylacrylamide (DMA) with *N,N'*-cystamine bis(acrylamide) (BAC) crosslinks (3.5 wt%) by free radical polymerization[38,39]. We anticipated that upon SH-analyte-sensing, compound **1** releases TPPTS inside the redox active material matrix. Subsequent amplification reactions reduce internal disulfide crosslinks, thereby physically transforming the hydrogel from gel to sol, making the process visible to the naked eye (Figure 1c). Since analyte detection occurs through the amplification system, only sub-stoichiometric amounts of SH-analyte are needed to trigger material dissolution. Consequently, we studied the material at hand by exposing it to various biologically relevant SH-analytes and evaluated their sensitivity and application for naked eye analyte detection.

4.2.1 KINETIC CONTROL OVER PHOSPHINE ACTIVATION

To evaluate the efficacy of the amplification strategy, we studied the SH-triggered release of TPPTS from compound **1**. Nucleophilic substitution with S-terminal nucleophiles on **1** result in the release of TPPTS and the formation of the nucleophile product (Figure 2a). We first exposed 2.0 mM of **1** to sub-stoichiometric amounts of **4** ranging from 0.1 to 0.8 mM and monitored the release of TPPTS by UV-vis absorbance at 260 nm (Figure 2b). When 40% (0.8 mM) thiol was used (vs. compound **1**), we observed complete release of TPPTS within ~20 hours (Figure 2b). As expected, the release was slower when less thiol was added to the system. However, the release of TPPTS could stoichiometrically be correlated to the amount of SH input. Indeed, we found a linear correlation ($R^2 = 0.99$) between thiol input and released TPPTS (Figure 2c).

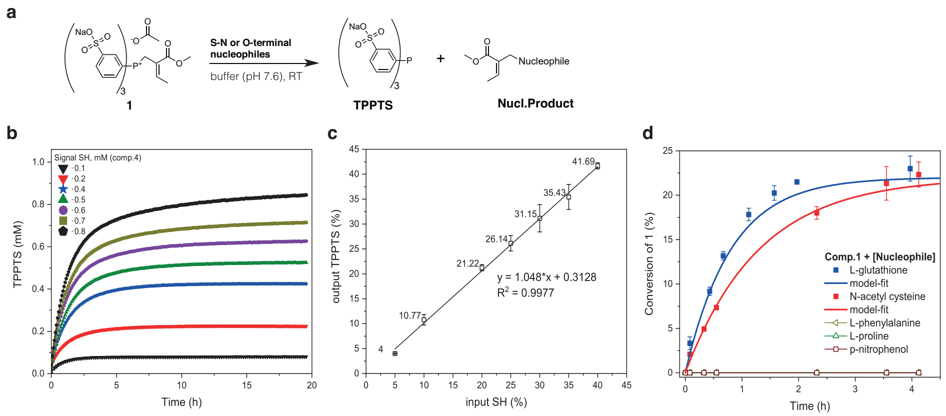

Figure 2: Kinetic control over TPPTS release. **(a)** Nucleophilic substitution reaction of compound **1** with S, N or O-terminal nucleophiles (L-glutathione, N-acetyl cysteine, L-proline, L-phenylalanine and p-nitrophenol), forming the nucleophilic substitution product and releasing TPPTS. **(b)** Reaction of compound **1** with a range of **4** (SH-signal) concentrations**,** forming 2-(acetylamino)ethanethiol (**2**) and TPPTS. TPPTS concentration vs. time for a range of **4** concentrations. **(c)** SH-signal input (%) and TPPTS output (%) diagram, showing the control of TPPTS release upon addition of **4**. Reactions were monitored by UV-vis at 260 nm and performed in duplicate. Conditions: phosphate buffer (0.1 M, pH 7.6), RT, 20h, 2 mM of **1** and indicated amounts of **4**. **(d)** NMR reactivity study using 0.067 mM of **1** (1.0 eq.) and 0.20 eq. of a range of different nucleophiles (indicated in figure) in aqueous buffer (2:8 D2O: phosphate buffer (0.1 M, pH = 7.6)) at 25 °C. Error bars represent standard deviation from duplicate runs. Solid lines represent the *k*-value model fit to the experimental data.

In addition, we conducted a reaction rate study to further understand the reactivity of **1** towards S, N and O-terminal nucleophiles with their order being L-glutathione > N-acetyl cysteine (Figure 2d). We can attribute the kinetic variations (k_{GSH} = 240 ± 14.8 vs. k_{cysteine}= 142 ± 2.7 $M^{-1}*h^{-1}$) between different thiol-compounds to the difference in nucleophilicity of the employed S-terminal nucleophile. In contrast, N-terminal nucleophiles, including L-proline and L-phenylalanine did not react with **1.** A similar observation was made for p-nitrophenol. This shows that the system displays a high sensitivity (Figure 2b) and selectivity (Figure 2d) towards S-terminal nucleophiles. Importantly, we did not observe the interference of Michael addition or other side reactions during our experiments.

As control we tested compound **1** without **4** in phosphate buffer (0.1 M, pH = 7.6) and in cell culture media (DMEM) by monitoring it over 24 hours with ^{1}H NMR spectroscopy (Figure S2 and S3). Over this time, we found that **1** is stable in the absence of thiol (in both cell culture and buffer) and we did not observe release of TPPTS via hydrolysis. Background interference such as hydrolysis or side reactions without trigger have been a consistent issue among self-propagating amplification reactions.[10] TPPTS alone in aqueous media showed negligible oxidation, forming less than 5% OTPPTS during the 24 hours experimental period under air (Figure S4).

4.2.2 KINETIC MODELLING OF PHOPSHINE ACTIVATION AND DISULFIDE REDUCTION

Prior to the experimental investigation of the entire amplification system, we conducted kinetic experiments for both (I) thiol-triggered substitution of **1** using **4** and (II) disulfide reduction of **3** by TPPTS (Figure 3a). A simplified mathematical model was developed based on a set of non-linear differentials describing (I) and (II) and solved numerically for a series of reactions. To begin, we used the experimentally determined pseudo-first order rate constants for each model which were obtained using UV-vis experiments (Figure S12a-b). By implementing the existence of intermediate species based on the mechanism of the nucleophilic substitution through P-salt intermediates proposed by Krische and coworkers[40] (Figure 3a-I), we found good agreement (R^2 = 0.89 - 0.97) between the model and our experimental data (Figure 3b). We noticed, however, that the model overestimated the TPPTS release at a later stage in the reaction, which becomes more pronounced with increasing SH concentrations.

We described the disulfide reduction kinetics using a two-step mechanism.[41,42] In the first step, nucleophilic attack by phosphine forms one equivalent of thiolate anion (S^-) and the S-alkylphosphonium ion adduct (PR_3^+-thiol-intermediate). The intermediate ion then undergoes subsequent hydrolysis to afford phosphine oxide and a second equivalent of S^- (Figure 3a-II). Applying this mechanism to our conditions, we were able to optimize reaction constants for all TPPTS variations, which resulted in excellent agreement (R^2 = 0.99) between model prediction and experimentally acquired UV-vis data (Figure 3c). However, further mechanistic insight is required to enhance the predictive capabilities and scope of applicability of this simplified model. Most importantly, describing each reaction step accurately in separate sub-models turns out to be a powerful means for individual reaction-step prediction in signal-amplification systems.

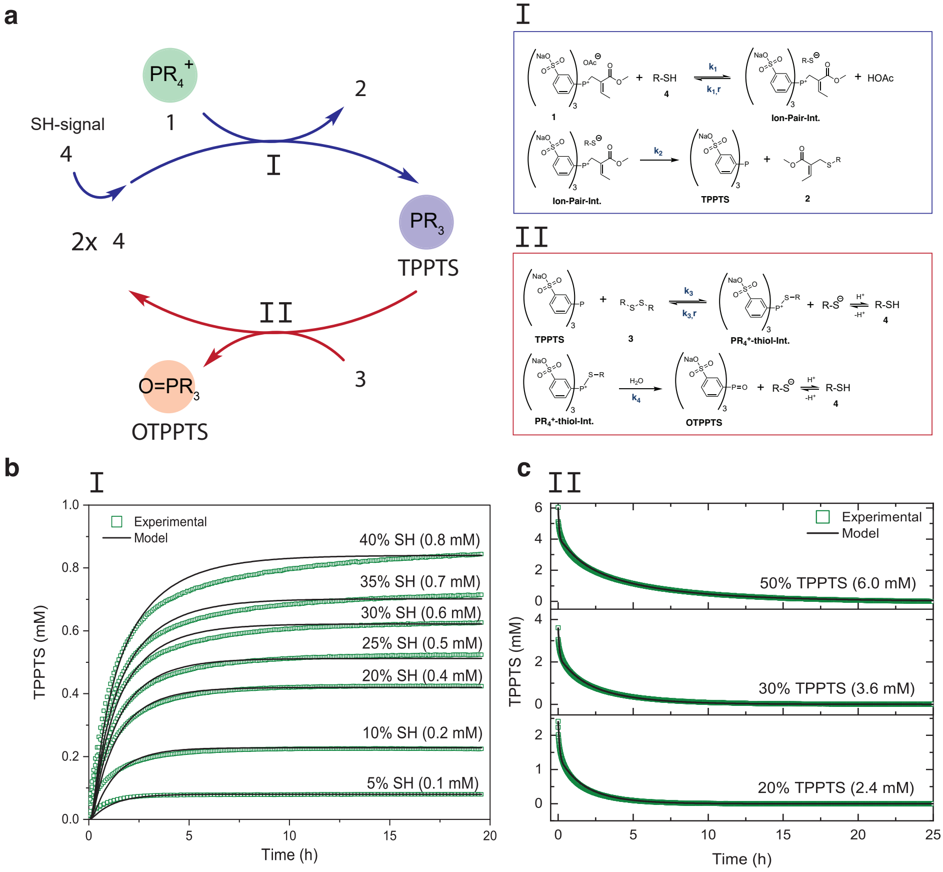

Figure 3: Nucleophilic substitution and disulfide reduction kinetics. **(a)** Schematic representation and full reaction pathway overview for nucleophilic substitution (I) and disulfide reduction (II) in the amplification system. **(b)** SH-triggered substitution kinetics of compound **1** (2.0 mM), measured by the appearance of TPPTS from UV-vis at 260 nm. **(c)** disulfide reduction kinetics for **3** (12.0 mM) at varying concentration of TPPTS, measured by the disappearance of TPPTS from UV-vis at 300 nm. All reactions were measured in 0.1 M phosphate buffer (pH = 7.6) at 25 °C. Representative samples from duplicate (average) runs (green line). Solid black lines correspond to the model fits to each condition. Statistical evaluation between kinetic model and experimental data can be found in Figure S13 - S16.

But the standard approach to develop these sub-models by using progression fitting is only sub-optimal, since the combined system and the interactions between species are not accounted for. For example, underlying short-lived species interactions, such as ion-pair interactions, clusters and/or electrostatic interactions are not well understood from separate reaction modelling and are often cumbersome to determine experimentally. This challenge can be partially overcome by turning towards model optimization. Optimization or re-evaluation of early on established reaction constants will be fundamental for signal-amplification modelling to establish first understanding and at the same time to identify potential species interactions, which are unexpected or have never been observed beforehand.

4.2.3 SIGNAL AMPLIFICATION – SMALL MOLECULE STUDY

Initially, we studied the kinetics of the signal amplification system by tracking the UV-vis absorbance changes of TPPTS. Amplification experiments were performed at optimized conditions with 9.0 mM phosphonium ion **1** (1.0 eq.) and 1.5 eq. of disulfide **3**. We used thiol-signal **4** as model trigger for the system (Figure 4a). When adding SH-trigger to the mixture**,** the release of TPPTS was monitored at λ = 300 nm upon conversion of **1** and the subsequent oxidation of released TPPTS by **3**. We monitored the kinetics of the reaction cascade for different ratios of SH-trigger (0.10, 0.15 and 0.25 eq.) (Figure 4b). Additionally, we used the kinetic model to describe the reaction and quantified the fit between model and experimental data by determining the coefficients of determination R^2.[43]

From the kinetic experiments, we found that TPPTS concentration increased with increasing SH-signal. As expected, the release of TPPTS (k_4 = 0.0020 $M^{-1}s^{-1}$) is approximately three times as fast as the oxidation of TPPTS in the presence of **3** (k_4 = 0.00071 $M^{-1}s^{-1}$) based on their rate determining step rate constants. As seen from Figure 4b, once the trigger is applied, the initiation speed and the maximum concentration of TPPTS from 0 to 5 hours differ notably (0 – 5 h), while TPPTS depletion (5 – 35 h) propagates at approximately the same rate. Using the kinetic model, we were able to predict the signal amplification cascade for concentrations of 10, 15 and 25% SH-trigger with R^2 – values of 0.91, 0.92 and 0.93, respectively. Although the model is in good agreement with experimental data, it overestimates the amplitudes of released TPPTS in all three cases. An explanation for the discrepancy could be the influence of electrostatic interactions between **1**, TPPTS and OTPPTS, that lead to lower reactivities during consumption, which have not been considered in our model. Importantly, however, these results confirmed that the amplification cascade detects and translates the amount of trigger, causing signal-dependent amplitude curves of released TPPTS and time-dependent consumption of **1**.

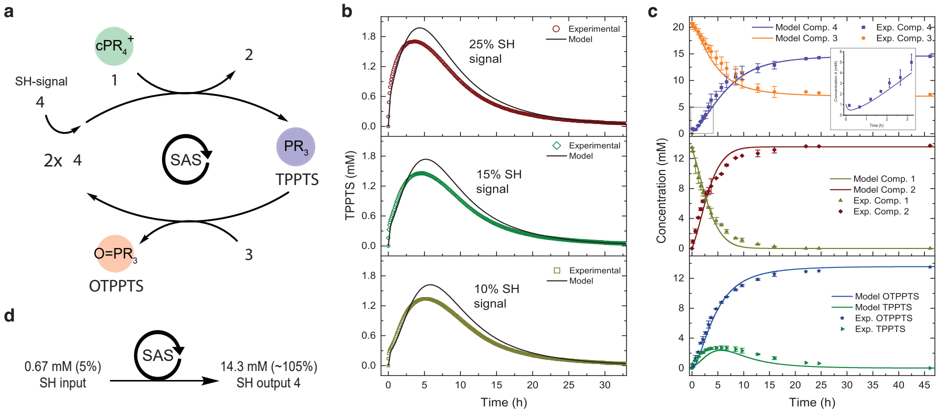

Figure 4: Kinetic experiments of the signal-amplification system and model predictions for species variation. (a) Schematic representation and full reaction pathway overview for nucleophilic substitution and disulfide reduction in the amplification system. (b) UV-vis kinetic experiments using compound **4** as SH-trigger, at concentrations of 0.95 mM (10%), 1.40 mM (15%) and 2.30 mM (25%). Conditions: 9.0 mM of compound **1** with 13.5 mM of **3** in phosphate buffer (pH = 7.6) at 25 °C. (c) NMR kinetic experiments using 13.5 mM of **1** (1.0 eq.), 1.5 eq. of disulfide **3** and 0.05 eq. of **4** in aqueous buffer (2:8 D_2O: phosphate buffer (0.1 M, pH = 7.6)) at 25 °C. Error bars represent standard deviation from duplicate runs for both UV-vis and ^{1}H NMR. Solid lines correspond to the model fits to each varying condition or species. (d) Schematic representation of signal amplification system output using 0.05 eq. of **4**.

Next, we investigated the reaction cascade using ^{1}H NMR to examine all species, including the amplification of the SH-trigger analyte **4**. First, we explored the background reaction (no thiol **4**) using 13.5 mM of **1** (1.0 eq.) and 1.5 eq. of **3** in aqueous buffer. The experiment revealed no conversion of **1** without signal initiation after 24 hours (Figure S5), which is a highly desirable feature for an amplification reaction[3].

Initiating the system using **4** (Figure 4c), we found that during the time-course of the reaction cascade by ^{1}H NMR (Figure S11), compound **4** exhibits a sigmoidal amplification profile, which is a typical attribute for auto-amplification systems.[3] In particular, the use of 0.67 mM SH-signal (~5%) to initiate the reaction resulted in thiol concentration increase to approximately 14.3 mM (~105%) after 45 hours, accounting for full conversion of **1** (Figure 4c-top & 4d). Matching this process, disulfide concentration quantitatively decreases ~13.5 mM from 20.3 to 7.4 mM. Simulations using the kinetic model for **3** (R^2 = 0.93) and **4** were consistent with the experimental data. Importantly, the model was able to describe the sigmoidal amplification profile of **4** in detail

(Figure 4c insert) and with high accuracy (R^2 = 0.96). Furthermore, we found that the production of **2** corresponds to the conversion of **1** (Figure 4c-middle). Here, our simulations substantiate the exponential decrease of **1** and increase of **2**, with R^2 - values of 0.98 (**1**) and 0.96 (**2**). Similarly, OTPPTS concentration is in excellent agreement with simulation results (R^2 = 0.98) (Figure 4c-bottom). Using ^{1}H NMR spectroscopy to track all species involved in the two-component reaction cycle and describing those with kinetic simulations, we were able to confirm successful amplification of thiol **4** though coupled nucleophilic substitution and disulfide reduction reactions.

4.2.4 NAKED-EYE THIOL ANALYTE DETECTION THROUGH SIGNAL-AMPLIFIED HYDROGEL DEGRADATION

Once we established the signal amplification strategy and obtained their model kinetics, we then sought to incorporate this strategy into a macromolecular-crosslinked hydrogel system for naked eye SH-analyte detection. We crosslinked DMA with BAC to form cube shaped polymer hydrogels with a crosslinker concentration of 4.6 mg/mL (3.5 wt% crosslinker). The obtained gels had a water content of 98 ± 0.81 wt%, dimensions of approximately 1.3 x 1.2 x 0.5 cm (L/W/H) and had been copolymerized with methacryloxyethyl thiocarbamoyl rhodamine B (0.001 wt%) as colour indicator to enable visualization of hydrogel degradation (Figure 5). To study the self-amplified material degradation process via dissolution of the polymer gels, we first conducted experiments by exposing hydrogels submerged in aqueous buffer (phosphate buffer, 0.1M, pH = 7.6) with 1.5 eq. of **1** (vs. crosslinker) to 0.05 eq. (5%) of **4** (vs. compound **1**) as model SH-trigger. We observed gradual gel dissolution was observed over the course of 168 hours, while no degradation occurred without thiol initiation (controls: only compound **1** without SH-trigger and no additives) (Figure 5a). Note that although no degradation on gels occurred in the absence of trigger during the observation period of 168 h, we found that gels started to degrade beyond approximately 13 days being exposed to air and light (data not shown).

Hydrogel degradation is based on the concept that, after addition of **4**, the self-propagating reaction with **1** successfully releases TPPTS within the hydrogel matrix, where it is free to diffuse and propagate the cascade through phosphine mediated disulfide reduction on crosslinker, generating new thiols (new signals). The progression of the self-propagation continues until complete physical degradation of the material (t = ~168h). In comparison, hydrogels exposed to TPPTS alone (1.5 eq. vs crosslinker) showed visibly faster degradation than the thiol triggered amplification system gels by complete dissolution within 50 hours.

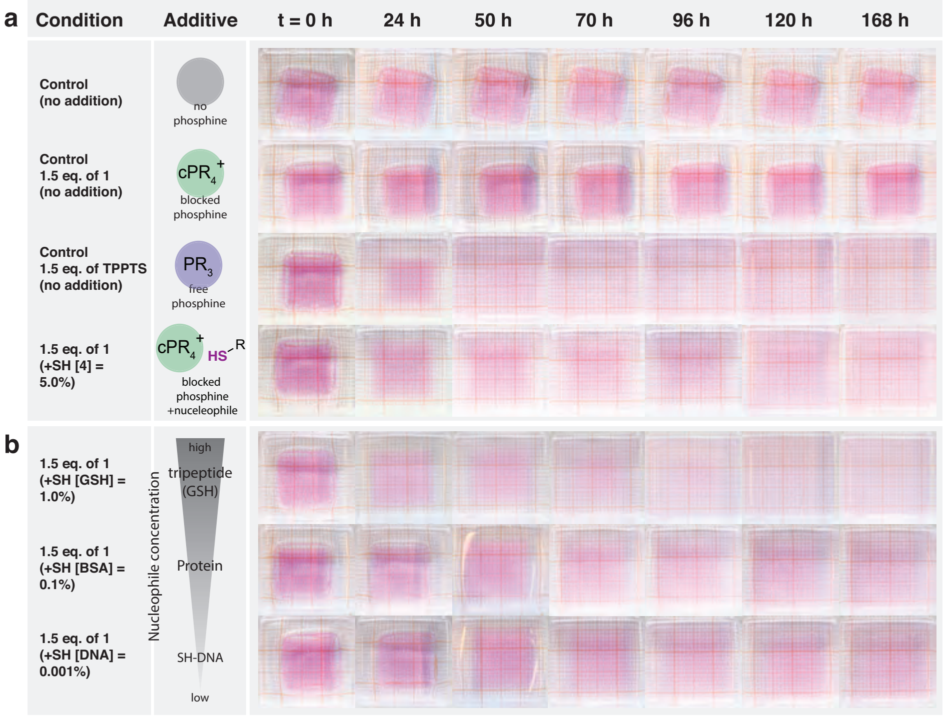

Figure 5: Time lapse photographs of hydrogel degradation using the amplification system triggered by SH-analytes. (a) Control gels with 1) no additives, 2) with 1.5 eq. of **1**, 3) 1.5 eq. of TPPTS and 4) 1.5 eq. of **1** and 5% (0.05 eq.) of **4**. (b) Gels with 1.5 eq. of **1** and SH-trigger addition of **1**) 1.0% (0.01 eq.) of L-glutathione, 2) 0.01% (0.0001 eq.) of bovine serum albumin and **3**) 0.001% (0.00001 eq.) of thiol functionalized DNA. Conditions: gels were submerged in 1.5 mL phosphate buffer (0.1M, pH = 7.6). All measurements were done in duplicate (see Figure S17 & S18).

Next, we initiated the system using different thiol triggers. We focused on biologically relevant thiol-analytes comprised of various sizes, including L-glutathione (SH-GSH), the protein bovine serum albumin (SH-BSA) and thiol functionalized DNA (SH-DNA) with concentrations of 132, 1.32 and 0.132 µM, respectively. Importantly, each SH-trigger (SH-BSA[44], SH-GSH and SH-DNA) contains one thiol equivalent per molecule. Note that SH-BSA has additional disulfide bridges, which account for an additional 27% disulfides in the hydrogel system. We hypothesized that variations in the concentration of SH-trigger would lead to a differential self-propagation speed and signal amplification rate which could be observed by the naked eye. Samples containing SH-DNA (0.001% SH vs. **1**), showed slower decomposition than compared to SH-BSA (0.01% SH) and SH-GSH (1.0% SH) (Figure 5b). Gel degradation rate increases with increasing concentration of SH-trigger due to higher TPPTS release at the start. As a result, the signal amplification rate of the system is increased according to SH-GSH > SH-BSA > SH-DNA (Figure 5b). Remarkably, the visual degradation between SH-BSA and SH-DNA is less than expected although the SH-BSA signal concentration is ten-fold larger compared to SH-DNA. We suspect that the 27% additional disulfides present in SH-BSA effect the overall degradation rate, which results in slower gel decomposition time.

Interestingly, we observed that SH-GSH (1.0%) showed faster decomposition than compared to SH-trigger **4** (5%). We rationalized this behavior to be related to the higher nucleophilicity[45] of glutathione than compared to **4**, which accelerates decomposition (Figure 5a/b) and overshadows over time their concentration difference.

4.2.5 DAMAGE-TRIGGERED HYDROGEL DESTRUCTION TRHOUGH CUT-GENERATED RADICAL INITIATION

Opening of sulfur crosslinks in soft-materials (e.g. hydrogels) has been frequently realized in the presence of reducing agents (e.g. trivalent phosphorous reagents[46]) and through thiols via thiol-disulfide exchange[47], whereas examples in which mechanical stress or force[48] is used as trigger are rare. To further evaluate our system, we were interested to see if compound **1** is capable of sensing mechanical impact through damage-generated radicals and subsequent TPPTS release to initiate the amplification cascade. Applying mechanical stresses on polymers and hydrogel networks is well-known to cause polymer chain cleavage at the C-C backbone bonds and the formation of radicals.[49–51] Similarly, mechanical-induced forces on disulfide-crosslinked hydrogel networks likely result in homolytic disulfide scission, leading to thiyl radicals.[48,52,53] These radicals then form thiols by abstracting hydrogens from water[53] or other donor molecules.[54] These newly formed thiols can then initiate the amplification system by releasing TPPTS from **1**.

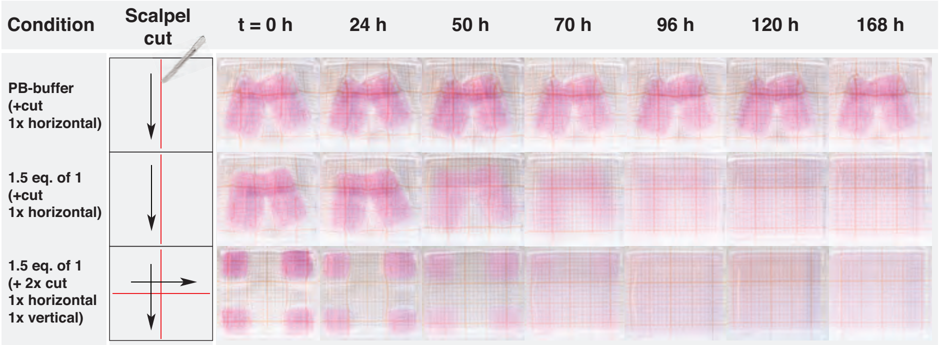

Figure 6: Time lapse photographs of hydrogel degradation using the self-amplification system triggered by damage (cut). (a) Control gels with 1) no additives and 1x horizontal cut, 2) 1.5 eq. of **1** and 1x horizontal cut, 3) 1.5 eq. of **1** and 2x cut (1x horizontal and 1x vertical). Conditions: gels were submerged in 1.5 mL phosphate buffer (0.1M, pH = 7.6). All measurements were done in duplicate (see Figure S19).

To test this hypothesis and evaluate thiyl radicals as potential triggers, we conducted experiments on gels (1.5 eq. of **1** vs. crosslinker) by applying force via cutting horizontally through the material using a scalpel and compared it to identical gels without **1** (Figure 6a). Consistent with earlier findings, we found that applied damage can indeed induce the amplification cascade leading to complete degradation of the gels after 168 hours. In contrast, gels without **1** remained stable during the entire observation time. To further confirm the effect of mechanical damage and to provide a correlation between material damage and its degradability, we carried out experiments for which we applied two cuts on the gels (1x horizontally and 1x vertically). Since more cuts generate more thiols, we hypothesised faster degradation due to higher activation of **1**. Indeed, from the comparison in Figure 6, it can be seen that gels which were cut two times degraded faster than gels with only one cut. In particular, single cut gels show complete dissolution after 120 h, while two times cut gels became a homogeneous solution after 96 h. Importantly, thiol availability is likely not the sole contributor to hydrogel degradation. A two-cut zone creates a larger interface for TPPTS diffusion than compared to a one-cut zone, which ultimately enhances the accessibility of phosphines to disulfide crosslinkers. In general, these results indicate that the material is capable of sensing force-induced damage, by translating the stimulus through the amplification system to respond by material degradation.

4.3 CONCLUSION

We have developed a new signal amplification system for detecting thiol compounds using the reactivity of allylic phosphonium ion **1** with thiols and disulfides. Importantly, upon complete removal of thiols from the system, we observed no background interference from hydrolysis or unwanted site reactions over the course of 24 hours. System activation by allylic substitution of TPPTS from **1** only commences in the presence of thiol analytes. Here, we used sub-stochiometric amounts of thiol to initiate a chain reaction that exponentially amplifies the input thiol signal. Experimental data is supported by a kinetic model that accurately describes the rates of all species involved in the amplification cycle and predicts variations in individual components, providing further insight into the system.

Combining this amplification strategy with disulfide crosslinked hydrogel structures enabled us to detect multiple thiol analytes, including L-glutathione, a protein, and DNA, by visual hydrogel degradation. The system is highly sensitive to SH-concentrations as low as 0.132 µM and across three orders of magnitude in concentration, and can even react to force-generated signals. Despite these advances the current system does have drawbacks, e.g. the reagents are not covalently linked to the material and the amplification process is slow. Nevertheless, this proof-of-concept for naked-eye detection is a promising step towards a new generation of responsive soft materials, such as coatings and adhesives, that can show an amplified response to low exposure of a specific applied stimulus, resulting in a macroscopic change in the material.

4.4 REFERENCES

1 P. Fratzl and F. G. Barth, *Nature*, 2009, **462**, 442–448.
2 N. C. Gianneschi, S. T. Nguyen and C. A. Mirkin, *J. Am. Chem. Soc.*, 2005, **127**, 1644–1645.
3 S. Goggins and C. G. Frost, *Analyst*, 2016, **141**, 3157–3218.
4 H. Mohapatra, K. M. Schmid and S. T. Phillips, *Chem. Commun.*, 2012, **48**, 3018–3020.
5 M. S. Baker and S. T. Phillips, *J. Am. Chem. Soc.*, 2011, **133**, 5170–5173.
6 E. Sella, R. Weinstain, R. Erez, N. Z. Burns, P. S. Baran and D. Shabat, *Chem. Commun.*, 2010, **46**, 6575–6577.
7 E. Sella, A. Lubelski, J. Klafter and D. Shabat, *J. Am. Chem. Soc.*, 2010, **132**, 3945–3952.
8 D.-G. Cho and J. L. Sessler, *Chem. Soc. Rev.*, 2009, **38**, 1647–1662.
9 X. Sun and E. V Anslyn, *Angew. Chem. Int. Ed.*, 2017, **56**, 9522–9526.
10 X. Sun, D. Shabat, S. T. Phillips and E. V Anslyn, *J. Phys. Org. Chem.*, 2018, **31**, e3827.
11 T. Yoshii, S. Onogi, H. Shigemitsu and I. Hamachi, *J. Am. Chem. Soc.*, 2015, **137**, 3360–3365.
12 K. S. McCully, *Nat. Med.*, 1996, **2**, 386–389.
13 P. Scrimin and L. J. Prins, *Chem. Soc. Rev.*, 2011, **40**, 4488–4505.
14 V. Delplace and J. Nicolas, *Nat. Chem.*, 2015, **7**, 771–784.
15 D.-H. Lee, S. A. Valenzuela, M. N. Dominguez, M. Otsuka, D. J. Milliron and E. V Anslyn, *Cell Reports Phys. Sci.*, 2021, **2**, 100552.
16 X. Sun, A. A. Boulgakov, L. N. Smith, P. Metola, E. M. Marcotte and E. V Anslyn, *ACS Cent. Sci.*, 2018, **4**, 854–861.
17 S. N. Semenov, L. J. Kraft, A. Ainla, M. Zhao, M. Baghbanzadeh, V. E. Campbell, K. Kang, J. M. Fox and G. M. Whitesides, *Nature*, 2016, **537**, 656–660.
18 Y.-H. Chen, W.-C. Chien, D.-C. Lee and K.-T. Tan, *Anal. Chem.*, 2019, **91**, 12461–12467.
19 R. Perry-Feigenbaum, E. Sella and D. Shabat, *Chem. Eur. J.*, 2011, **17**, 12123–12128.
20 J.-A. Gu, V. Mani and S.-T. Huang, *Analyst*, 2015, **140**, 346–352.
21 X. Sun, S. D. Dahlhauser and E. V Anslyn, *J. Am. Chem. Soc.*, 2017, **139**, 4635–4638.
22 K. Arimitsu, M. Miyamoto and K. Ichimura, *Angew. Chem. Int. Ed.*, 2000, **112**, 3567–3570.
23 H. Mohapatra, H. Kim and S. T. Phillips, *J. Am. Chem. Soc.*, 2015, **137**, 12498–12501.
24 H. Kim, M. S. Baker and S. T. Phillips, *Chem. Sci.*, 2015, **6**, 3388–3392.
25 W. Seo and S. T. Phillips, *J. Am. Chem. Soc.*, 2010, **132**, 9234–9235.
26 A. M. DiLauro, G. G. Lewis and S. T. Phillips, *Angew. Chem. Int. Ed.*, 2015, **127**, 6298–6303.
27 G. I. Peterson, M. B. Larsen and A. J. Boydston, *Macromolecules*, 2012, **45**, 7317–7328.
28 T. Wu, X. Feng and X. Sun, *Polym. Chem.*, 2022, **13**, 922–928.
29 B. Klemm, R. W. Lewis, I. Piergentili and R. Eelkema, *Nat. Commun.*, 2022, **13**, 6242.
30 R. W. Lewis, B. Klemm, M. Macchione and R. Eelkema, *Chem. Sci.*, 2022, **13**, 4533–4544.
31 J. Zhuang, B. Zhao, X. Meng, J. D. Schiffman, S. L. Perry, R. W. Vachet and S. Thayumanavan, *Chem. Sci.*, 2020, **11**, 2103–2111.
32 Z. S. Gardner, T. J. Schumacher, C. T. Ronayne, G. P. Kumpati, M. J. Williams, A. Yoshimura, H. Palle, C. Mani, J. Rumbley and V. R. Mereddy, *Bioorg. Med. Chem. Lett.*, 2021, **45**, 128136.
33 L. Meier, M. Ferreira and M. M. Sa, *Heteroat. Chem.*, 2012, **23**, 179–186.
34 G. Martelli, M. Orena and S. Rinaldi, *European J. Org. Chem.*, 2011, **35**, 7199–7206.
35 Y. Du, X. Lu and C. Zhang, *Angew. Chem. Int. Ed.*, 2003, **42**, 1035–1037.
36 X.-L. Liu, L.-Y. Niu, Y.-Z. Chen, Y. Yang and Q.-Z. Yang, *Sensors Actuators B Chem.*, 2017, **252**, 470–476.

37 M. Liu, M. Sovrovic, H. Suga and S. A. K. Jongkees, *Org. Biomol. Chem.*, 2022, **20**, 3081–3085.

38 G. Sicilia, C. Grainger-Boultby, N. Francini, J. P. Magnusson, A. O. Saeed, F. Fernández-Trillo, S. G. Spain and C. Alexander, *Biomater. Sci.*, 2014, **2**, 203–211.

39 Y. Gao, S. Zong, Y. Huang, N. Yang, H. Wen, J. Jiang and J. Duan, *Carbohydr. Polym.*, 2020, **231**, 115690.

40 C. Cho and M. J. Krische, *Angew. Chem. Int. Ed.*, 2004, **43**, 6689–6691.

41 L. E. Overman and E. M. O'Connor, *J. Am. Chem. Soc.*, 1976, **98**, 771–775.

42 L. E. Overman, D. Matzinger, E. M. O'Connor and J. D. Overman, *J. Am. Chem. Soc.*, 1974, **96**, 6081–6089.

43 L. Magee, *Am. Stat.*, 1990, **44**, 250–253.

44 S. Raja, T. Thiruselvi, A. B. Mandal and A. Gnanamani, *Sci. Rep.*, 2015, **5**, 1–11.

45 R. J. Mayer and A. R. Ofial, *Angew. Chem. Int. Ed.*, 2019, **58**, 17704–17708.

46 Y. Lu, L. You and C. Chen, *Chem. Commun.*, 2022, **58**, 12439–12442.

47 I. Altinbasak, S. Kocak, R. Sanyal and A. Sanyal, *Biomacromolecules*, 2022, **23**, 3525–3534.

48 J. Lee, M. N. Silberstein, A. A. Abdeen, S. Y. Kim and K. A. Kilian, *Mater. horizons*, 2016, **3**, 447–451.

49 H. T. Baytekin, B. Baytekin and B. A. Grzybowski, *Angew. Chemie Int. Ed.*, 2012, **51**, 3596–3600.

50 T. Matsuda, R. Kawakami, R. Namba, T. Nakajima and J. P. Gong, *Science.*, 2019, **363**, 504–508.

51 M. K. Beyer and H. Clausen-Schaumann, *Chem. Rev.*, 2005, **105**, 2921–2948.

52 R. Auvergne, M.-H. Morel, P. Menut, O. Giani, S. Guilbert and J.-J. Robin, *Biomacromolecules*, 2008, **9**, 664–671.

53 K. R. Fitch and A. P. Goodwin, *Chem. Mater.*, 2014, **26**, 6771–6776.

54 M.-H. Morel, A. Redl and S. Guilbert, *Biomacromolecules*, 2002, **3**, 488–497.

4.5 SUPPLEMENTARY INFORMATION

4.5.1 Instrumentation, materials and characterisation

All reagents and solvents were used without further purification unless otherwise stated. Methyl 2-(1-acetoxyethyl)acrylate (acrylate-1, 98%), triphenylphosphine-3,3′,3′′-trisulfonic acid trisodium salt (TPPTS, ≥95.0%), N-acetylcysteamine (compound **4**, 95%), N,N-dimethylacrylamide (DMA, 99%), cystamine dihydrochloride (≥98.0%), acetic anhydride (≥99%), methacryloxyethyl thiocarbamoyl rhodamine B, tetramethylethylenediamine (TEMED, 99%) and ammonium persulfate (APS, 98%) were purchased from Sigma Aldrich, TCI Europe or Polysciences Inc. For the preparation of aqueous buffers, solid salts were used: sodium phosphate monobasic and sodium phosphate dibasic, purchased from Sigma Aldrich. Unless stated otherwise, all stock solutions were prepared in D_2O/phosphate buffer mixture 2:8 (0.1 M, pH = 7.6). All buffers were pH adjusted using sodium hydroxide (1 M) and hydrochloric acid (1 M). DMA was passed through basic alumina prior to use to remove inhibitor. ESI-MS was performed using LTQ XL spectrometer equipped with Shimadzu HPLC setup operating at 0.2 mL/min flow rate with water/MeCN mobile phase containing 0.1 vol% formic acid and Discovery C18 column. Photographs of the hydrogels were taken on a Canon EOS 600D single reflex camera with a Canon Macro Lens EF 100 mm 1:2.8 USM. UV-vis spectroscopic experiments were performed with an Analytik Jena Specord 250 spectrophotometer using quartz cuvettes with a 1 mm path length, a volume of 0.4 mL and a temperature controller set to 25°C used for all UV-Vis related experiments.

4.5.2 NMR spectroscopy

NMR spectra were recorded on an Agilent-400 MR DD2 NMR instrument at 25°C (399.7 MHz for ^{1}H, 100.5 MHz for ^{13}C and 161.9 MHz for ^{31}P) using residual solvent signals as internal reference. Sodium trimethylsilylpropanesulfonate (DSS) was used as internal standard for NMR kinetic experiments with reference resonance at 0.0 ppm. To suppress the water peak, PRESAT or ES_suppression configuration (suppress one highest peak) was used. NMR spectra were processed by MNova NMR software (Mestrelab Research).

4.5.2.1 Fitting pseudo-first order reaction rate

The pseudo-first order reaction rate constants were determined by fitting the conversion of SM3 ([B]t) over time with the following equation:

$$\ln\left(\frac{[B]_t}{[B]_0}\right) = -k[A]_0 * t \qquad \textbf{Eq.1}$$

$[B]_0$ = initial concentration of compound **1** at t = 0, 0.067 mM (1.0 eq.); $[B]_t$ = the concentration of **1** at every time point obtained from ^{1}H NMR, with DSS as the standard; *k* is the pseudo-first order reaction rate constant ($M^{-1}*h^{-1}$) and $[A]_0$ = initial concentration of nucleophile (0.2 eq.).

4.5.3 Hydrogel preparation

DMA–BAC hydrogels (3.5% wt%) were synthesised by free radical polymerization. In all cases monomer mole ratios were BAC: DMA:Methacryloxyethyl thiocarbamoyl rhodamine B of 1:14:0.001. Typically, DMA (110 mg, 1.1 mmol) and BAC (20 mg, 0.08 mmol) were dissolved in deionized water (2.9 mL). Stock solutions of methacryloxyethyl thiocarbamoyl rhodamine B (50 µL, 0.04 mg, 1 µmol in DMSO) and TEMED (50 µL, 14.2 mg, 0.12 mmol) were prepared and added to the reaction mixture. Nitrogen was bubbled through the solution for 2 minutes. The polymerization was initiated by addition of APS solution (50 µL, 14 mg, 0.06 mmol) and quickly added to a mould where the mixture was allowed to proceed at room temperature. Gel formation occurred within 1 h. The hydrogels were removed from their mould and dialyzed for 48 hours against water.

4.5.3.1 Remaining thiol removal: post treatment of hydrogels

To eliminate any remaining thiols within the gel matrix, the gels were submerged in 1 mL of phosphate buffer (0.1 M, pH = 7.6) containing acrylate-1 (5.0 mg/mL). The gels were left in solution for 8 hours to react and hereafter were dialyzed for 48 hours against water before further usage.

4.5.3.2 Water content of hydrogels

The water content of the hydrogels was determined by using the gravimetric method. The wet weight (W_w) was measured after removing surface moisture of the hydrogel by wiping with a lens cleaning paper. The hydrogels were then dried in a drying oven for 24 hours at 50°C. Hereafter, the dried gels were weighed and the dry weight (W_d) was recorded. The water content was calculated according to Eq. 2:

$$water\ content\ (\%) = \frac{W_w - W_d}{W_w} * 100 \qquad \textbf{Eq.2}$$

Measurements were performed in duplicate and the results of water content was expressed as the mean ± standard deviation.

4.5.4 UV-vis spectroscopy

4.5.4.1 Calibration lines

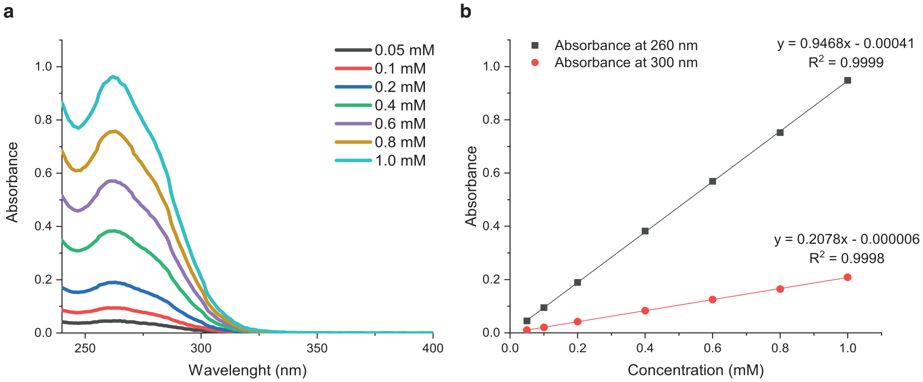

Figure S1: Extinction coefficient for TPPTS in phosphate buffer (0.1 M, pH = 7.6) at 260 nm: 4.74 $mM^{-1}cm^{-1}$ and at 300 nm: 1.04 $mM^{-1}cm^{-1}$. **(a)** UV-vis absorbance spectra of TPPTS at different concentrations. **(b)** Absorbance at 260 and 300 nm of TPPTS at different concentrations.

4.5.4.2 UV-vis experiments for nucleophilic substitution reaction

Stock solutions of compound **1** and **4** were prepared in phosphate buffer (0.1 M, pH = 7.6). The experiments were performed using 2.0 mM of **1** (0.74 mg, 1.0 eq.) and varying concentration of **4** (0.05, 0.10, 0.20, 0.25, 0.30, 0.35 and 0.40 eq.). The stock solution of **1** was added first to the UV-cuvette, followed by the addition of **4**, then shaken for 5 seconds and hereafter placed immediately in the UV-vis spectrophotometer for analysis. UV-vis spectra were recorded at wavelength of 260 nm every 30s for 19 hours at a constant temperature (set to 25°C).

4.5.4.3 UV-vis experiments for amplification cycle reaction

Stock solutions of compound **1**, **3** and **4** were prepared in phosphate buffer (0.1 M, pH = 7.6). The experiments were performed using 9.0 mM of **1** (3.33 mg, 1.0 eq.), 13.5 mM of **3** (1.6 mg, 1.5 eq.) and varying concentration of **4** (0.10, 0.15 and 0.20 eq.). The stock solution of **1** and **3** was added first to the UV-cuvette, followed by the addition of **4**, then shaken for 5 seconds and hereafter placed immediately in the UV-vis spectrophotometer for analysis. UV-vis spectra were recorded at wavelength of 300 nm every 30s for 36 hours at a constant temperature (set to 25°C).

4.5.5 Molecular stability tests

4.5.5.1 NMR observation of compound 1 in buffer media

Compound **1** (5.0 mg, 6.75 µM, 1.0 eq.) and DSS internal standard (1.47 mg, 1.0 eq.) were dissolved in 0.5 mL D_2O/phosphate buffer (2:8, 0.1 M, pH = 7.6). The reaction was followed by ^1H NMR spectroscopy for 24 hours.

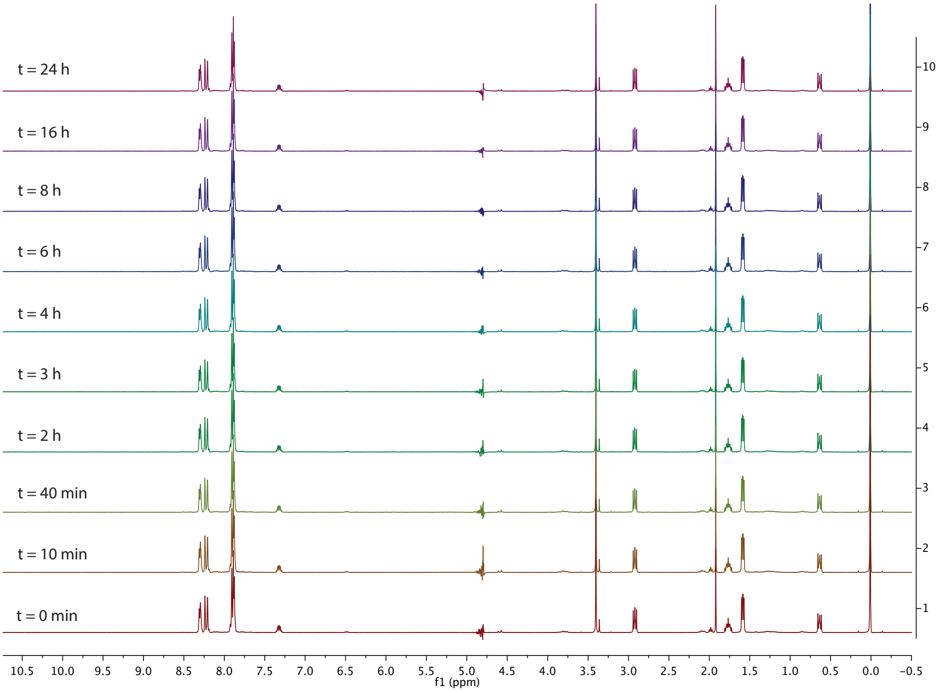

Figure S2: Stability observation of **1** in ^1H NMR at different time points for 24 hours. The reaction was carried out in D_2O/phosphate buffer mixture 2:8 (0.1 M, pH = 7.6). The spectra were aligned with the D_2O peak. The peak attributed to ~ 0.0 ppm corresponds to DSS internal standard.

4.5.5.2 NMR observation of compound 1 in cell-culture media

Compound **1** (5.0 mg, 6.75 µM, 1.0 eq.) and DSS internal standard (1.47 mg, 1.0 eq.) were dissolved in 0.5 mL D_2O/Dulbecco's Modified Eagle Medium (DMEM) 2:8. The reaction was followed by ^1H NMR spectroscopy for 22 hours.

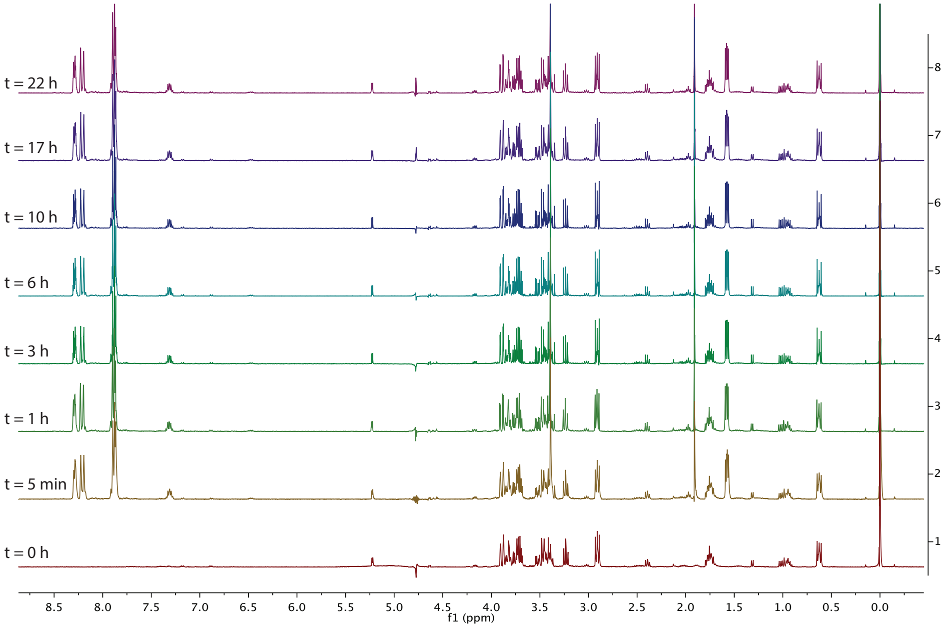

Figure S3: Stability observation of **1** in ^1H NMR at different time points for 22 hours. The reaction was carried out in D_2O/Dulbecco's Modified Eagle Medium (2:8). The spectra were aligned with the D_2O peak. The peak attributed to ~ 0.0 ppm corresponds to DSS internal standard.

4.5.5.3 NMR observation of TPPTS in buffer media

TPPTS (3.84 mg, 6.75 µM, 1.0 eq.) and DSS internal standard (1.47 mg, 1.0 eq.) were dissolved in 0.5 mL D_2O/phosphate buffer (2:8, 0.1 M, pH = 7.6). The reaction was immediately followed by NMR for 24 hours.

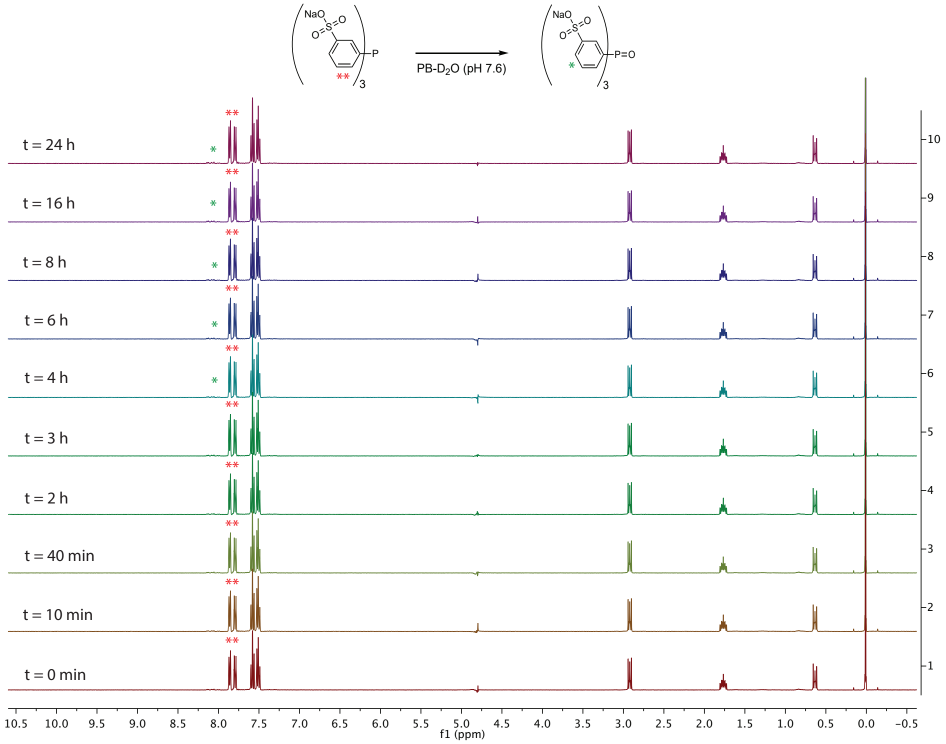

Figure S4: Stability observation of TPPTS in ^{1}H NMR at different time points for 24 hours. The reaction was carried out in D_2O/phosphate buffer mixture 2:8 (0.1 M, pH = 7.6). The spectra were aligned with the D_2O peak. The peak attributed to ~ 0.0 ppm corresponds to DSS internal standard.

4.5.5.4 NMR observation of 1 and 2 in buffer media

Compound **3** (1.91 mg, 8.10 µM, 1.5 eq.), acrylate-1 (3.49 mg, 3.0 eq.) and DSS internal standard (1.47 mg, 1.0 eq.) were mixed in 0.4 mL phosphate buffer (pH = 7.6) and shaken for 30 minutes. To this solution compound **1** (5.0 mg, 1.0 eq.) in 0.1 mL H_2O was added and the mixture was shaken for another 30 minutes before freeze dried. The remains were solubilized in 0.5 mL (H_2O/D_2O 8:2). The final solvent conditions were 0.5 mL D_2O/phosphate buffer 2:8, 0.1 M, pH = 7.6). The reaction was immediately followed by ^{1}H NMR spectroscopy for 24 hours.

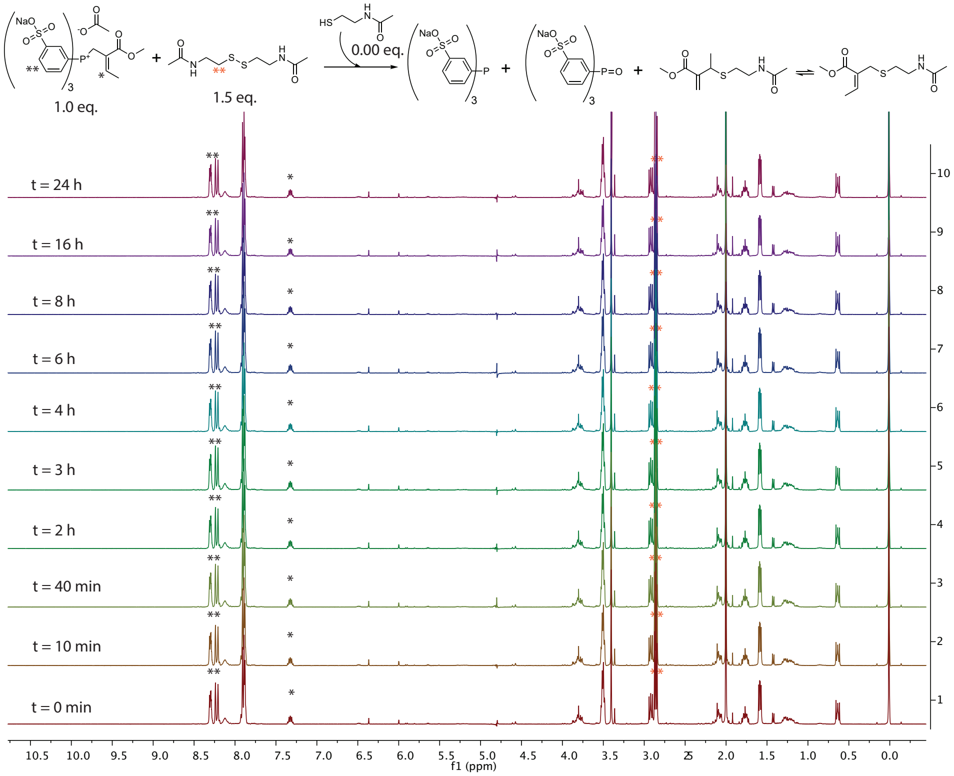

Figure S5: Stability observation of compound **1** and **2** in ^{1}H NMR at different time points for 24 hours. The reaction was carried out in D_2O/phosphate buffer mixture 2:8 (0.1 M, pH = 7.6). The spectra were aligned with the D_2O peak. The peak attributed to ~ 0.0 ppm corresponds to DSS internal standard.

4.5.6 Kinetic experiments of nucleophilic reactivity

4.5.6.1 NMR observation of reactivity of compound 1 with 20% L-glutathione signal (SH-nucleophile)

Compound **1** (5.0 mg, 6.75 µM, 1.0 eq.) and DSS internal standard (1.47 mg, 1.0 eq.) were mixed in 0.4 mL D_2O/phosphate buffer 2:8, 0.1 M, pH = 7.6 and shaken. To this solution L-glutathione (0.41 mg, 0.2 eq.) in 0.1 mL phosphate buffer was added and the mixture was shortly shaken and immediately followed by ^{1}H NMR spectroscopy.

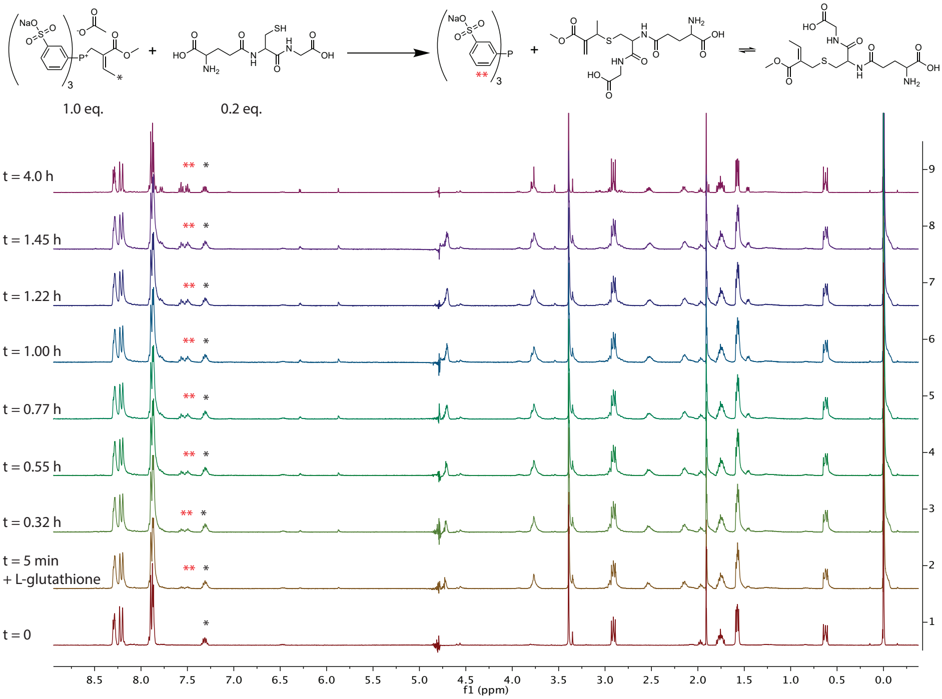

Figure S6: Reactivity study of compound **1** with L-glutathione in ^1H NMR at different time points for 4 hours. The reaction was carried out in D_2O/phosphate buffer mixture 2:8 (0.1 M, pH = 7.6). The spectra were aligned with the D_2O peak. The peak attributed to ~ 0.0 ppm corresponds to DSS internal standard.

4.5.6.2 NMR observation of reactivity of compound 1 with 20% N-acetyl cysteine signal (SH-nucleophile)

Compound **1** (5.0 mg, 6.75 µM, 1.0 eq.) and DSS internal standard (1.47 mg, 1.0 eq.) were mixed in 0.4 mL D_2O/phosphate buffer 2:8, 0.1 M, pH = 7.6 and shaken. To this solution N-acetyl cysteine (0.23 mg, 0.2 eq.) in 0.1 mL phosphate buffer was added and the mixture was shortly shaken and immediately followed by ^1H NMR spectroscopy.

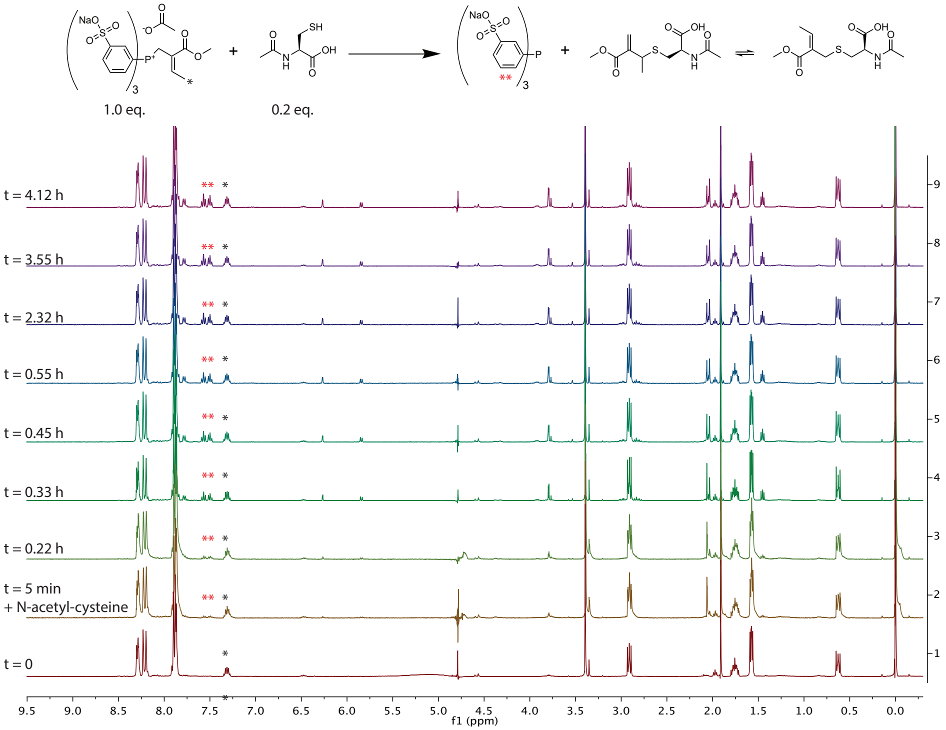

Figure S7: Reactivity study of compound **1** with N-acetyl cysteine in ^{1}H NMR at different time points for 4 hours. The reaction was carried out in D_2O/phosphate buffer mixture 2:8 (0.1 M, pH = 7.6). The spectra were aligned with the D_2O peak. The peak attributed to ~ 0.0 ppm corresponds to DSS internal standard.

4.5.6.3 NMR observation of reactivity of compound 1 with 20% L-proline signal (NH-nucleophile)

Compound **1** (5.0 mg, 6.75 µM, 1.0 eq.) and DSS internal standard (1.47 mg, 1.0 eq.) were mixed in 0.4 mL D_2O/phosphate buffer 2:8, 0.1 M, pH = 7.6 and shaken. To this solution L-proline (0.13 mg, 0.2 eq.) in 0.1 mL phosphate buffer was added and the mixture was shortly shaken and immediately followed by ^{1}H NMR spectroscopy.

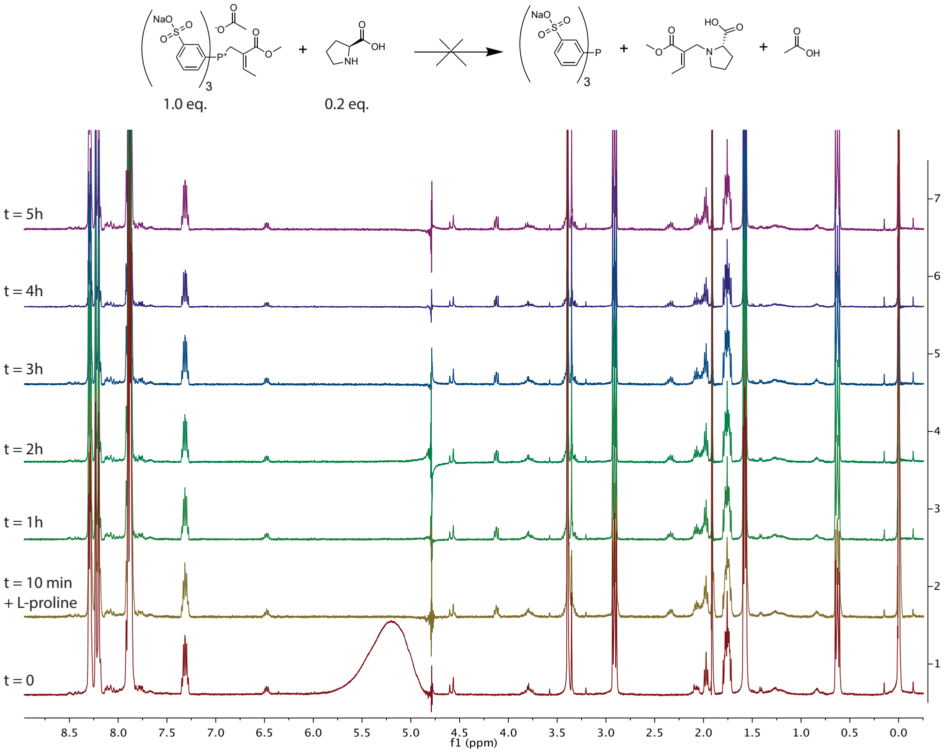

Figure S8: Reactivity study of compound **1** with L-proline in ^{1}H NMR at different time points for 5 hours. The reaction was carried out in D_2O/phosphate buffer mixture 2:8 (0.1 M, pH = 7.6). The spectra were aligned with the D_2O peak. The peak attributed to ~ 0.0 ppm corresponds to DSS internal standard.

4.5.6.4 NMR observation of reactivity of compound 1 with 20% L-phenylalanine signal (NH_2-nucleophile)

Compound **1** (5.0 mg, 6.75 µM, 1.0 eq.) and DSS internal standard (1.47 mg, 1.0 eq.) were mixed in 0.4 mL D_2O/phosphate buffer 2:8, 0.1 M, pH = 7.6 and shaken. To this solution L-phenylalanine (0.16 mg, 0.2 eq.) in 0.1 mL phosphate buffer was added and the mixture was shortly shaken and immediately followed by ^{1}H NMR spectroscopy.

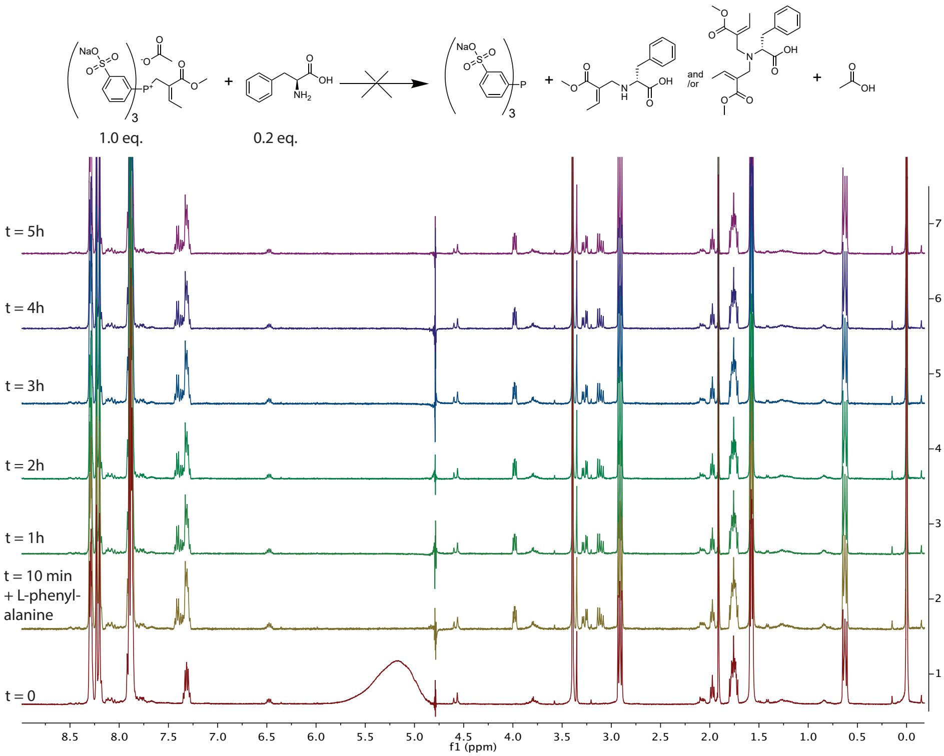

Figure S9: Reactivity study of compound **1** with L-phenylalanine in ^{1}H NMR at different time points for 5 hours. The reaction was carried out in D_2O/phosphate buffer mixture 2:8 (0.1 M, pH = 7.6). The spectra were aligned with the D_2O peak. The peak attributed to ~ 0.0 ppm corresponds to DSS internal standard.

4.5.6.5 NMR observation of reactivity of compound 1 with 20% p-nitrophenol signal (O-nucleophile)

Compound **1** (5.0 mg, 6.75 µM, 1.0 eq.) and DSS internal standard (1.47 mg, 1.0 eq.) were mixed in 0.4 mL D_2O/phosphate buffer 2:8, 0.1 M, pH = 7.6 and shaken. To this solution p-nitrophenol (0.19 mg, 0.2 eq.) in 0.1 mL phosphate buffer was added and the mixture was shortly shaken and immediately followed by ^{1}H NMR spectroscopy.

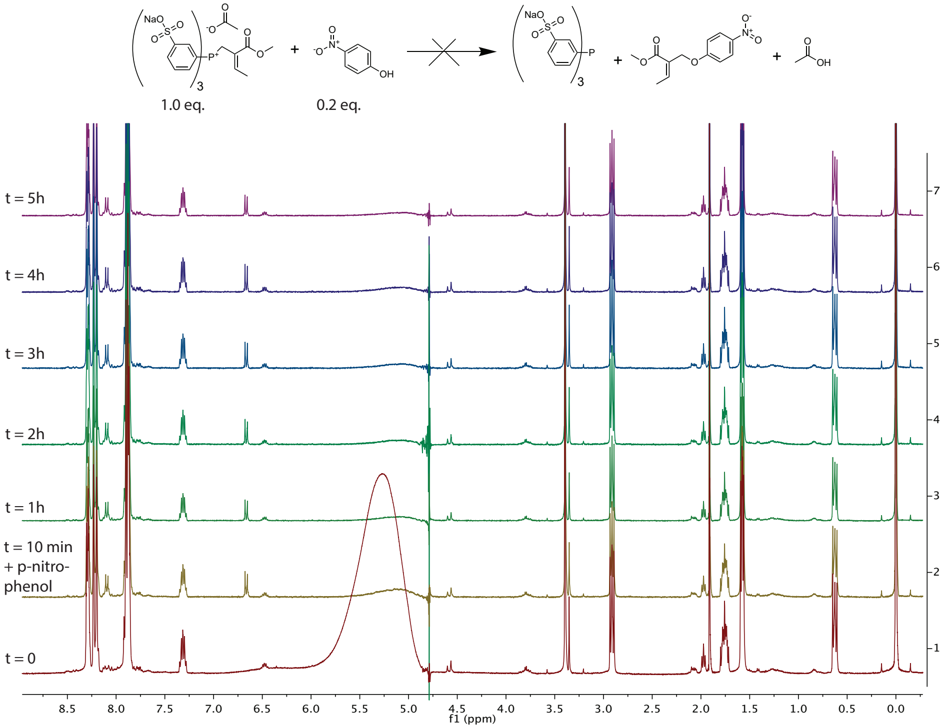

Figure S10: Reactivity study of compound **1** with p-nitrophenol in ^{1}H NMR at different time points for 5 hours. The reaction was carried out in D_2O/phosphate buffer mixture 2:8 (0.1 M, pH = 7.6). The spectra were aligned with the D_2O peak. The peak attributed to ~ 0.0 ppm corresponds to DSS internal standard.

4.5.7 Kinetic experiments of signal-amplification cycle

4.5.7.1 NMR observation of signal-amplification cycle with 5% signal

Compound **3** (1.91 mg, 8.10 µM, 1.5 eq.), acrylate-2 (3.49 mg, 3.0 eq.) and DSS internal standard (1.47 mg, 1.0 eq.) were mixed in 0.4 mL phosphate buffer (pH = 7.6) and shaken for 30 minutes. To this solution compound **1** (5.0 mg, 1.0 eq.) in 0.1 mL H_2O was added and the mixture was shaken for another 30 minutes before freeze dried. The remains were solubilized in 0.5 mL (H_2O/D_2O 8:2). The final solvent conditions were 0.5 mL D_2O/phosphate buffer 2:8, 0.1 M, pH = 7.6). The reaction was immediately followed by ^{1}H NMR spectroscopy to capture t = 0. At t = 10 minutes, compound **4** (0.04 mg, 0.05 eq.) was added to the NMR tube and the reaction was continuously measured at the appropriate time points over 24 hours.

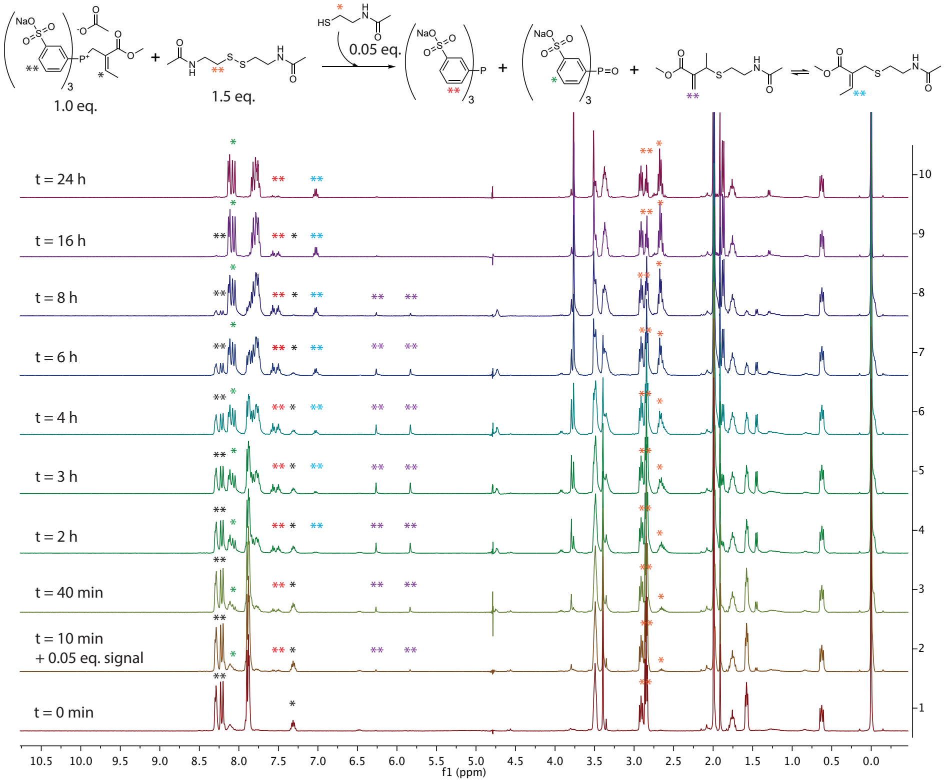

Figure S11: Auto-amplification cycle observation with 5% SH-signal in ^{1}H NMR at different time points for 24 hours. The reaction was carried out in D_2O/phosphate buffer mixture 2:8 (0.1 M, pH = 7.6). The spectra were aligned with the D_2O peak. The peak attributed to ~ 0.0 ppm corresponds to DSS internal standard.

4.5.8 Kinetic model

4.5.8.1 UV-vis spectroscopy – rate constant determination

The nucleophilic substitution reaction (1), was performed at pseudo-first order regime - kinetics by using one of the reactants in excess. We performed kinetic experiments using 0.002 M (1.0 eq.) of **1** and exposed it to 0.0002 M (0.1 eq.) of **4**. All measurements were carried out in 0.1 M phosphate buffer (pH = 7.6) and at room temperature 25 °C. The pH was verified after the reaction was completed (~20 hours), and no change was observed.

Nucleophilic substitution reaction (1)

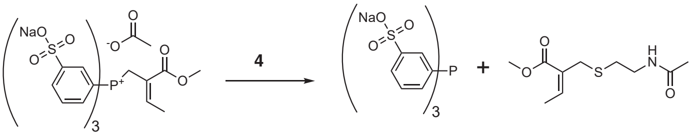

1 **TPPTS** **2**

t = 0	$[A]_0$	$[A]_0$	0
t = t	$[A]_t = [A]_0 – [C]_t$	$[B]_t = [B]_0 – [C]_t$	$[C]_t$

$[A]_0$ is the excess compound **1** concentration, [B] the concentration of compound **4** and $[C]_t$ the product TPPTS concentration over time. The pseudo first-order regime - reaction rate constant was determined by fitting the production of TPPTS over time with the following equation:

$$ln\left[1-\frac{[C]_t}{[B]_0}\right] = -k_1[A]_0t \qquad \textbf{Eq.3}$$

, where $[B]_0$ = initial concentration of **4** at t_0, 0.0002 M; $[C]_t$ = the concentration of TPPTS at every specified time obtained from UV-vis spectroscopy (Figure S12a); k_1 is the rate constant ($M^{-1}\ s^{-1}$), $[A]_0$ = initial concentration of **1**, 0.002 M. Similarly, for the disulfide reduction reaction (2), we used compound **3** in excess of 30 mM (1.0 eq.) and exposed it to 3.0 mM (0.1 eq.) of TPPTS. All measurements were carried out in 0.1M phosphate buffer (pH = 7.6) and at room temperature 25 °C. The pH was verified after the reaction was completed (~25 hours), and no change was observed.

Disulfide reduction reaction (2)	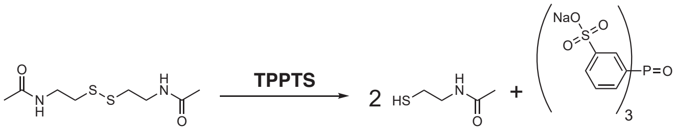 **3**	**4**	**OTPPTS**
t = 0	$[A]_0$	$[A]_0$	0
t = t	$[A]_t = [A]_0 – [C]_t$	$[B]_t = [B]_0 – [C]_t$	$[C]_t$

$[A]_0$ is the excess compound 3 concentration, [B] the concentration of TPPTS and $[C]_t$ is the product OTPPTS concentration over time. The pseudo first-order reaction rate constant was determined by fitting the conversion of TPPTS over time with the following equation:

$$ln\left[\frac{[B]_t}{[B]_0}\right] = -k_2[A]_0t \qquad \textbf{Eq.4}$$

, where $[B]_0$ = initial concentration of 3 at t_0, 0.030 M; $[B]_t$ = the concentration of TPPTS at every specified time point, obtained from UV-vis spectroscopy (Figure S12b); k_2 is the reaction rate constant ($M^{-1}\ s^{-1}$), $[A]_0$ = initial concentration of TPPTS, 0.003 M.

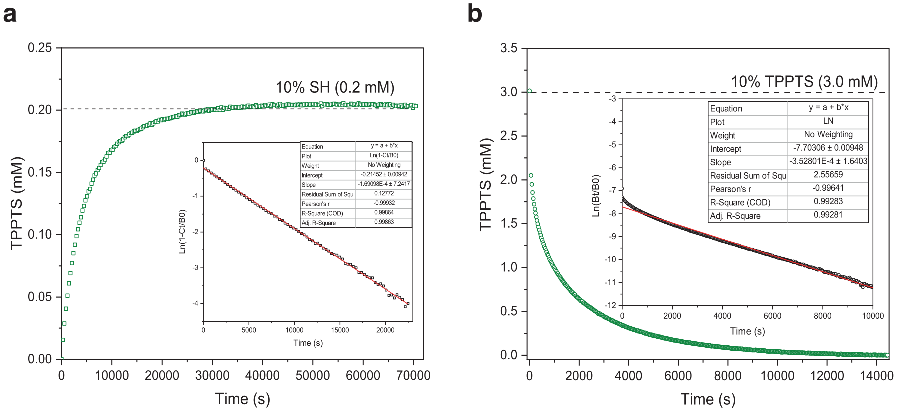

Figure S12: TPPTS concentrations obtained by UV-vis measurement and calculated slopes for the (a) nucleophilic substitution and (b) disulfide reduction reaction. Conditions: (a) 0.002 M (1.0 eq.) of **1** and 0.0002 M (0.1 eq.) of **4**, (b) 0.030 M (1.0 eq.) of **3** and 0.003 M (0.1 eq.) of TPPTS in 0.1 M phosphate buffer (pH = 7.6) at 25 °C.

The linearity of ln(1-[C_t]/[B_0]) and ln[B_t]/[B_0] versus time graphs gave the reaction rate constants of k_1 = 8.450*10^{-2} $M^{-1}s^{-1}$ and k_2 = 1.176*10^{-2} $M^{-1}s^{-1}$ for the nucleophilic substitution and disulfide reduction reaction, respectively.

4.5.8.2 Forward reaction: TPPTS release modelling

A simplified mathematical model was developed based on a set of linear differentials describing the nucleophilic substitution reaction of **1** with **4** and solved numerically for a series of reactions, which were compared to experimental measurements from UV-vis. To begin we developed a one-step reaction model, based on Scheme S1:

Scheme S1: Forward reaction (nucleophilic substitution) of **1** with **4** for one-step model.

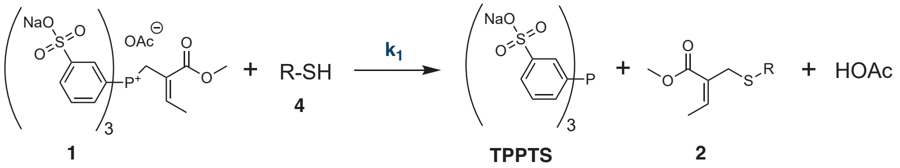

Rate equations of all compounds involved in the TPPTS release were established according to a one-step second order reaction model, as shown below:

$$\frac{d[TPPTS]}{dt} = +k_1.[1].[4] \quad \textbf{Eq. 5}$$

$$\frac{d[1]}{dt} = -k_1.[1].[4] \quad \textbf{Eq. 6}$$

$$\frac{d[4]}{dt} = -k_1.[1].[4] \quad \textbf{Eq. 7}$$

$$\frac{d[2]}{dt} = +k_1.[1].[4] \quad \textbf{Eq. 8}$$

$$\frac{d[HOAc]}{dt} = +k_1.[1].[4] \quad \textbf{Eq. 9}$$

This set of ordinary differential equations was then solved over the experimental timeframe. The rate constant measured in the pseudo-first-order regime (Section 4.1) was used to achieve the TPPTS concentration profiles at different signal levels (thiol concentration). Figure S13, illustrates the comparison between model predictions and the measured TPPTS concentration progression. By using the experimentally determined k_1-value for the prediction of TPPTS release, we found that the model cannot predict satisfactory the experimental data for low concentrations of SH-input **4**.

After attempts at optimizing the rate constant, no single value was found to make the predictions match the experimental TPPTS concentration progression. Thus, inspired by previous work from Krische and coworkers[1], on the mechanism of this reaction a two-step reaction model was proposed, as shown in Scheme S2:

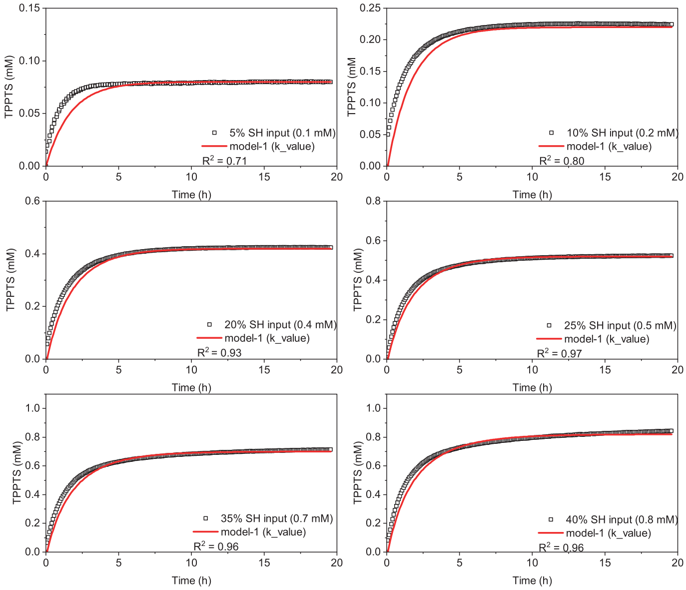

Figure S13: TPPTS concentrations obtained by UV-vis measurement and model predictions (red line) with one-step reaction pathway using experimentally determined k_1-value for different concentrations of SH-signal input. Conditions: 0.002 M (1.0 eq.) of **1** and appropriate amounts of **4** in 0.1 M phosphate buffer (pH =7.6) at room temperature 25 °C. All experimental measurements were done in duplicate. R^2 values are shown as indicator for fitting between experimental measurements and model prediction.

Scheme S2: Forward reaction (nucleophilic substitution) of **1** with **4** for two-step model.

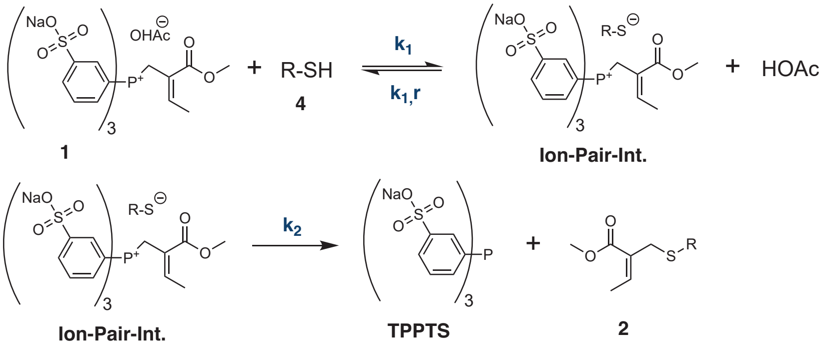

In this mechanism, a reversible acid/base reaction between (acetate) and (thiol), leads to the formation of an intermediate compound (Ion-Pair-Int.), which decomposes to TPPTS and **2**. Following, rate equations were developed according to this new model, as shown below:

$$\frac{d[TPPTS]}{dt} = +k_2.[Ion - Pair - Int.] \qquad \textbf{Eq. 10}$$

$$\frac{d[1]}{dt} = -k_1.[1].[4] + k_{1r}.[Ion - Pair - Int.].[HOAc] \qquad \textbf{Eq. 11}$$

$$\frac{d[4]}{dt} = -k_1.[1].[4] + k_{1r}.[Ion - Pair - Int.].[HOAc] \qquad \textbf{Eq. 12}$$

$$\frac{d[2]}{dt} = +k_2.[Ion - Pair - Int.] \qquad \textbf{Eq. 13}$$

$$\begin{aligned}\frac{d[Ion - Pair - Int.]}{dt} &= +k_1.[1].[4] - k_{1r}.[Ion - Pair - Int.].[HOAc] \\ &\quad - k_2.[Ion - Pair - Int.]\end{aligned} \qquad \textbf{Eq. 14}$$

$$\frac{d[HOAc]}{dt} = +k_1.[1].[4] - k_{1r}.[Ion - Pair - Int.].[HOAc] \qquad \textbf{Eq. 15}$$

These new rate constants were then calculated by fitting the model predicted TPPTS concentration profile to the experimental data. By using least squares method, k_1, k_{1r} and k_2 were determined to be 0.1314 $M^{-1}s^{-1}$, 0.998 M^{-1} s^{-1} and 0.0020 $M^{-1}s^{-1}$.

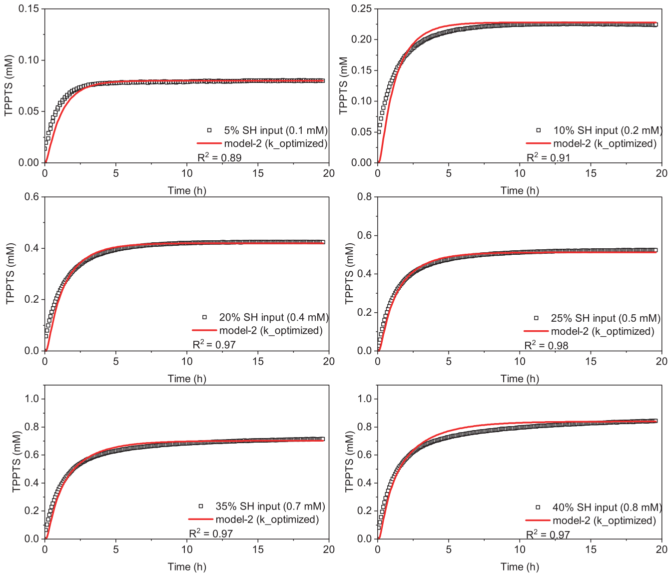

Figure S14: TPPTS concentrations obtained by UV-vis measurement and model predictions (red line) with two-step reaction pathway using the optimized k-values for different concentrations of SH-signal input. Conditions: 0.002 M (1.0 eq.) of **1** and appropriate amounts of **4** in 0.1 M phosphate buffer (pH = 7.6) at room temperature 25 °C. All experimental measurements were done in duplicate. R^2 values are shown as indicator for fitting between experimental measurements and model prediction.

Accuracy of the predicted TPPTS concentration profiles with the two-step model, using above rate constants, were measured at different initial concentrations. By using the optimized k-values for the prediction of TPPTS release, we found good agreement between model and the experimental data for a variety of SH-input **4** (Figure S14).

4.5.8.3 Backward reaction: disulfide reduction modelling

A simplified mathematical model was developed based on a set of linear differentials describing the disulfide reduction reaction of **3** with TPPTS and solved numerically for a series of reactions, which were compared to experimental measurements from UV-vis. To begin we developed a one-step reaction model, based on Scheme S3:

Scheme S3: Backward reaction (disulfide reduction) of **3** with TPPTS for one-step model.

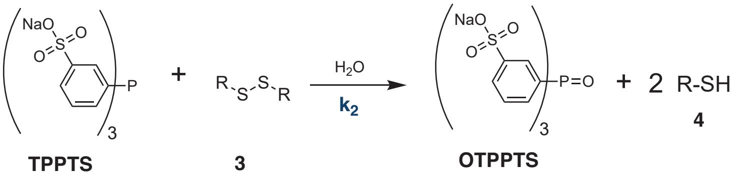

Rate equations for all of the species in the disulfide reduction, based on a one-way second order reaction rate, have been developed as following:

$$\frac{d[TPPTS]}{dt} = -k_2.[TPPTS].[3]$$ **Eq. 16**

$$\frac{d[3]}{dt} = -k_2.[TPPTS].[3]$$ **Eq. 17**

$$\frac{d[OTPPTS]}{dt} = k_2.[TPPTS].[3]$$ **Eq. 18**

$$\frac{d[4]}{dt} = 2.k_2.[TPPTS].[3]$$ **Eq. 19**

By using the rate constant attained through pseudo-first order analysis, the aforementioned system of ordinary differential equations was solved with the initial concentrations, resulting in concentration profiles for all the species over the experimental timeframe. Figure S15, illustrates the comparison between the predictions and actual TPPTS concentration profiles at different initial conditions. We found that the model cannot predict satisfactory the experimental data for all concentrations of TPPTS.

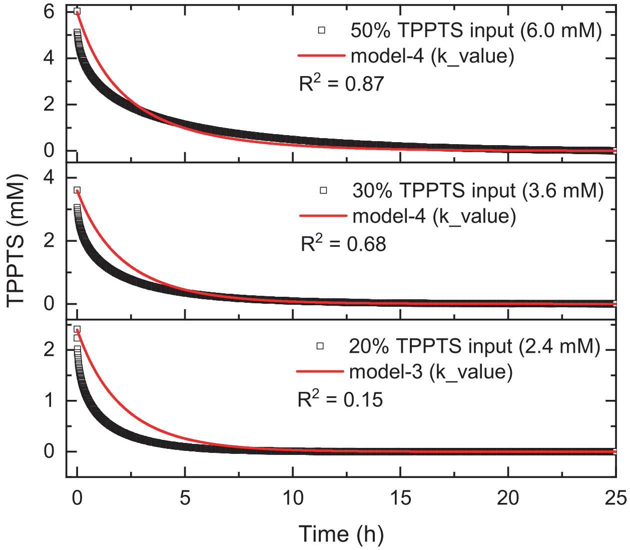

Figure S15: TPPTS concentrations obtained by UV-vis measurement and model predictions (red line) with one-step reaction pathway using the experimentally determined k_2-value for different concentrations of TPPTS input. Conditions: 0.012 M (1.0 eq.) of **3** and appropriate amounts of TPPTS in 0.1 M phosphate buffer (pH = 7.6) at 25 °C. All experimental measurements were done in duplicate. R^2 values are shown as indicator for fitting between experimental measurements and model prediction.

Simply optimizing the rate constant did not significantly reduce the discrepancy between the predictions and the actual data. Instead, a two-step model was proposed as described by Bach and coworkers[2], forming a phosphine-thiol intermediate (PR_3^+-thiol-Int.) and releasing one thiol **4** within each step, according to Scheme S4:

Scheme S4: Backward reaction (disulfide reduction) of **3** with TPPTS for two-step model.

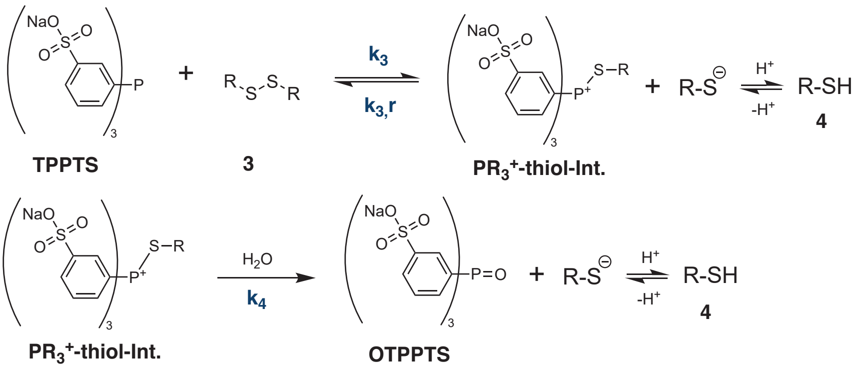

Following rate equations were developed according to this new model, as shown below:

$$\frac{d[TPPTS]}{dt} = -k_3.[TPPTS].[3] + k_{3r}.[PR_3^+ - thiol - int.].[4] \qquad \textbf{Eq. 20}$$

$$\frac{d[3]}{dt} = -k_3.[TPPTS].[3] + k_{3r}.[PR_3^+ - thiol - int.].[4] \qquad \textbf{Eq. 21}$$

$$\frac{d[OTPPTS]}{dt} = k_4.[PR_3^+ - thiol - int.] \qquad \textbf{Eq. 22}$$

$$\frac{d[4]}{dt} = k_3.[TPPTS].[3] - k_{3r}.[PR_3^+ - thiol - int.].[4] + k_4.[PR_3^+ - thiol - int.] \qquad \textbf{Eq. 23}$$

$$\frac{d[PR_3^+ - thiol - int.]}{dt} = k_3.[TPPTS].[3] - k_{3r}.[PR_3^+ - thiol - int.].[4] - k_4.[PR_3^+ - thiol - int.] \qquad \textbf{Eq. 24}$$

The TPPTS concentration profile, predicted by the new model, was fitted to the experimental findings and through least squares method the rate constants were achieved. k_3, k_{3r} and k_4 are 9.3*10^{-2} $M^{-1}s^{-1}$, 0.74 $M^{-1}s^{-1}$ and 7.1*10^{-4} $M^{-1}s^{-1}$, respectively. These values were consistent over changes in initial conditions. Figure S16, compares the predictions with the optimized rate constants to the actual experimental data. By using the optimized *k*-values for the prediction of TPPTS conversion, we found excellent agreement between model and the experimental data (Figure S16).

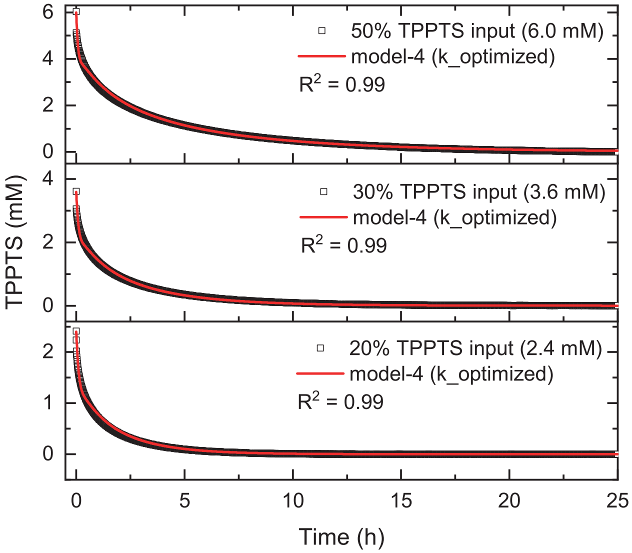

Figure S16: TPPTS concentrations obtained by UV-vis measurement and model predictions (red line) with two-step reaction pathway using the optimized *k*-values for different concentrations of TPPTS input. Conditions: 0.012 M (1.0 eq.) of **3** and appropriate amounts of TPPTS in 0.1 M phosphate buffer (pH = 7.6) at 25 °C. All experimental measurements were done in duplicate. R^2 values are shown as indicator for fitting between experimental measurements and model prediction.

4.5.9 Hydrogels – signal-amplification experiments

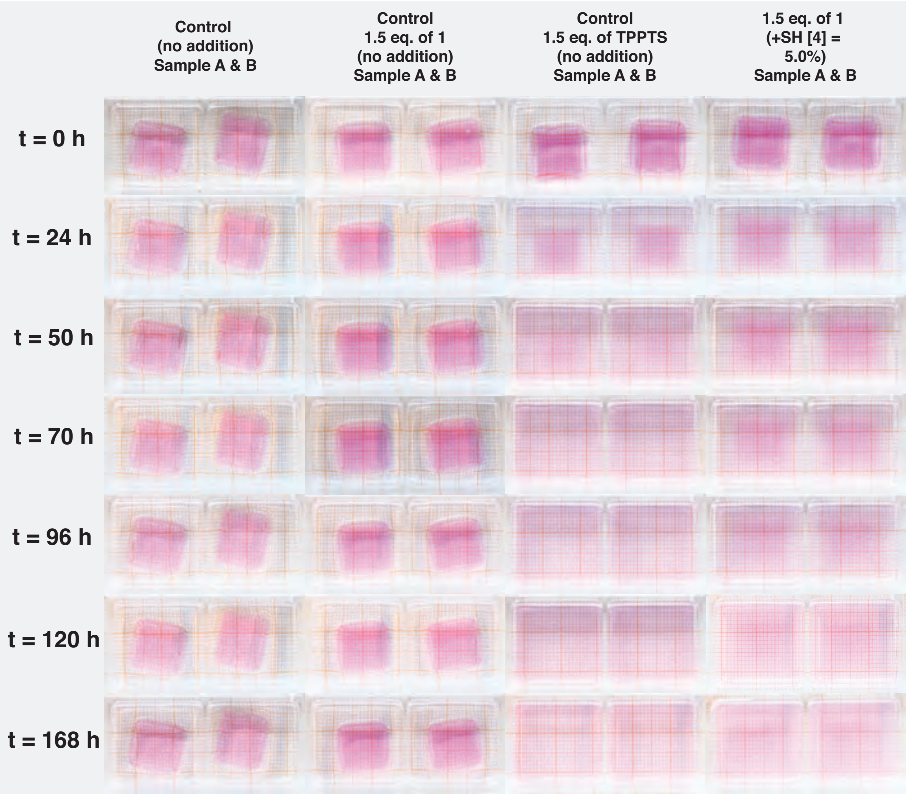

Figure S17: Time lapse photographs (in duplicate) of hydrogel degradation using the self-amplification system triggered by SH-analytes. (a) Control gels with 1) no additives, 2) with 1.5 eq. of **1**, 3) 1.5 eq. of TPPTS and 4) 1.5 eq. of **1** and 5% (0.05 eq.) of **4**. (b) Gels with 1.5 eq. of **1** and SH-trigger addition of 1) 1.0% (0.01 eq.) of glutathione, 2) 0.1% (0.001 eq.) of bovine serum albumin and 3) 0.001% (0.00001 eq.) of thiol functionalized DNA. Conditions: gels were submerged in 1.5 mL phosphate buffer (0.1 M, pH = 7.6).

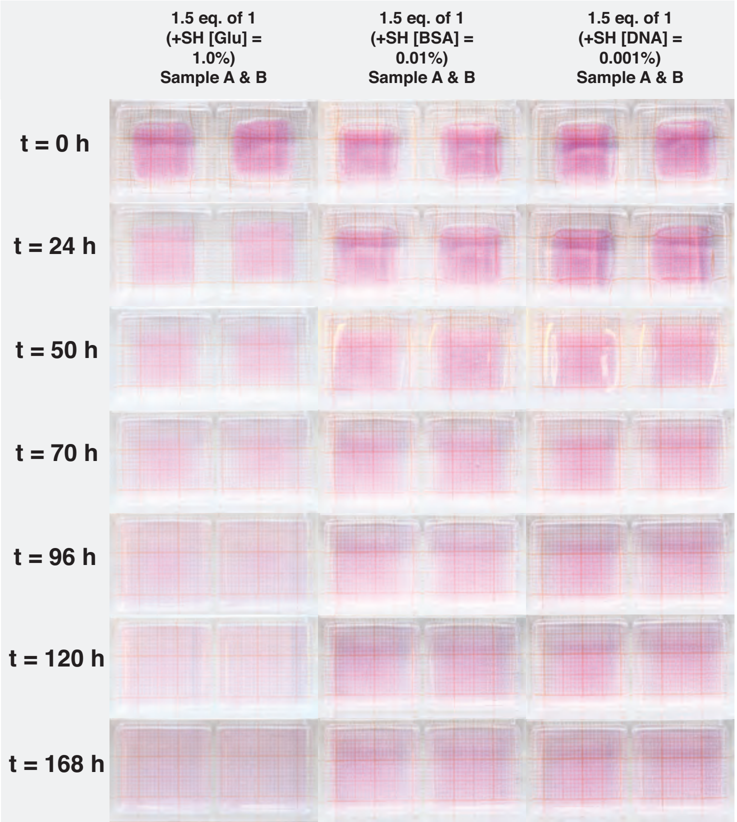

Figure S18: Time lapse photographs (in duplicate) of hydrogel degradation using the self-amplification system triggered by SH-analytes. Gels with 1.5 eq. of **1** and SH-trigger addition of 1) 1.0% (0.01 eq.) of glutathione, 2) 0.01% (0.0001 eq.) of bovine serum albumin and 3) 0.001% (0.00001 eq.) of thiol functionalized DNA. Conditions: gels were submerged in 1.5 mL phosphate buffer (0.1 M, pH = 7.6).

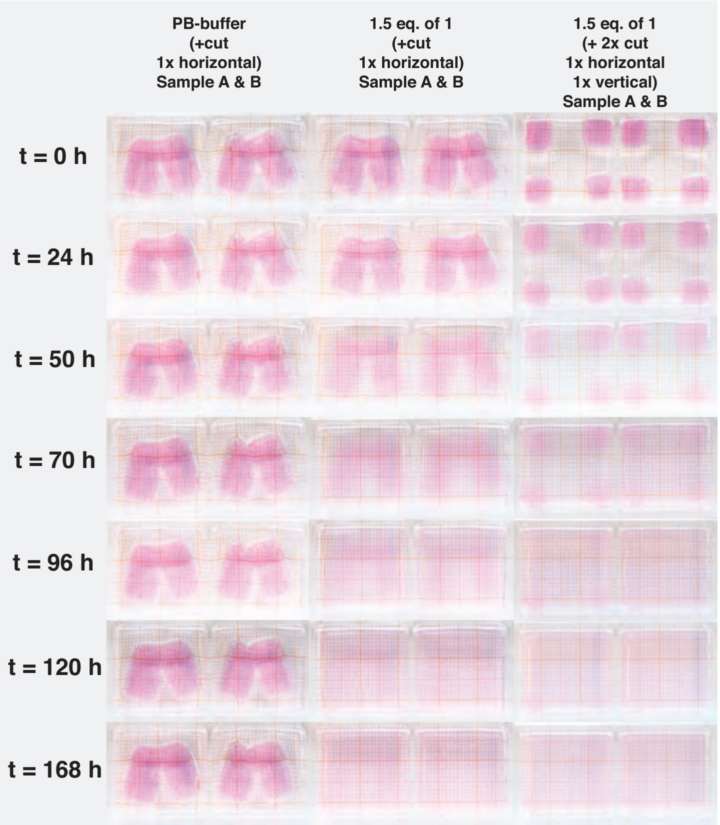

Figure S19: Time lapse photographs (in duplicate) of hydrogel degradation using the self-amplification system triggered by damage (cut). (a) Control gels with 1) no additives and 1x horizontal cut, 2) 1.5 eq. of **1** and 1x horizontal cut, 3) 1.5 eq. of 1 and 2x cut (1x horizontal and 1x vertical). Conditions: gels were submerged in 1.5 mL phosphate buffer (0.1 M, pH = 7.6).

4.5.10 Synthesis procedure

4.5.10.1 Synthesis of trisodium 3,3',3''-((2-(methoxycarbonyl)but-2-en-1-yl)phosphoniotriyl)tribenzenesulfonate) acetate (**1**)

Acrylate-1 (0.26 mmol, 43.9 mg, 1.0 eq.) and trisodium tris(3-sulfophenyl)phosphine (TPPTS) (0.16 mmol, 92.3 mg, 0.64 eq.) are dissolved in H_2O (1.0 mL) and stirred for 1 hour. The solution is then freeze dried to give the title compound (0.16 mmol, 116.8 mg, 97%) as white solid as an inseparable mixture of (E/Z) isomers in a 92:8 ratio (based on ^{1}H NMR).

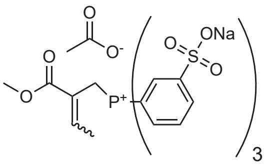

^{1}H NMR (400 MHz, D$_2$O + 1 µL DMSO, for E-isomer) δ: 8.21 – 8.06 (m, 6H), 7.74 (t, J = 5.8 Hz, 7H), 7.18 (p, J = 6.3 Hz, 1H), 4.45 (d, J = 14.4 Hz, 2H), 3.26 (s, 3H), 1.77 (s, 3H), 1.44 (t, J = 6.3 Hz, 3H). **^{13}C NMR** (101 MHz, D$_2$O + 1 µL DMSO, for E-isomer) δ: 182.26, 168.26 (d, J = 1.8 Hz), 150.07 (d, J = 10.0 Hz), 145.51 (d, J = 12.7 Hz), 137.84 (d, J = 10.2 Hz), 133.33 (d, J = 2.8 Hz), 132.06 (d, J = 12.6 Hz), 131.57 (d, J = 11.4 Hz), 120.87 (d, J = 9.9 Hz), 118.44 (d, J = 86.2 Hz), 53.39, 24.04, 23.60, 15.78 (d, J = 2.8 Hz). **^{31}P NMR** (161.9 MHz, D$_2$O + 1 µL DMSO, for E-isomer) δ: 20.79. **IR (KBr):** 3066**,** 2955 (C-H), 1715 (C=O), 1644 (C=C), 1581, 1407, 1398 (S=O), 1291, 1209, 1199 (S=O), 1102, 1039 (S=O), 993, 931, 843, 800, 792 (H-Ph), 727.

3.5.10.2 Synthesis of methyl 2-(((2-acetamidoethyl)thio)methyl)but-2-enoate (**2**)

Acrylate-1 (0.17 mmol, 30 mg, 1.0 eq.) and compound **4** (0.16 mmol, 19 mg, 0.91 eq.) were mixed in 1 mL buffer (pH ~8.0). After 48 hours the solution was extracted with ethyl acetate. The organic fraction was dried with Na$_2$SO$_4$, filtered and concentrated under reduced pressure to give compound 2 as colourless oil (0.136 mmol, 31.5 mg, 86%) as an inseparable mixture of (E/Z) isomers in a 80:20 ratio (based on ^{1}H NMR).

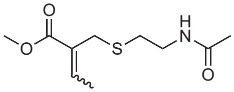

^{1}H NMR (400 MHz, CDCl$_3$, for E-isomer) δ: 6.94 (q, J = 7.2 Hz, 1H), 6.25 (s, 1H), 3.74 (s, 3H), 3.46 (q, J = 7.4 Hz, 2H), 3.45 (s, 2H), 2.64 (t, 2H), 1.98 (s, 3H), 1.86 (d, J = 7.2 Hz, 3H). **^{13}C NMR** (101 MHz, CDCl$_3$, for E-isomer) δ: 170.31, 167.33, 140.27, 129.83, 52.00, 38.64, 32.03, 26.76, 23.16, 14.64. **MS** (ESI+) m/z: 232.00 (M+H) (expected: 232.09).

3.5.10.3 Synthesis of N,N-diacetylcystamine (**3**)

N,N-diacetylcystamine was prepared as described elsewhere[3] with slight modifications. Briefly, a mixture of cysteamine dihydrochloride (10 mmol, 1.0 g, 1.0 eq.), KOH (20 mmol, 1.1 g, 2.0 eq.) and NaHCO$_3$ (30 mmol, 2.5 g, 3.0 eq.) were dissolved in a round-bottom flask containing 10 mL H$_2$O. After the dropwise addition of acetic anhydride (10 mmol, 1.0 g, 1.0 eq.), the solution was stirred at room temperature for 10 min. The pH was then adjusted to 7.3 using 4.0 M HCl. The resulting mixture was then extraction with 50 mL ethyl acetate three times and washed with brine. The organic layers were then dried with Na$_2$SO$_4$, filtered and concentrated under reduced pressure. After drying, the title compound was recrystalized 2x times in ethyl acetate, giving a white crystalline solid (2.4 mmol, 567 mg, 54%).

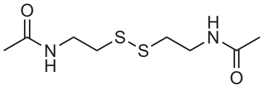

^{1}H NMR (400 MHz, DMSO-d6) δ: 8.03 (s, 2H), 3.30 (q, J = 6.6 Hz, 4H), 2.75 (t, J = 6.8 Hz, 4H), 1.80 (s, 6H). **^{13}C NMR** (101 MHz, DMSO-d6) δ: 169.31, 37.94, 37.25, 22.55.

3.5.10.4 Synthesis of N,N- Bis (acryloyl) cystamine (BAC)

BAC was prepared as described elsewhere[4]. Briefly, a mixture of cystamine dihydrochloride (6.9 mmol, 1.5 g, 1.0 eq.) was dissolved in a round-bottom flask containing 7.0 mL H_2O and cooled to 0 ºC. Two syringes filled with 1) acryloyl chloride solution (20.6 mmol, 1.9 g, 3.0 eq.) in 2 mL DCM and 2) NaOH (27.4 mmol, 1.1 g, 4.0 eq.) in 3 mL H_2O were simultaneously dropwise added to the solution and stirred for 16 hours at room temperature. After freeze drying, BAC was purified by recrystallization from ethyl acetate (3.57 mmol, 931 mg, 52%).

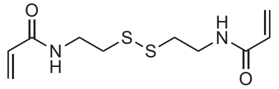

^{1}H NMR (400 MHz, DMSO-d6) δ: 8.30 (s, 1H), 6.22 (dd, J = 17.1, 10.1 Hz, 0H), 6.09 (d, J = 17.0 Hz, 0H), 5.59 (d, J = 10.2 Hz, 0H), 3.42 (q, J = 6.4 Hz, 2H), 2.82 (t, J = 6.8 Hz, 2H). **^{13}C NMR** (101 MHz, DMSO-d6) δ: 164.73, 131.55, 125.33, 37.93, 37.08.

3.5.10.5 Synthesis of tris(sodium-m-sulfonatophenyl)phosphanoxide (OTPPTS)

OTPPTS was prepared as described elsewhere[5]. Briefly, TPPTS (0.065 mmol, 37 mg) is dissolved in 1.0 mL of hydrogen peroxide (10% in water) and then the mixture is stirred overnight. Hereafter, the solution is freeze dried, giving OTPPTS as a white solid (0.063 mmol, 37 mg, 97%).

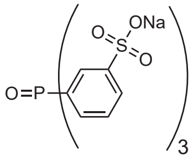

^{1}H NMR (400 MHz, D_2O + 5 µL DMSO) δ: 8.09 – 7.71 (m, 6H), 7.58 (dtd, J = 15.5, 7.7, 5.6 Hz, 6H). **^{13}C NMR** (101 MHz, D_2O + 5 µL DMSO) δ: 144.48, 144.36, 135.71, 135.60, 131.21, 131.19, 131.03, 130.90, 130.17, 129.49, 129.37. **^{31}P NMR** (161.9 MHz, D_2O + 5 µL DMSO) δ: 34.26.

4.5.11 NMR spectra

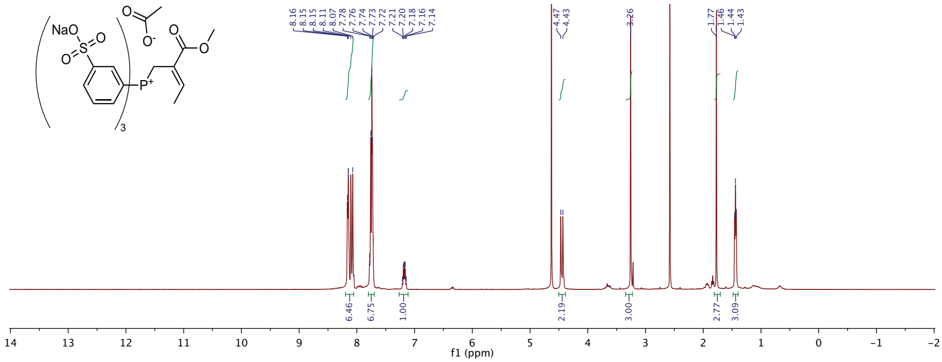

Figure S20: ^{1}H NMR, compound **1** in D_2O + 1 µL DMSO.

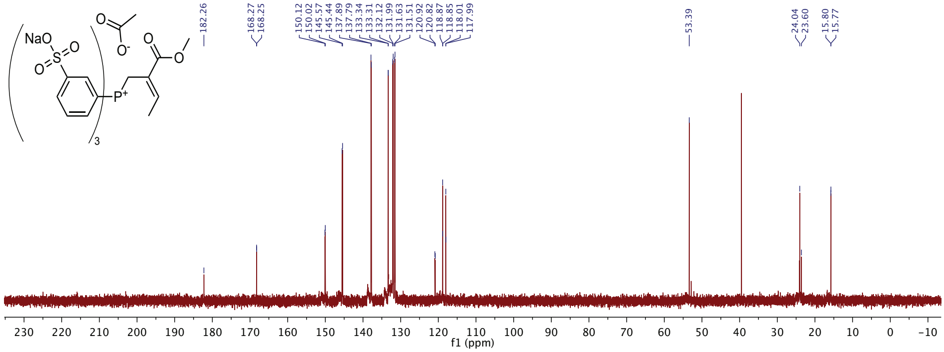

Figure S21: ^{13}C NMR, compound **1** in D_2O + 1 µL DMSO.

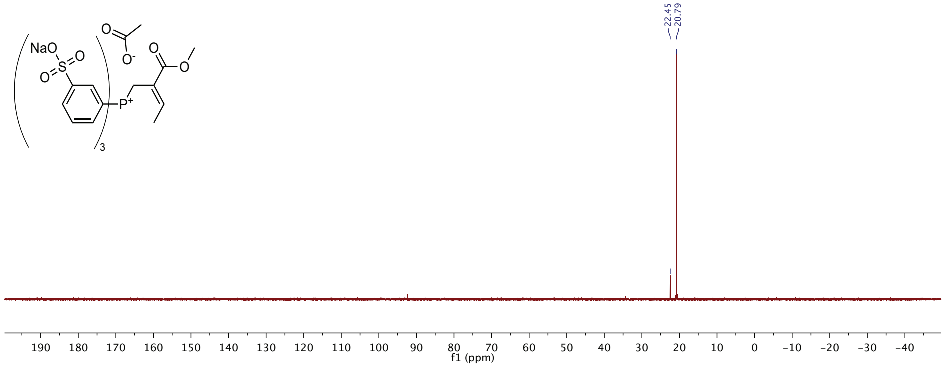

Figure S22: ^{31}P NMR, compound **1** in D_2O + 1 µL DMSO.

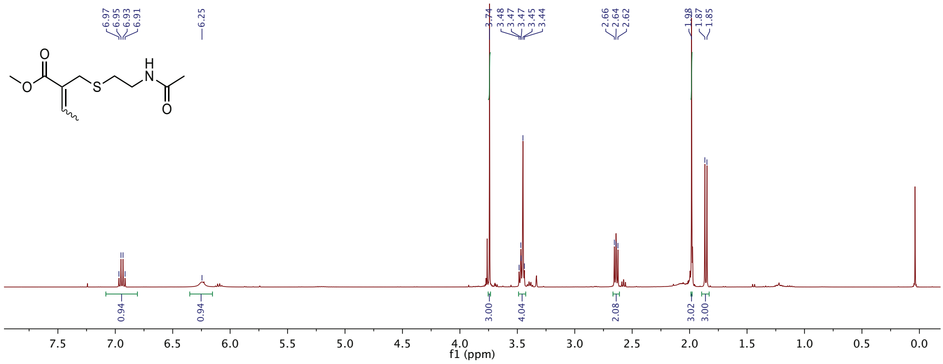

Figure S23: ^{1}H NMR, compound **2** in $CDCl_3$.

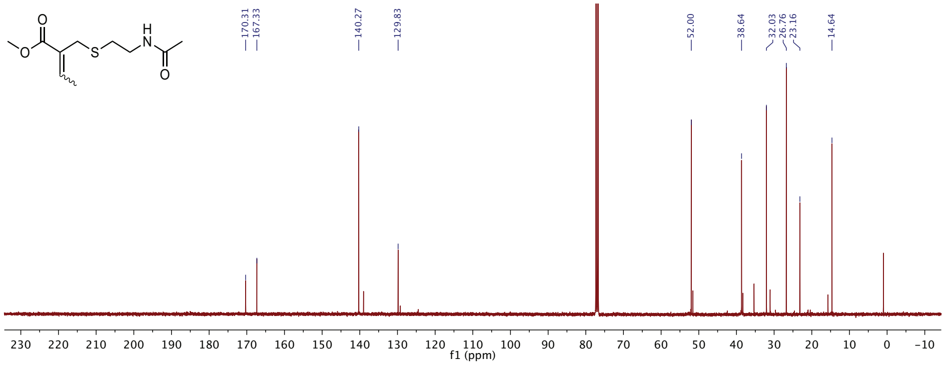

Figure S24: ^{13}C NMR, compound **2** in $CDCl_3$.

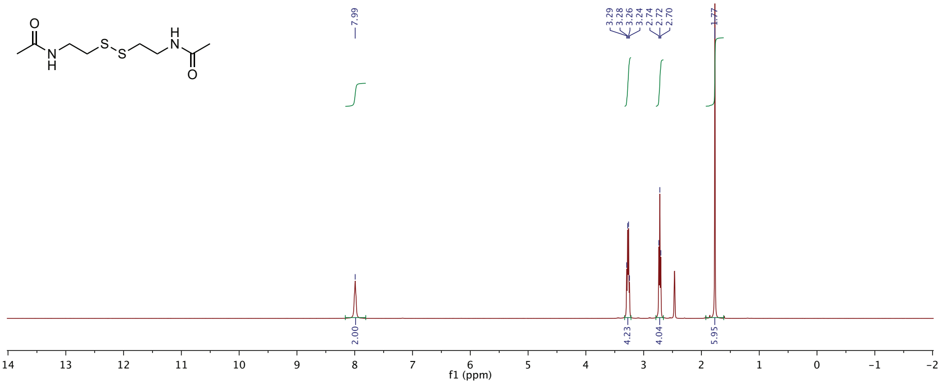

Figure S25: ^{1}H NMR, compound **3** in DMSO-d6.

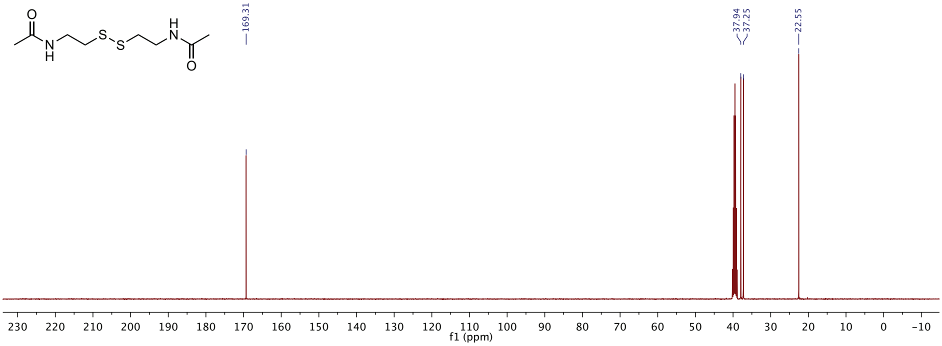

Figure S26: ^{13}C NMR, compound **3** in DMSO-d6.

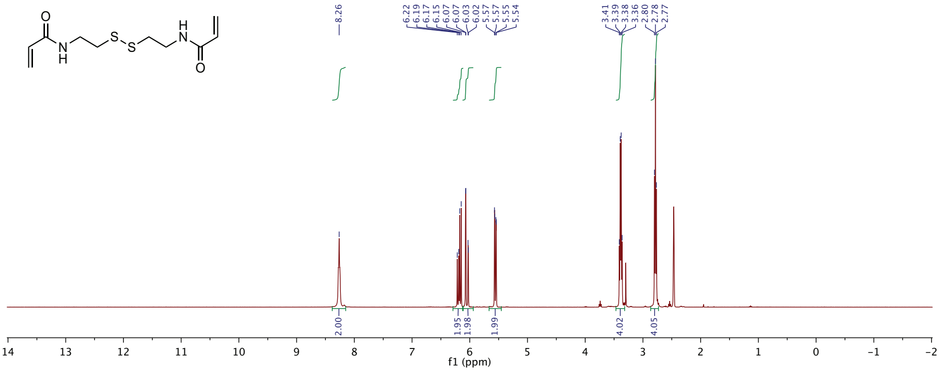

Figure S27: ^{1}H NMR, compound BAC in DMSO-d6.

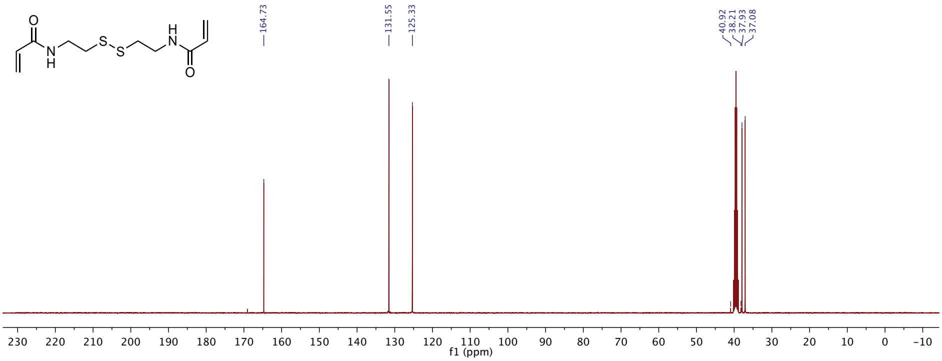

Figure S28: ^{13}C NMR, compound BAC in DMSO-d6.

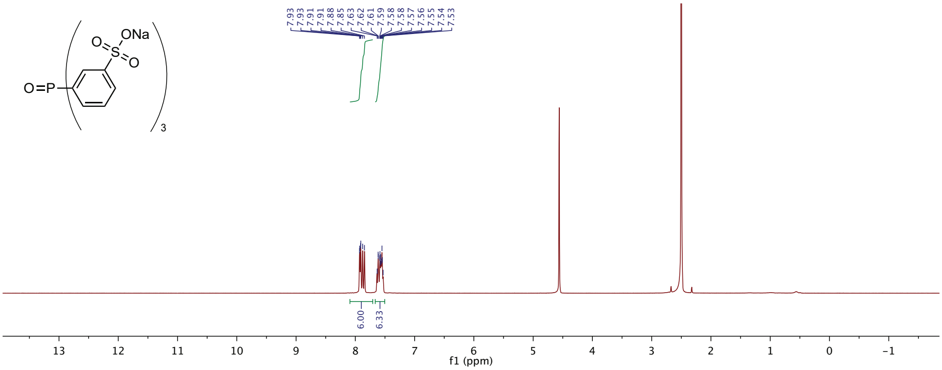

Figure S29: ^{1}H NMR, compound OTPPTS in D_2O + 5 µL DMSO.

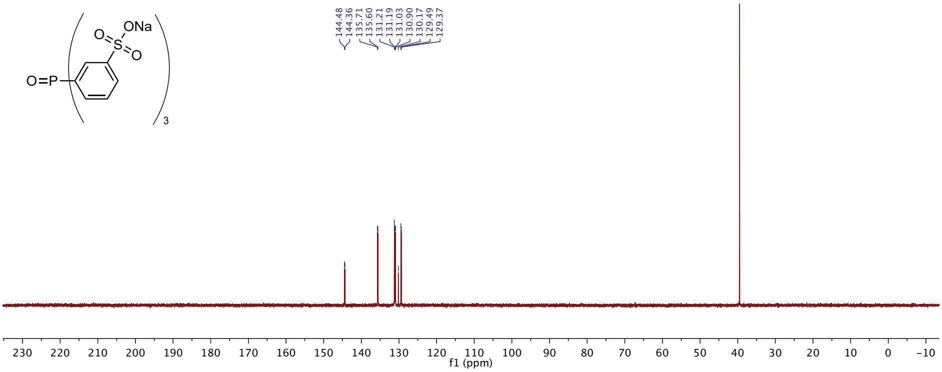

Figure S30: ^{13}C NMR, compound OTPPTS in D_2O + 5 µL DMSO.

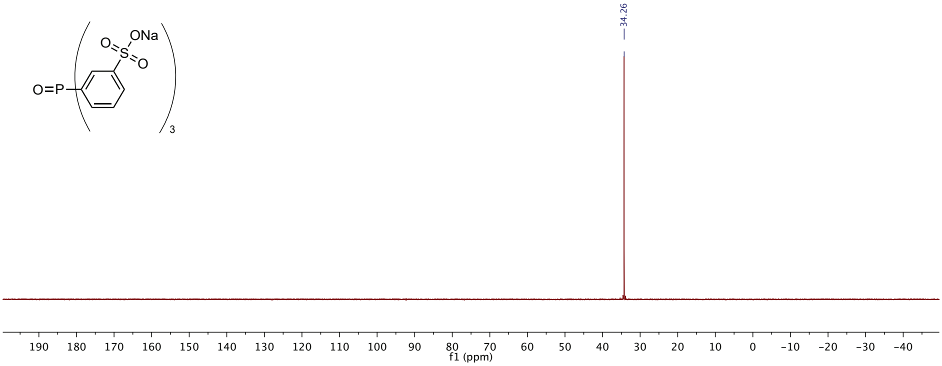

Figure S31: ^{31}P NMR, compound OTPPTS in D_2O + 5 µL DMSO.

4.5.12 2D NMR spectra

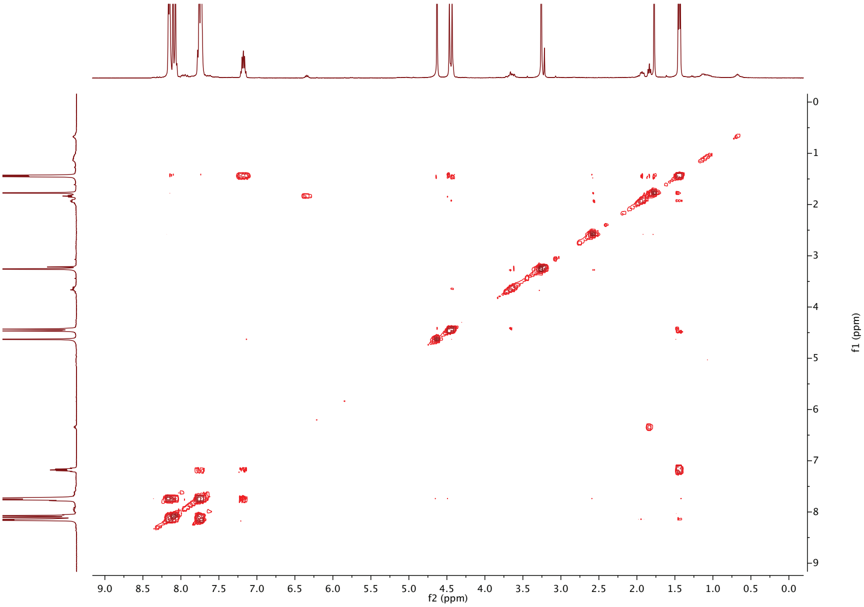

Figure S32: gCOSY, compound **1** in D_2O + 1 µL DMSO.

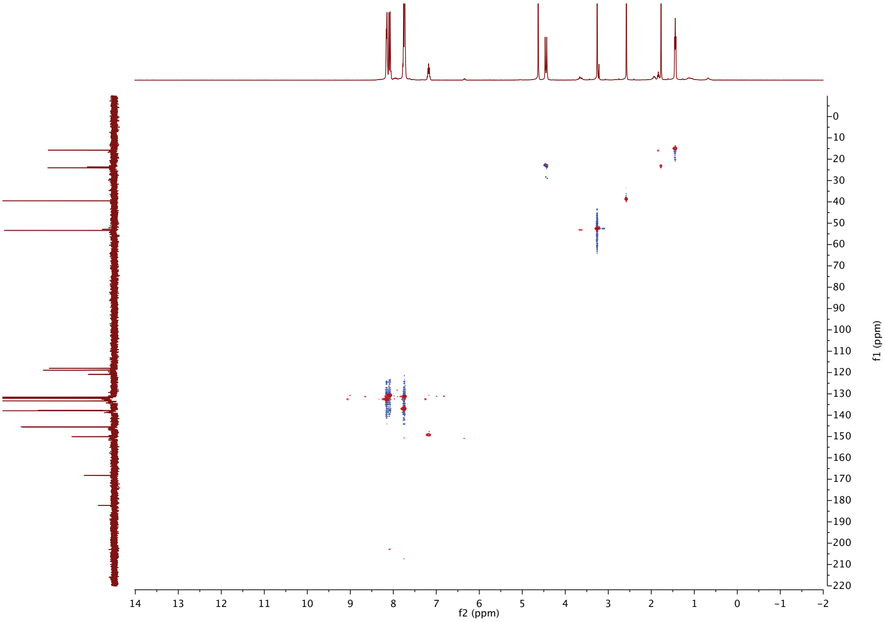

Figure S33: gHSQC, compound **1** in D_2O + 1 µL DMSO.

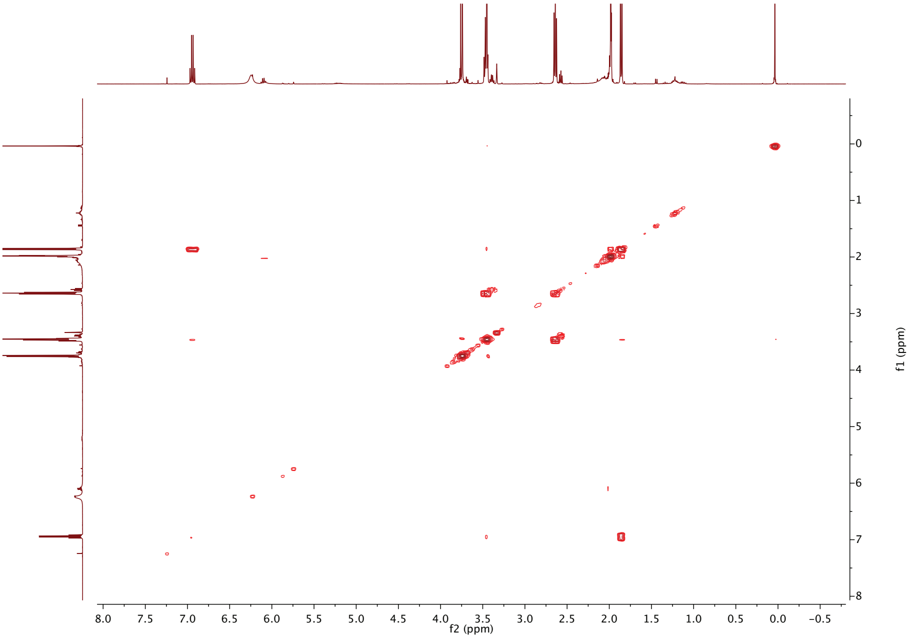

Figure S34: gCOSY, compound **2** in CDCl$_3$.

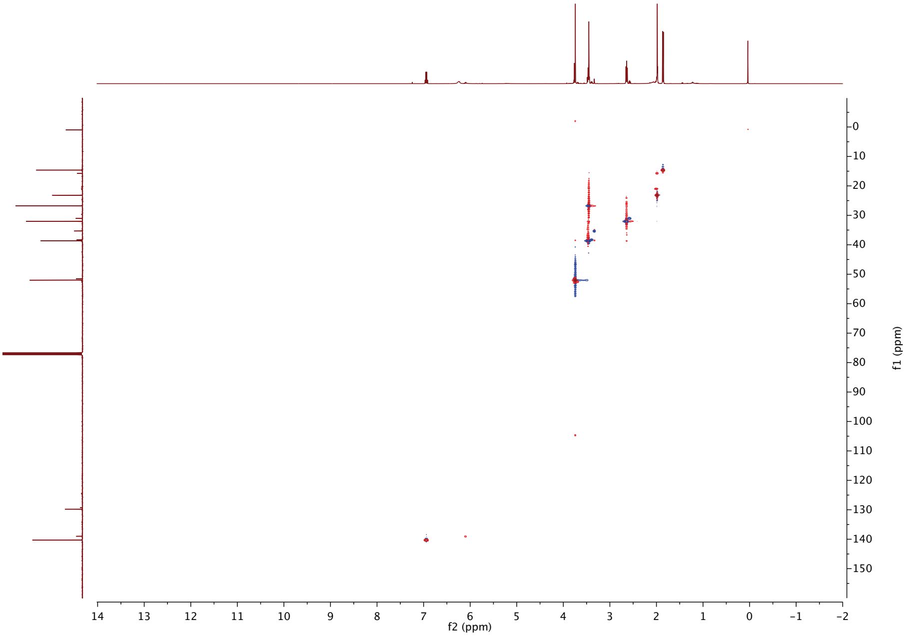

Figure S35: gHSQC, compound **2** in CDCl$_3$.

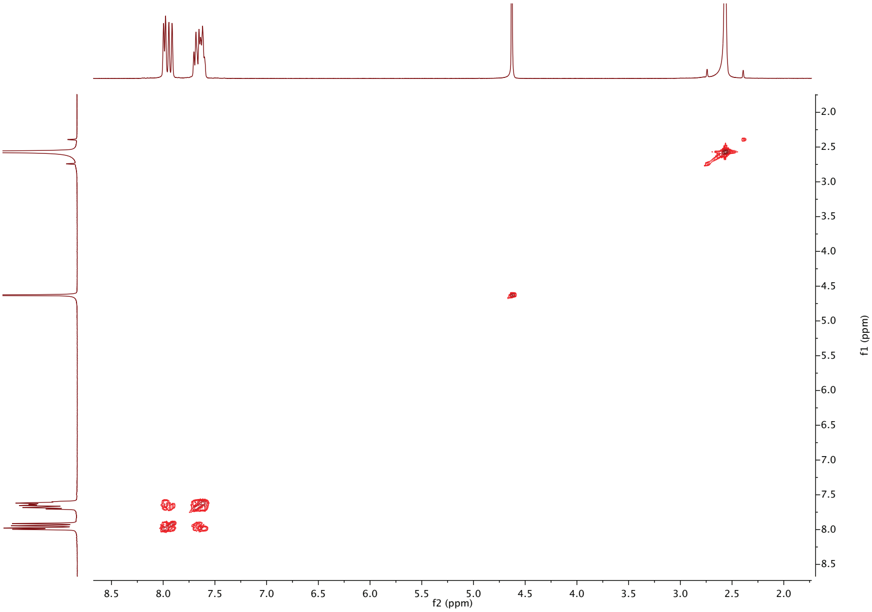

Figure S36: gCOSY, compound OTPPTS in D_2O + 5 µL DMSO.

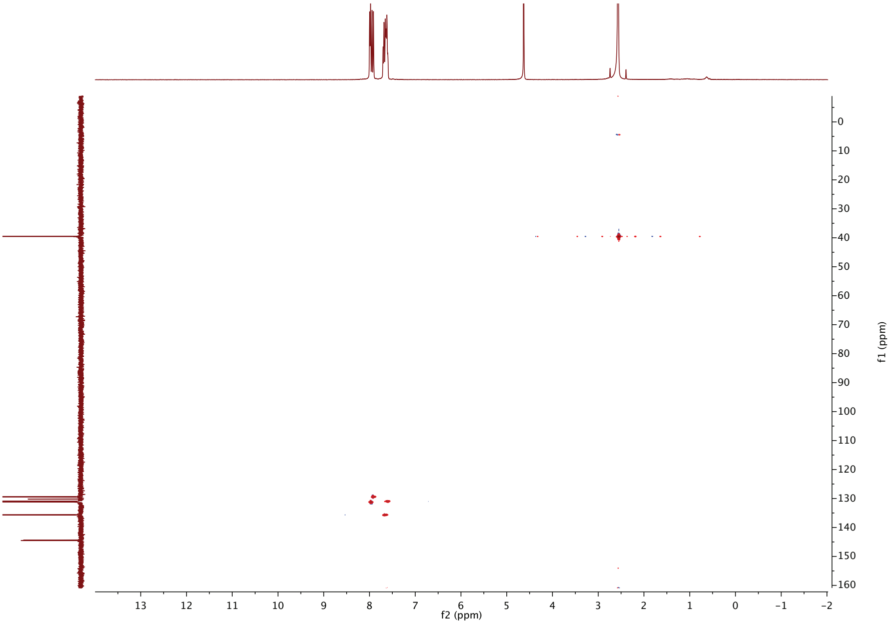

Figure S37: gHSQC, compound OTPPTS in D_2O + 5 µL DMSO.

4.5.13 LC-MS data

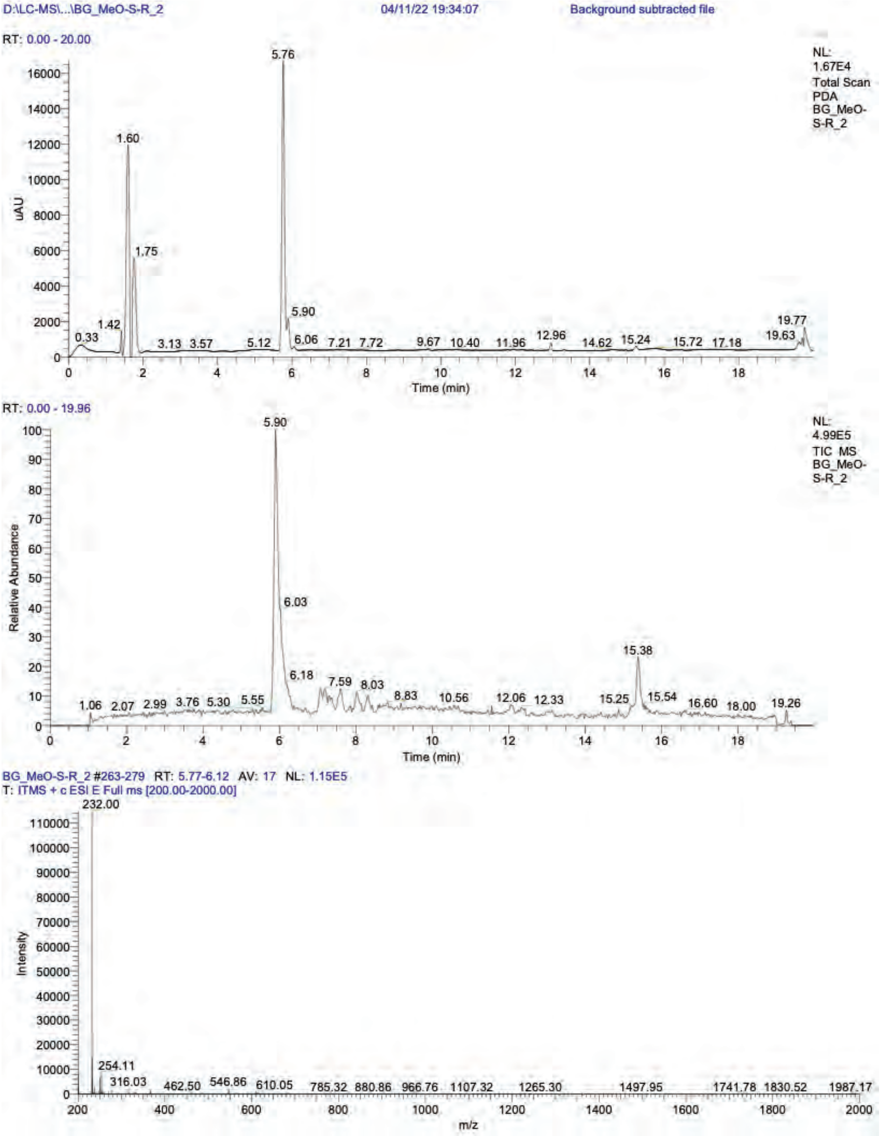

Figure S38: LCMS data for compound **2**.

4.5.14 Supplementary references

1 C. Cho and M. J. Krische, Angew. Chem. Int. Ed., 2004, **43**, 6689–6691.
2 O. Dmitrenko, C. Thorpe and R. D. Bach, J. Org. Chem., 2007, **72**, 8298–8307.
3 F. Maglangit, S. Alrashdi, J. Renault, L. Trembleau, C. Victoria, M. H. Tong, S. Wang, K. Kyeremeh and H. Deng, Org. Biomol. Chem., 2020, **18**, 2219–2222.
4 Y. Sun, X. Yan, T. Yuan, J. Liang, Y. Fan, Z. Gu and X. Zhang, Biomaterials, 2010, **31**, 7124–7131.
5 C. Larpent and H. Patin, Tetrahedron, 1988, **44**, 6107–6118.

5

NUCLEOPHILE-TRIGGERED PRODRUG RELEASE FROM POLYMER HYDROGELS

We present a new method to obtain tertiary amine-based prodrugs with dual functionality, enabling (i) signal-triggered drug activation and (ii) covalent incorporation in polymer materials through a clickable azido-group unit on the molecular prodrug scaffold. Using nucleophilic substitution on an electron deficient azido-phenyl allyl bromide scaffold, we were able to obtain prodrugs from a variety of amine drug candidates. Subsequent drug activation was initiated by using S or N-terminal biomarker nucleophiles including amino acids, a neurotransmitter, and glutathione as chemical signals. Hydrogel scaffolds labelled with anti-cancer or antibiotic prodrugs were tested in aqueous and cellular media. Through this strategy, we achieved controlled drug release for in vitro cancer models (2D monolayer), which showed complete wound closure inhibition of A549 small lung cancer cells upon signal activation. We anticipate that this new strategy for the development of responsive prodrug-conjugate incorporated materials will lead to further advancements in drug delivery and specialized therapeutics.

This chapter is submitted as:
B. Klemm, M. Tavasso, I. Piergentili, M. Satijn, T. G. Brevé, P. E. Boukany and R. Eelkema. Signal-triggered release of allyl-caged tertiary amine drugs from polymer hydrogels. (2024)

5.1 INTRODUCTION

The strategy of linking signal-responsive prodrugs to a carrier material is a promising approach to improve the selectivity of chemotherapy drugs.[1–3] Besides the improved water solubility, it enables controlled drug release profiles via temporal-, or local activation.[4] Prodrugs or caged drugs are chemically modified therapeutics that are inactive until their activation via stimulus-induced removal of the cage group.[5] In cancer therapy models, a variety of stimuli have been used as triggers for controlled drug activation via chemical de-caging, including pH[6,7], glutathione (GSH)[8,9], reactive oxygen species (ROS)[10,11], hypoxia[12] or enzymes[13–15], amongst others[16–18].

A common feature found in many prodrug systems to obtain controlled response, is their dependency on linker units such as self-immolative spacers[4] or a metabolically cleavable connection. Specifically, for self-immolative systems, prodrug constructs require at least one functional group that allows attachment to a targeting or depot scaffold.[5,19] Several linker types have been developed, including oximes/imines[20], hydrazone[21] and disulfide bonds[22–24] for a variety of drug candidates. Despite these advancements, many synthetic challenges remain, especially the incorporation of prodrugs into a carrier material. Indeed, the majority of prodrugs rely on carrier systems for water solubility.[5] So far, material development for prodrugs is based either on non-covalent linkage, including encapsulation[25,26], self-assembly[26–28] or is achieved through complex synthesis procedures, which is often limited to polymer conjugates[29,30] or dendrimer systems[13].

An alternative concept to achieve signal-reversible prodrugs was introduced by Pillow and co-workers.[24] The authors developed a drug delivery platform that combined a self-immolative spacer together with tertiary or heteroaryl amine drugs to form quaternary ammonium conjugates, which could be connected to a carrier protein. Here, a generic, scalable and straightforward coupling strategy of linker and drug molecules for the development of signal-responsive prodrug carriers would be highly advantageous.

In this work, we sought to use our previously reported chemistry on Morita-Baylis-Hillmann (MHB)-adducts[31–37] to develop a new tertiary amine-prodrug platform with biomarker signal-triggered drug activation for controlled delivery (Figure 1a). This system constitutes a straightforward and widely applicable method for the formation of stable quaternary amine prodrug conjugates from various amine-containing therapeutics, without the need for long or cumbersome synthetic routes. By using the embedded azide functionality on the prodrug together with an alkyne-functionalized dextran and a bis-azide crosslinker, we developed prodrug conjugated hydrogel structures to demonstrate its material compatibility. The traceless cleavage of conjugated drugs in the material matrix is realized upon the addition of nucleophilic biomarker signals, leading to controlled drug activation (Figure 1b). We incorporated anticancer prodrugs in a hydrogel and used this material to inhibit *in vitro* A549 cancer cell proliferation (2D monolayer) to demonstrate signal-controlled drug release.

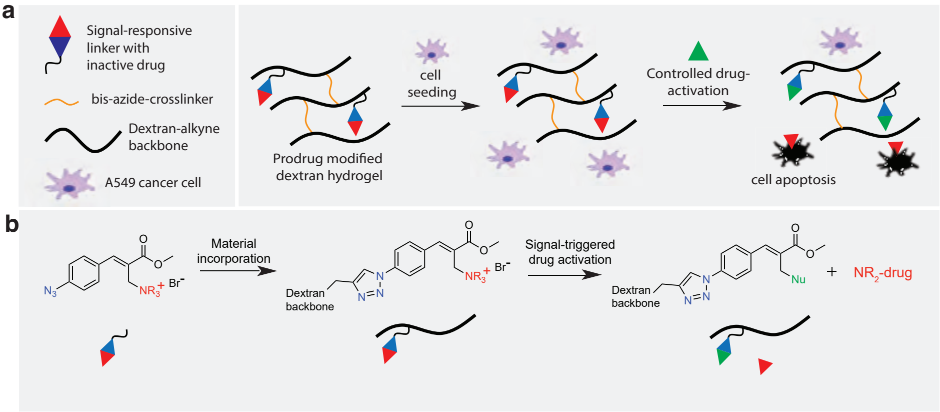

Figure 1: Schematic representation of the dextran-based hydrogel system with signal-responsive prodrugs. **(a)** Alkyne modified dextran is conjugated with signal-responsive prodrugs and crosslinked with a bis-azide crosslinker using standard Cu-click conditions. Biological signals trigger release and activation of anti-cancer drugs from the hydrogels, leading to cancer cell proliferation inhibition or apoptosis. **(b)** Signal responsive prodrug-linker used as molecular scaffold on the hydrogel backbone and anticancer drug release upon signal activation.

5.2 RESULTS AND DISCUSSION

5.2.1 PRODRUG SYNTHESIS AND KINETIC CONTROL OVER DRUG RELEASE

For the development of signal-responsive prodrugs, we envisioned the connection of tertiary amine therapeutics through quaternary ammonium salts by using nucleophilic substitution on electron deficient MBH-bromides (Figure 2). Our group recently demonstrated that MBH-acetates together with tertiary nitrogen nucleophiles form metastable, positively charged quaternary nitrogen adducts in buffered aqueous solution[31,34,35] and outlined their potential for biomedical applications. To realize quaternary ammonium salt prodrugs, we designed a three-step synthesis route. We synthesized the clickable allyl bromide scaffold **1** through an MBH reaction between methyl acrylate and 4-azidobenzaldehyde and subsequent bromination of the product using phosphorous tribromide (see experimental details in Supplementary Information). Tertiary amine drugs **2**-**6** spontaneously react with **1** under ambient conditions, followed by precipitation in THF to give prodrug conjugates **8**-**12** in moderate to good yields (Figure 2a). We demonstrate the generality of the concept using a broad range of different therapeutics, including an anti-cancer drug (**6**), but also an antibiotic (**3**), muscle relaxant (**4**), anti-depressant (**5**) and an anesthetic (**2**) (Figure 2b).

The addition of S or N-terminal nucleophiles (signal **14-17**, Figure 2b) on the prodrug conjugates reverses the quaternary nitrogen back to the neutral tertiary amine, releasing and thereby activating the drug molecule. Importantly, this results in traceless drug release. The substitution of the nucleophile on quaternary amine salts likely proceeds via conjugate addition followed by elimination of the allylic leaving group from the enolate, mechanisms that are related to E1cB type eliminations and the MBH-reaction. As signals, we employ a broad range of biological nucleophiles, including N-acetyl cysteine (signal **14**), GSH (signal **15**), L-proline (signal **16**) or L-adrenaline (signal **17**). To examine whether our linker design would allow traceless release of a tertiary amine upon reaction with a nucleophile signal, we combined prodrug precursor **1** with tertiary amine **DABCO** (**7**) as model drug to form prodrug **13** (Figure 3a). Here, prodrug **13** was treated with thiol signals (**14** and **15**) and secondary amine signals (**16** and **17**) and followed with ^{1}H NMR spectroscopy over time. Exposure of prodrug **13** (39 mM in 1:9 DMSO-d_6/phosphate buffer (pH = 7.4, 0.1 M)) to **14** and **15** (1.0 eq.) led to thiol-mediated nucleophilic substitution and generation of free **DABCO** within minutes (Supplementary Figure S1 and S2).

As a result of the substitution with various nucleophiles (**14-17**), nucleophile products **18** - **20** are formed in the reaction. Similarly to previous research[38], we found that the reactivity of N-acetyl cysteine (**14**) and GSH (**15**) was approximately equal with their half-life being 4.5 and 1.5 min, respectively. In contrast, N-terminal nucleophiles **16** and **17** (1.0 eq., Supplementary Figure S3 and 4), showed much slower release kinetics compared to thiols with conversions reaching 53 and 35% after 160 hours and half-life of 62 and 247 hours, respectively (Figure 3c and insert). These kinetic differences are attributed to the difference in nucleophilicity between thiols and secondary amines[39] and confirm our previous findings[31,35].

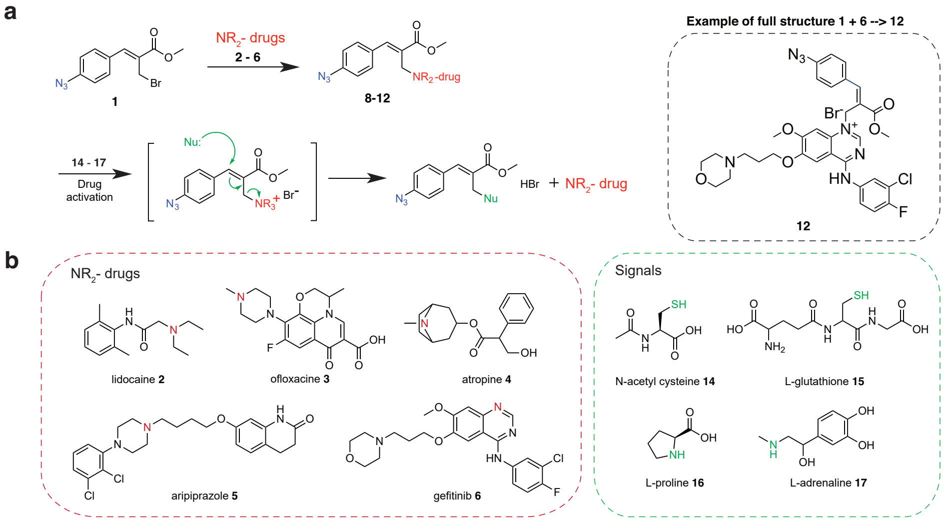

Figure 2: Nucleophile-triggered prodrug development, structures of used therapeutics and biological signals for drug activation **(a)** Prodrug synthesis (**8** to **12**). **(b)** Chemical structure of drugs (**2-6**: lidocaine (anesthetic), aripiprazole (anti-psychotic), ofloxacine (antibiotic), atropine (muscle-relaxant), gefitinib (anti-cancer) that contain tertiary-amines as reactive groups (red) for prodrug development and biological signals (**14** to **17**) with N-or S terminal reactive groups (green) used to activate drug release from prodrugs (**8** to **12**) via nucleophilic substitution reaction.

After confirming the nucleophile-triggered model drug release of free **DABCO** from prodrug **13**, we studied the release of amine drug variations from prodrugs using **16** (Figure 3b). Initial trials showed that prodrug-candidates **11** and **12** were not soluble using our standard protocol with DMSO-d_6/phosphate buffer = 3:7 and required a too large fraction of non-aqueous solvent for dissolution, reducing the use of release experiment data. However, prodrug **8, 9** and **10** (including atropine **4**, ofloxacine **3** and lidocaine **2**) were soluble and could be studied further in the small molecule release experiments. Upon introduction of **16** to the system (prodrug:signal = 1:1.2), we observed the complete release of amine drugs, alongside the formation of nucleophile product **20** within 65 hours (Figure 3d) with their half-life being $t_{1/2}$ = 4.6, 3.3 and 1.3 hours for prodrugs **10, 8** and **9**, respectively. We assume that these differences in their release kinetics are related to the drugs aqueous solubility, as seen in other drug delivery systems.[40]

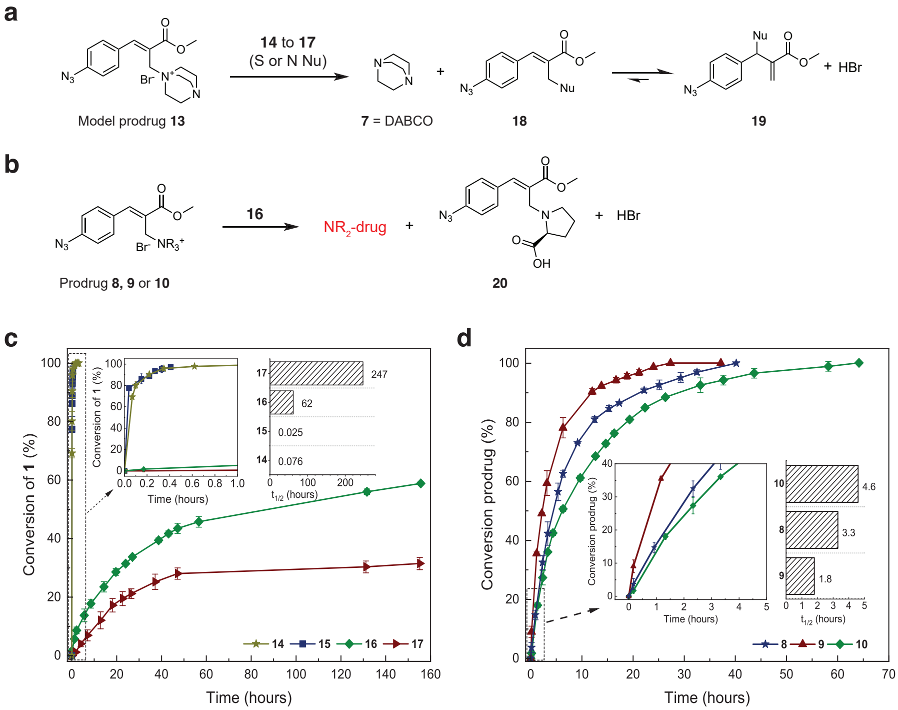

Figure 3: Small molecule release study from model prodrug **13** using different biological signals (**14** to **17**) and kinetic drug release study from different prodrugs (**8, 9** and **10**) using L-proline (**16**). **(a)** DABCO **7** release from **13** using signal **14** (N-acetyl-cysteine), **15** (L-glutathione), **16** (L-proline) or **17** (L-adrenaline). **(b)** Drug release from prodrugs **10, 9** and **8** using **16**. Conversion of the reactants was monitored by ^1H NMR over time in DMSO-*d6*/phosphate buffer (pH = 7.4, 0.1 M) 1:9 (DABCO release) and 3:7 (drug release) at room temperature. **(c)** DABCO **7** release (Supplementary Figure S1-4) from prodrug model **13** (39 mM, 1.0 eq.) with signals **14** – **17** (1.0 eq.). **(d)** Drug (**2**, **3** and **4**) release (Supplementary Figure S5-7) using signal **16** from corresponding prodrugs: **16** (9.6 mM, 1.20 eq.) addition to prodrugs **8, 9** and **10** (1.0 eq.). The error bars represent the standard deviation of duplicate measurements.

5.2.2 PRODRUG MATERIAL INCORPORATION AND DRUG ACTIVATION IN DEXTRAN BASED HYDROGELS

After successful drug activation from signal-responsive prodrugs, we investigated their material compatibility to alkyne-substituted hydrogel scaffolds and drug release during signal activation by visual inspection of fluorescence intensity changes (Figure 4a). To assess concentration changes upon signal-triggered drug release, we used drug **3** (ofloxacin) as a model. Free ofloxacin exhibits strong blue emission under 365 nm UV irradiation, whereas its prodrug analogue emits green fluorescence (Supplementary Figure S10), due to the quaternization of the piperazinyl motif on ofloxacin[41]. This allows the visual distinction between prodrug **9** and free drug **3** under UV-light (Figure 4b). Dextran-based hydrogel scaffolds containing drug **3** were constructed using a two-step Cu-click reaction procedure. First, reaction of alkyne-dextran (500 kDa, degree of substitution (DS) = 41%, Supplementary Figure S8) with 0.1 eq. prodrug **9** vs free alkyne units, using CuBr and activating ligand tris(3-hydroxypropyltriazolylmethyl)amine (THTPA) in DMF, gave prodrug-modified, alkyne-dextran chains (Supplementary Figure S9). We then reacted this construct with PEG-bis-azide crosslinker (poly(ethylene glycol) bisazide, M_n = 1100 g/mol) in H_2O using $CuSO_4$, sodium ascorbate and THTPA, which resulted in gelation after 30 min. This procedure afforded transparent, self-supporting hydrogel objects with dimensions of 1.1 x 1.1 x 0.5 cm (Figure 4b).

The morphology of the hydrogels was analyzed by scanning electron microscopy (SEM) before and after prodrug modification. Besides a slightly smaller pore size, the interior morphology of the hydrogels showed no significant differences between hydrogels with prodrug and compared to non-modified control hydrogels (Supplementary Figure S11). After several washing steps, the prodrug modified hydrogels continued to exhibit green fluorescence, indicating the presence of the covalently attached prodrug. Encouraged by these results, we started to qualitatively investigate drug activation from hydrogels by adding ~100 µM signal **15** to our prodrug-modified hydrogel patch and compared it to a non-signal activated hydrogel as control (Figure 4c). Visual inspection of the hydrogels over 12 hours at specific time intervals under 365 nm UV light revealed a clear distinction between signal-activated and non-activated hydrogels, as well as their time-dependent fluorescence increase.

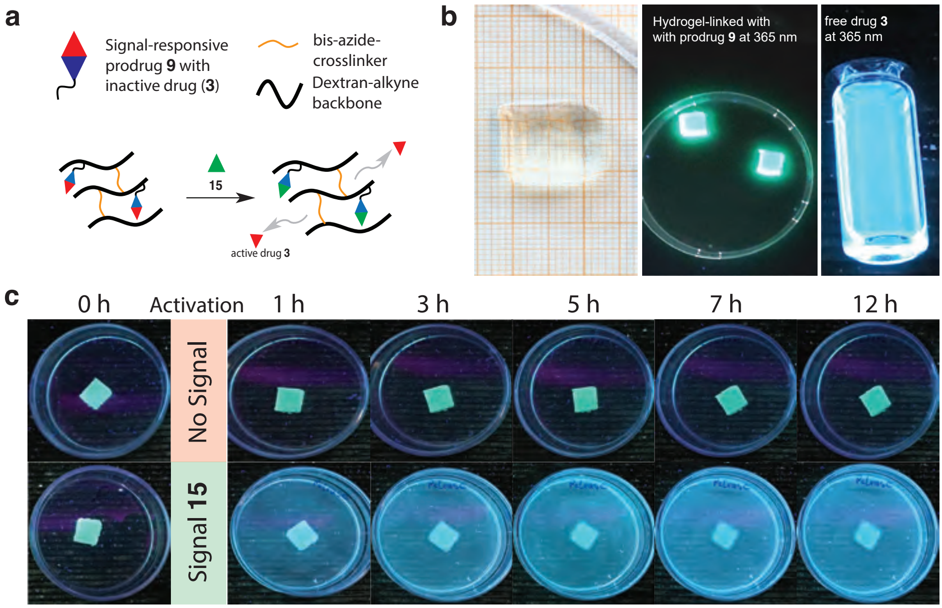

Figure 4: Prodrug linker incorporation in hydrogel scaffold and signal-activated drug release. **(a)** Schematic representation of signal activated drug release from dextran-based hydrogel scaffolds using **15**. **(b)** (left) Photograph of transparent self-supporting dextran-based hydrogel modified with prodrug **9**, (middle) dextran-based hydrogels modified with prodrug **9** under 365 nm UV-light in DMSO:PB = 1:9 solution, (right) free drug **3** in DMSO:PB = 1:9 solution under 365 nm UV-light. **(c)** Signal-triggered drug **3** release from dextran-based hydrogel patch using **15**, visualized under 365nm UV light.

5.2.3 *IN VITRO* – SIGNAL-ACTIVATED DRUG RELEASE FROM POLYMERIC HYDROGELS

To demonstrate drug release from the prodrug-conjugated hydrogels via controlled signal activation in live cell media, we supplied hydrogel patches containing the caged anticancer drug gefitinib (drug **6**, Figure 5a ‘red’) to A549 lung cancer cells and subjected these to **15** (GSH, Figure 5a ‘green triangle’) (Figure 5a). GSH plays an important role in the cellular redox balance but also in cancer cell proliferation.[42] Furthermore, GSH has been found at elevated levels in various human cancer tissues[42,43], which makes it a prime candidate for signal-triggered drug delivery.[44] Gefitinib is an FDA approved reversible epidermal growth factor receptor (EGFR) tyrosine kinase inhibitor, which is used for treating advanced non-small cell lung cancer, from which A549 cells are derived.[45,46]

We evaluated cell proliferation in the presence of prodrug-conjugated hydrogel patches during 72 hours wound healing assay via brightfield microscopy at incubator conditions. Proliferation results are shown in Figure 5b, at t = 0 h and t = 72 h, where cellular wound closure can be used to qualitatively identify cell proliferation (wound closure) or inhibition (no wound closure) and furthermore quantify the change in cell density (from 0 to 72 h with time intervals of 6 h) during proliferation (Figure 5c). As expected, control experiments including a negative control (hydrogel only, no prodrug + 1% DMSO) and a positive control (hydrogel, no prodrug + 100 µM drug **6** in 1% DMSO) showed 97.8 ± 2.0% and 5.4 ± 12.3% wound closure after 72 h, respectively. The dextran-based hydrogel patch and 1% DMSO also show no cytotoxicity towards A549 cells. On the contrary, addition of 100 µM (46 µg/mL) of drug **6** leads to overall ~94% cell proliferation inhibition at the end of the observation period (Figure 5b – positive control), which agrees with literature values.[47] Next, we observed cell proliferation in the presence of hydrogel patches containing 5.0 mM conjugated prodrug **12** (0.04 eq. **12** vs alkyne units) and with or without signal-trigger drug activation (400 µM of **15**). From the experimental results, we found a gradual wound closure increase within the first ~36h. Remarkably, this was followed by a plateau with maxima at 25.2 ± 7.0% wound closure from 36 to 72 h (Figure 5b/c, hydrogel-linked **12**, + signal **15**). Significantly, A549 cells in the presence of hydrogels and treated without GSH signal displayed 99.4 ± 1.0% wound closure, which confirms the absence of drug leakage or cytotoxic background interference (Figure 5b/c, hydrogel-linked **12**, no signal).

We observed a lag time (~36 h, change in avg. cell density < 1%) in the wound healing assay during signal-triggered drug release, which is likely linked to the kinetics of the nucleophilic substitution reaction limited by diffusion to prodrug **12**, and similarly to the diffusion of drug **6** from the hydrogel matrix. Indeed, such diffusion limitations related drug release lag time from a hydrogel matrix is often observed.[48] Additionally, we performed cell proliferation tests using only hydrogel, no prodrug and 400 µM of **15** (Supplementary Figure S12), which showed no significant changes in cell proliferation compared to the positive control (Figure 5c).

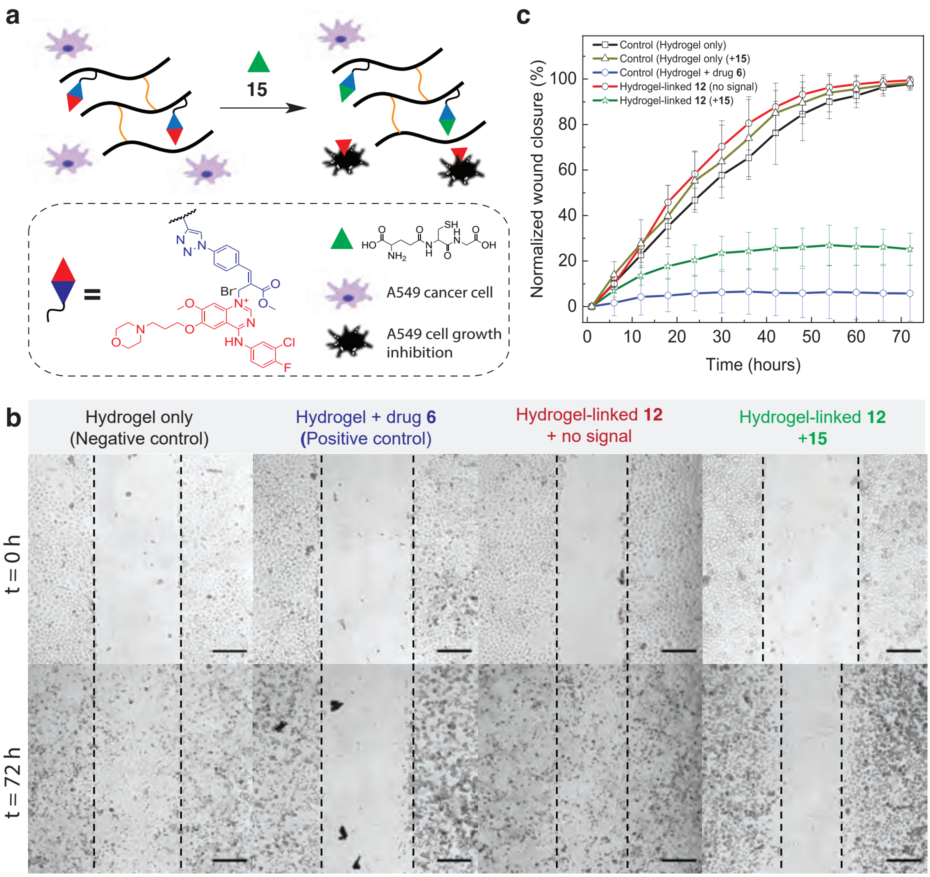

Figure 5: In-vitro signal-activated drug release from polymeric hydrogels. **(a)** Schematic representation and components of the signal-triggered drug activation from dextran-based, prodrug incorporated hydrogels in the presence of A549 lung cancer cells. **(b)** Brightfield microscopy pictures at t = 0 h and t = 72 h from wound healing assay (black dotted lines are added for comparison). Hydrogel/reactants and additives (i) hydrogel, no prodrug/1% DMSO, (ii) hydrogel, no prodrug/100 µM drug **6** in 1% DMSO, (iii) hydrogel with 5.0 mM prodrug **12**/1% DMSO and (iv) hydrogel with 5.0 mM prodrug **12**/1%DMSO and 400 µM **15**. Scale bar inserts = 250 µm. **(c)** Normalized wound closure (%) calculated from cell proliferation assay observation based on cell density changes over 72 hours observation period. The error bars represent the standard deviation of triplet measurements.

5.3 CONCLUSION

We herein introduce signal-responsive drug release from hydrogel scaffolds using nucleophilic signal sensitive prodrug linkers. This proof of concept is based on electron deficient azido-phenyl allyl bromides, which enable facile prodrug development via nucleophilic substitution of tertiary amine drugs. An azido functionality on the molecular scaffold enables straightforward covalent conjugation to alkyne-substituted polymer gels. Simply mixing of clickable linker **1** with tertiary amine drugs in THF results in precipitation of prodrug products and circumvents lengthy synthesis procedures. Using this strategy, we were able to obtain prodrugs from a variety of drug precursors, e.g. anti-cancer, antibiotic, muscle relaxant, anti-depressant or anesthetic, making this method not only easy to use but generally versatile and potentially widely applicable. We obtained control over drug activation kinetics by using S or N-terminal chemical signals, with their order being L-glutathione ≈ N-acetyl cysteine >> L-proline > L-adrenaline. Signal-triggered release experiments using visual fluorescence increase gave clear indication of substantial drug release upon signal activation compared to non-triggered gels. Finally, we successfully demonstrate this strategy by GSH-triggered activation of an anticancer drug from a prodrug hydrogel construct in the presence of A549 cancer cells and observed drug release induced cell growth inhibition of ~74.8 ± 7.0% after 72 h during wound healing experiments.

5.4 REFERENCES

1 R. Zhang, X. Zhao, A. Jia, C. Wang and H. Jiang, *Int. J. Biol. Macromol.*, 2023, 125993.

2 M. Zhang, W. Hu, C. Cai, Y. Wu, J. Li and S. Dong, *Mater. Today Bio*, 2022, **14**, 100223.

3 X. Wang, C. Li, Y. Wang, H. Chen, X. Zhang, C. Luo, W. Zhou, L. Li, L. Teng and H. Yu, *Acta Pharm. Sin. B*, 2022, **12**, 4098–4121.

4 A. Alouane, R. Labruère, T. Le Saux, F. Schmidt and L. Jullien, *Angew. Chem. Int. Ed.*, 2015, **54**, 7492–7509.

5 V. Abet, F. Filace, J. Recio, J. Alvarez-Builla and C. Burgos, *Eur. J. Med. Chem.*, 2017, **127**, 810–827.

6 C. Zhang, Q. Yuan, Z. Zhang and Y. Tang, *Molecules*, 2023, **28**, 399.

7 O. O. Krasnovskaya, V. M. Malinnikov, N. S. Dashkova, V. M. Gerasimov, I. V Grishina, I. I. Kireev, S. V Lavrushkina, P. A. Panchenko, M. A. Zakharko and P. A. Ignatov, *Bioconjug. Chem.*, 2019, **30**, 741–750.

8 J. Li, M. Yuan, T. Qiu, M. Lu, S. Zhan, Y. Bai, M. Yang, X. Liu and X. Zhang, *J. Biomater. Sci. Polym. Ed.*, 2023, **34**, 650–673.

9 J. Zhuang, B. Zhao, X. Meng, J. D. Schiffman, S. L. Perry, R. W. Vachet and S. Thayumanavan, *Chem. Sci.*, 2020, **11**, 2103–2111.

10 I. Piergentili, P. R. Bouwmans, L. Reinalda, R. W. Lewis, B. Klemm, H. Liu, R. M. de Kruijff, A. G. Denkova and R. Eelkema, *Polym. Chem.*, 2022, **13**, 2383–2390.

11 Z. Zhao, X. Liu, M. Hou, R. Zhou, F. Wu, J. Yan, W. Li, Y. Zheng, Q. Zhong and Y. Chen, *Adv. Mater.*, 2022, **34**, 2110560.

12 S. Zhou, X. Hu, R. Xia, S. Liu, Q. Pei, G. Chen, Z. Xie and X. Jing, *Angew. Chem. Int. Ed.*, 2020, **59**, 23198–23205.

13 A. Gopin, S. Ebner, B. Attali and D. Shabat, *Bioconjug. Chem.*, 2006, **17**, 1432–1440.

14 H. Jin, J. Lu and X. Wu, *Bioorg. Med. Chem.*, 2012, **20**, 3465–3469.

15 G. Fumagalli, L. Polito, E. Colombo, F. Foschi, M. S. Christodoulou, F. Galeotti, D. Perdicchia, I. Bassanini, S. Riva and P. Seneci, *ACS Med. Chem. Lett.*, 2019, **10**, 611–614.

16 F. M. H. de Groot, C. Albrecht, R. Koekkoek, P. H. Beusker and H. W. Scheeren, *Angew. Chem. Int. Ed.*, 2003, **42**, 4490–4494.

17 E. Procházková, J. Filo, M. Cigáň and O. Baszczyňski, *European J. Org. Chem.*, 2020, **2020**, 897–906.

18 H. Hu, J. Wan, X. Huang, Y. Tang, C. Xiao, H. Xu, X. Yang and Z. Li, *Nanoscale*, 2018, **10**, 10514–10527.

19 R. Mahato, W. Tai and K. Cheng, *Adv. Drug Deliv. Rev.*, 2011, **63**, 659–670.

20 G. Zhao, L. Long, L. Zhang, M. Peng, T. Cui, X. Wen, X. Zhou, L. Sun and L. Che, *Sci. Rep.*, 2017, **7**, 3383.

21 Y. Bae, N. Nishiyama, S. Fukushima, H. Koyama, M. Yasuhiro and K. Kataoka, *Bioconjug. Chem.*, 2005, **16**, 122–130.

22 S. Cerritelli, D. Velluto and J. A. Hubbell, *Biomacromolecules*, 2007, **8**, 1966–1972.

23 L. Qian, J. Fu, P. Yuan, S. Du, W. Huang, L. Li and S. Q. Yao, *Angew. Chem. Int. Ed.*, 2018, **130**, 1548–1552.

24 L. R. Staben, S. G. Koenig, S. M. Lehar, R. Vandlen, D. Zhang, J. Chuh, S.-F. Yu, C. Ng, J. Guo and Y. Liu, *Nat. Chem.*, 2016, **8**, 1112–1119.

25 Q. Chen, X. Huang, G. Zhang, J. Li, Y. Liu and X. Yan, *RSC Adv.*, 2023, **13**, 1684–1700.

26 X. Xu, Y. Jiang and C. Lu, *Anal. Chem.*, 2022, **94**, 10221–10226.

27 D. Wang, C. Du, S. Wang, L. Li, T. Liu, J. Song, Z. He, Y. Zhai, B. Sun and J. Sun, *ACS Appl. Mater. Interfaces*, 2022, **14**, 51200–51211.

28 P. Zhong, H. Meng, J. Qiu, J. Zhang, H. Sun, R. Cheng and Z. Zhong, *J. Control. Release*, 2017, **259**, 176–186.

29 T. Eom, W. Yoo, Y.-D. Lee, J. H. Park, Y. Choe, J. Bang, S. Kim and A. Khan, *J. Mater.*

Chem. B, 2017, **5**, 4574–4578.
30 J. Anderski, L. Mahlert, J. Sun, W. Birnbaum, D. Mulac, S. Schreiber, F. Herrmann, D. Kuckling and K. Langer, *Int. J. Pharm.*, 2019, **557**, 182–191.
31 B. Klemm, R. W. Lewis, I. Piergentili and R. Eelkema, *Nat. Commun.*, 2022, **13**, 6242.
32 B. Klemm, A. Roshanasan, I. Piergentili, J. van Esch and R. Eelkema, *J. Am. Chem. Soc.*, 2023, **145**, 21222–21230.
33 B. Wu, R. W. Lewis, G. Li, Y. Gao, B. Fan, B. Klemm, J. Huang, J. Wang, M. A. C. Stuart and R. Eelkema, *Chem. Sci.*, 2023, **14**, 1512–1523.
34 R. W. Lewis, A. Muralidharan, B. Klemm, P. E. Boukany and R. Eelkema, *Polym. Chem.*, 2023, **14**, 1591–1601.
35 R. W. Lewis, B. Klemm, M. Macchione and R. Eelkema, *Chem. Sci.*, 2022, **13**, 4533–4544.
36 A. Sharko, B. Spitzbarth, T. M. Hermans and R. Eelkema, *J. Am. Chem. Soc.*, 2023, **145**, 9672–9678.
37 B. Spitzbarth and R. Eelkema, *Chem. Commun.*, 2023, **59**, 11174–11187.
38 T. Sun and C. Jiang, *Adv. Drug Deliv. Rev.*, 2023, 114773.
39 R. J. Mayer and A. R. Ofial, *Angew. Chem. Int. Ed.*, 2019, **58**, 17704–17708.
40 R.-Y. Han, J.-Y. Fang, K. C. Sung and O. Y. P. Hu, *Int. J. Pharm.*, 1999, **177**, 201–209.
41 Z. Li, Q. Yang, R. Chang, G. Ma, M. Chen and W. Zhang, *Dye. Pigment.*, 2011, **88**, 307–314.
42 S. Singh, A. R. Khan and A. K. Gupta, *J Exp Ther Oncol*, 2012, **9**, 303–316.
43 A. Gupta, S. Srivastava, R. Prasad, S. M. Natu, B. Mittal, M. P. S. Negi and A. N. Srivastava, *Respirology*, 2010, **15**, 349–356.
44 S. J. T. Rezaei, V. Amani, M. R. Nabid, N. Safari and H. Niknejad, *Polym. Chem.*, 2015, **6**, 2844–2853.
45 J. K. Rho, Y. J. Choi, J. K. Lee, B.-Y. Ryoo, S. H. Yang, C. H. Kim and J. C. Lee, *Lung cancer*, 2009, **63**, 219–226.
46 M. G. Kris, R. B. Natale, R. S. Herbst, T. J. Lynch Jr, D. Prager, C. P. Belani, J. H. Schiller, K. Kelly, H. Spiridonidis and A. Sandler, *Jama*, 2003, **290**, 2149–2158.
47 Y. Hu, L. Shi, Y. Su, C. Zhang, X. Jin and X. Zhu, *Biomater. Sci.*, 2017, **5**, 792–799.
48 G. Kalosakas and E. Panagopoulou, *Processes*, 2022, **10**, 2592.

5.5 SUPPLEMENTARY INFORMATION

5.5.1 Instrumentation, materials and characterisation

All reagents and solvents were used without further purification unless otherwise stated. Ofloxacine (≥99%, **3**), Atropine (≥99%, **4**), Aripiprazole (>98.0%, **5**), Gefitinib (>98.0%, **6**), Lidocaine (≥99%, **2**), DABCO (≥99%, **7**), dextran (500 kDa), glycydyl propargyl ether poly(ethylene glycol) bisazide (average Mn 1100), L-proline (**14**, ≥99%), N-acetyl cysteine (**15**, ≥99%), L-adrenaline (**16**, >98.0%), L-glutathione (**17**, ≥98%), 4-formylphenylboronic acid (≥95.0%), methyl acrylate (99%) and phosphorous tribromide (99%) were purchased from Sigma Aldrich or TCI Europe. For the preparation of aqueous buffers, solid salts were used: sodium phosphate monobasic and sodium phosphate dibasic, purchased from Sigma Aldrich. Unless stated otherwise, all stock solutions were prepared in d_6-DMSO/phosphate buffer mixture 1:9 (0.1 M, pH = 7.4). All buffers were pH adjusted using sodium hydroxide (1 M) and hydrochloric acid (1 M). ESI-MS was performed using LTQ XL spectrometer equipped with Shimadzu HPLC setup operating at 0.2 mL/min flow rate with water/MeCN mobile phase containing 0.1 vol% formic acid and Discovery C18 column. Photographs of the hydrogels were taken on a Canon EOS 600D single reflex camera with a Canon Macro Lens EF 100 mm 1:2.8 USM.

5.5.2 NMR Spectroscopy

NMR spectra were recorded on an Agilent-400 MR DD2 NMR instrument at 25°C (399.7 MHz for ^{1}H, 100.5 MHz for ^{13}C and 376 MHz for ^{19}F) using residual solvent signals as internal reference. Sodium trimethylsilylpropanesulfonate (DSS) was used as internal standard for NMR kinetic experiments with reference resonance at 0 ppm. To suppress the water peak, PRESAT or ES_suppression configuration (suppress one highest peak) was used. NMR spectra were processed by MNova NMR software (Mestrelab Research).

5.5.3 NMR kinetics

5.5.3.1 Prodrug-activation using different biologically relevant signals (general procedure)

13 (2.04 mg, 10 mM, 1.0 eq.) and DSS as internal standard (1.0 eq.) were dissolved in 0.4 mL d_6-DMSO/phosphate buffer mixture. Then, **14**-**17** (1.2 eq.)

dissolved in 0.1 mL buffer mixture was added to the reaction mixture. The reaction was immediately followed by ^{1}H-NMR.

5.5.3.1.1 Activation of 13 using signal 14 (N-acetyl cysteine)

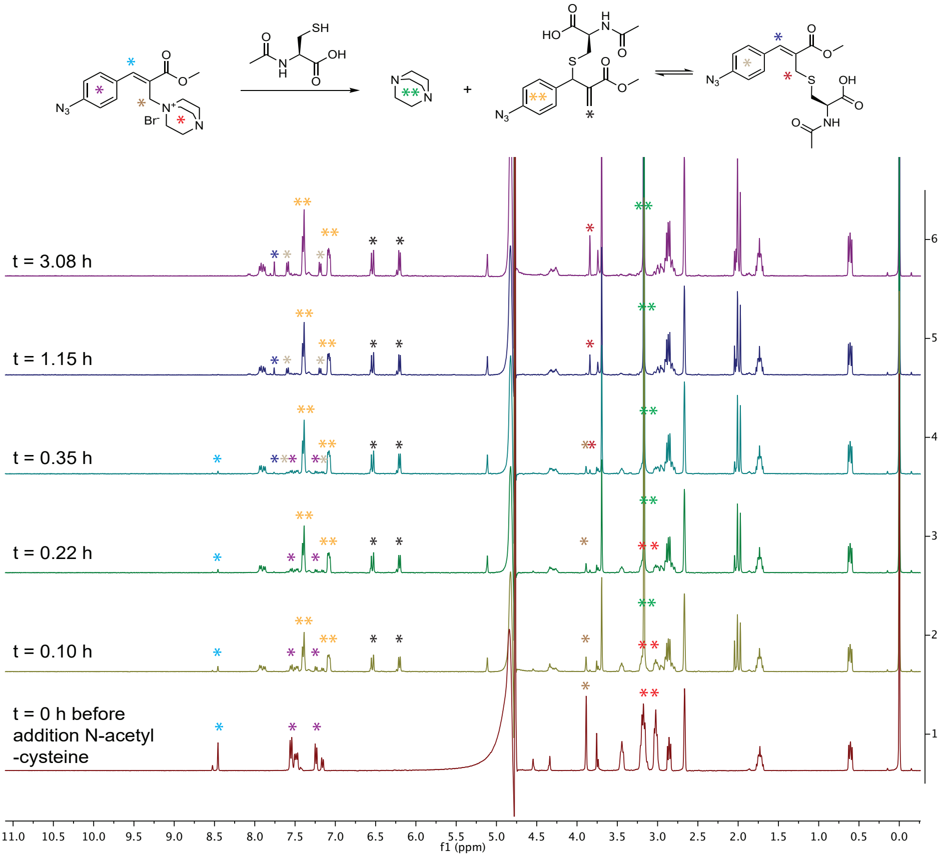

Figure S1: Reaction spectra of **13** with signal **14** followed by ^{1}H NMR at different time points. The reaction was carried out in d$_6$-DMSO/phosphate buffer mixture 1:9 (0.1 M, pH = 7.0). The peak attributed to ~ 0.0 ppm corresponds to DSS internal standard and was used to align the spectra.

5.5.3.1.2 Activation of 13 using signal 15 (L-glutathione)

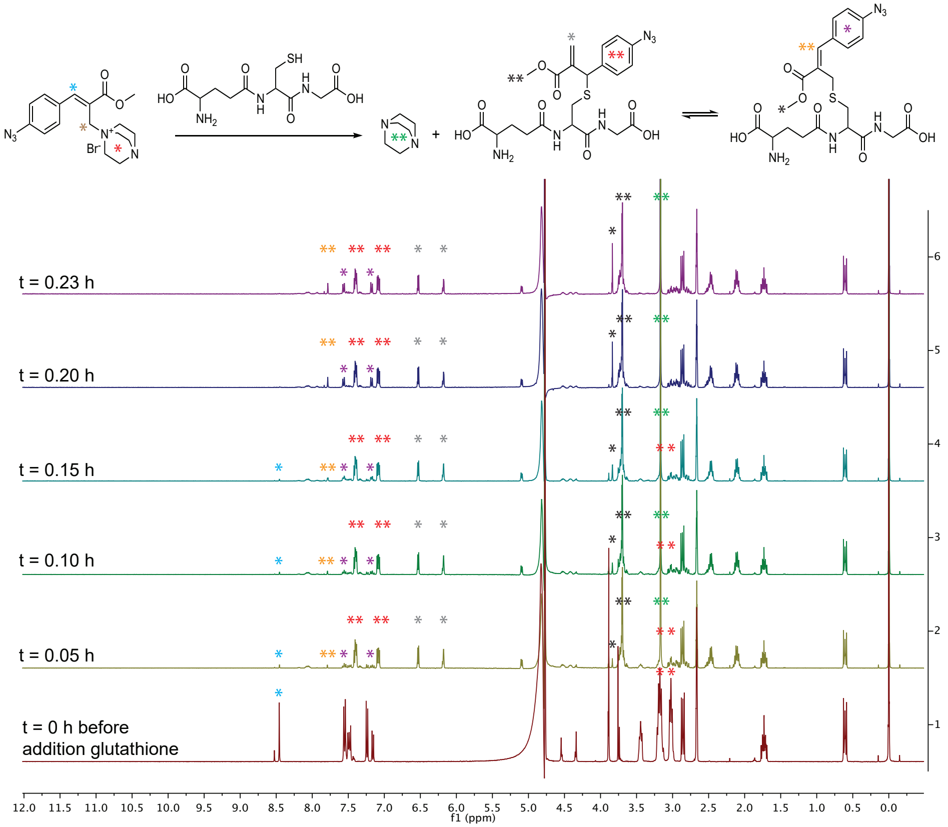

Figure S2: Reaction spectra of **13** with signal **15** followed by ^1H NMR at different time points. The reaction was carried out in d_6-DMSO/phosphate buffer mixture 1:9 (0.1 M, pH = 7.0). The peak attributed to ~ 0.0 ppm corresponds to DSS internal standard and was used to align the spectra.

5.5.3.1.3 Activation of 13 using signal 16 (L-proline)

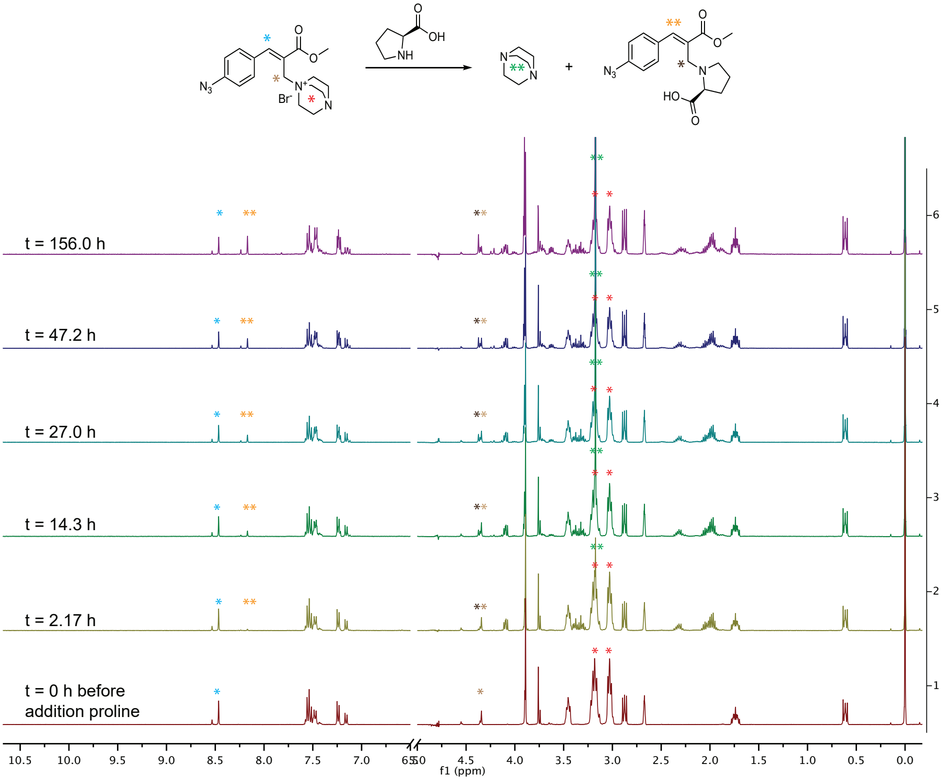

Figure S3: Reaction spectra of **13** with signal **16** followed by ^{1}H NMR at different time points. The reaction was carried out in d_6-DMSO/phosphate buffer mixture 1:9 (0.1 M, pH = 7.0). The peak attributed to ~ 0.0 ppm corresponds to DSS internal standard and was used to align the spectra.

5.5.3.1.4 Activation of 13 using signal 17 (L-adrenaline)

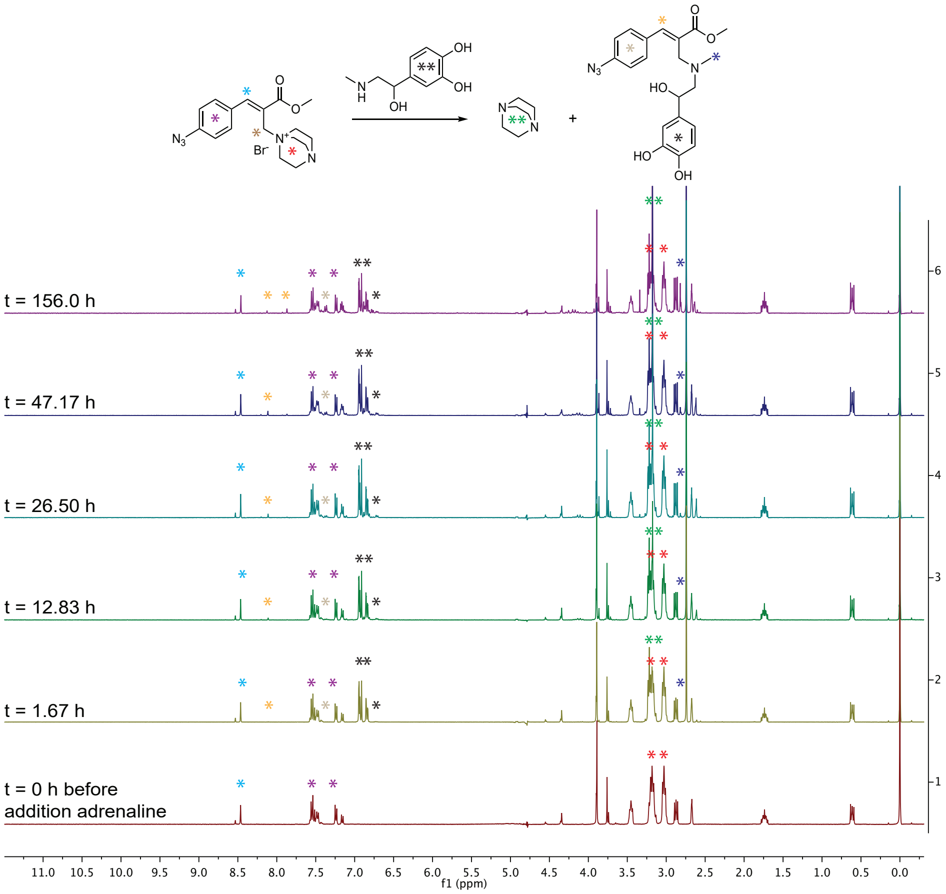

Figure S4: Reaction spectra of **13** with signal **17** followed by ^{1}H NMR at different time points. The reaction was carried out in d$_6$-DMSO/phosphate buffer mixture 1:9 (0.1 M, pH = 7.0). The peak attributed to ~ 0.0 ppm corresponds to DSS internal standard and was used to align the spectra.

5.5.3.2 Activation of prodrugs 8 - 10 using signal 16 (general procedure)

Corresponding prodrug **8**, **9** or **10** (2.1 – 2.6 mg, 8.0 mM, 1.0 eq.) and DSS as internal standard (1.0 eq.) were dissolved in 0.4 mL *d*$_6$-DMSO/phosphate buffer mixture. Then, **16** (1.2 eq.) dissolved in 0.1 mL buffer mixture was added to the reaction mixture. The reaction was immediately followed by NMR.

5.5.3.2.1 Activation of prodrug 8 – Lidocaine

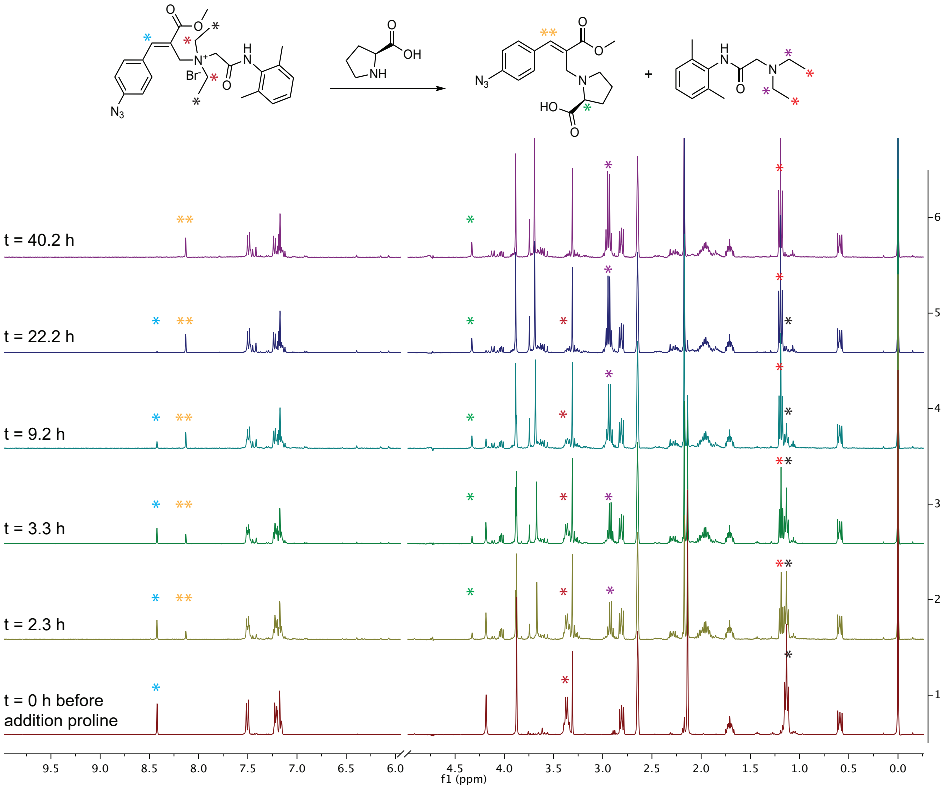

Figure S5: Reaction spectra of **8** with signal **16** followed by ^{1}H NMR at different time points. The reaction was carried out in d$_6$-DMSO/phosphate buffer mixture 3:7 (0.1 M, pH = 7.0). The peak attributed to ~ 0.0 ppm corresponds to DSS internal standard and was used to align the spectra.

5.5.3.2.2 Activation of prodrug 9 – Ofloxacine

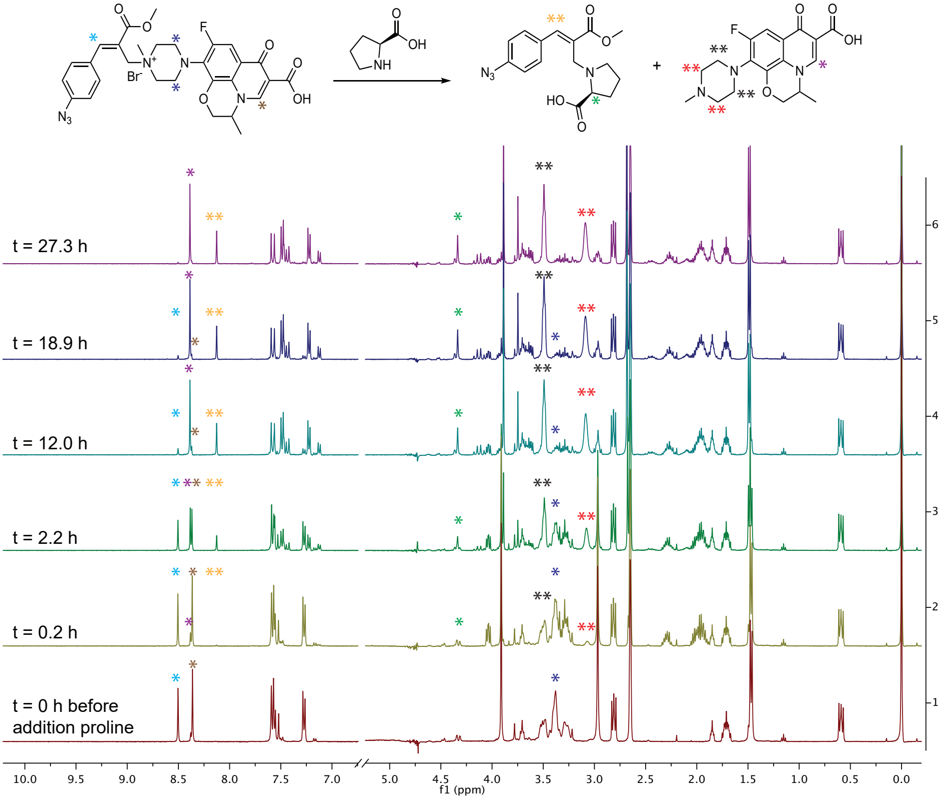

Figure S6: Reaction spectra of **9** with signal **16** followed by ^{1}H NMR at different time points. The reaction was carried out in d$_6$-DMSO/phosphate buffer mixture 3:7 (0.1 M, pH = 7.0). The peak attributed to ~ 0.0 ppm corresponds to DSS internal standard and was used to align the spectra.

5.5.3.2.3 Activation of prodrug 10 – Atropine

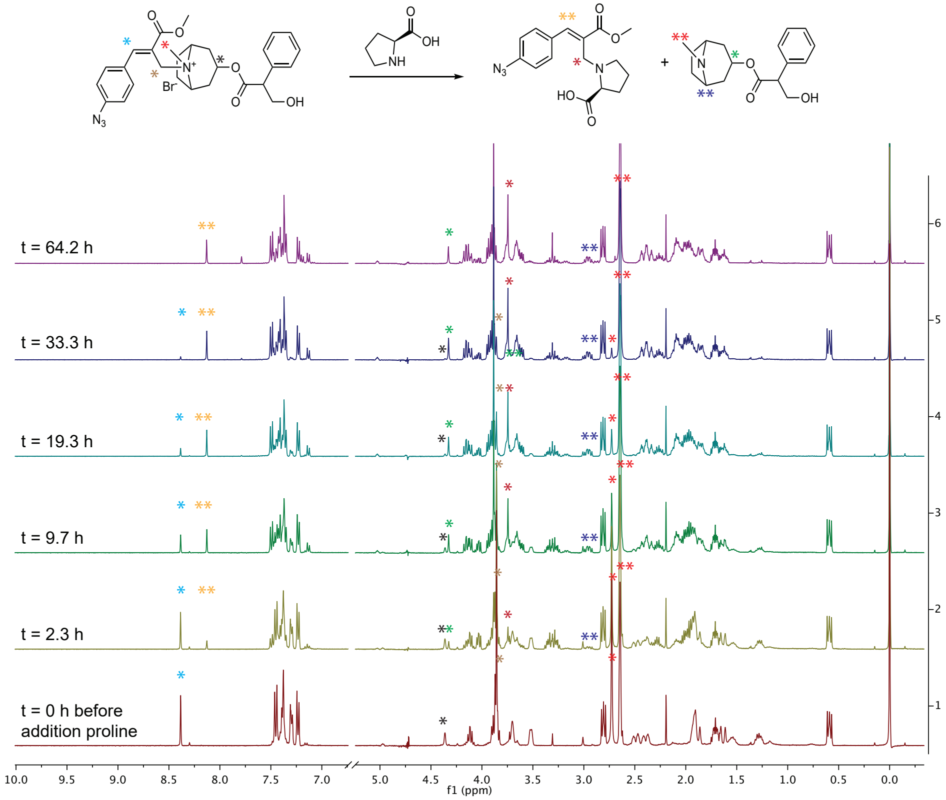

Figure S7: Reaction spectra of **10** with signal **16** followed by ^{1}H NMR at different time points. The reaction was carried out in d$_6$-DMSO/phosphate buffer mixture 3:7 (0.1 M, pH = 7.0). The peak attributed to ~ 0.0 ppm corresponds to DSS internal standard and was used to align the spectra.

5.5.4 Dextran alkyne synthesis

Dextran (500 kDa, 3.4 g, 0.0068 mmol) was dissolved in a NaOH solution (30 ml, 0.1 M) and heated to 35 ºC. Hereafter, glycydyl propargyl ether (5 mL, 52 mmol) is added dropwise and the solution was stirred overnight at 35 ºC. After cooling the reaction mixture to RT, the solution is poured in ethanol (600 mL) to precipitate alkyne modified dextran. The supernatant is decanted and the residue is re-dissolved in 150 mL demineralized water and dialyzed (MWCO = 3.5 kDa) against demineralized water for 72 hours (4 x 2 L). After freeze drying the resultant solution, the pure alkyne modified dextran was obtained as a white fluffy powder.

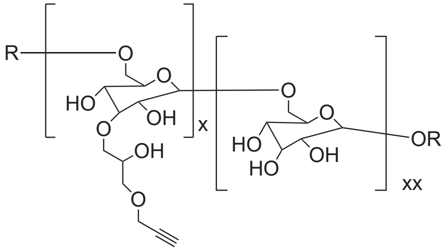

^{1}H NMR (400 MHz, D_2O) δ: 5.49, 5.34, 5.18, 5.00 (anomeric CH, 1H), 4.28 (s, 3H), 4.03 – 3.47 (m, 9H), 2.97 (s, 1H). **^{13}C NMR** (101 MHz, D_2O) δ: 97.66, 79.50, 76.13, 73.33, 71.34, 70.70, 70.11, 69.44, 68.80, 65.45, 58.24

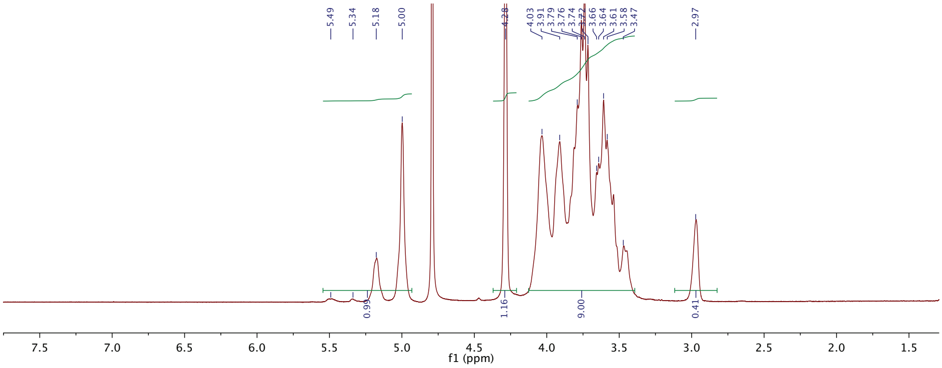

Figure S8: ^{1}H-NMR spectrum of alkyne modified dextran (500 kDa) in D_2O. Degree of substitution (DS) = 41% (ratio between alkyne peak (2.97 ppm) and the sum of anomeric proton peaks (5.49 to 5.00 ppm)).

5.5.5 Dextran hydrogel preparation

5.5.5.1 Dextran alkyne – chain modification with drug linker 9 and 12 (pre-click)

A 15 wt% dextran alkyne solution was prepared by dissolving 50 mg of dextran alkyne in DMF (0.3 mL) and hereafter shaken for 30 min before further usage. Corresponding drug linker (**9**: 8.0 mg, 0.012 mmol; **12**: 3.6 mg, 0.005 mmol) was solubilized in 0.2 mL DMF and shortly shaken. Next, a Cu-click solution was prepared containing CuBr (0.15 mg, 0.0020 mmol) and tris-hydroxypropyltriazolylmethylamine (THTPA) (0.25 mg, 0.0006 mmol). After degassing both solutions with argon for 10 min, the Cu-click solution (50 µL) was added to the dextran alkyne solution, covered with an argon blanket and then shaken vigorously for 48 hours.

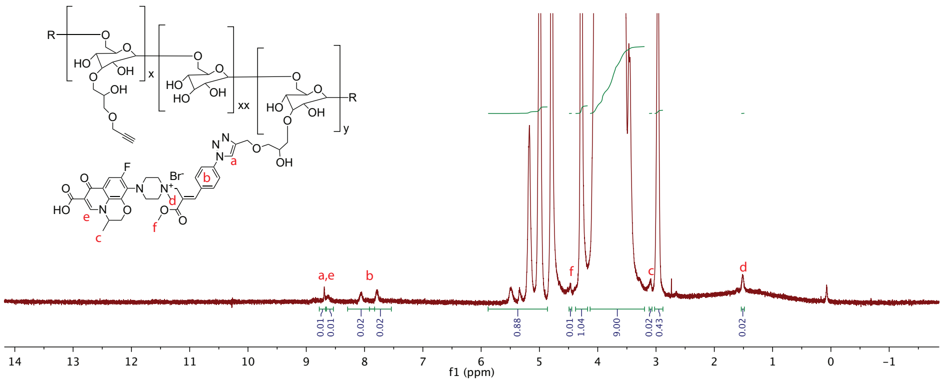

Figure S9: ^{1}H-NMR spectrum of ofloxacin modified alkyne-dextran (500 kDa) in D_2O.

5.5.5.2 Dextran alkyne – chain crosslinking (post-click)

A Cu-click solution was prepared by solubilizing $CuSO_4$ (0.15 mg, 0.0020 mmol), sodium ascorbate (1.2 mg, 0.0061 mmol) and THTPA (0.25 mg, 0.0006 mmol) in H_2O. Next, crosslinker (poly(ethylene glycol) bisazide, Mn = 1.100 g/mol, 5.0 mg, 0.0047 mmol) was dissolved in 0.15 mL DMF, added to the pre-clicked dextran-alkyne solution and shaken shortly before the Cu-click solution (50 µL) was added. Immediately, after addition, the solution was transferred into a mold where it was left for gelation for 30 min. After gelation was complete, the hydrogel was removed from the mold and placed into a dialysis membrane (MWCO = 8 kDA) were it was dialyzed for at least 6 h each, against DMSO, then against H_2O (2x) for 6 h, then EDTA aqueous solution (0.05 M) and again against H_2O, before further usage (Figure S10).

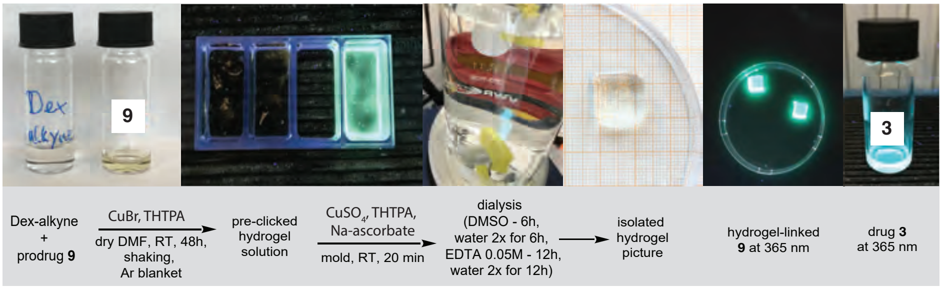

Figure S10: Drug-modified dextran-alkyne hydrogel fabrication procedure.

5.5.5.3 SEM analysis of dextran alkyne with/without chain modification using drug linker 9

Hydrogels were prepared using the procedure described in section 4.2 using alkyne-modified dextran for control hydrogels. For prodrug-modified hydrogels, prodrug incorporated alkyne-dextran was used. After their preparation, both hydrogels were submerged in liquid nitrogen and hereafter freeze dried. The freeze-dried samples were then analyzed by SEM.

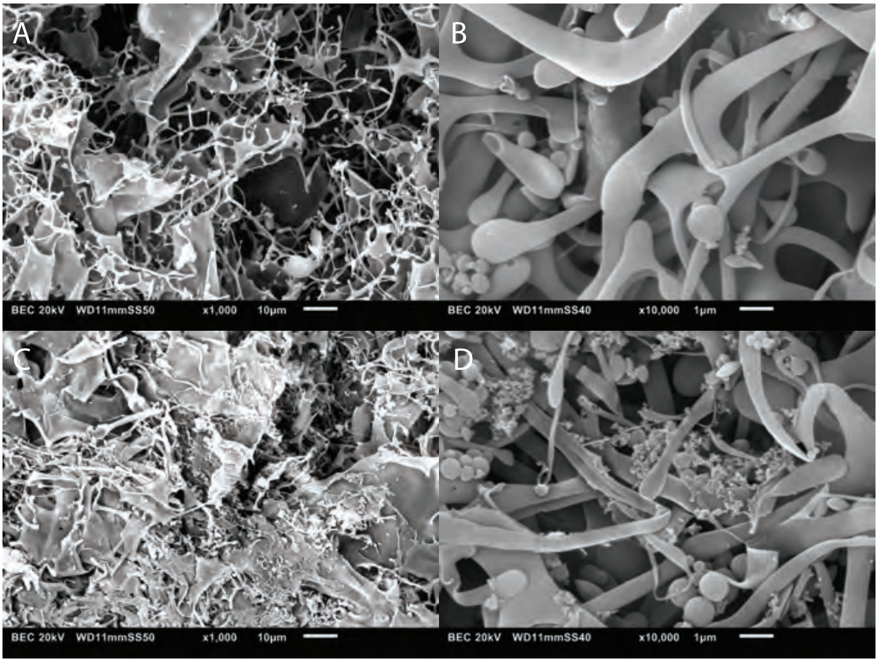

Figure S11: A) and B) SEM images taken of alkyne-modified dextran hydrogels. C) and D) SEM images taken of ofloxacin/prodrug **9** modified dextran alkyne hydrogels.

5.5.6 Signal triggered pro-drug activation/release studies with A549 cells

5.5.6.1 Cell culture and maintenance

A549 (lung epithelial adenocarcinoma) cell line was acquired by ATCC and cultured in Dulbecco's Modified Eagle Medium High Glucose (DMEM, Sigma) containing 4.5 g/L glu- cose, L-glutamine without sodium pyruvate, supplemented with 10% Fetal Bovine Serum (FBS, Sigma) and 1% Antibiotic-Antimycotic solution (Gibco). The cells were kept at 37°C and 5% CO_2 in sterile conditions and sub-cultured at least twice a week (never exceeding passage number 20). Cell were frequently tested for mycoplasma absence.

5.5.6.2 Wound-closure assay

The wound healing assay was carried out in a µ-Slide 4 well chambered coverslip (ibidi). A cell suspension containing $5x10^4$ cells/mL, obtained via trypsinization, was pipetted in each well to reach 70-80% confluence of the monolayer within 3 days. The cell-free gap was created on day 4 via direct manipulation: a 10 µL pipette tip was used to scratch the cell monolayer and generate the wound. Hydrogel, reactants and additives were added to each chamber, according to the tested conditions, immediately prior to the start of the experiment.

5.5.6.3 Wound-closure evaluation

To maintain favorable conditions for the cell monolayer, all experiments were conducted at 37℃ and 5% CO_2 using a stage top incubator (ibidi). Brightfield images were taken every hour for a total of 72 hours on an inverted microscope (Zeiss Axio-Observer Z1) equipped with an EMCCD camera (Andor ixon 3) with a resolution of 512 x 512 pixels and a moving stage, which allowed for the imaging of multiple conditions per experiment. Data analysis was performed with a machine-learning-based (bio)image analysis tool called ilastik (Heidelberg Collaboratory for Image Processing HCI) via Pixel and Object classification workflow. The software enabled for optimal binarization of low-contrast brightfield images with a small training dataset. The binarized image sequences were then processed in ImageJ (v1.53t, National Institute of Health, USA) for evaluation of the wound closure over time. The normalized wound closure (%) is defined in Eq.1 as follows:

$$\left(1-\frac{A(t)}{A_0}\right)\ x\ 100 \qquad \textbf{Eq.1}$$

, where A0 and A(t) are respectively the wound area at time 0, corresponding to the beginning of the experiment, and the wound area at time 1 to 72 (in hours).

5.5.6.4 Wound-closure evaluation – GSH only

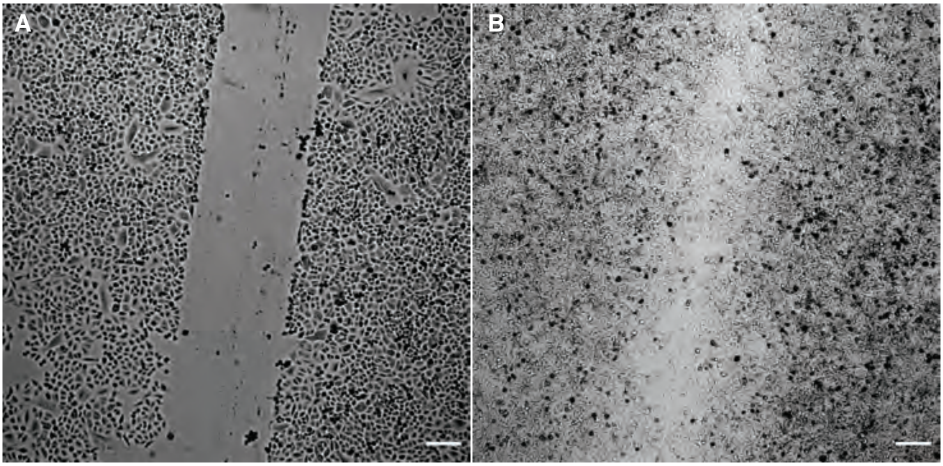

Figure S12: Brightfield images taken of wound closure experiment with only hydrogel, no prodrug and 400 µM of 15 at (A) 0 hours and (B) 72 hours. Scale bar inserts = 250 µm.

5.5.7 Synthesis of compounds

5.5.7.1 Synthesis of 4-Azidobenzaldehyde

A mixture of 4-formylphenylboronic acid (33.0 mmol, 4.95 g, 1.0 eq.), sodium azide (89.2 mmol, 5.8 g, 2.7 eq.) and copper(II)acetate (3.3 mmol, 0.6 g, 0.1 eq.) are stirred for 24 hours in methanol (180 mL). After completion, the reaction mixture is concentrated on celite under reduced pressure and purified by silica column chromatography (5:5 petroleum ether:ethyl acetate) to yield the title compound as an yellow oil (25.1 mmol, 3.7 g, 76%).

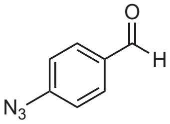

^{1}H NMR (400 MHz, $CDCl_3$) δ 9.86 (s, 1H), 7.80 (d, J = 8.5 Hz, 2H), 7.08 (d, J = 8.4 Hz, 2H). **^{13}C NMR (**101 MHz, $CDCl_3$) δ: 190.6, 146.4, 133.3, 131.6, 131.6, 119.6. **IR (ATR)** (cm^{-1}): 2109, 1689, 1594, 1502, 1280, 1211, 1165, 1126, 827, 781.

5.5.7.2 Synthesis of methyl 2-((4-azidophenyl)(hydroxy)methyl)acrylate

4-Azidobenzaldehyde (25.1 mmol, 3.7 g, 1.0 eq.), methyl acrylate (75.4 mmol, 6.8 mL, 3.0 eq.), triethanolamine (20.1 mmol, 3.0 g, 0.8 eq.) and DABCO (25.1 mmol, 2.8 g, 1.0 eq.) are added to a flask with 20 mL THF and stirred at RT for 4 days. After completion the reaction mixture is diluted with water and extracted three times with DCM. The organic layers are then dried with Na_2SO_4 and concentrated under reduced pressure. The residue is then purified by silica column chromatography (8:2 petroleum ether:ethyl acetate) to yield the title compound as pale yellow oil (8.1 mmol, 1.9 g, 32%).

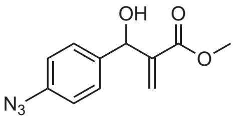

^{1}H NMR (400 MHz, $CDCl_3$) δ: 7.26 (d, J = 8.5 Hz, 2H), 6.90 (d, J = 8.2 Hz, 2H), 6.24 (s, 1H), 5.77 (s, 1H), 5.43 (s, 1H), 3.62 (s, 3H), 3.25 (s, 1H). **^{13}C NMR (**101 MHz, $CDCl_3$) δ: 166.6, 141.8, 139.5, 138.1, 128.1, 126.0, 119.0, 72.5, 52.0. **IR (ATR)** (cm^{-1}): 3284, 2954, 2872, 2117, 1716, 1589, 1436, 1261, 1161, 1057, 829, 748.

5.5.7.3 Synthesis of (Z) methyl 2-((4-azidophenyl)(hydroxy)methyl) acrylate (**1**)

Methyl 2-((4-azidophenyl)(hydroxy)methyl)acrylate (8.1 mmol, 1.9 g. 1.0 eq.) is dissolved in anhydrous DCM (40 mL) and cooled to 0 degrees Celcius. PBr_3 (1M DCM solution, 1.33 mL, 0.9 eq.) is then added dropwise under an argon atmosphere. After completion the reaction is stopped by adding ice. The mixture is then extracted with DCM and washed twice with water. The organic layers are then dried with Na_2SO_4, filtered and concentrated under reduced pressure. The residue is then purified by silica column chromatography (9.5:0.5 petroleum ether:ethyl acetate) to yield methyl 3-(4-azidophenyl)-2-(bromomethyl)acrylate as white-yellowish solid (1.9 g, 6.4 mmol, 80%).

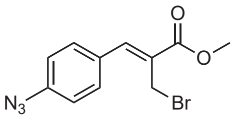

^{1}H NMR (400 MHz, $CDCl_3$) δ: 7.70 (s, 1H), 7.57 – 7.49 (m, 2H), 7.09 – 7.01 (m, 2H), 4.32 (s, 2H), 3.81 (s, 3H). **^{13}C NMR** (101 MHz, $CDCl_3$) δ: 166.6, 141.9, 141.6, 131.5, 130.9, 128.2, 119.5, 52.5, 26.7. **IR (ATR)** (cm^{-1}): 2112, 1711, 1601, 1502, 1433, 1266, 1215, 1188, 1153, 1080, 833, 768.

5.5.7.4 Synthesis of (Z,E) 1-(3-(4-azidophenyl)-2-(methoxycarbonyl)allyl)-1,4-diazabicyclo[2.2.2]octan-1-ium bromide (**13**)

3-(4-azidophenyl)-2-(bromomethyl)acrylate (0.081 mmol, 23.9 mg, 1.0 eq.) and DABCO (0.083 mmol, 9.35 mg, 1.0 eq.) are dissolved in THF (1.0 mL) and stirred overnight. The resulting precipitate is washed with diethyl ether and collected to give the title compound as a yellowish solid (0.07 mmol, 28.3 mg, 86%).

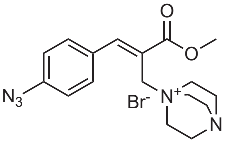

^{1}**NMR** (400 MHz, MeOD) (E - configuration, 67%) δ: 8.42 (s, 1H), 7.62 (d, J = 8.8 Hz, 2H), 7.23 (d, J = 8.6 Hz, 2H), 4.56 (s, 2H), 3.91 (s, 3H), 3.24 – 3.15 (m, 6H), 3.10 – 3.00 (m, 6H). (Z - configuration, 33%) δ: 7.52 (s, 1H), 7.50 (d, J = 4.6 Hz, 2H), 7.12 (d, J = 8.7 Hz, 2H), 4.36 (s, 2H), 3.75 (s, 3H), 3.51 – 3.39 (m, 6H), 3.27 – 3.16 (m, 6H). ^{13}**C NMR** (101 MHz, MeOD) (E - configuration, 67%) δ: 168.4, 152.3, 143.8, 132.4, 131.7, 121.2, 121.0, 59.1, 53.6, 53.6, 46.2. (Z - configuration, 33%) δ: 168.8, 151.0, 143.4, 132.4, 132.1, 120.9, 119.9, 68.5, 53.7, 53.0, 46.2. **MS** (ESI+) m/z: 328.13 (M-Br) (expected m/z: 328.18).

5.5.7.5 Synthesis of 1-(3-(4-azidophenyl)-2-(methoxycarbonyl)allyl)-1,4-lidocaine bromide (**8**)

3-(4-azidophenyl)-2-(bromomethyl)acrylate (0.143 mmol, 42.2 mg, 1.0 eq.) and lidocaine (0.129 mmol, 30.3 mg, 0.9 eq.) are dissolved in CH_3CN (1.0 mL) and stirred overnight. The residue is then purified by silica column chromatography (20:1 DCM:MeOH) to yield the title compound as an orange-yellow oil (45.9 mg, 0.087 mmol, 67%).

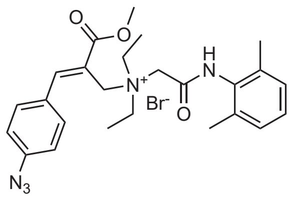

^{1}**NMR** (400 MHz, MeOD) δ: 8.41 (s, 1H), 7.56 (d, J = 8.5 Hz, 2H), 7.21 (d, J = 8.6 Hz, 2H), 7.12 (q, J = 5.4 Hz, 3H), 5.01 (s, 2H), 4.28 (s, 2H), 3.92 (s, 3H), 3.47 (qd, J = 13.4, 7.0 Hz, 4H), 2.22 (s, 6H), 1.20 (t, J = 7.1 Hz, 6H).). ^{13}**C NMR** (101 MHz, MeOD) δ: 167.3, 162.4, 151.3, 142.2, 135.2, 132.6, 130.6, 130.3, 127.9, 127.5, 121.4, 119.6, 56.1, 55.3, 53.2, 52.2, 17.2, 7.3. **MS** (ESI+) m/z: 450.07 (M-Br) (expected m/z: 450.25).

5.5.7.6 Synthesis of 1-(3-(4-azidophenyl)-2-(methoxycarbonyl)allyl)-1,4-aripiprazole bromide (**11**)

3-(4-azidophenyl)-2-(bromomethyl)acrylate (0.173 mmol, 51.2 mg, 1.0 eq.) and aripiprazole (0.158 mmol, 70.8 mg, 0.9 eq.) are dissolved in THF (1.0 mL) and stirred for 5 days. The resulting precipitate is washed with diethyl ether and collected to give the title compound as a pale-yellow solid (0.0645 mmol, 48 mg, 41%).

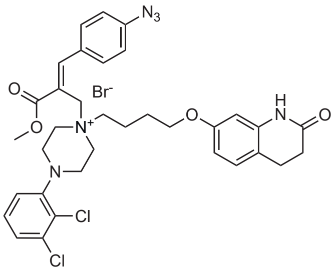

^{1}NMR (400 MHz, DMSO) δ: 10.02 (s, 1H), 8.34 (s, 1H), 7.70 (d, J = 8.4 Hz, 2H), 7.43 – 7.32 (m, 2H), 7.25 (d, J = 8.4 Hz, 2H), 7.14 (dd, J = 7.6, 2.0 Hz, 1H), 7.06 (d, J = 8.3 Hz, 1H), 6.47 (dd, J = 8.2, 2.5 Hz, 1H), 6.43 (d, J = 2.5 Hz, 1H), 4.71 (s, 2H), 3.86 (s, 3H), 3.75 (t, J = 6.2 Hz, 2H), 3.49 – 3.36 (m, 6H), 3.20 (d, J = 13.4 Hz, 2H), 2.79 (t, J = 7.5 Hz, 2H), 2.41 (dd, J = 8.5, 6.5 Hz, 2H), 1.54 (t, J = 5.6 Hz, 2H), 1.40 (t, J = 7.2 Hz, 2H). **^{13}C NMR** (101 MHz, DMSO) δ: 170.7, 167.5, 158.1, 151.0, 149.4, 141.9, 139.7, 133.1, 131.8, 130.5, 128.9 (d, J = 5.3 Hz), 126.6, 126.0, 120.7 (d, J = 9.2 Hz), 120.3, 116.2, 107.8, 102.2, 67.3, 58.2, 53.5, 44.6, 31.2, 25.9, 24.4, 19.0. **MS** (ESI+) m/z: 663.15 (M-Br) (expected m/z: 663.22).

5.5.7.7 Synthesis of 1-(3-(4-azidophenyl)-2-(methoxycarbonyl)allyl)-1,4-ofloxacin bromide (**9**)

3-(4-azidophenyl)-2-(bromomethyl)acrylate (0.175 mmol, 51.8 mg, 1.0 eq.) and ofloxacin (0.166 mmol, 60.0 mg, 0.95 eq.) are dissolved in CH_3CN (2.5 mL) and stirred for 48 hours. The resulting precipitate is washed with ethyl acetate and then diethyl ether and collected to give the title compound as a pale-yellow solid (0.083 mmol, 54.4 mg, 50%).

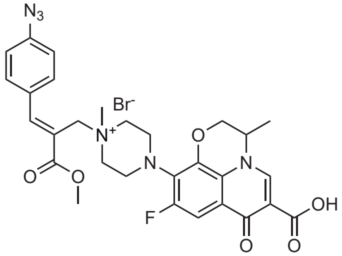

^{1}NMR (400 MHz, DMSO) δ: 8.99 (s, 1H), 8.35 (s, 1H), 7.73 (d, J = 8.2 Hz, 2H), 7.60 (d, J = 12.0 Hz, 1H), 7.26 (d, J = 8.6 Hz, 2H), 4.94 (d, J = 7.1 Hz, 1H), 4.72 (s, 2H), 4.55 (d, J = 12.1 Hz, 1H), 4.39 (d, J = 11.8 Hz, 1H), 3.86 (s, 3H), 3.69 – 3.34 (m, 9H), 2.95 (s, 3H), 1.45 (d, J = 6.7 Hz, 3H). **^{13}C NMR** (101 MHz, DMSO) δ: 176.8 (d, J = 3.3 Hz), 167.5, 166.3, 156.7, 154.3, 151.0, 146.9, 141.7, 140.8 (d, J = 6.5 Hz), 132.0, 130.6, 130.5, 130.3, 125.1, 120.9 (d, J = 9.4 Hz), 120.4, 120.3, 119.6, 107.3, 103.7 (d, J = 23.9 Hz), 68.8, 67.5, 60.4, 58.5, 55.3, 53.4, 45.8, 44.1, 25.6, 18.4. **^{19}F NMR** (376 MHz, DMSO) δ: -120.24 (d, J = 12.1 Hz). **MS** (ESI+) m/z: 577.13 (M-Br) (expected m/z: 577.22).

5.5.7.8 Synthesis of 1-(3-(4-azidophenyl)-2-(methoxycarbonyl)allyl)-1,4-atropine bromide (**10**)

3-(4-azidophenyl)-2-(bromomethyl)acrylate (0.169 mmol, 50.2 mg, 1.0 eq.) and atropine (0.141 mmol, 40.8 mg, 0.83 eq.) are dissolved in THF (1.5 mL) and stirred overnight. The residue is then purified by silica column chromatography (90:10 DCM:MeOH) to yield the title compound as an white-yellowish oil (54.1 mg, 0.092 mmol, 66%).

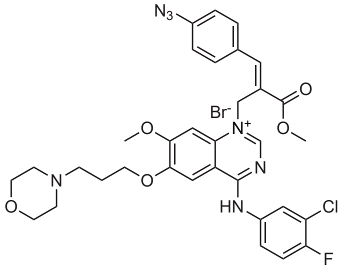

^{1}**NMR** (400 MHz, MeOD) δ: 8.40 (s, 1H), 7.52 (d, J = 8.2 Hz, 2H), 7.41 – 7.29 (m, 5H), 7.24 (d, J = 8.5 Hz, 2H), 5.04 (t, J = 5.8 Hz, 1H), 4.48 (s, 2H), 4.23 – 4.09 (m, 1H), 3.92 (s, 3H), 3.87 – 3.76 (m, 4H), 3.67 (s, 1H), 2.79 (s, 3H), 2.63 – 2.39 (m, 2H), 2.25 – 2.12 (m, 2H), 1.97 (d, J = 17.0 Hz, 2H), 1.79 – 1.58 (m, 2H). ^{13}**C NMR** (101 MHz, MeOD) δ: 171.3, 167.3, 150.9, 142.2, 135.7, 130.5, 130.3, 128.6, 128.5, 127.8, 127.5, 121.8, 119.7, 67.4, 67.1, 63.1 (d, J = 13.8 Hz), 54.6, 54.4, 52.1, 39.4, 31.9 (d, J = 3.4 Hz), 24.2, 23.9. **MS** (ESI+) m/z: 505.20 (M-Br) (expected m/z: 505.24).

5.5.7.9 Synthesis of 1-(3-(4-azidophenyl)-2-(methoxycarbonyl)allyl)-1,4-gefitinib bromide (**12**)

3-(4-azidophenyl)-2-(bromomethyl)acrylate (0.67 mmol, 200 mg, 1.0 eq.) and gefitinib (0.2 mmol, 90 mg, 0.3 eq.) are dissolved in THF (1.5 mL) and stirred overnight. The resulting precipitate is washed with diethyl ether and collected to give the title compound as a light-greenish solid (47 mg, 0.063 mmol, 31 %).

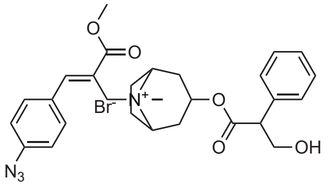

^{1}**NMR** (400 MHz, DMSO) δ: 11.46 (s, 1H), 9.83 (s, 1H), 8.95 (s, 1H), 8.33 (s, 1H), 8.07 (s, 1H), 7.95 (d, J = 6.9 Hz, 1H), 7.68 (t, J = 5.9 Hz, 1H), 7.56 (dq, J = 8.8, 5.8, 4.5 Hz, 3H), 7.18 (dd, J = 8.5, 2.3 Hz, 2H), 6.85 (s, 1H), 5.64 (s, 2H), 4.33 (s, 2H), 3.98 (d, J = 13.2 Hz, 2H), 3.75 – 3.64 (m, 7H), 3.54 (dd, J = 29.5, 9.8 Hz, 3H), 3.33 (s, 1H), 3.12 (d, J = 10.0 Hz, 2H), 2.28 (d, J = 11.1 Hz, 2H). ^{13}**C NMR** (101 MHz, DMSO) δ: 166.41, 158.21, 157.03, 154.69, 152.53, 149.40, 145.01, 141.92, 135.83, 133.93, 132.22, 130.30, 129.93, 129.47, 127.58, 126.30 (d, J = 7.7 Hz), 123.78, 120.05, 119.79 (d, J = 18.8 Hz), 117.50 (d, J = 22.1 Hz), 107.82, 106.44, 99.03, 67.93, 67.45, 63.79, 57.05, 54.11, 52.95, 51.71, 49.22, 25.56, 23.33. ^{19}**F NMR**

(376 MHz, DMSO) δ: -118.24. **MS** (ESI+) m/z: 663.33 (M+H-Br) (expected m/z: 662.23) and m/z: 1347.45 (2M+Na-Br) (expected m/z: 1347.35).

5.5.7.10 Synthesis of N-acetyl-S-(1-(4-azidophenyl)-2(methoxycarbonyl) allyl) cysteine (**19**)

(Z,E) 1-(3-(4-azidophenyl)-2-(methoxycarbonyl)allyl)-1,4-diazabicyclo [2.2.2] octan-1-ium bromide (4**a**) (0.091 mmol, 37.4 mg, 1.0 eq.) and N-acetyl cysteine (0.086 mmol, 14.1 mg, 0.94 eq.) are dissolved in H_2O (1.0 mL) and stirred for 2 hours. The resulting mixture is extracted with ethyl acetate and then evaporated to give the title compound as a bright-yellow oil (22.7 mg, 0.06 mmol, 69%).

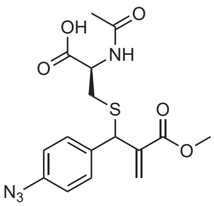

^{1}**NMR** (400 MHz, DMSO) δ: 12.78 (s, 1H), 8.23 (d, J = 9.2 Hz, 1H), 7.35 – 7.25 (m, 2H), 7.10 – 6.93 (m, 2H), 6.39 (d, J = 14.8 Hz, 1H), 6.09 (d, J = 17.2 Hz, 1H), 5.09 (d, J = 8.7 Hz, 1H), 4.43 – 4.27 (m, 1H), 3.59 (s, 3H), 2.80 – 2.58 (m, 2H), 1.82 (s, 3H). ^{13}**C NMR** (101 MHz, DMSO) δ: 171.99, 169.31, 165.57 (d, J = 7.1 Hz), 139.54, 139.12, 138.45, 136.32 (d, J = 5.3 Hz), 129.70, 127.36 (d, J = 19.1 Hz), 119.19 (d, J = 2.1 Hz), 52.09, 51.89, 51.48, 48.35 (d, J = 27.7 Hz), 33.33 (d, J = 17.6 Hz), 22.33. **MS** (ESI+) m/z: 378.78 (M+H) (expected m/z: 378.10).

5.5.8 NMR Spectra

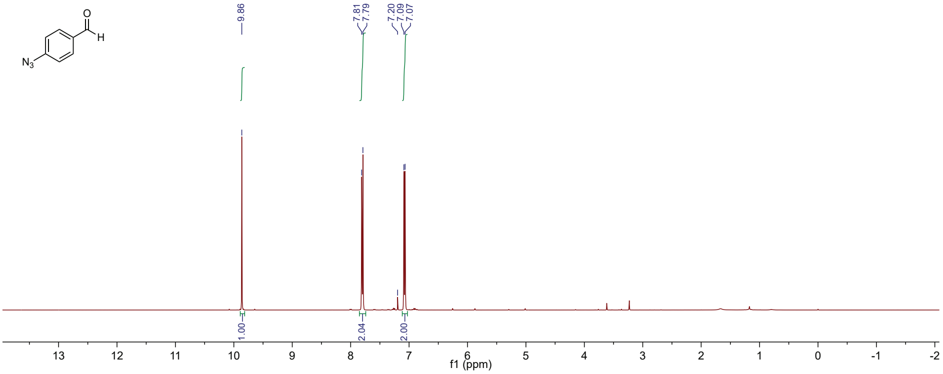

Figure S13: ^{1}H NMR, 4-azidobenzaldehyde in $CDCl_3$.

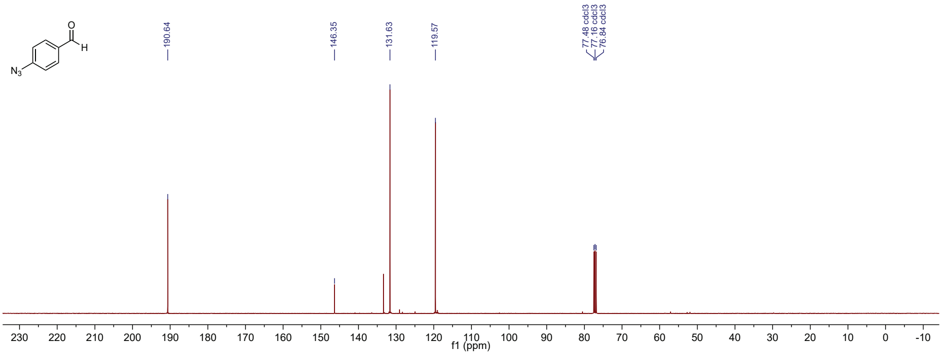

Figure S14: ^{13}C NMR, 4-azidobenzaldehyde in $CDCl_3$.

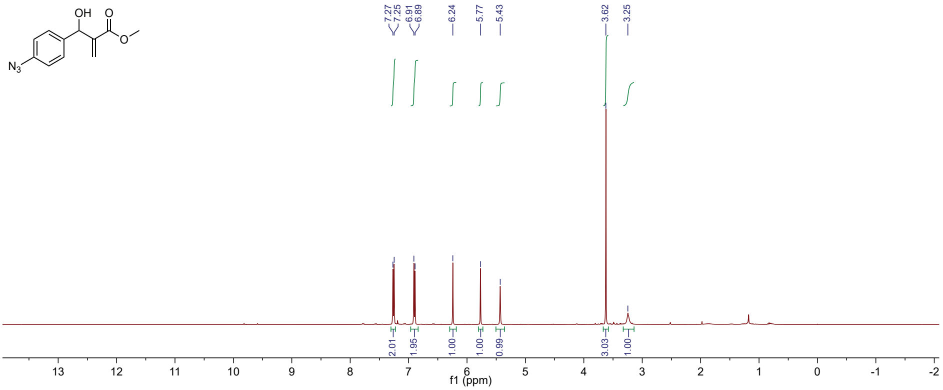

Figure S15: ^{1}H NMR, methyl 2-((4-azidophenyl)(hydroxy)methyl)acrylate in $CDCl_3$.

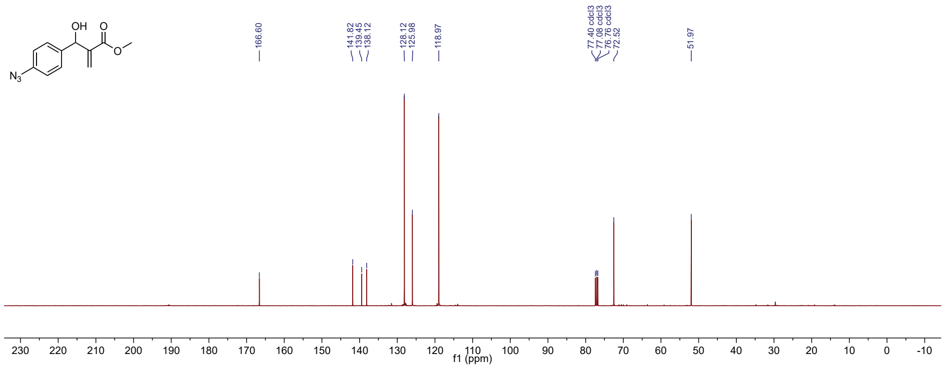

Figure S16: ^{13}C NMR, methyl 2-((4-azidophenyl)(hydroxy)methyl)acrylate in CDCl$_3$.

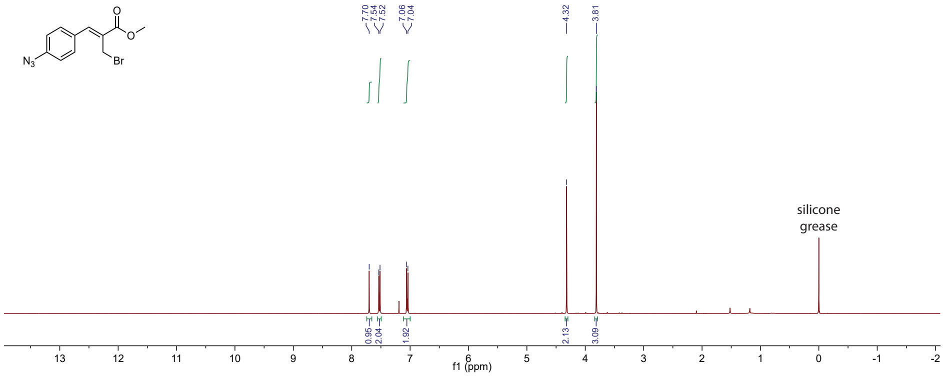

Figure S17: ^{1}H NMR, compound **1** in CDCl$_3$.

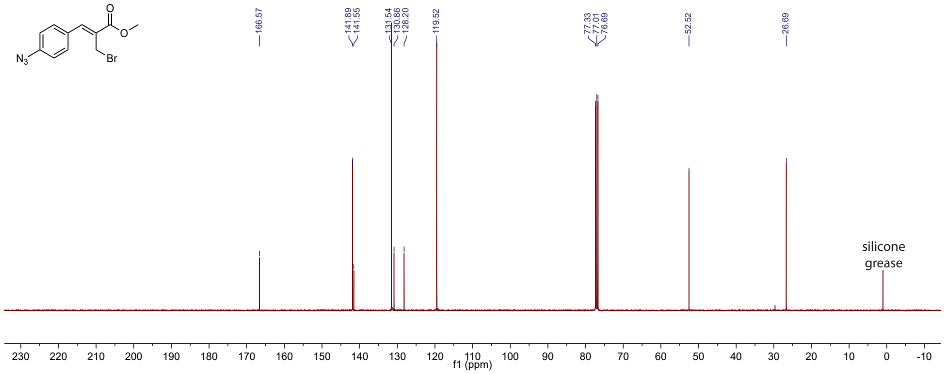

Figure S18: ^{13}C NMR, compound **1** in CDCl$_3$.

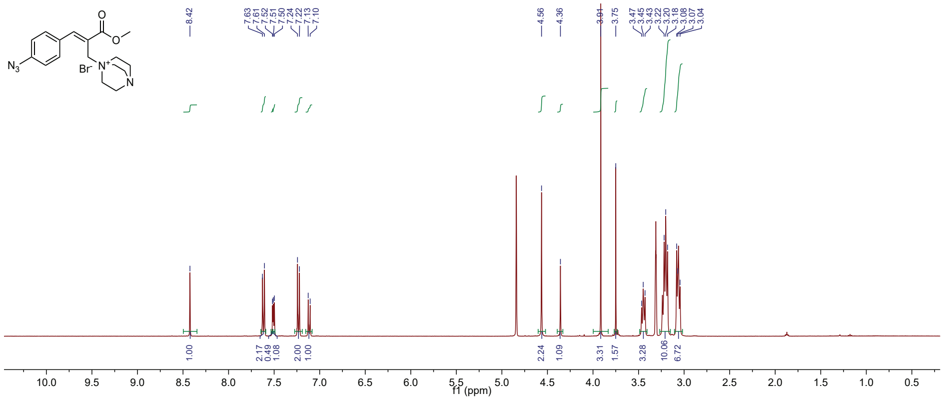

Figure S19: ^{1}H NMR, compound **13** in MeOD.

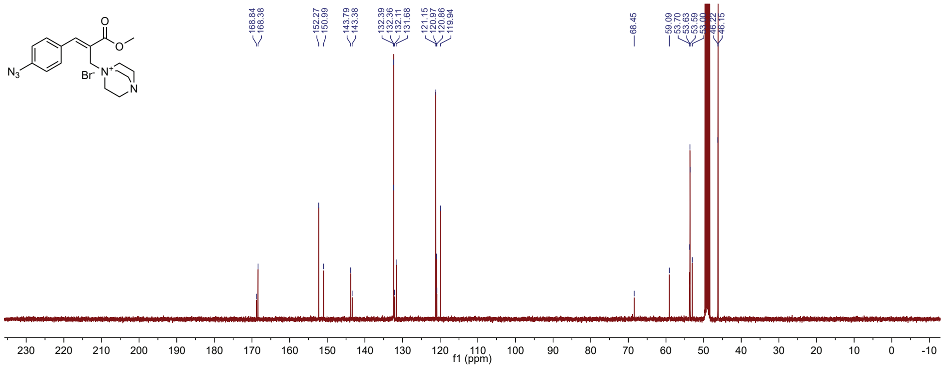

Figure S20: ^{13}C NMR, compound **13** in MeOD.

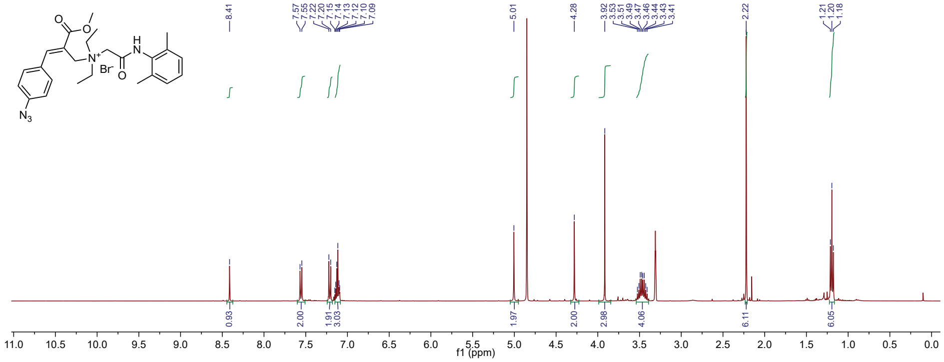

Figure S21: ^{1}H NMR, compound **8** in MeOD.

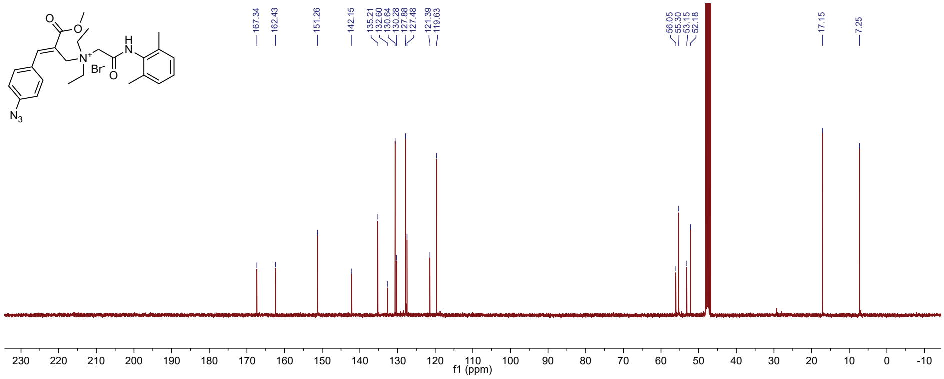

Figure S22: ^{13}C NMR, compound **8** in MeOD.

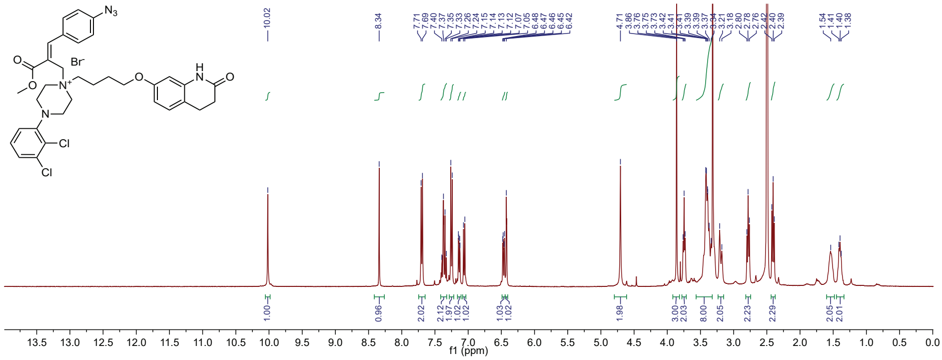

Figure S23: ^{1}H NMR, compound **11** in d_6-DMSO.

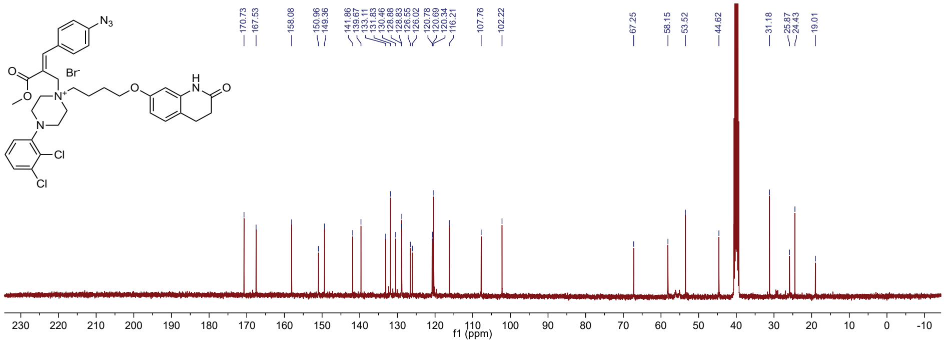

Figure S24: ^{13}C NMR, compound **11** in d_6-DMSO.

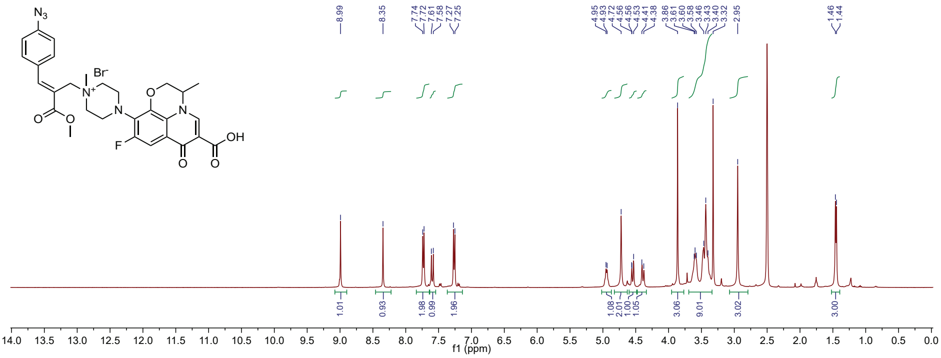

Figure S25: ^{1}H NMR, compound **9** in d_6-DMSO.

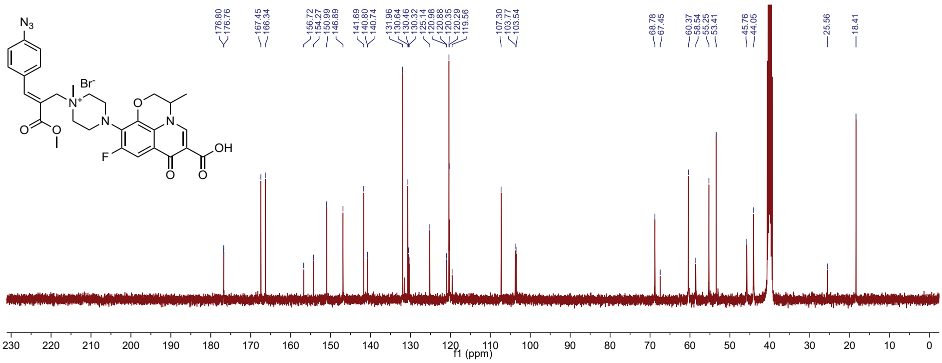

Figure S26: ^{13}C NMR, compound **9** in d_6-DMSO.

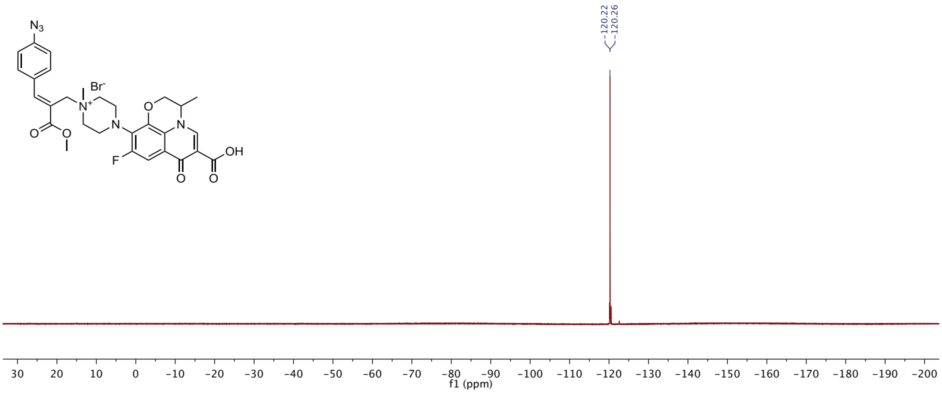

Figure S27: ^{19}F NMR, compound **9** in d_6-DMSO.

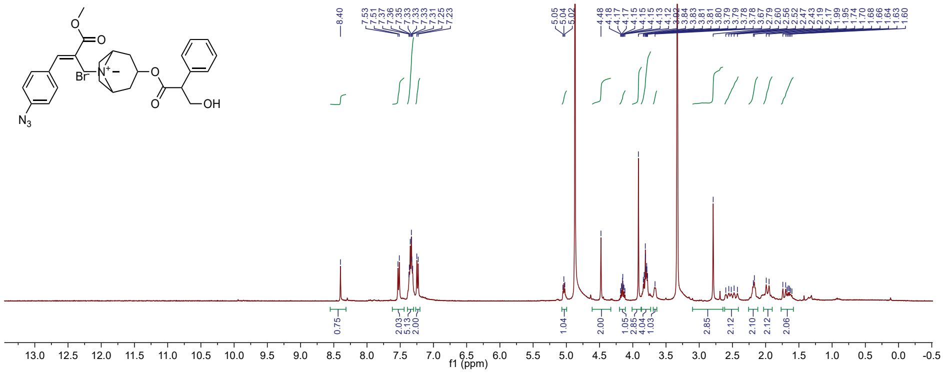

Figure S28: ^{1}H NMR, compound **10** in MeOD.

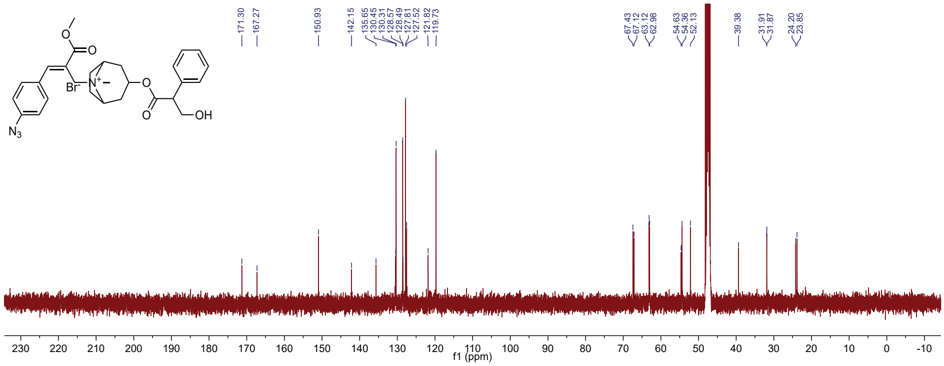

Figure S29: ^{13}C NMR, compound **10** in MeOD.

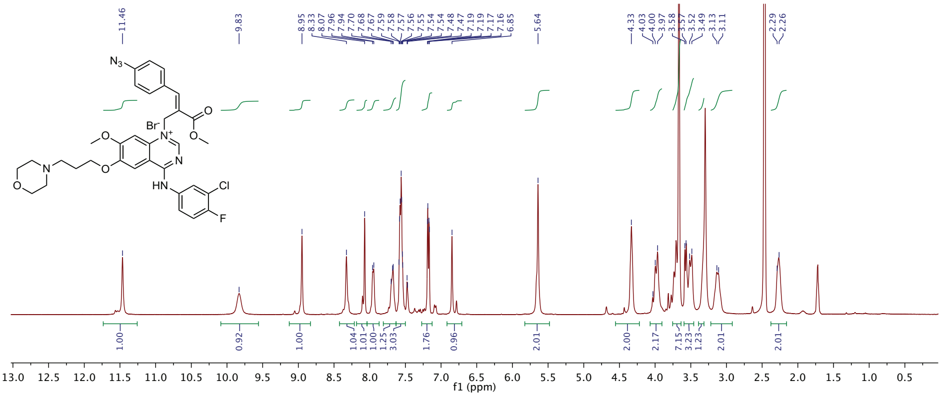

Figure S30: ^{1}H NMR, compound **12** in d$_6$-DMSO.

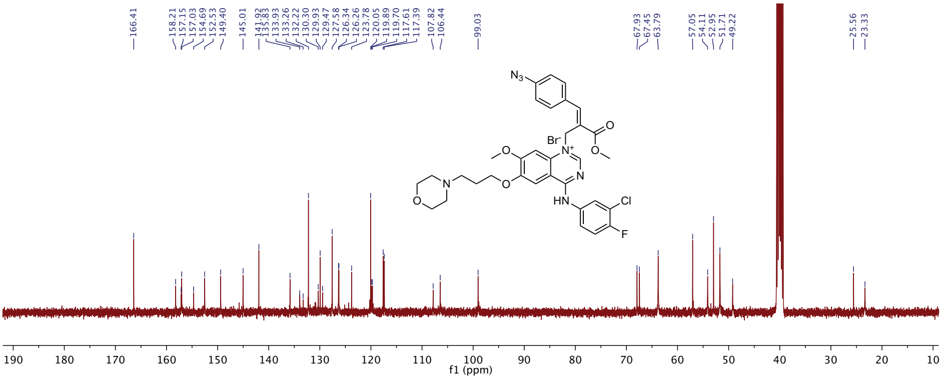

Figure S31: ^{13}C NMR, compound **12** in d$_6$-DMSO.

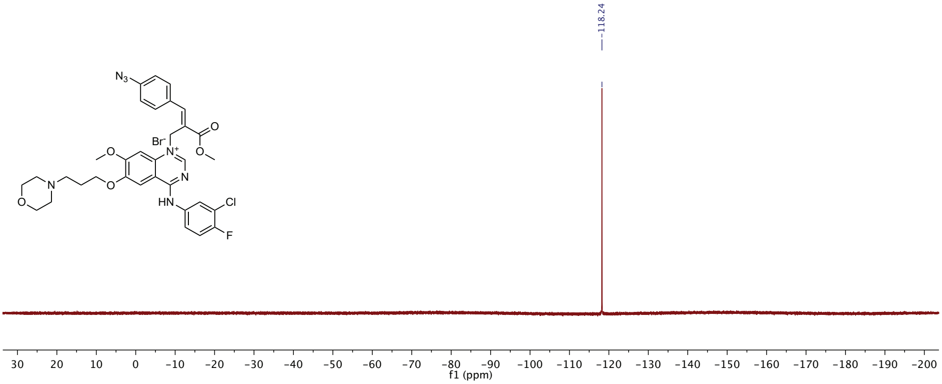

Figure S32: ^{19}F NMR, compound **12** in d$_6$-DMSO.

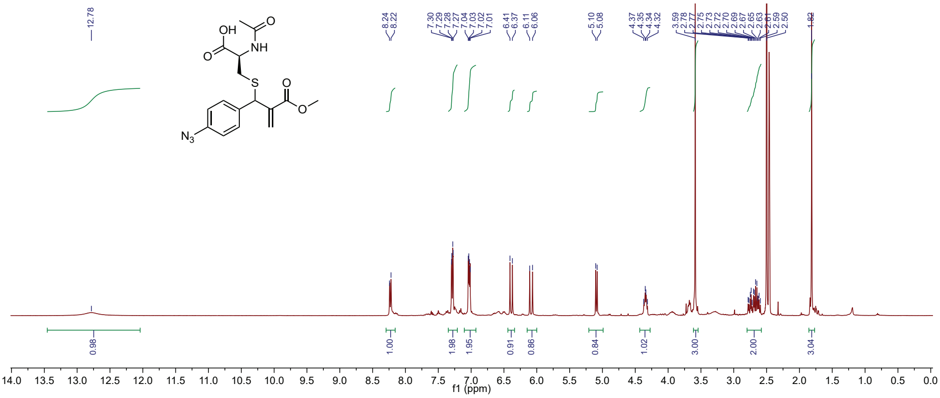

Figure S33: ^{1}H NMR, compound **19** in d$_6$-DMSO.

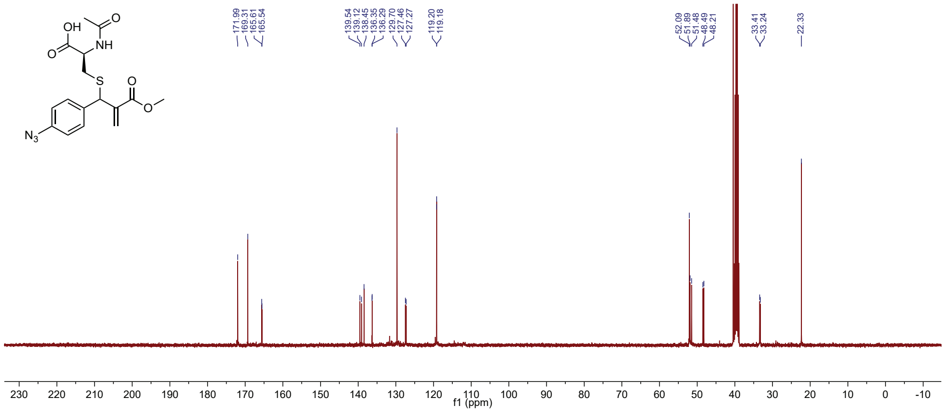

Figure S34: ^{13}C NMR, compound **19** in d$_6$-DMSO.

5.5.9 2-D NMR Spectra

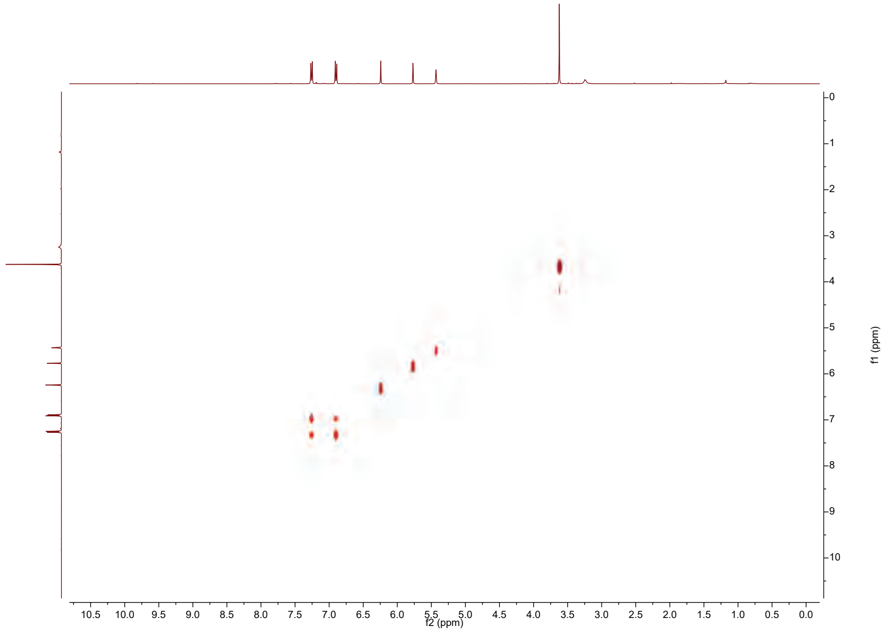

Figure S35: gCOSY of methyl 2-((4-azidophenyl)(hydroxy)methyl)acrylate in $CDCl_3$.

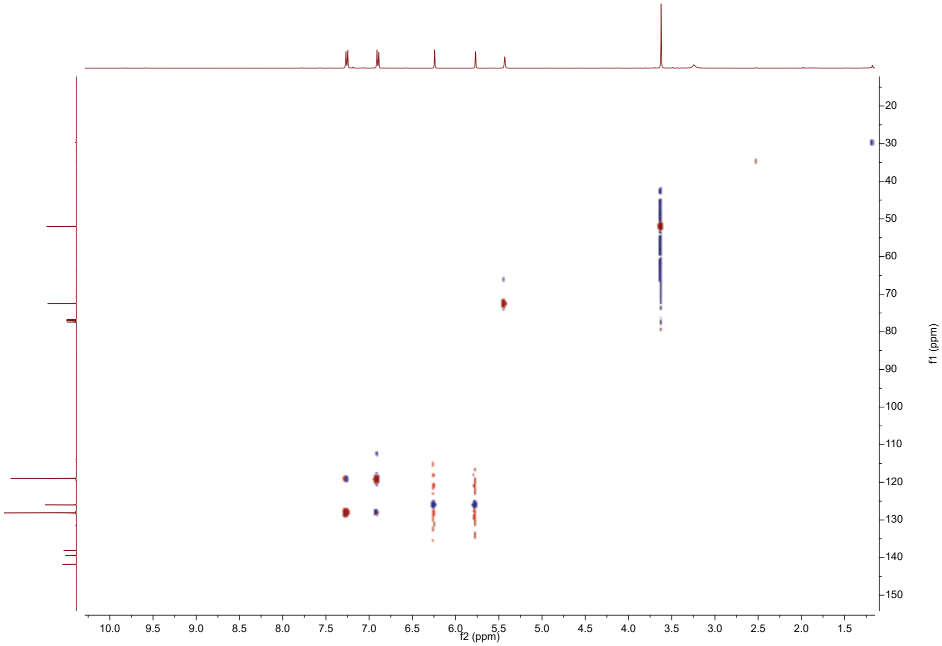

Figure S36: gHSQC of methyl 2-((4-azidophenyl)(hydroxy)methyl)acrylate in $CDCl_3$.

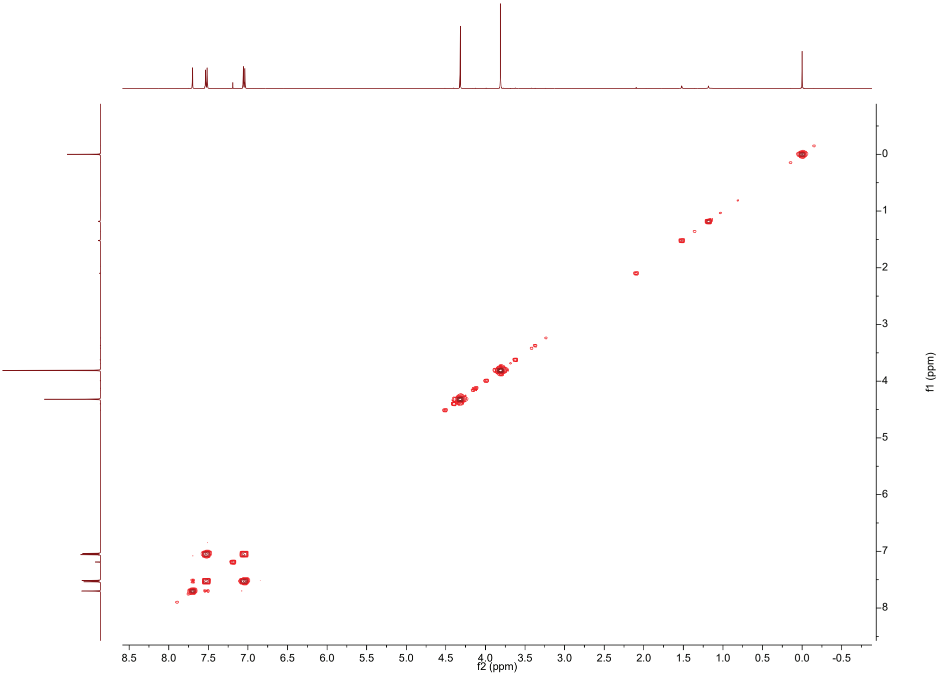

Figure S37: gCOSY of compound **1** in $CDCl_3$.

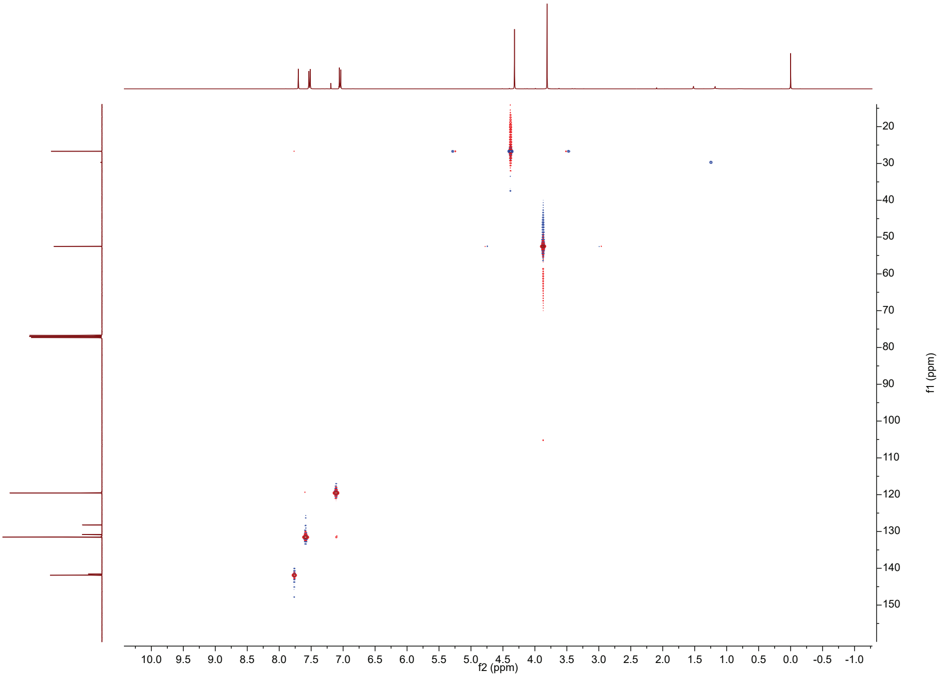

Figure S38: gHSQC of compound **1** in $CDCl_3$.

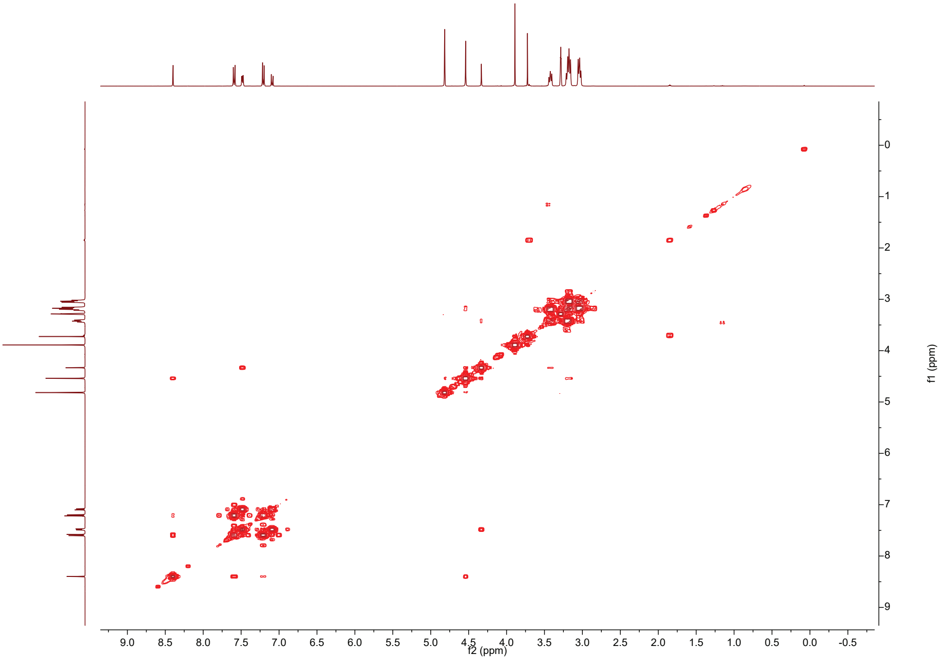

Figure S39: gCOSY of compound **13** in MeOD.

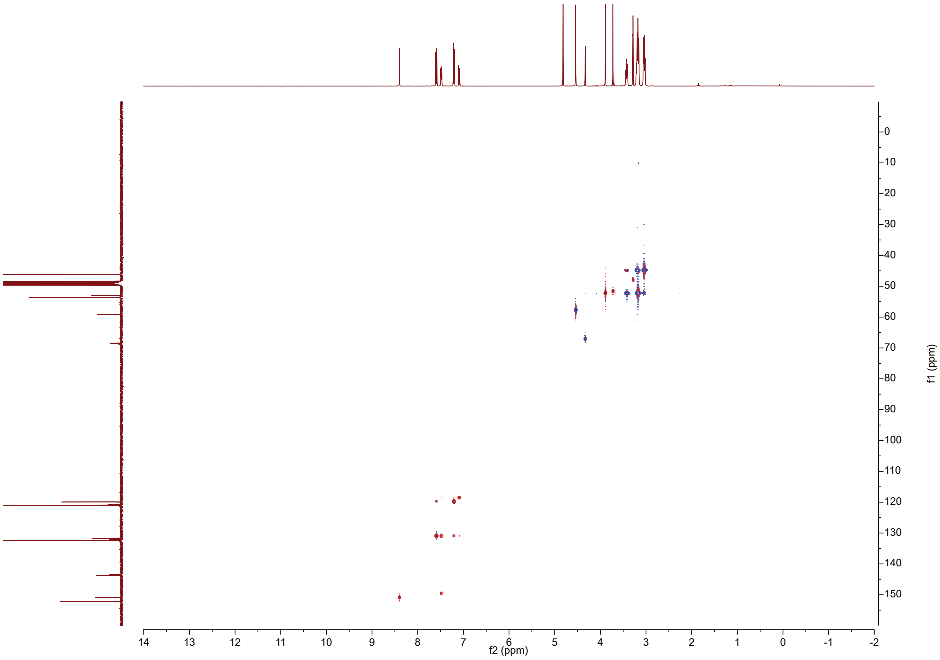

Figure S40: gHSQC of compound **13** in MeOD.

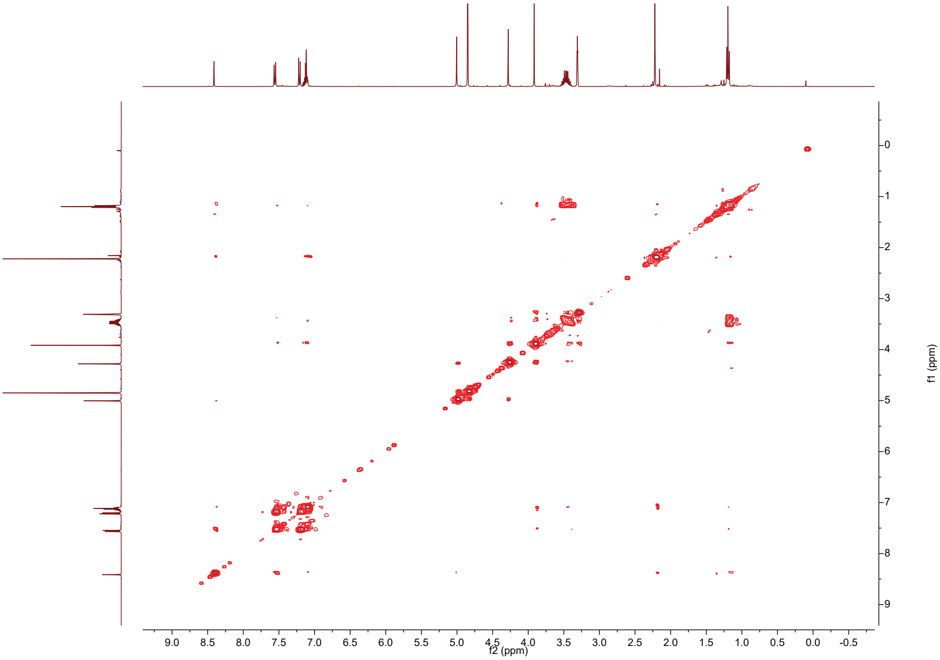

Figure S41: gCOSY of compound **8** in MeOD.

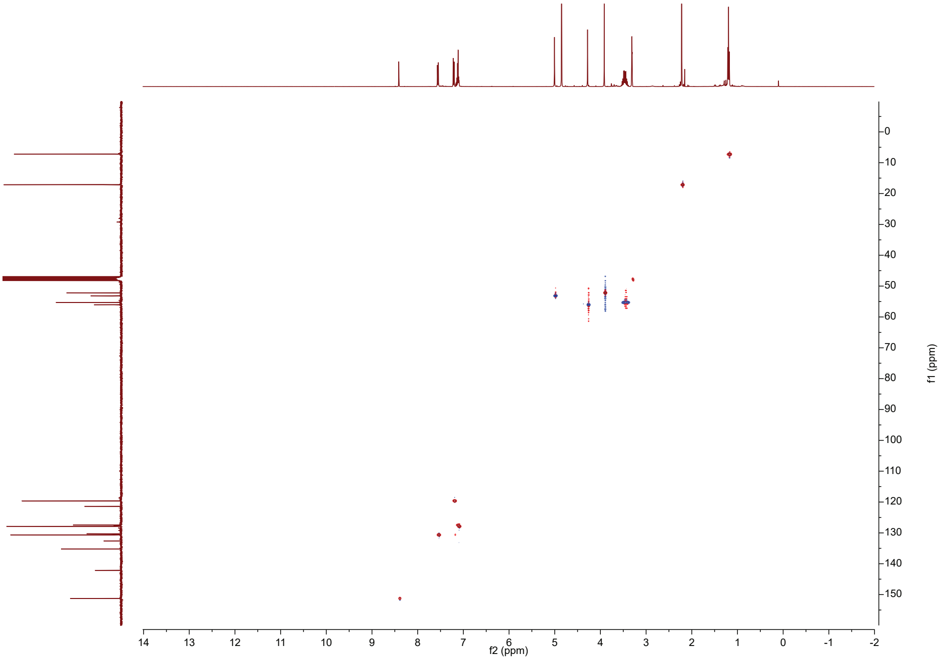

Figure S42: gHSQC of compound **8** in MeOD.

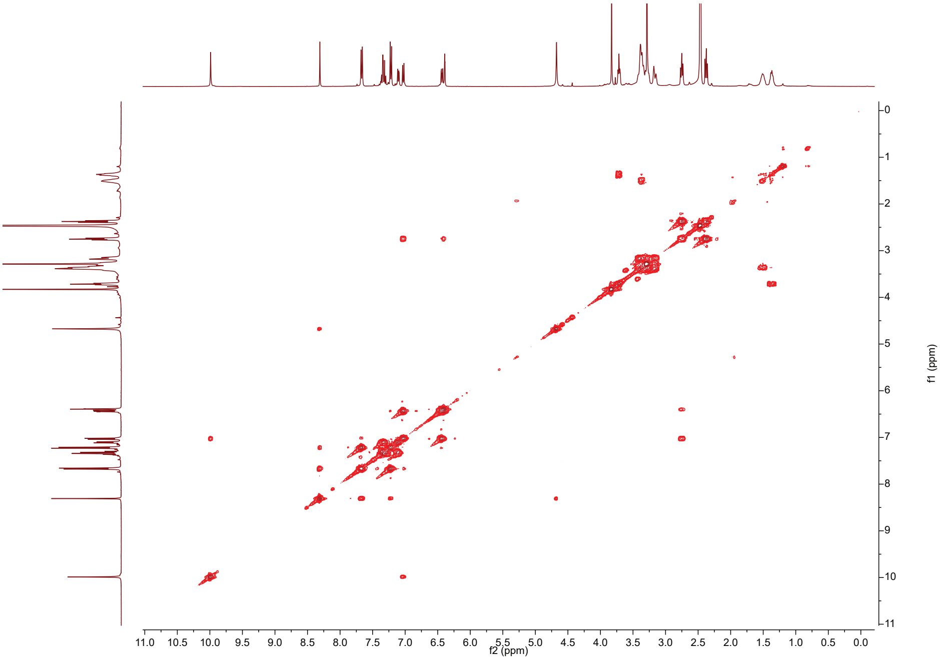

Figure S43: gCOSY of compound **11** in d_6-DMSO.

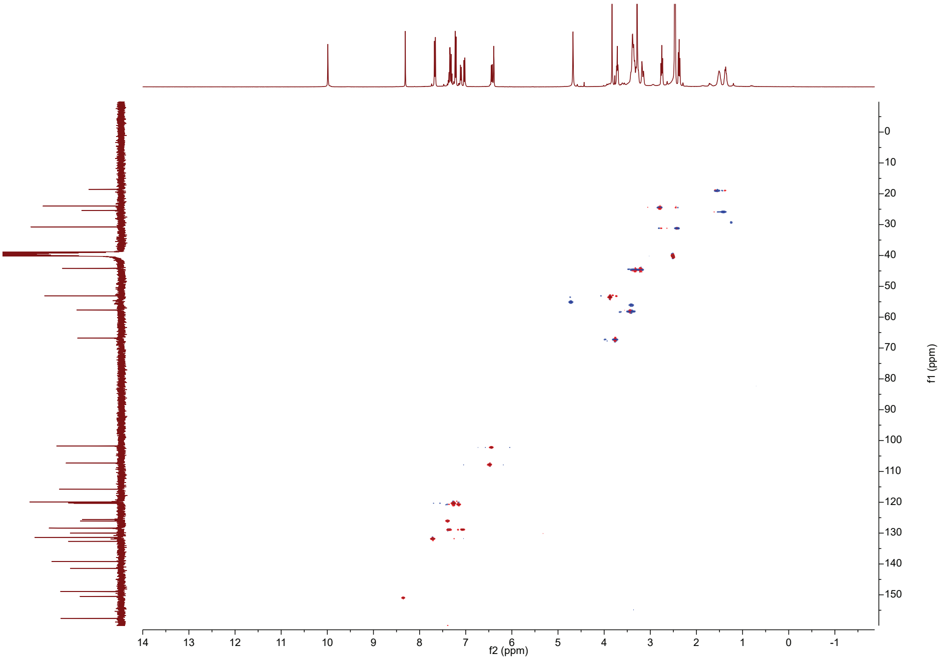

Figure S44: gHSQC of compound **11** in d_6-DMSO.

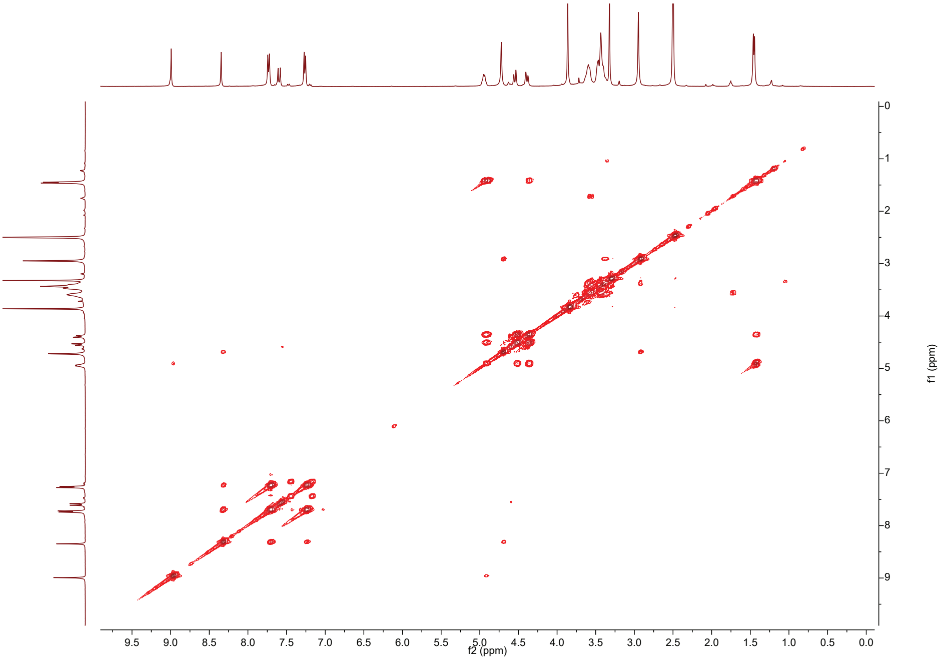

Figure S45: gCOSY of compound **9** in d_6-DMSO.

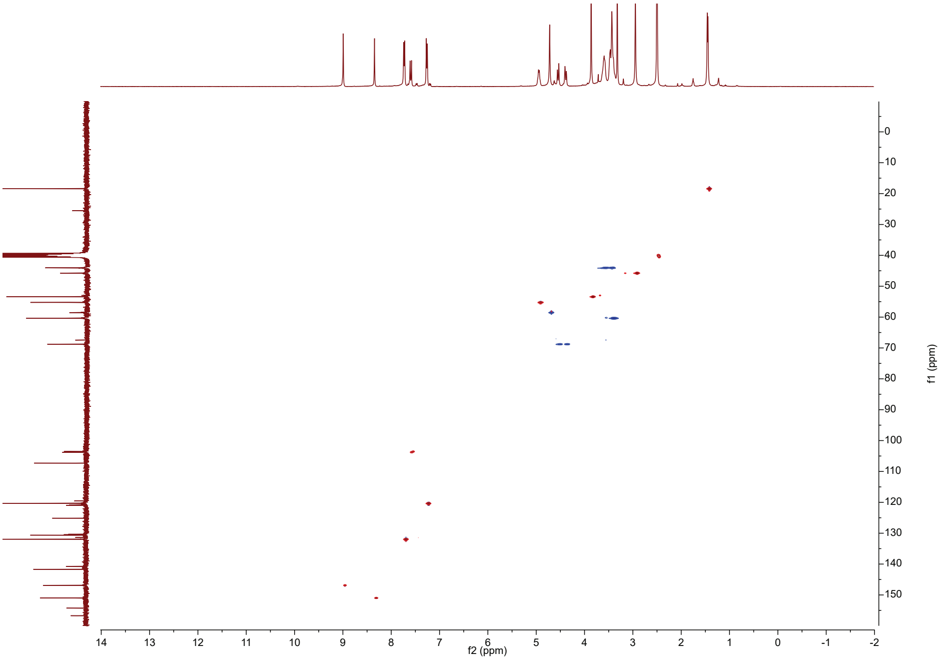

Figure S46: gHSQC of compound **9** in d_6-DMSO.

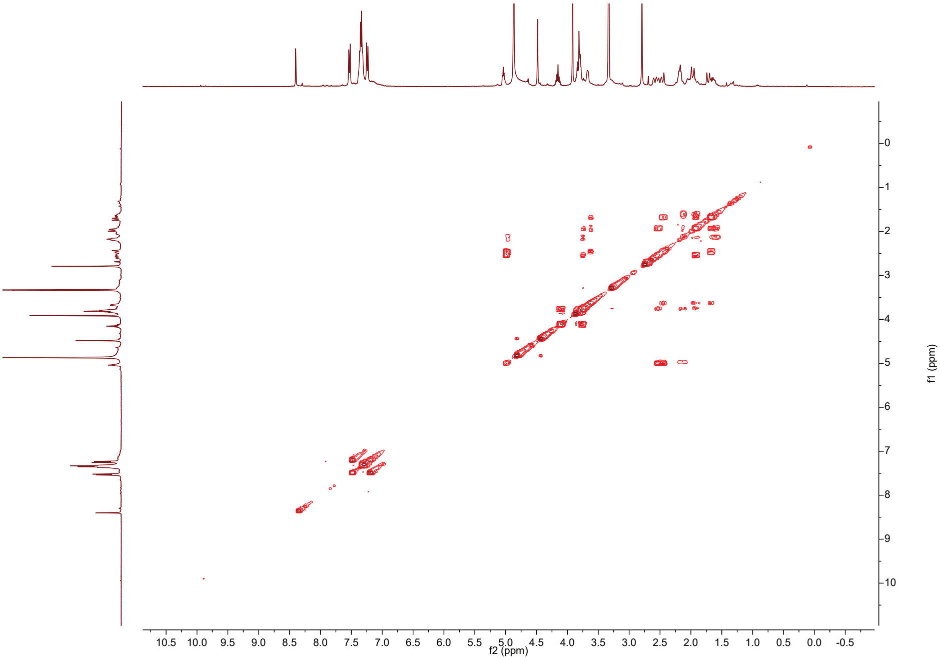

Figure S47: gCOSY of compound **10** in MeOD.

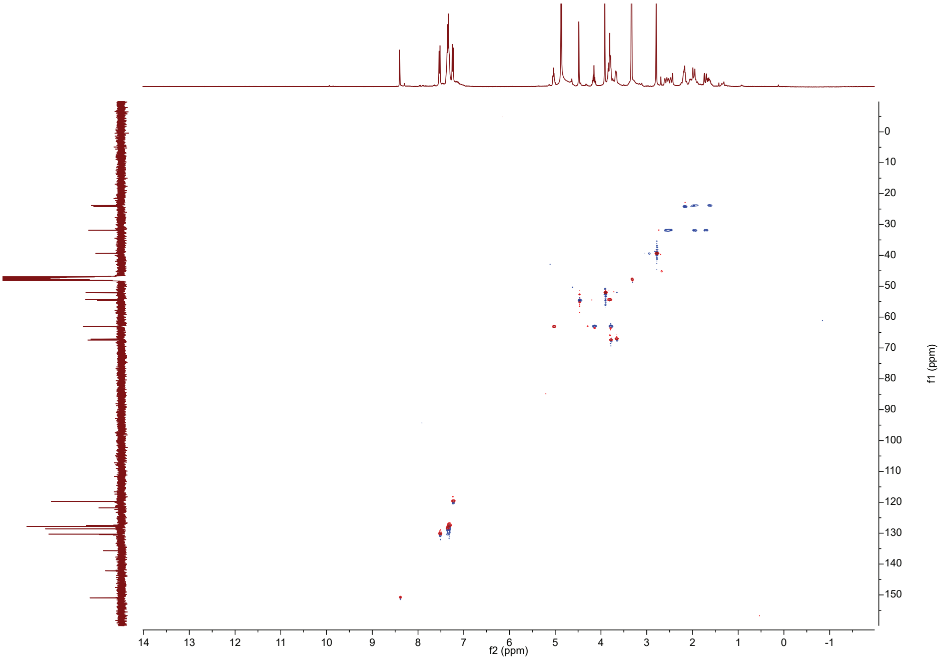

Figure S48: gHSQC of compound **10** in MeOD.

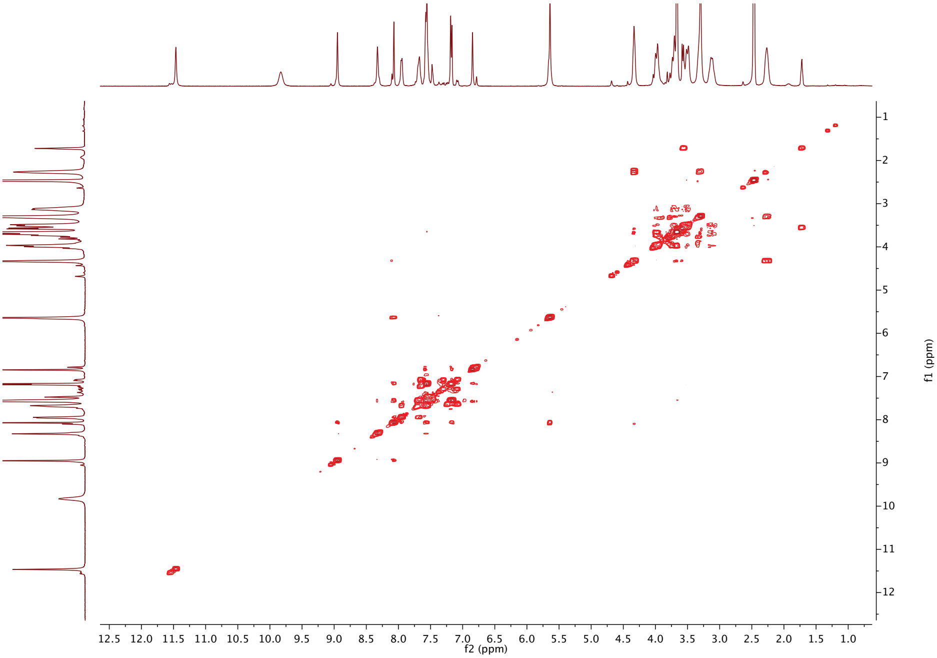

Figure S49: gCOSY of compound **12** in d_6-DMSO.

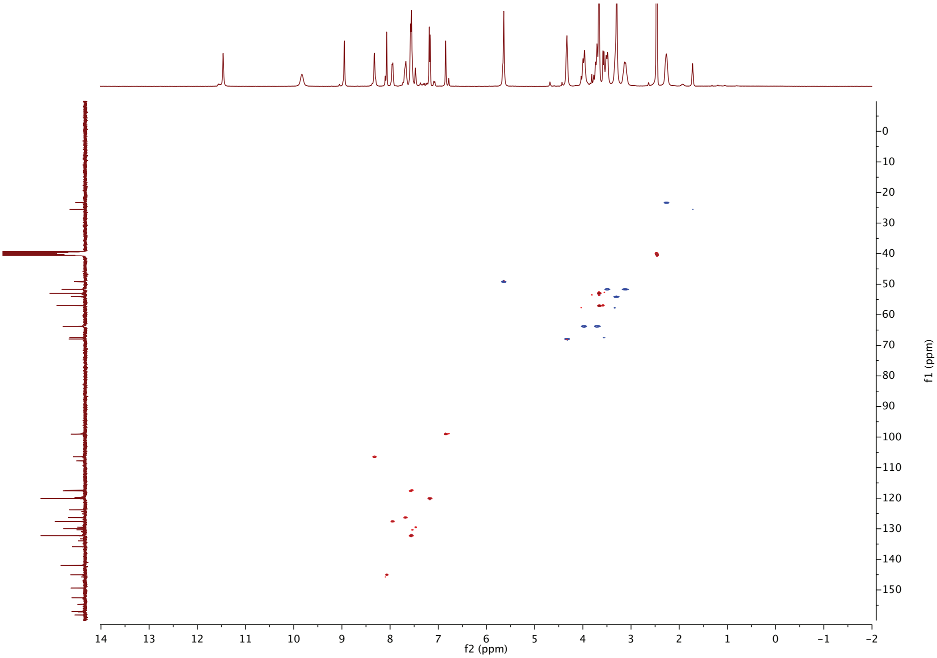

Figure S50: gHSQC of compound **12** in d_6-DMSO.

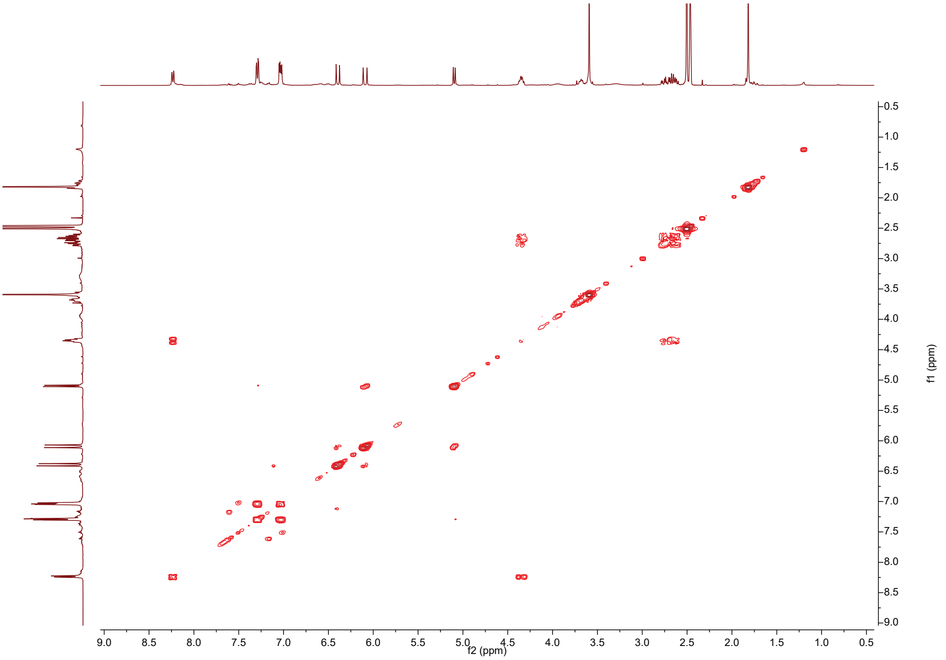

Figure S51: gCOSY of compound **19** in d$_6$-DMSO.

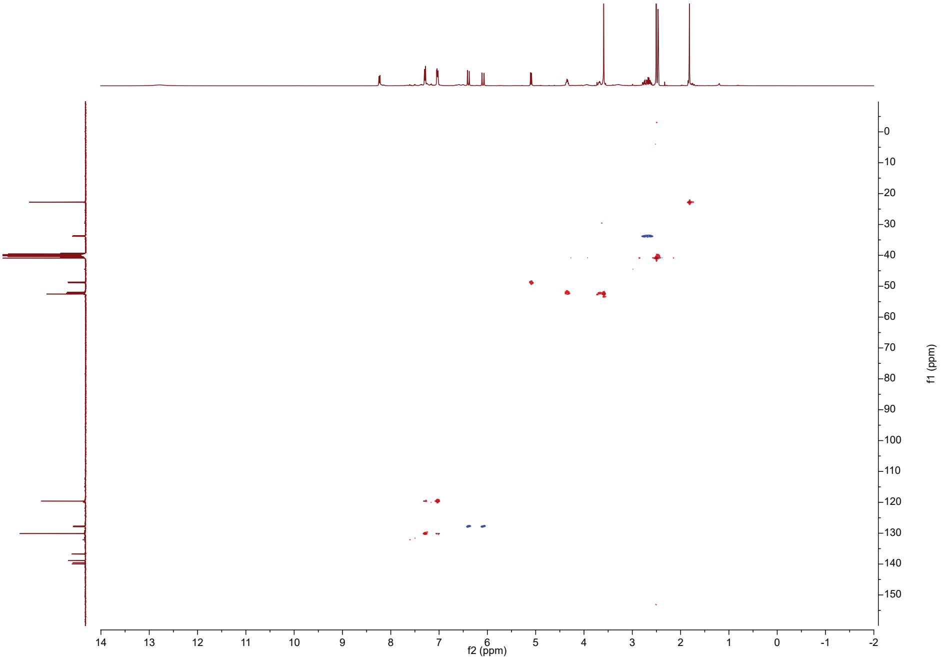

Figure S52: gHSQC of compound **19** in d$_6$-DMSO.

5.5.10 LC-MS data

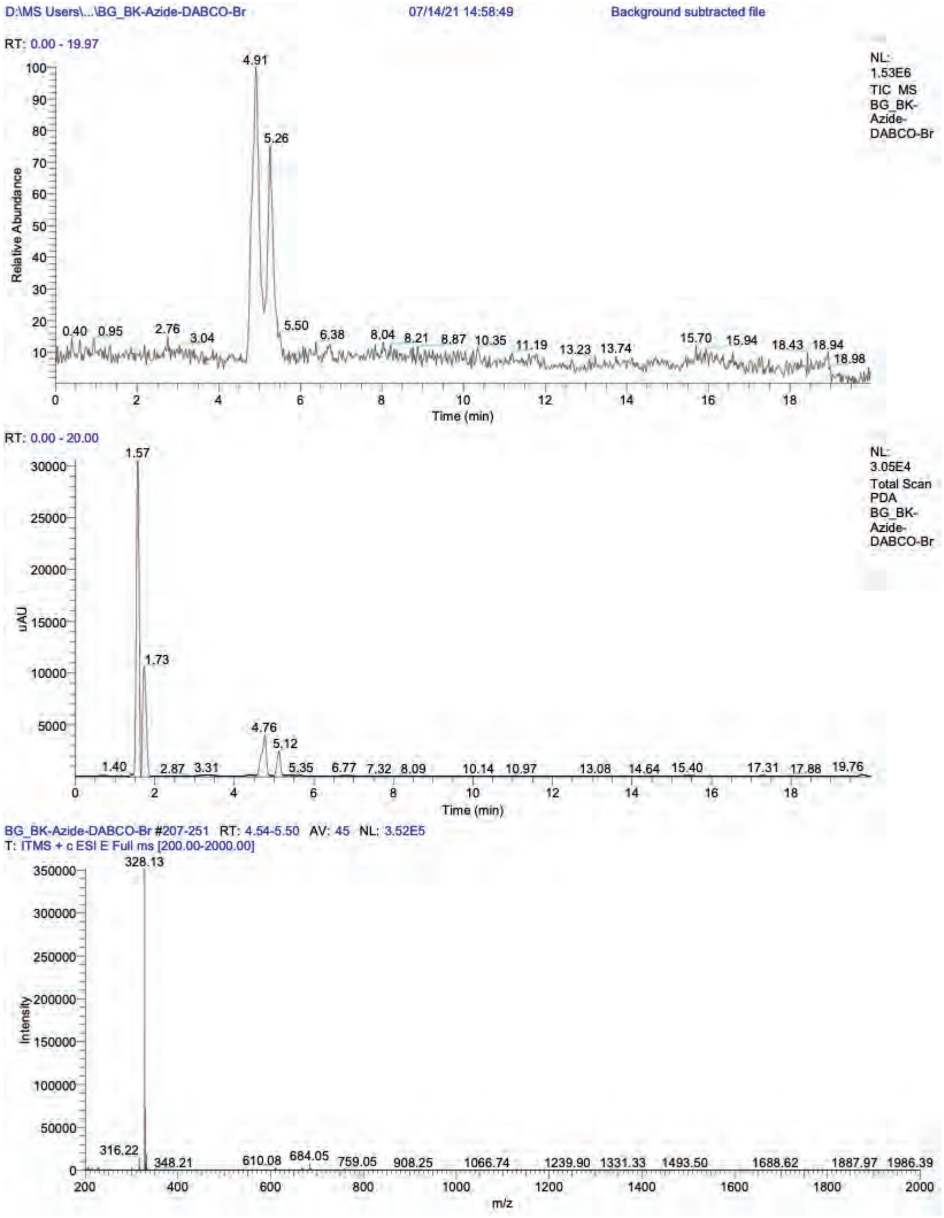

Figure S53: LCMS-data for compound **13**.

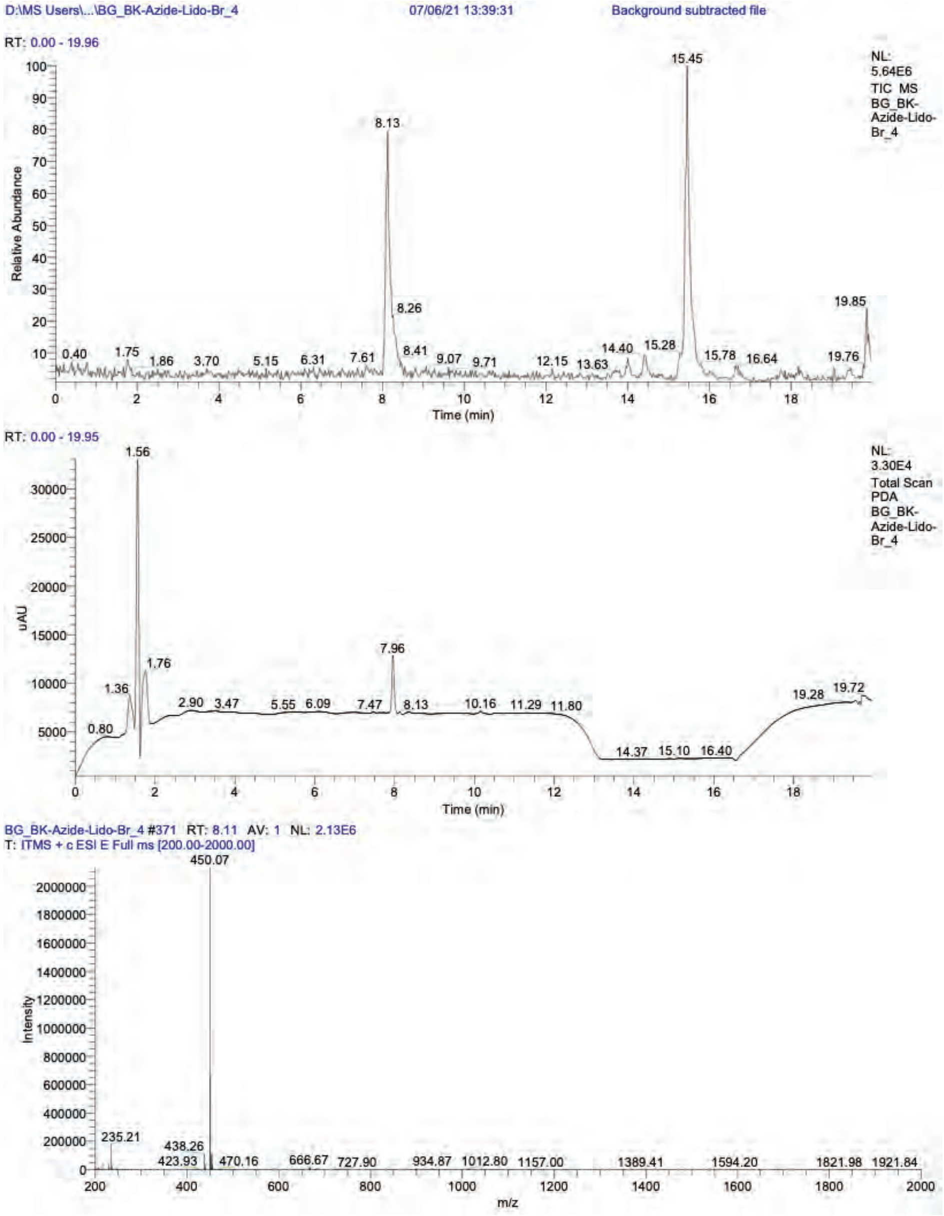

Figure S54: LCMS-data for compound **8**.

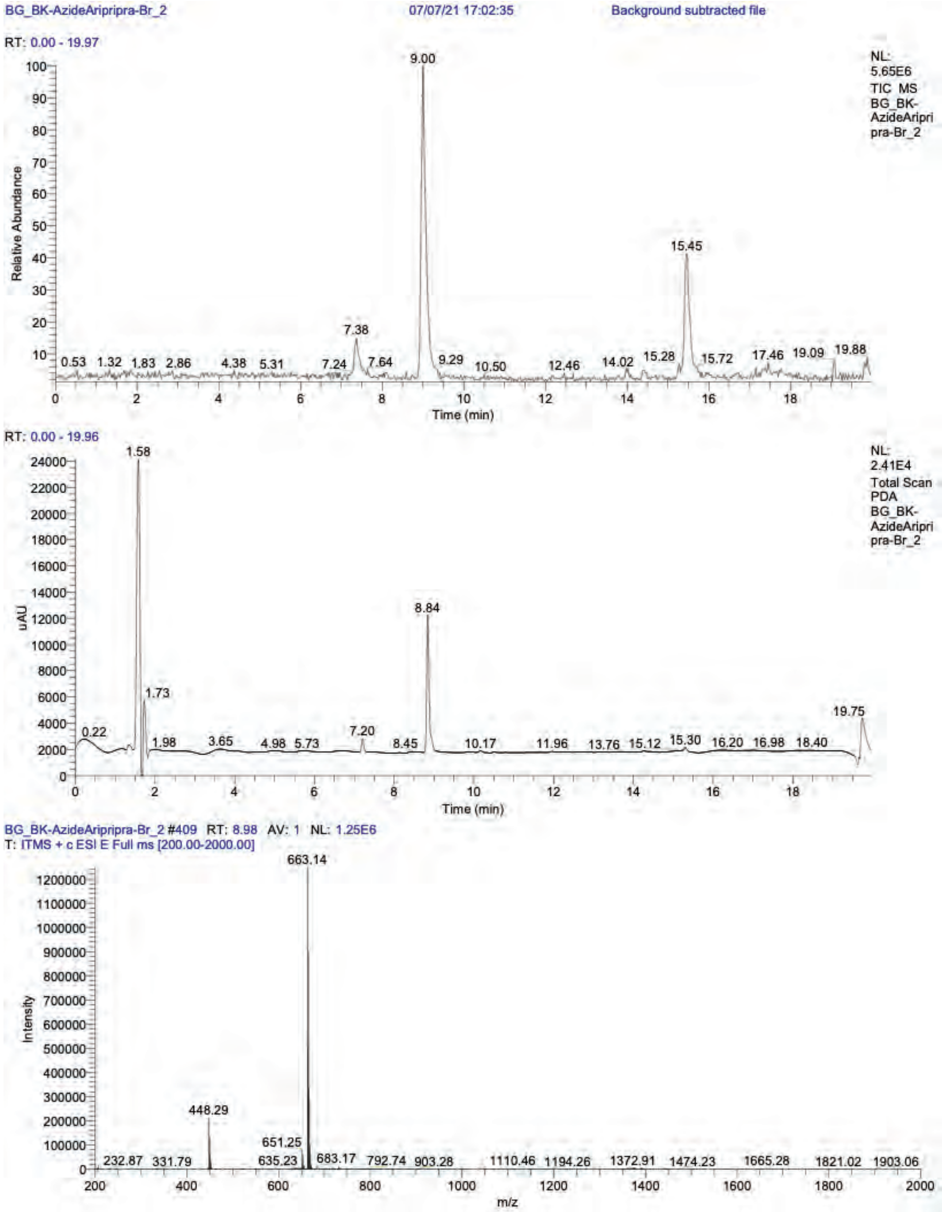

Figure S55: LCMS-data for compound **11**.

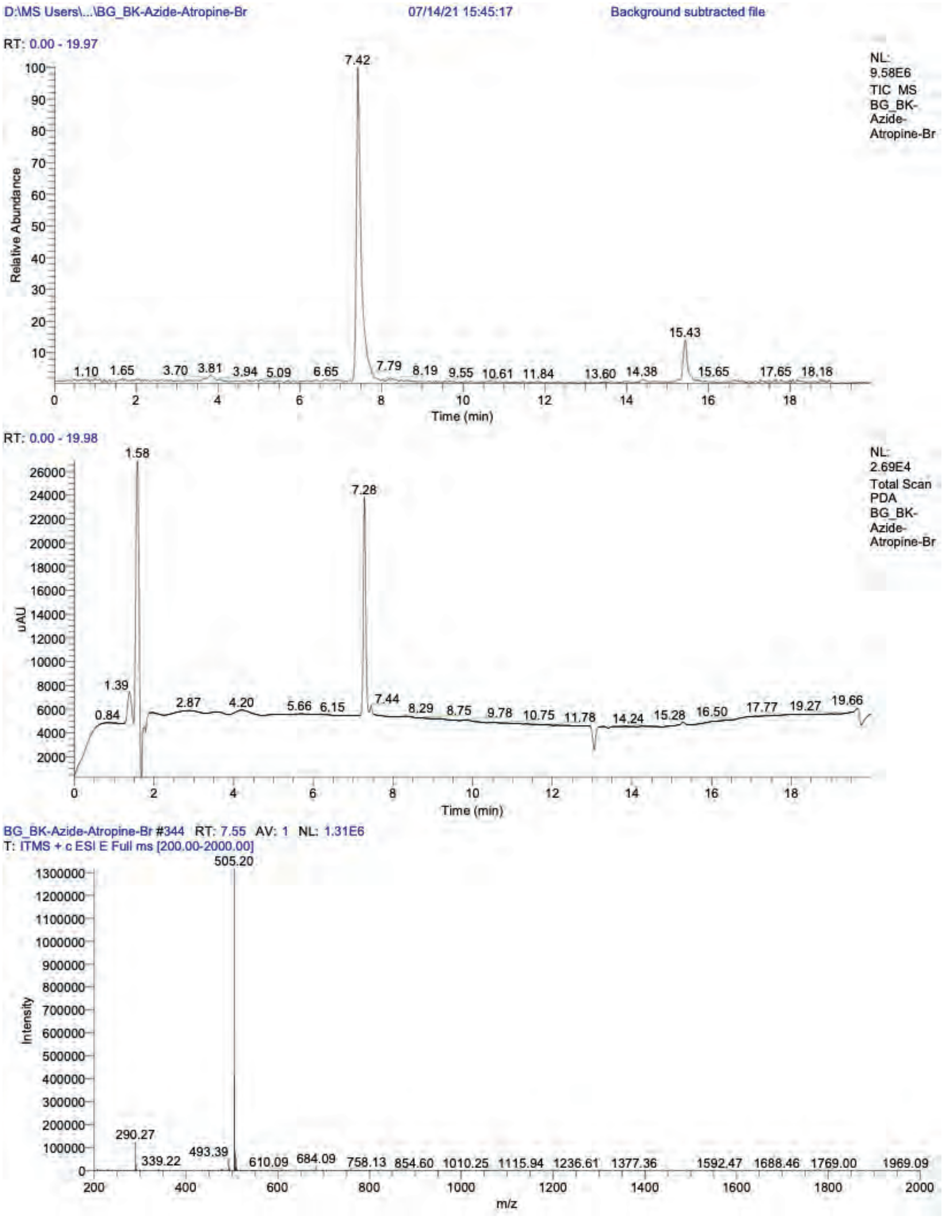

Figure S56: LCMS-data for compound **9.**

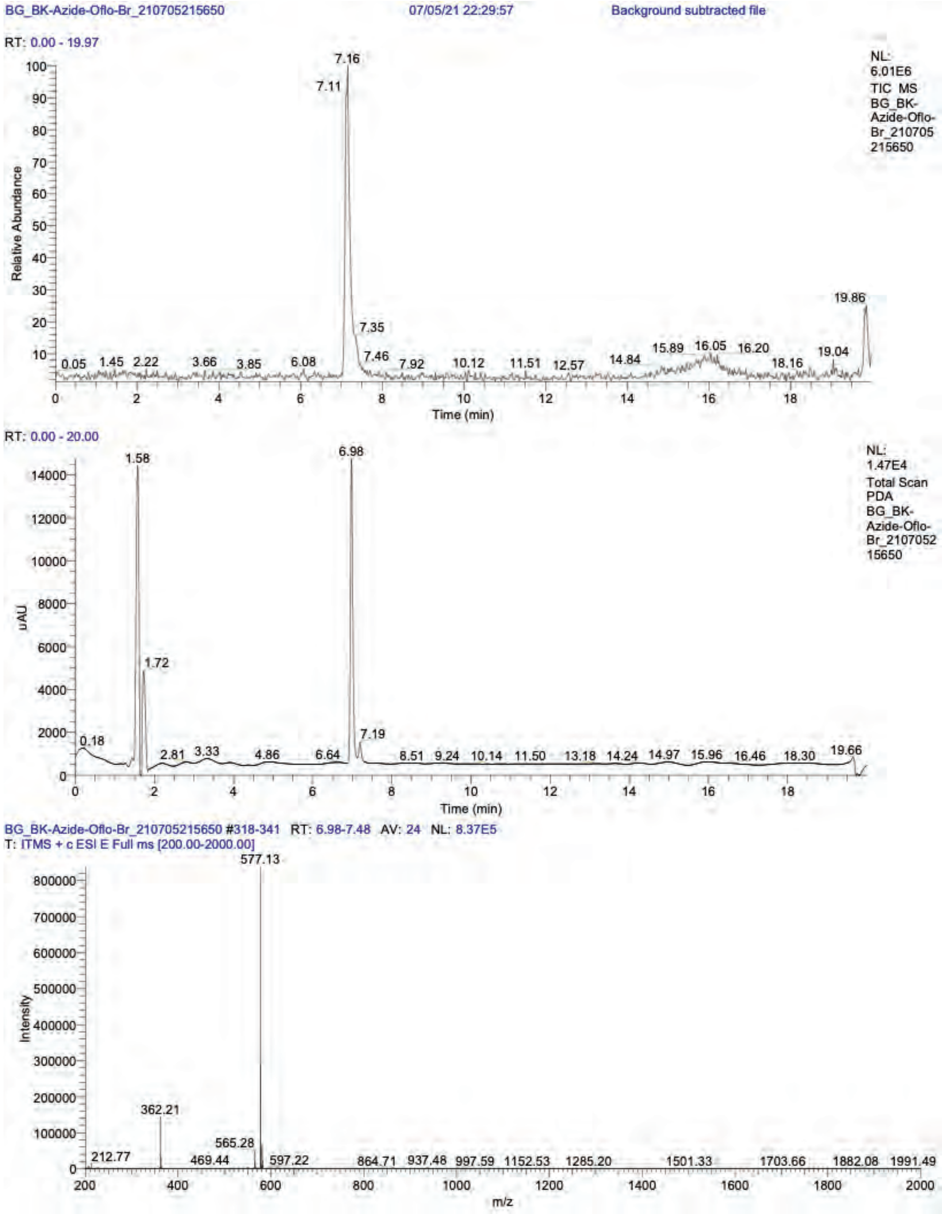

Figure S57: LCMS-data for compound **10.**

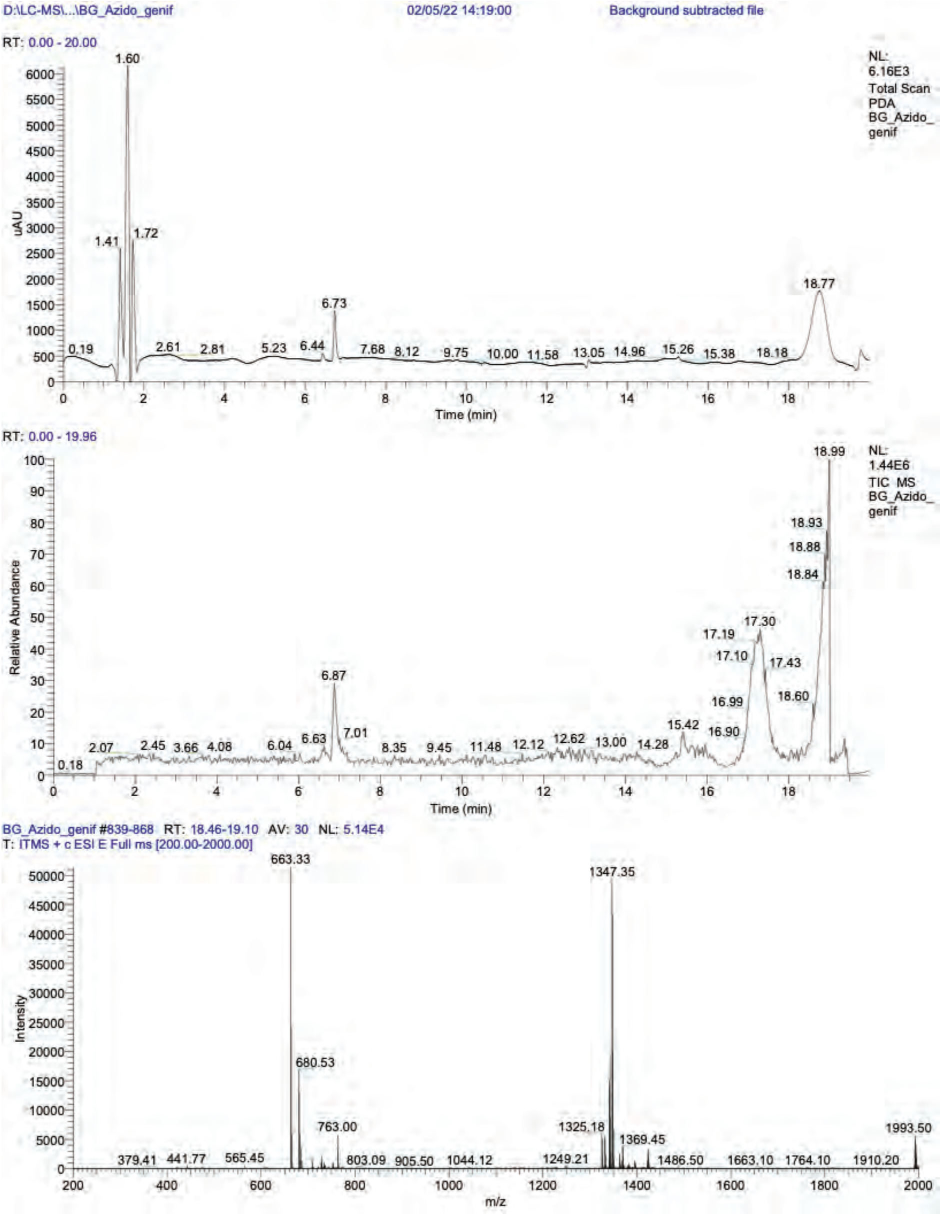

Figure S58: LCMS-data for compound **12.**

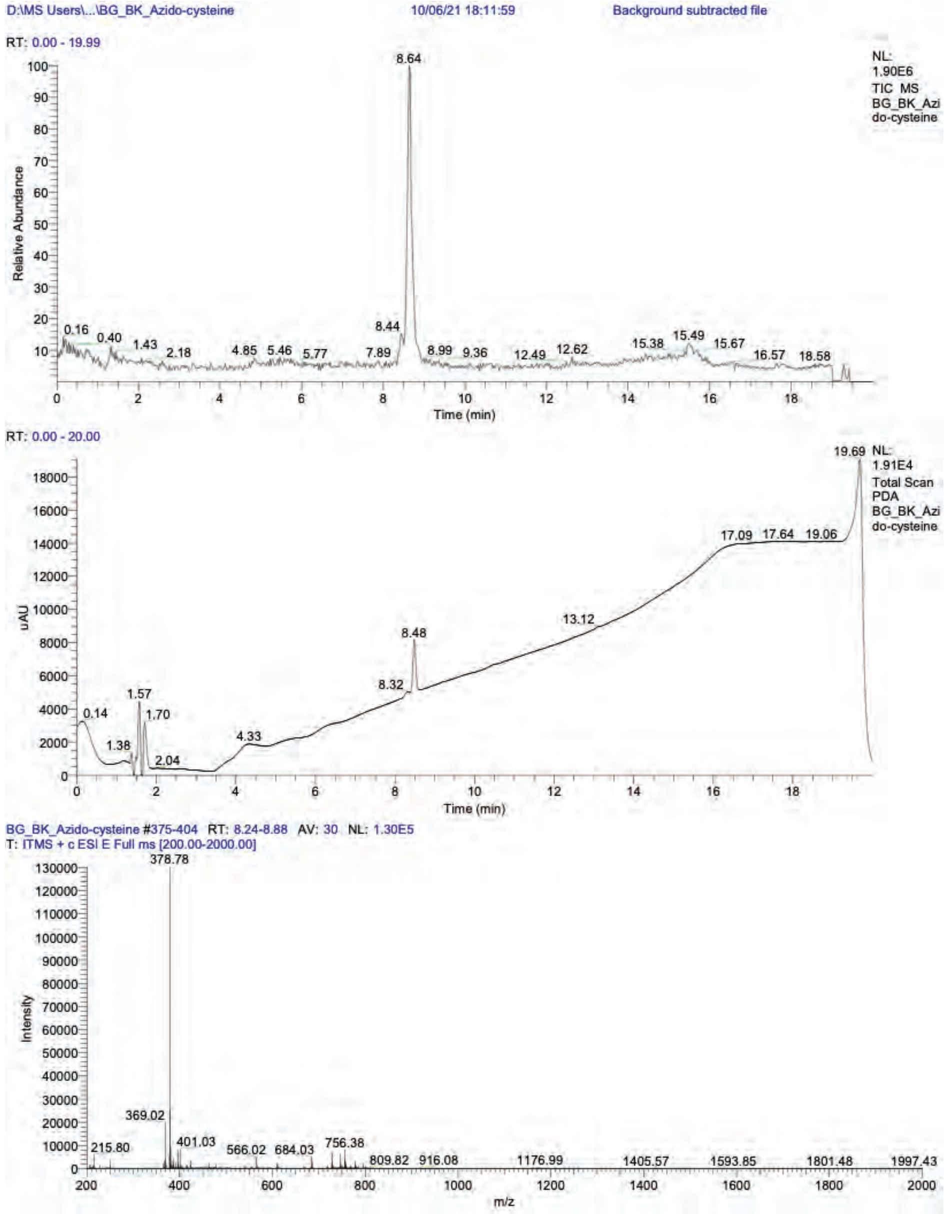

Figure S59: LCMS-data for compound **19**.

SUMMARY

Signal transduction in living systems enables adaptive and interactive response to external stimuli. These rudimentary primary processes developed by nature are currently absent in synthetic materials. Implementing these processes in materials can have widespread advances in regenerative medicine, diagnostics or nanomachines. Taking inspiration from nature, organocatalytic reactions will be used in the design of new strategies for signal-responsive materials. These systems undergo physical or mechanical changes in response to stimuli triggered chemical transformations, enabling signal-recognition, signal-translation and ultimately leading to pre-programmed material response. In this thesis, small molecules, usually used as organocatalysts, are implemented in materials to develop signal-triggered and autonomous systems for applications such as controlled drug delivery, autonomous actuators or detection platforms.

In **Chapter 2**, organocatalytic reactions in aqueous media are discussed and evaluated on their potential implications/applicability in chemical biology or biomedicine. First, different activation modes of organocatalysts are introduced and landmark contributions are discussed. Importantly, this chapter focuses on nucleophilic and general/specific base catalysis, since nucleophilic substitution chemistry (*Chapter 2, Supplementary Table S1, reaction 4*) plays a crucial role in the following chapters. Several reactions are evaluated based upon functional groups, solvent/co-solvent ratio, toxicity of catalyst or reactants, pK_a but also reaction conditions such as the microenvironment or additives. The consideration of all these criteria is fundamental to identify suitable reaction candidates for biologically relevant applications.

Amongst the organocatalysis-mediated reactions presented in **Chapter 2**, nucleophilic substitution chemistry is selected for the development of a new chemical reaction network (CRN) in **Chapter 3**. Here, the allylic compound diethyl(α-acetoxymethyl) vinylphosphonate (DVP) is used as fuel in combination with S- or N-terminal nucleophiles to operate the CRN. The CRN enables control over the formation of positive charges on a tertiary amine substrate. Incorporation of the CRN in diverse polymer materials leads to a temporally programmed transition from collapsed and hydrophobic to solvated, hydrophilic polymer chains and vice versa by controlling polymer-solvent interactions. We demonstrate this concept via controlled manipulation of material properties (e.g. stimuli-induced or autonomous control), including micelles assembly/disassembly and hydrogel swelling/de-swelling.

In **Chapter 4**, we describe an approach for detecting thiol analytes through a self-propagating amplification cycle that triggers macroscopic degradation of a hydrogel scaffold. The cycle is designed to detect thiol-analytes via nucleophilic substitution of phosphine from allylic phosphonium salt. The liberated phosphine reduces a disulfide to form two thiols, closing the cycle and ultimately resulting in exponential amplification of the thiol input. Mathematical model simulations are used to predict the behaviour of the amplification cycle in response to varying signal input. The amplified response of the cycle on disulfide-crosslinked hydrogels is demonstrated towards multiple thiol analytes, both molecular (small molecules and glutathione) and macromolecular (DNA, bovine serum albumin) biomolecules. Furthermore, we show that the self-propagating amplification cycle could be initiated by force-generated molecular scission, enabling damage-triggered hydrogel destruction.

In **Chapter 5**, we introduce signal-responsive, tertiary amine-based prodrugs, their incorporation into the polymeric backbone of hydrogels and signal-controlled drug release from hydrogel scaffolds. Specifically, we develop here a Morita-Baylis-Hillman (MBH)-adduct which forms quaternary amine prodrug-linkers with various tertiary amine-based drug candidates. Based on the pre-existing azide-functionality on the molecular scaffold, a click reaction with alkyne-modified polymers enables covalent prodrug-linkage with hydrogel structures. Drug activation is then achieved through nucleophilic substitution on prodrugs by addition of biological S- or N-terminal nucleophiles. By using this strategy, we also demonstrate controlled drug release upon signal activation for an *in vitro* anticancer drug release assay, achieving ~100% wound closure inhibition of small lung cancer cells (A549).

In **conclusion**, this research shows how the implementation of moieties sensitive to nucleophilic substitution reactions in high water content materials lead to precise control of the material properties. By utilizing tertiary amines or trivalent phosphines together with electron deficient Morita-Baylis-Hillman (MBH) adducts, charged MBH-salts are formed. These salts are reversible upon addition of S or N-terminal nucleophiles. Combining this chemistry with polymeric materials (e.g. hydrogels or micelles) enables control over material properties, ranging from micellar assembly/disassembly, hydrogel swelling/-de-swelling, analyte detection via material degradation to drug activation from hydrogel scaffolds. This concept can pave the way to the development of the next generation soft materials, where signal or time-programmed control over charge density allows for interactive and adaptive material properties.

SAMENVATTING

Signaaltransductie in levende systemen maakt een adaptieve en interactieve reactie op externe stimuli mogelijk. Deze door de natuur ontwikkelde rudimentaire primaire processen ontbreken momenteel in synthetische materialen. Het implementeren van deze processen in materialen kan grote vooruitgang opleveren in de regeneratieve geneeskunde, diagnostiek of nanomachines. Geïnspireerd door de natuur zullen organokatalytische reacties worden gebruikt bij het ontwerpen van nieuwe strategieën voor signaalgevoelige materialen. Deze systemen ondergaan fysieke of mechanische veranderingen als reactie op door stimuli veroorzaakte chemische transformaties, waardoor signaalherkenning en signaalvertaling mogelijk zijn en uiteindelijk leiden tot een voorgeprogrammeerde materiële respons. In dit proefschrift worden kleine moleculen, meestal gebruikt als organokatalysatoren, geïmplementeerd in materialen om signaalgestuurde en autonome systemen te ontwikkelen voor toepassingen zoals gecontroleerde medicijnafgifte, autonome actuatoren of detectieplatforms.

In **Hoofdstuk 2** worden organokatalytische reacties in waterige media besproken en geëvalueerd op hun potentiële implicaties/toepasbaarheid in de chemische biologie of biogeneeskunde. Eerst worden verschillende activeringswijzen van organocatalysatoren geïntroduceerd en worden belangrijke bijdragen besproken. Belangrijk is dat dit hoofdstuk zich richt op nucleofiele en algemene/specifieke basekatalyse, aangezien nucleofiele substitutiechemie (*hoofdstuk 2, aanvullende tabel S1, reactie* 4) een cruciale rol speelt in de volgende hoofdstukken. Verschillende reacties worden geëvalueerd op basis van functionele groepen, oplosmiddel/co-oplosmiddelverhouding, toxiciteit van katalysator of reactanten, pKa maar ook reactieomstandigheden zoals de micro-omgeving of additieven. De overweging van al deze criteria is van fundamenteel belang om geschikte reactiekandidaten voor biologisch relevante toepassingen te identificeren.

Van de organokatalyse-gemedieerde reacties die in **Hoofdstuk 2** worden gepresenteerd, wordt nucleofiele substitutiechemie geselecteerd voor de ontwikkeling van een nieuw chemisch reactienetwerk (CRN) in **Hoofdstuk 3**. Hier wordt de allylische verbinding diethyl(α-acetoxymethyl)vinylfosfonaat (DVP) gebruikt als brandstof in combinatie met S- of N-terminale nucleofielen om de CRN te laten werken. De CRN maakt controle mogelijk over de vorming van positieve ladingen op een tertiair aminesubstraat. Opname van het CRN in diverse polymeermaterialen leidt tot een in de tijd geprogrammeerde overgang van ingestorte en hydrofobe naar gesolvateerde, hydrofiele polymeerketens en vice versa door de interacties tussen polymeer en oplosmiddel te controleren. We demonstreren dit concept via gecontroleerde manipulatie van materiaaleigenschappen (bijvoorbeeld door stimuli geïnduceerde of autonome controle), inclusief de montage/demontage van micellen en het zwellen/ontzwellen van hydrogel.

In **Hoofdstuk 4** beschrijven we een aanpak voor het detecteren van thiolanalyten via een zichzelf voortplantende amplificatiecyclus die macroscopische afbraak van een hydrogelsteiger teweegbrengt. De cyclus is ontworpen om thiol-analyten te detecteren via nucleofiele substitutie van fosfine uit allylisch fosfoniumzout. Het vrijgekomen fosfine reduceert een disulfide om twee thiolen te vormen, waardoor de cyclus wordt gesloten en uiteindelijk resulteert in een exponentiële versterking van de thiolinvoer. Wiskundige modellensimulaties worden gebruikt om het gedrag van de versterkingscyclus te voorspellen als reactie op variërende signaalinvoer. De versterkte respons van de cyclus op disulfide-verknoopte hydrogels wordt aangetoond tegen meerdere thiolanalyten, zowel moleculaire (kleine moleculen en glutathion) als macromoleculaire (DNA, runderserumalbumine) biomoleculen. Bovendien laten we zien dat de zichzelf voortplantende amplificatiecyclus kan worden geïnitieerd door door kracht gegenereerde moleculaire splitsing, waardoor door schade veroorzaakte hydrogelvernietiging mogelijk wordt.

In **Hoofdstuk 5** introduceren we signaalresponsieve, op tertiaire amines gebaseerde prodrugs, hun integratie in de polymere ruggengraat van hydrogels en signaalgecontroleerde medicijnafgifte uit hydrogelsteigers. Concreet ontwikkelen we hier een Morita-Baylis-Hillman (MBH)-adduct dat quaternaire amine-prodrug-linkers vormt met verschillende op tertiaire amine gebaseerde kandidaat-geneesmiddelen. Gebaseerd op de reeds bestaande azide-functionaliteit op het moleculaire platform, maakt een klikreactie met alkyn-gemodificeerde polymeren covalente prodrug-koppeling met hydrogelstructuren mogelijk. Geneesmiddelactivatie wordt vervolgens bereikt door nucleofiele substitutie op prodrugs door toevoeging van biologische S- of N-terminale nucleofielen. Door deze strategie te gebruiken demonstreren we ook gecontroleerde medicijnafgifte na signaalactivatie voor een in vitro antikankertest voor medicijnafgifte, waarbij ~100% remming van de wondsluiting van kleine longkankercellen wordt bereikt (A549).

Concluderend laat dit onderzoek zien hoe de implementatie van groepen die gevoelig zijn voor nucleofiele substitutiereacties in materialen met een hoog watergehalte leidt tot nauwkeurige controle van de materiaaleigenschappen. Door tertiaire aminen of driewaardige fosfinen te gebruiken samen met elektron-deficiënte Morita-Baylis-Hillman (MBH)-adducten, worden geladen MBH-zouten gevormd. Deze zouten zijn omkeerbaar na toevoeging van S- of N-terminale nucleofielen. Het combineren van deze chemie met polymere materialen (bijv. hydrogels of micellen) maakt controle over materiaaleigenschappen mogelijk, variërend van micellaire assemblage/demontage, hydrogelzwelling/-de-zwelling, analytdetectie via materiaaldegradatie tot medicijnactivatie vanuit hydrogelsteigers. Dit concept kan de weg vrijmaken voor de ontwikkeling van de volgende generatie zachte materialen, waarbij signaal- of tijdgeprogrammeerde controle over de ladingsdichtheid interactieve en adaptieve materiaaleigenschappen mogelijk maakt.

Acknowledgements

Although the PhD was a lot of hard work, I really enjoyed it, having the freedom and flexibility to pursuit and explore different chemistries and materials and combine it to make something unique, was worth it all along. I learned so much during this time. Clearly, I won't miss the work on the weekends, but I will miss the people with who I shared this experience, who stood by my side during hard times and during all successes, without their help and support this thesis would not have been accomplished.

First of all, I would like to like to thank my daily supervisor and promoter **Rienk Eelkema**. Thank you for giving me the opportunity to do my PhD research in your group. I am proud of what we and the other collaborators have achieved! You were always very patient with me and helped me through many challenging times with guidance and advice. I greatly appreciate our discussions and that although you are very busy, you always did make time for my questions. Many thanks also to my co-promoter **Jan van Esch** for insightful questions during the group meetings and my yearly meetings. Also, thanks for accepting me at the ASM research group, where I felt very welcomed from the start. **Gabrie Meesters**, thank you for being my mentor during my PhD journey, I really enjoyed our discussions and I am very grateful of your support on my personal development, the invaluable life-lessons and career advices. **Pouyan E. Boukany** thank you for being part of my committee and for the collaboration that led to chapter 5 of this thesis. Many thanks also to **Margherita Tavasso**, who worked long hours in the mammalian lab to biologically validate the chemistry developed in chapter 5. **Wolter Jager**, thanks for giving me your precursor materials to do experiments on fluorescence as well as all the discussions we had about it. **Ger Koper** and **Laura Rossi** thank you for your experience and critical input during our ASM group discussions/meetings. **Stephen Picken**, thanks for being part of my committee and thanks for the nice chats and discussions we had in front of the Applied Science building. **Eduardo Mendes**, I really enjoyed our talks during my master thesis and afterwards. It was a pleasure and valuable experience working with you. To all the **PI's of ASM**, I learned a lot from you and I would like to express my gratitude, you have been encouraging, supportive and challenged me during my PhD time to further improve my skills and knowledge. **Stephen Eustace** thanks for taking care of the NMR and helping me troubleshoot it even during the weekends. We made a great team and you taught me a lot.

Furthermore, I would like to thank all other committee members: **Atsushi Urakawa**, **Marleen Kamperman** and **Christian A. Nijhuis** for taking the time to read and assess my PhD thesis.

Gary, thanks for being such a good friend during all those years we know each other (~14+ years) and also thanks for your support during the actual defence day as one of my paranymphs.

Next, I would like to thank my ASM colleagues who I shared over 4.5 years of great memories. **Tobias**, thanks for being one of my paranymphs and for always listening to my frustrations and bringing things into perspective. We shared countless great moments together, either during coffee breaks, Thursday drinks, Hanos shopping's, daily chit-chat, BBQs or that one time when you dropped your phone while driving bike with Hendrick. You are a good friend and great BBQ master. **Lars**, I really appreciate your honesty, your interesting perspectives and all the advices you gave me, many thanks for that. It is great to talk with you about personal development and future plans. **Reece** thanks for your support on the material development, all the insightful discussions on (polymer) chemistry and the nice collaborations which led to quality work as well as all the good times outside the lab. **Sarah** and **Suellen** thanks for saying properly 'goodmorning' in the corridors, you came a long way, it is approved ☺. **Sarah**, thanks for continuing to organize the ASM after-work drinks. Not to forget, I really enjoyed seeing you driving a 'locked' bike. **Suellen**, thanks for the Brazilian coffee tasting, and that you were always in for Thursday drinks as well as the good times outside the lab. **Qian** and **Meng**, thanks for everything. Cannot explain how much I enjoyed our 'hotpot' dinners, excursions to explore the Netherlands and our science/project talks. I am sure we will see each other one day again. **Yongjun**, **Bowen, Guotai** and **Tobias**, I will never forget our conference trip to Lecce, we had so much fun. Thanks for making this a great memory. **Bowen**, I really appreciate your help with the rheology and your patience with me. Our travels to Milan, Venice and the summer school in Italy was great fun and your proposal to go to a Chinese restaurant in Venice, turned out to be great, HAHA. **Guotai**, we had always good times being the ones working late hours. I am really impressed by your determination and valued your critical attitude towards research. Also, many thanks to **Jungchen**, it was always great to have you around, you are always smiling, keep up this happiness it is contagious. **Nancy**, **Fan** and **Yu**, it was great to share many ASM dinners and drinks together and discuss (non) work-related topics. **Peggy**, your encouraging words and your cheerful attitude is a great to have around, many thanks for that. You are full of surprises and an experience on its own. **Michelle**, it was a great experience to work on the review paper together, you have a lot of theoretical knowledge. **Ardeshir**, big thanks to you for all the great work and help on the modelling part of chapter 4. I always enjoyed the time we spend on discussing work and non-work-related topics. **Hendrik**, **Elmira**, **Benni**, **Anastiasia** and **Sahil**, it was great to have you around and share experiences from the ASM-group. **Mariano**, thank you for the nice chats in the lab, you thought me a lot of tips & tricks to master columns, I really appreciated that. **Marcel**, **Duco** and **Sietse**, thanks for all the help in the labs, taking care of the labs and your company during many ASM-dinners and drinks. **Duco**, thanks for the help with the SEM, your advices and suggestions in and around the lab were very useful. **Marcel**, thanks for the company during Thursday drinks, it's always great to talk to you. **Susan** and **Fanny**, you were always very kind and helped me a lot to find my way around in the labs and all questions I had. Your advices and guidance at the beginning helped me a lot. Many thanks. **Thomasz**, **Serhii**, **Vasudevan**, **Matija**, **Vincent**, **Jos**, **Kai, Emma, Angie, Cansel** and **Yiming**, thanks for the warm welcome to the ASM-group and the great time we had, you guys introduced me to the Thursday drinks. I am glad to have experienced this.

Kailun and **Sanjana**, it was always great to see you at the coffee corner and catch up about research, accomplishments and general stuff. I really enjoyed your presence and your positive outlook. Many thanks for all the encouragements.

Georgy and **Richard,** I will be missing our weekend work-sessions, where we share experiences during a coffee break outside, no matter what the weather was. **Georgy**, thank you for all the knowledge, help, guidance and advices from science to life in general. It was great to have you around and to be able to approach you for any problems you were always happy to help. Many thanks for that. **Veby** and **Els**, a big thank you for taking care of all the administrative stuff, especially during the few times I needed to renew my TU Delft access. Also, **Veby** many thanks for the nice talks, your happiness and cheerful personality was/is always appreciated.

Also, many thanks to all students I have worked with: **Max**, **Mernoush** and **Emmily**. I really enjoyed working with you, it was a great experience with many insightful experiments and good results. Your work helped me a lot and I wish you all the best in your future and careers.

To the Italian group: **Edo**, **Francesca** and **Filippo**, **Cate** and **Andrea**, **Jackopino**, **Jack** and **Rochi**, **Billy**, **Giups** and **Isa**, **Lara** and **Daniele** and the other guys, thanks for accepting the 'German' into your group. You guys made my weekends and free-time much more colourful. Thanks a lot.

Finally, I would like to thank my family, my parents **Beate** and **Robert,** my grandma's, **Steffi** and **Christine** and my grandpa **Horst** for their unconditional support throughout my life**.** *Ich kann euch nicht genug danken fuer alles was ihr fuer mich getan habt oder wie oft ihr mich unterstuetzt habt. Ich bin sehr froh, dass ich euch habe und mich immer auf euch verlassen kann. Ich habe euch sehr lieb und Vielen Dank fuer Alles!*

The best at the end. **Irene**, thanks for always being there for me and for believing in me, without your support I would not have come so far. As it turns out, we make a great team at work and outside of work. You understand me and accept me for who I am, I deeply cherish our relationship. I am excited to see what the future holds for us and I am looking forward to our next adventures.

So, this is it here I am writing the last part of my thesis and it feels really good to finally finish this chapter of my life. A valuable chapter, indeed!

Thanks everybody.

Benjamin Klemm

About the author

Benjamin Klemm was born on the 6th of July, 1989 in Karl-Marx-Stadt, jetzt Chemnitz, Germany. He obtained his Bachelor Degree in Water Management at the Hogeschool Zeeland, Vlissingen in 2013. After graduating, he continued his studies with the Joint Master Degree in Water Technology at Wageningen University, University of Groningen and University of Twente. The following year, he started the MSc. Degree in Chemical Engineering at Delft University of Technology. In 2016, he started as research intern in the group of Francesco Picchioni in the Chemical Engineering department at Groningen University. He obtained his Master Degree in Water Technology in August 2016 with the thesis entitled “Chemical additives for enhanced oil recovery” under the supervision of Prof. Picchioni. After the master thesis in the Advanced Soft Matter group of Prof. Dr. Jan van Esch, Benjamin obtained the Honours Master Degree in Chemical Engineering from TU Delft under the supervision of Dr. Eduardo Mendes in October 2017, with the thesis “Cell based drug delivery devices using photo-polymerized hydrogel backpacks for cellular hitchhiking”. In the same year, he joined the Advanced Soft Matter group as PhD student under the supervision of Dr. Rienk Eelkema. His research focused on realizing interactive organic materials with a stimuli-response behaviour inspired by cellular signal transduction. Since December 2022, he is Scientist Innovator at TNO in the Materials Solutions department in Eindhoven.

List of publications

- **Klemm, B.**, Tavasso, M., Piergentili, I., Satijn, M., Brevé, T.G., Boukany, P.E. and Eelkema, R. Signal-triggered release of allyl-caged tertiary amine drugs from polymer hydrogels. *manuscript submitted.*
- **Klemm, B.**, Roshanasan, A., Piergentili, I., van Esch, J. H., & Eelkema, R. (**2023**). Naked-eye thiol analyte detection via self-propagating, amplified reaction cycle. *Journal of the American Chemical Society*.
- Piergentili, I., Cai, M., **Klemm, B.**, Xu, B., Luo, S., & Eelkema, R. (**2023**). Enhancing trigger sensitivity of nanocarriers through organocatalytic oxidant activation. *Cell Reports Physical Science*, 4(9).
- Piergentili, I., Hilberath, T., **Klemm, B.**, Hollmann, F., & Eelkema, R. (**2023**). Enhancing the ROS Sensitivity of a Responsive Supramolecular Hydrogel Using Peroxizyme Catalysis. *Biomacromolecules*.
- Wu, B., Lewis, R. W., Li, G., Gao, Y., Fan, B., **Klemm, B.**, ... & Eelkema, R. (**2023**). Chemical signal regulated injectable coacervate hydrogels. *Chemical Science*, 14(6), 1512-1523.
- Lewis, R. W., Muralidharan, A., **Klemm, B.**, Boukany, P. E., & Eelkema, R. (**2023**). Nucleophile responsive charge-reversing polycations for pDNA transfection. *Polymer Chemistry*, 14(14), 1591-1601.
- **Klemm, B.**, Lewis, R. W., Piergentili, I., & Eelkema, R. (**2022**). Temporally programmed polymer–solvent interactions using a chemical reaction network. *Nature Communications*, 13(1), 6242.
- Lewis, R. W., **Klemm, B.**, Macchione, M., & Eelkema, R. (**2022**). Fuel-driven macromolecular coacervation in complex coacervate core micelles. *Chemical Science*, 13(16), 4533-4544.
- Piergentili, I., Bouwmans, P. R., Reinalda, L., Lewis, R. W., **Klemm, B.**, Liu, H., ... & Eelkema, R. (**2022**). Thioanisole ester based logic gate cascade to control ROS-triggered micellar degradation. *Polymer Chemistry*, 13(16), 2383-2390.
- Li, G., Trausel, F., van Der Helm, M. P., **Klemm, B.**, Brevé, T. G., van Rossum, S. A., ... & Eelkema, R. (**2021**). Tuneable control of organocatalytic activity through host–guest chemistry. *Angewandte Chemie International Edition*, 60(25), 14022-14029.
- Liu, Q., Zhao, M., Mytnyk, S., **Klemm, B.**, Zhang, K., Wang, Y., ... & van Esch, J. H. (**2019**). Self-Orienting Hydrogel Micro-Buckets as Novel Cell Carriers. *Angewandte Chemie*, 131(2), 557-561.
- van Der Helm, M. P., **Klemm, B.**, & Eelkema, R. (**2019**). Organocatalysis in aqueous media. *Nature Reviews Chemistry*, 3(8), 491-508.
- **Klemm, B.**, Picchioni, F., van Mastrigt, F., & Raffa, P. (**2018**). Starlike branched polyacrylamides by RAFT polymerization—part I: synthesis and characterization. *ACS omega*, 3(12), 18762-18770.
- **Klemm, B.**, Picchioni, F., Raffa, P., & van Mastrigt, F. (**2018**). Star-like branched polyacrylamides by RAFT polymerization, part II: performance evaluation in enhanced oil recovery (EOR). *Industrial & Engineering Chemistry Research*, 57(27), 8835-8844.